

Międzyuczelniany Wydział Biotechnologii
Uniwersytetu Gdańskiego i Gdańskiego Uniwersytetu Medycznego

mgr Kamila Agnieszka Butowska

Wybrane koniugaty doksorubicyny jako
potencjalne układy w terapii
przeciwnowotworowej
Selected doxorubicin conjugates for anticancer therapy

Praca przedstawiona
Radzie Dyscypliny Nauki Biologiczne Uniwersytetu Gdańskiego
celem uzyskania stopnia doktora
w dziedzinie nauk ścisłych i przyrodniczych
w dyscyplinie nauki biologiczne

Promotor: dr hab. Jacek Piosik, prof. UG
Międzyuczelniany Wydział Biotechnologii Uniwersytetu Gdańskiego
i Gdańskiego Uniwersytetu Medycznego

Drugi Promotor: prof. dr hab. Janusz Rak
Wydział Chemii Uniwersytetu Gdańskiego

GDAŃSK 2021

W latach 2017–2020 część doświadczalna niniejszej pracy została wykonana na Międzyuczelnianym Wydziale Biotechnologii Uniwersytetu Gdańskiego i Gdańskiego Uniwersytetu Medycznego oraz na Wydziale Chemii Uniwersytetu Gdańskiego.



W latach 2020–2021 część doświadczalna niniejszej pracy została wykonana na Wydziale Inżynierii Uniwersytetu Pensylwanii w ramach stypendium przyznanego przez Narodową Agencję Wymiany Akademickiej (Program im. Wilhelminy Iwanowskiej).



Dziękuję!

Dr. hab. Jackowi Piosikowi za wolność naukową, zrozumienie, życzliwość, duże pokłady cierpliwości i popieranie kolejnych, nawet tych najbardziej zaskakujących, pomysłów na badania naukowe.

Prof. dr. hab. Januszowi Rakowi za opiekę, zaufanie i wsparcie na każdym etapie pracy. Co ważniejsze, za godziny spędzone na rozmowach przy kawie, które były inspiracją, motywacją oraz pozwoliły mi uwierzyć, że mogę osiągnąć wiele. Za bycie zawsze, gdy tego potrzebowałam!

Prof. Michaelowi J. Mitchellowi za życzliwość, nieograniczone możliwości rozwoju i wskazanie nowej drogi naukowej, która okazuje się być moją przyszłością.

Pracowni Biofizyki, Katedrze Chemii Fizycznej i Zespołowi prof. Mitchell'a za miłą atmosferę pracy i wspomnienia.

Samancie, Witkowi, Magdzie, Lidce, Paulinie, Karinie, Ani C. i Agnieszce, za pomoc w realizacji badań, wsparcie merytoryczne i współpracę. Jednak przede wszystkim za to, że po tych kilku latach mogę Was nazwać Waszą moją chemiczną rodziną, bez której nie przetrwałabym tych szalonych godzin w laboratorium.

Mamie, Tacie i Bratu, za to, że zawsze czułam Wasze wsparcie, miłość, ochronę i za wszystkie próby zrozumienia czym się zajmuję naukowo. Za to, że mam miejsce, które mogę nazwać domem.

Przyjaciółom, którzy pojawili się na różnych etapach mojego życia i nigdy nie zniknęli. Za to, że pomimo dzielących nas kilometrów, nigdy nie pozwolili czuć mi się samotną. Byliście ramieniem, w które mogłam się wypłakać, uśmiechem, przetańczonymi godzinami, rozmowami... byliście wszystkim czego można sobie wymarzyć.

Wszystkim, którzy pomogli mi znaleźć się na tym etapie kariery.

*„A PhD is so much more than a degree.
It can break you down into your most vulnerable form,
but has the potential to build you back together to become
a resilient, determined, humble, and knowledgeable researcher.
This process takes time and patience.
Please don't give up on yourself. It's not just about getting
the degree. It's about becoming who you are meant to be.”*

Wyniki opisane w niniejszej pracy zostały opublikowane w następujących artykułach

Publikacje oryginalne:

- [P1] **K. Butowska**, W. Kozak, M. Zdrowowicz, S. Makurat, M. Rychłowski, A. Hać, A. Herman-Antosiewicz, J. Piosik, J. Rak, *Cytotoxicity of doxorubicin conjugated with C₆₀ fullerene. Structural and in vitro studies*. Structural Chemistry, **2019**, 30, 2327–2338.
Współczynnik wpływu: 1.887
- [P2] **K. Butowska**, K. Żamojć, M. Kogut, W. Kozak, D. Wyrzykowski, W. Wicz, J. Czub, J. Piosik, J. Rak, *The product of matrix metalloproteinase cleavage of doxorubicin conjugate for anticancer drug delivery: calorimetric, spectroscopic, and molecular dynamic studies on peptide-doxorubicin binding to DNA*. International Journal of Molecular Sciences, **2020**, 21, 6923.
Współczynnik wpływu: 5.923 (autor korespondencyjny)

Publikacje oryginalne w recenzji:

- [P3] **K. Butowska**, W. Kozak, M. Kogut, Z. Pietralik-Molińska, A. Moliński, K. Kitowska, M. Kozak, J. Czub, R. Sądej, J. Rak, J. Piosik, *MMPs-sensitive release of doxorubicin as a strategy for cancer targeted therapy*. Materials, **2021**
Współczynnik wpływu: 3.623 (drugi autor korespondencyjny)
- [P4] **K. Butowska**, X. Han, N. Gong, R. El-Mayta, R. M. Haley, W. Zhong, W. Guo, M. J. Mitchell, *Doxorubicin-conjugated siRNA lipid nanoparticles for combination cancer therapy*. Acta Pharmacologica Sinica B, **2021**
Współczynnik wpływu: 11.043 (współdzielony pierwszy autor)

Publikacje przeglądowe:

- [P5] **K. Butowska**, A. Woziwodzka, A. Borowik, J. Piosik, *Polymeric nanocarriers: a transformation in doxorubicin therapies*. Materials, **2021**, 14, 2135.
Współczynnik wpływu: 3.623

Sumaryczny współczynnik wpływu: 26.099

Wyniki opisane w niniejszej pracy zostały zaprezentowane na konferencjach

Referat ustny:

- [K1] **K. Butowska**, W. Kozak, A. Hać, J. Piosik, J. Rak, A. Herman-Antosiewicz, *Fullerene C₆₀ – conjugated doxorubicin for advance tumor therapy*, 2nd International Conference on Biotechnology, Walencja, Hiszpania, **2019**.

Poster:

- [PS1] **K. Butowska**, W. Kozak, J. Rak, J. Piosik, *Synthesis and characterization conjugated doxorubicin for drug delivery*, 7th International Conference on Radiation in Various Fields of Research, Herceg Novi, Czarnogóra, **2019**.

Spis treści

Wykaz stosowanych skrótów	8
Streszczenie	10
Abstract	12
I. Cele pracy	13
II. Przegląd literaturowy.....	14
1. Systemy dostarczania leków	14
2. Terapie przeciwnowotworowe.....	20
III. Badania własne.....	24
1. Dostarczanie doksorubicyny przy użyciu fulerenu C60 jako nośnika [P1].....	24
2. Dostarczanie doksorubicyny poprzez nośnik wrażliwy na działanie metaloproteinaz macierzy pozakomórkowej [P2, P3].....	28
3. Dostarczanie doksorubicyny oraz siRNA za pomocą nanocząstek lipidowych [P4].....	35
IV. Podsumowanie.....	42
V. Literatura	45
VI. Wykaz rysunków i tabel.....	52
VII. Kopie publikacji wchodzących w skład pracy doktorskiej.....	55
1. K. Butowska, W. Kozak, M. Zdrowowicz, S. Makurat, M. Rychłowski, A. Hać, A. Herman-Antosiewicz, J. Piosik, J. Rak, Cytotoxicity of doxorubicin conjugated with C ₆₀ fullerene. Structural and in vitro studies. <i>Structural Chemistry</i> , 2019, 30, 2327–2338. [P1].....	55
2. K. Butowska, K. Żamojć, M. Kogut, W. Kozak, D. Wyrzykowski, W. Wiczek, J. Czub, J. Piosik, J. Rak, The product of matrix metalloproteinase cleavage of doxorubicin conjugate for anticancer drug delivery: calorimetric, spectroscopic, and molecular dynamic studies on peptide-doxorubicin binding to DNA. <i>International Journal of Molecular Sciences</i> , 2020, 21, 6923. [P2]	80
3. K. Butowska, W. Kozak, M. Kogut, Z. Pietralik-Molińska, A. Moliński, K. Kitowska, M. Kozak, J. Czub, R. Sądej, J. Rak, J. Piosik, MMPs-sensitive release of doxorubicin as a strategy for cancer targeted therapy. <i>Materials</i> , 2021 [P3]	101
4. K. Butowska, X. Han, N. Gong, R. El-Mayta, R. M. Haley, W. Zhong, W. Guo, M. J. Mitchell, Doxorubicin-conjugated siRNA lipid nanoparticles for combination cancer therapy. <i>Acta Pharmacologica Sinica B</i> , 2021 [P4]	120

5. <i>K. Butowska, A. Woźniowska, A. Borowik, J. Piosik, Polymeric nanocarriers: a transformation in doxorubicin therapies. Materials, 2021, 14, 2135. [P5]</i>	140
VIII. Oświadczenia współautorów.....	160
IX. Spis dorobku naukowego.....	184
1. <i>Pozostałe publikacje niewchodzące w skład rozprawy doktorskiej.....</i>	<i>184</i>
2. <i>Rozdziały w monografiach.....</i>	<i>185</i>
3. <i>Granty i stypendia badawcze.....</i>	<i>185</i>
4. <i>Stáže naukowe.....</i>	<i>185</i>
5. <i>Konferencje.....</i>	<i>185</i>
6. <i>Nagrody i wyróżnienia.....</i>	<i>187</i>

Wykaz stosowanych skrótów

4-pep – tetrapeptyd leucyna–alanina–glicyna–glicyna (ang. *tetrapeptide leucine–alanine–glycine–glycine*)

8-pep – oktapeptyd glicyna–prolina–leucyna–glucyna–leucyna–alanina–glicyna–glicyna (ang. *octapeptide glycine–proline–leucine–glycine–leucine–alanine–glycine–glycine*)

AFM – mikroskopia sił atomowych (ang. *atomic force microscopy*)

ASO – antysensowne oligonukleotydy (ang. *antisense oligonucleotides*)

Bcl-2 – heterogenna grupa białek regulująca proces apoptozy (ang. *B-cell leukemia/lymphoma-2*)

C₆₀ – fuleren C₆₀ (ang. *fullerene C₆₀*)

DBU – 1,8-diazabicyklo[5.4.0]undek-7-en (ang. *1,8-diazabicyclo[5.4.0]-7-ene*)

DCC – *N,N'*-dicykloheksylokarbodiimid (ang. *N,N'-dicyclohexylcarbodiimide*)

DCM – dichlorometan (ang. *dichloromethane*)

DDS – systemy dostarczające leki (ang. *drug delivery systems*)

DFT – teoria funkcjonału gęstości (ang. *density functional theory*)

DLS – dynamiczne rozpraszanie światła (ang. *dynamic light scattering*)

DMF – dimetyloformamid (ang. *dimethylformamide*)

DNA – kwas deoksyrybonukleinowy (ang. *deoxyribonucleic acid*)

DOX – doksorubicyna (ang. *doxorubicin*)

FDA – Agencja Żywności i Leków (ang. *Food and Drug Administration*)

Fmoc – grupa fluorenylmetoksykarbonylowa (ang. *fluorenylmethoxycarbonyl group*)

HPLC – wysokosprawna chromatografia cieczowa (ang. *high performance liquid chromatography*)

HT-1080 – linia komórkowa włókniakomięsaka (ang. *human fibrosarcoma*)

IC₅₀ – stężenie związku, przy którym proliferacja komórek jest zahamowana o 50% w stosunku do komórek kontrolnych (ang. *half-maximal inhibitory concentration*)

ITC – izotermiczna kalorymetria miareczkowa (ang. *isothermal titration calorimetry*)

LNP – nanocząstka lipidowa (ang. *lipid nanoparticle*)

MALDI/TOF – laserowa jonizacja wspomaganą matrycą z detektorem czasu przelotu (ang. *the matrix-assisted laser desorption/ionization time of flight*)

MDA MB 231 – linia komórkowa potrójnie ujemnego gruczolakoraka piersi (ang. *triple negative breast adenocarcinoma*)

MCF-7 – linia komórkowa estrogenozależnego raka sutka (ang. *luminal A breast adenocarcinoma*)

MeOH – metanol (ang. *methanol*)

MMPs – metaloproteinazy macierzy zewnątrzkomórkowej (ang. *matrix metalloproteinases*)

MTT – bromek 3-(4,5-dimetyltiazol-2-yl)-2,5-difenylo-1H-tetrazolowy (ang. *3-[4,5-dimethylthiazole-2-yl]-2,5-diphenyltetrazolium bromide*)

NMR – spektroskopia magnetycznego rezonansu jądrowego (ang. *nuclear magnetic resonance*)

NHS – *N*-hydroksysukcynoimid (ang. *N-hydroxysuccinimide*)

PC3 – linia komórkowa ludzkiego raka prostaty (ang. *prostate adenocarcinoma*)

PEG – poli(tlenek etylenu) (ang. *polyethylene glycol*)

RISC – indukowany przez RNA kompleks białkowy (ang. *RNA-induced silencing complex*)

SD – odchylenie standardowe (ang. *standard deviation*)

SDS-PAGE – poliakrylamidowa elektroforeza w warunkach denaturujących (ang. *sodium dodecyl sulfate-polyacrylamide gel electrophoresis*)

siRNA – mały interferujący kwas rybonukleinowy (ang. *small interfering ribonucleic acid*)

SRB – sulfrodamina B (ang. *sulforhodamine B*)

T47D – linia komórkowa estrogenozależnego raka sutka (ang. *luminal A breast adenocarcinoma*)

TEA – trietyloamina (ang. *triethylamine*)

TEM – elektronowy mikroskop transmisyjny (ang. *transmission electron microscopy*)

TFA – kwas trifluorooctowy (ang. *trifluoroacetic acid*)

WHO – Światowa Organizacja Zdrowia (ang. *World Health Organization*)

WST-1 – sól tetrazolowa 2-(4-jodofenylo)-3-(4-nitrofenylo)-5-(2,4-disulfofenylo) (ang. *2-(4-iodophenyl)-3-(4-nitrophenyl)-5-(2,4-disulfophenyl)-2H tetrazolium monosodium salt*)

Streszczenie

Ukierunkowane dostarczanie leków przy udziale biomateriałów cieszy się w ostatnich latach znacznym zainteresowaniem, szczególnie w odniesieniu do chemioterapii nowotworów. Stanowi ono ciekawą strategię pokonywania barier biologicznych, w tym chemiooporności komórek nowotworowych oraz pozwala na dostarczenie i kontrolowane lokalne uwalnianie zwykle cytotoksycznego leku bez jednoczesnego uszkodzenia zdrowych komórek i tkanek. Na przestrzeni kilku ostatnich dekad obserwowany jest imponujący postęp w dziedzinie biomateriałów. Wysiłki badaczy zmierzają do opracowania nośnika wykazującego się biokompatybilnością oraz zwiększoną efektywnością działania. Nośniki wykorzystywane obecnie różnią się m. in. wielkością, ładunkiem, jak również sposobem wiązania leku. Do najczęściej stosowanych należą nanocząstki polimerowe i ich koniugaty oraz liposomy, czy nanocząstki lipidowe. Pomimo istnienia szerokiego spektrum inteligentnych biomateriałów o korzystnym działaniu, wykazują one również wiele cech niepożądanych, tj. niską efektywność w dostarczaniu i uwalnianiu leku lub toksyczność względem zdrowych komórek. Uzasadnione więc wydaje się poszukiwanie kolejnych, lepszych nośników, ukierunkowanych ponadto na wybrane rodzaje nowotworów. Nośniki charakteryzujące się tą ostatnią cechą posiadają znaczny potencjał kliniczny, przy czym ich opracowywanie nadal stanowi niemałe wyzwanie.

Celem niniejszej pracy doktorskiej było zaprojektowanie, scharakteryzowanie i zbadanie aktywności biologicznej nośników leku przeciwnowotworowego – doksorubicyny, jako potencjalnych narzędzi do ukierunkowanego dostarczania substancji aktywnej do komórek nowotworowych. W ramach pracy doktorskiej opracowano trzy układy służące do przenoszenia doksorubicyny: (1) koniugat fuleren–doksorubicyna połączony kowalencyjnie poprzez poli(tlenek) etylenu, (2) koniugat wrażliwy na działanie metaloproteinaz macierzy zewnątrzkomórkowej, których wzrost aktywności jest obserwowany w komórkach zmienionych nowotworowo, oraz (3) nanocząstkę lipidową z doksorubicyną połączoną kowalencyjnie z jej powierzchnią i enkapsulowanym małym interferującym RNA, w celu represji genu *bcl-2* prowadzącego do deregulacji ekspresji antyapoptycznego białka Bcl-2. Wszystkie nośniki zostały zsyntezowane i poddane badaniom eksperymentalnym *in vitro* przy wykorzystaniu kilku linii komórek nowotworowych. W przypadku najbardziej obiecującego układu wykonano również badania *in vivo*. Dodatkowo, w celu dokładniejszej charakterystyki badanych układów posłużono się obliczeniami teoretycznymi, których wyniki pozostają w dobrej zgodności z danymi eksperymentalnymi. Wykonane eksperymenty *in vitro* i *in vivo*

dotyczące potencjalnych efektów cytotoksycznych i terapeutycznych sugerują, że koniugat wrażliwy na działanie enzymów oraz nanocząstki lipidowe są obiecującymi kandydatami na efektywne nośniki dokсорubicyny. Podjęta tematyka i analizowane zagadnienia wydają się być istotne z punktu widzenia wiedzy o biomateriałach jako układach stosowanych w terapii przeciwnowotworowej, jak również ich zastosowania w aspekcie potencjalnych aplikacji i badań klinicznych.

Abstract

Recently targeted drug delivery, in cancer chemotherapy in particular, has received considerable attention. It seems to be an interesting strategy to overcome biological barriers, including the chemoresistance of cancer cells which provides a controlled local release of usually cytotoxic drug without damaging healthy cells and tissues.

The last few decades have seen impressive progress in the field of biomaterials. Researcher's efforts are aimed at developing a delivery platform that exhibits biocompatibility and increased drug transportation efficiency. The currently used carriers differ in size, charge, as well as the way how a drug is coupled to the carrier. The most commonly used cargo platforms include polymer nanoparticles and their conjugates, liposomes, and lipid nanoparticles. Despite the wide range of intelligent biomaterials, they suffer from numerous drawbacks, i.e. low efficiency of drug delivery and release or toxicity to healthy cells. Therefore, there is a need for new, more effective carriers, in addition selectively targeting diverse types of cancer cells. The latter feature has significant clinical potential, but development of such carriers still remains a challenge.

The present dissertation aimed at designing, characterizing, and studying the biological activity of targeted drug carriers as potential tools for the delivery of an anticancer drug, doxorubicin, to cancer cells. As a result of the current doctoral project, three systems for doxorubicin transportation have been developed: (1) fullerene-doxorubicin conjugate linked covalently *via* polyethylene glycol, (2) a conjugate sensitive to the increased activity of matrix metalloproteinases, that is observed in neoplastic cells, and (3) lipid nanoparticles covalently linked with doxorubicin and encapsulated small interfering RNA to repress the bcl-2 gene, resulting in downregulation of the anti-apoptotic protein Bcl-2. All carriers were synthesized and subjected to *in vitro* experimental studies, utilizing several cancerous cell lines. Then, the most promising systems were additionally studied *in vivo*. Moreover, theoretical calculations were performed to characterize the developed systems in a more detailed way. The results of modeling were in agreement with the experimental data. The outcomes coming from the *in vitro* and *in vivo* experiments, evaluating the potential cytotoxic and therapeutic effects of the analyzed systems, suggest that the enzyme-sensitive conjugate and lipid nanoparticles are promising doxorubicin carriers. The results of this doctoral dissertation contribute to our knowledge regarding biomaterials as delivery systems used in anti-cancer therapy, as well as suggest their potential role in medical applications and future clinical trials.

I. Cele i zakres pracy

Systemy dostarczające leki w sposób kontrolowany dają wiele korzyści. Leki uwalniane miejscowo z takich nośników pozwalają na zredukowanie skutków ubocznych wynikających z prowadzonej terapii oraz zwiększenie jej efektywności. Co najważniejsze, systemy te stają się coraz bardziej precyzyjne, wykorzystując zaawansowane biomateriały, jak również nowe generacje leków, co w przyszłości może przyczynić się do powstania nowych form leczenia.

Głównym celem niniejszej rozprawy doktorskiej było zaprojektowanie i otrzymanie nośników doksorubicyny, będących potencjalnymi układami do zastosowania w terapii przeciwnowotworowej.

Zakres pracy obejmuje przegląd literaturowy, ze szczególnym uwzględnieniem informacji zawartych w pracy przeglądowej, wchodzącej w skład rozprawy doktorskiej [P5], rozszerzony o obecny stan wiedzy. Główna część rozprawy opiera się na otrzymanych wynikach eksperymentalnych, które dodatkowo poparte zostały wynikami obliczeń teoretycznych. Rezultaty składające się na niniejszą pracę zostały przedstawione w formie dwóch prac oryginalnych [P1-P2] oraz dwóch manuskryptów w recenzji [P3-P4].

W toku prac badawczych zrealizowano poniższe cele:

- Synteza koniugatu fuleren C₆₀-doksorubicyna połączonego kowalencyjnie poprzez poli(tlenek etylenu) [P1].
- Synteza koniugatu wrażliwego na działanie metaloproteinaz macierzy zewnątrzkomórkowej [P2, P3].
- Synteza nanocząstki lipidowej z kowalencyjnie połączoną doksorubicyną i enkapsulowanym małym interferującym kwasem rybonukleinowym [P4].
- Charakterystyka fizykochemiczna otrzymanych nośników i identyfikacja kluczowych parametrów do wydajnego dostarczania doksorubicyny [P1-P4].
- Badanie *in vitro* toksyczności nośników wobec ludzkich linii komórkowych [P1-P4].
- Badanie *in vivo* efektów terapeutycznych najlepiej rokującego nośnika [P4].

II. Przegląd literaturowy

1. Systemy dostarczania leków

XX wiek przyniósł ogrom zmian w dziedzinie farmakologii, chemii materiałów i inżynierii biomedycznej. Obserwowano coraz częstsze użycie systemów kontrolowanego uwalniania leków (DDSs) przy stopniowej miniaturyzacji projektowanych układów.^{1,2} 29 grudnia 1959 roku podczas dorocznego spotkania Amerykańskiego Towarzystwa Fizycznego w Caltech, Richard Feynman wygłosił jeden z najbardziej inspirujących i wizjonerskich wykładów połowy XX w., pt. *There's Plenty of Room at the Bottom*.³ Rozważania Feynman'a dotyczące możliwości manipulacji materią i otrzymywania materiałów o rozmiarach rzędu nanometrów miały znaczący wpływ na rozwój dziedziny jaką jest nanotechnologia. Jednak koncepcja użycia nanomateriałów jako DDSs, została wykorzystana dopiero wiele lat później.

Historia DDSs sięga roku 1960, kiedy to Judah Folkman opracował kapsułki z gumy silikonowej (*Silastic*[®]) o przedłużonym uwalnianiu leku nasercowego.^{4,5} Dekadę później, Alza Corporation, firma założona przez Alejandro Zaffaroniego wprowadziła na rynek wkładkę do oka zawierającą lek przeciw jaskrze (*Ocusert*[®]) oraz wkładkę domaciczną uwalniającą steroidowy lek antykoncepcyjny.⁶ W kolejnych latach, na rynku pojawił się podskórny implant antykoncepcyjny *Norplant*[®] wykorzystujący poli(dimetylosiloksan), a także kapsułka osmotyczna zbudowana z octanu celulozy i niewielkiej ilości poli(tlenku etylenu) (PEG).^{7,8} Przełomowym odkryciem było opracowanie przez Roberta Langer'a i wspomnianego już Folkman'a makroskopowych niedegradowalnych układów polimerowych umożliwiających dostarczanie leków wielkocząsteczkowych, jak białka, w postaci aktywnej.⁹ Jednak z czasem koncepcja ta ewoluowała w stronę polimerów biodegradowalnych, co zaowocowało wprowadzeniem na rynek preparatu *Depot*[®], stosowanego w leczeniu raka prostaty i terapii hormonalnej.¹⁰

W jednym ze swoich wystąpień w roku 2016 Robert Langer, który uznawany jest za autorytet w dziedzinie biomateriałów przedstawił uwagi krytyczne recenzentów, oceniających jego aplikacje grantowe na przestrzeni 1980–1993 roku. Brzmiały one następująco:

„*This approach will not work because...*

- *The polymers cannot be synthesized* (1981)

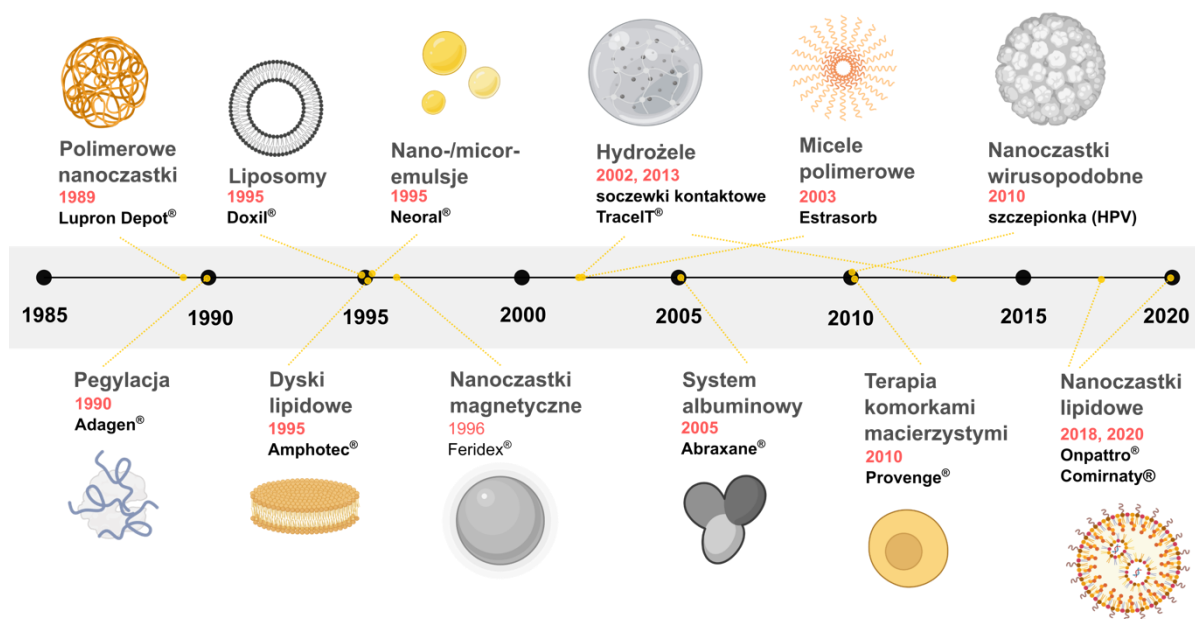
- *The polymers will react with encapsulated drug* (1983)
- *The polymers are fragile* (1985)
- *The polymer–drug system would be toxic* (1986)
- *The drug will not diffuse far enough to kill remaining tumor* (1988)
- *Even if it does, it is a very poor drug* (1990)
- *The drug delivery systems cannot be manufactured* (1993)”

Przytoczone uzasadnienia recenzentów doskonale pokazują jak długą drogę przeszliśmy podczas ostatnich czterech dekad prac nad DDSs. Po rozwiązaniu pierwszego zasugerowanego przez recenzenta problemu badawczego i udowodnieniu, że zaproponowane polimery można zsyntezować, pojawił się kolejny argument przeciwko pomysłowi zastosowania polimerów jako DDSs. Przełomem był rok 1996, gdy Agencja Żywności i Leków (FDA) zaakceptowała implant *Gliadel*[®] jako pierwszą w historii terapię dostarczającą lek przeciwnowotworowy bezpośrednio w okolicy guza, glejaka wielopostaciowego.¹¹

Systemy DDS zbudowane zarówno z naturalnych jak i syntetycznych polimerów, wykazują szereg właściwości fizykochemicznych, które umożliwiają celowany transport leków.¹² Szerokie zastosowanie znalazły polikaprolakton, poliakrylamid, poli(metakrylan metylu), czy wcześniej wspomniany PEG, wchodzące w skład polimerów syntetycznych.¹³ Natomiast wśród polimerów naturalnych najczęściej wyróżniany jest chitozan i algininian.¹⁴ Obecnie syntezowanych jest coraz więcej DDSs, które różnią się architekturą, modyfikacją powierzchni i specyficnością, co wynika z konieczności dostosowania nośnika do leku, który ma być transportowany. Idealne DDSs powinny charakteryzować się wysoką stabilnością i rozpuszczalnością, oraz w sposób kontrolowany uwalniać lek z nośnika, np. poprzez dyfuzję czy dysocjację.¹⁵ Z biologicznego punktu widzenia, DDSs powinny wydłużać okres półtrwania leku, być biodegradowalne i biokompatybilne, a dodatkowo posiadać zdolność do gromadzenia się w tkankach nowotworowych, czyli wykazywać tzw. efekt zwiększonej przepuszczalności i retencji (EPR).¹⁶

Na przestrzeni lat polimerowe DDSs stawały się coraz bardziej złożone, tworząc np. kopolimery, koniugaty polimer–lek i koniugaty polimer–białko.^{17,18} Dodatkowo, wszystkie wspomniane podklasy polimerowych DDSs zaczęły stawać się układami o rozmiarach nanometrycznych. Zgodnie z ogólną definicją, za nanomateriały uznaje się materiały posiadające w co najmniej jednym wymiarze rozmiar od 1 do 100 nm.¹⁹ Stąd też badania nad

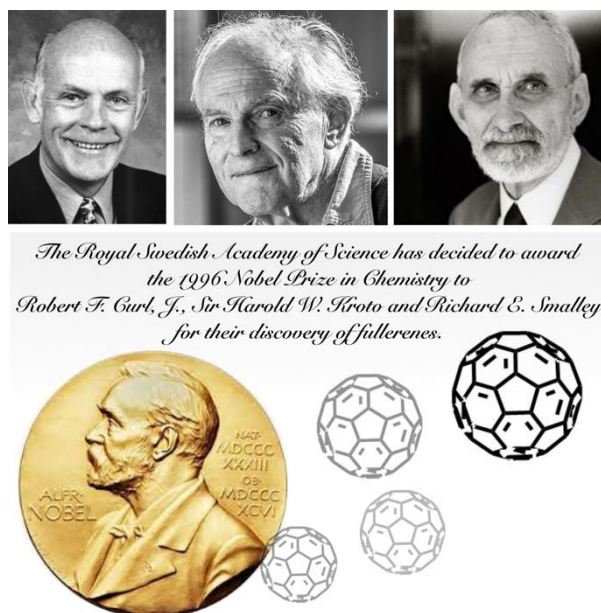
nanomateriałami skupiały się nie tylko na wspomnianych polimerowych DDSs, ale i na cząstkach o innym pochodzeniu lecz o rozmiarach w skali nanometrów (**Rys. 1**). Innymi stosowanymi nanocząstkami według doniesień literaturowych, które znajdują się w centrum uwagi naukowców jako potencjalne DDSs są nanocząstki pochodzenia węglowego (fuleren C_{60} , nanorurki), nanocząstki metaliczne (nanocząstki srebra czy złota) oraz nanocząstki magnetyczne (magnetyt Fe_3O_4).



Rysunek 1. Historyczna oś czasu przedstawiająca zmiany zachodzące w dziedzinie DDSs wraz z przykładami komercyjnie dostępnych leków.

W roku 1996 Harold Kroto, Robert Curl i Richard Smalley zostali uhonorowani Nagrodą Nobla za wkład w odkrycie alotropowej odmiany węgla – fulerenu C_{60} (**Rys. 2**).²⁰ Z chemicznego punktu widzenia cząsteczka fulerenu C_{60} składa się ze sprzężonych dwunastu pierścieni pentagonalnych i dwudziestu pierścieni heksagonalnych, które tworzą pustą w środku bryłę geometryczną.²¹ Właśnie ze względu na strukturę chemiczną fulerenu C_{60} wykazuje on właściwości fizykochemiczne zbliżone do sprzężonych węglowodorów aromatycznych. Fuleren C_{60} charakteryzuje się wysokim powinowactwem elektronowym, stąd wynika jego łatwość do redukcji. Ponadto fuleren C_{60} łatwo ulega reakcji addycji.^{22,23} Stosunkowo łatwa możliwość modyfikowania powierzchni fulerenu C_{60} skłoniła naukowców do poszukiwania nowych zastosowań tej odmiany alotropowej węgla w naukach farmaceutycznych i bioinżynieryjnych. Liczne badania naukowe wskazują na potencjalne wykorzystanie fulerenu C_{60} jako środka kontrastowego do łatwego obrazowania tkanek

zmienionych chorobowo, czy też nośnika leków przeciwnowotworowych i przeciwbakteryjnych.²⁴



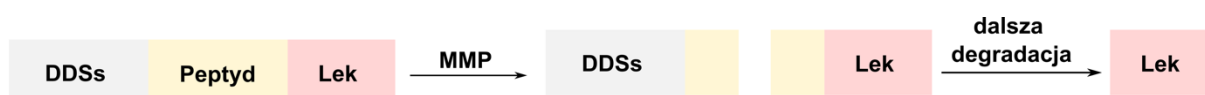
Rysunek 2. Laureaci Nagrody Nobla w dziedzinie chemii nagrodzeni w 1996 roku za odkrycie fulerenów.

Dalsze badania pokazały, że nanocząstki polimerowe, węglowe czy też nieorganiczne w połączeniu z ligandami czy przeciwciałami mogą prowadzić do otrzymania DDSs wykorzystywanych w terapiach celowanych.²⁵ Wśród stosowanych ligandów dużym zainteresowaniem cieszy się kwas foliowy, aptamery i transferyna, które oddziałują z receptorami znajdującymi się na powierzchni komórek nowotworowych.²⁶ Interesujące jest również wykorzystanie przeciwciał monoklonalnych, np. trastuzumab i alemtuzumab, rozpoznających specyficznie antygeny.²⁷ Ponadto, ciekawą koncepcją modyfikacji DDSs jest zmiana struktury chemicznej nośników w taki sposób, aby stały się one wrażliwe na bodźce zewnętrzne lub środowisko charakterystyczne dla komórek nowotworowych.

Liczne dane literaturowe oraz powszechnie dostępna wiedza w zakresie biologii molekularnej nowotworów wskazują, iż komórki te wytwarzają środowisko odróżniające je od środowiska charakteryzującego zdrowe tkanki. Mikrośrodowisko guzów litych odgrywa istotną rolę w progresji, przerzutowaniu i oporności na terapie przeciwnowotworowe. Bez wątpienia, do charakterystycznych cech nowotworów należą hipoksja, wysokie ciśnienie śródmiąższowe oraz zaburzenia w działaniu pompy jonowej.²⁸ Te ostatnie powodują znaczny wyrzut jonów H^+ , co skutkuje wzrostem pH wewnątrz komórki nowotworowej (7.3–7.6), a jego spadek do

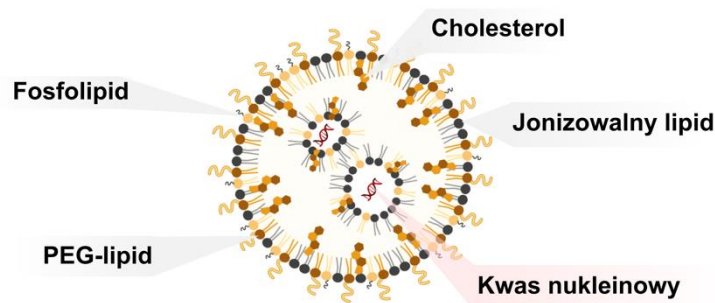
pH 6.8 w macierzy pozakomórkowej.²⁹ W związku z powyższym zaczęto wcielać do struktury DDSs wiązania wrażliwe na środowisko kwaśne, jak np. wiązanie hydrazonowe.³⁰ Doskonałym przykładem zastosowania tego wiązania jest Aldorubicyna, inaczej nazywana INNO-206. Aldorubicyna jest klinicznie przebadanym prolekiem doksorubicyny (DOX), posiadającym w swojej strukturze wiązanie hydrazonowe oraz dodatkową grupę maleimidową.³¹ Związek ten po podaniu dożylnym wiąże się z albuminą przedłużając okres półtrwania DOX w krwioobieg, a następnie uwalnia ją w środowisku kwaśnym poprzez hydrolizę wiązania hydrazonowego.³²

W niektórych przypadkach nowotworów obserwowana jest wzmożona ekspresja metaloproteinaz macierzy zewnątrzkomórkowej (MMP).³³ MMP należą do grupy metalozależnych (Zn^{2+}) enzymów proteolitycznych należących do endopeptydaz odkrytych w 1962 roku.³⁴ Do tej pory opisano 22 rodzaje MMP występujących u człowieka, które ze względu na różnice w budowie domenowej i swoistości substratowej zostały podzielone na kilka grup, jak matrylizyny (MMP-7) czy żelatynazy (MMP-2/-9).³⁵ MMP biorą udział w wielu procesach fizjologicznych i wytwarzane są przez większość prawidłowych komórek, m. in. przez fibroblasty oraz komórki dendryczne. Zwiększoną aktywność MMP obserwuje się w procesach patologicznych, takich jak nowotworzenie.³⁶ Zgodnie z literaturą przedmiotu łańcuchy peptydowe wrażliwe na działanie MMP wprowadzone do struktury nośników ulegają hydrolizie, a co za tym idzie uwalniają lek bezpośrednio do komórek nowotworowych.³⁷ Sam mechanizm uwalniania leku z nośników wrażliwych na MMP odbywa się dwuetapowo. W pierwszym etapie następuje hydroliza wiązania peptydowego przy udziale MMP, prowadząca do produktu pośredniego, którego dalsza degradacja, katalizowana działaniem dodatkowych wewnątrzkomórkowych proteaz, skutkuje uwolnieniem leku (**Rys. 3**).³⁸ W ostatnich latach opracowano sondę zawierającą fragment peptydowy wrażliwy na MMP-2 do obrazowania guzów, prolek będący koniugatem albuminy i DOX, jak również micelle obniżające efekty uboczne stosowanej terapii ze względu na celowane uwalnianie cytostatyku.³⁹



Rysunek 3. Schemat dwuetapowego uwalniania leku z nośnika wrażliwego na działanie metaloproteinaz macierzy zewnątrzkomórkowej (MMP).

Prawdziwy przełom w badaniach nad efektywnym dostarczaniem leków nastąpił w roku 2020, kiedy to dopuszczono, w zaledwie kilka miesięcy, do awaryjnego użytku szczepionkę przeciw wirusowi SARS-Cov2 (*COMIRNATY*[®]), która swoje działanie opiera na dostarczaniu mRNA poprzez nanocząstki lipidowe (LNP).⁴⁰ Historia DDS pochodzenia lipidowego sięga lat 90. XX wieku, kiedy otrzymywano nowe formy lipidowych DDS: układy polimerowo–lipidowe, liposomy z enkapsulowaną DOX (*Doxil*[®]), immunoliposomy oraz lipidy kationowe.⁴¹ Liposomy zbudowane z fosfolipidów ulegają spontanicznej samoorganizacji w pęcherzyki, umożliwiając umieszczenie leku wewnątrz ich struktury.⁴² Dodatkowo, lipidy kationowe, różniące się strukturą od liposomów, umożliwiają przenoszenie kwasów nukleinowych, jednak wykazują pewne ograniczenia w zastosowaniu *in vivo* ze względu na toksyczność w miejscu podania.⁴³ Alternatywą dla lipidów kationowych są LNP zbudowane z czterech komponentów pełniących różne funkcje: jonizowalnego lipidu, fosfolipidu, cholesterolu i PEG połączonego z łańcuchem alkilowym zakotwiczonym w dwuwarstwie lipidowej (PEG-lipid; **Rys. 4**).⁴⁴ Cholesterol, ze względu na sztywną strukturę stabilizuje LNP, a fosfolipid przyczynia się do fuzji z błonami komórkowymi i endosomalnymi, co sprzyja wychytowi komórkowemu. Ponadto, PEG-lipid zmniejsza opsonizację (zjawisko oporności swoistej) i poprawia rozpuszczalność. Najważniejszy komponent – jonizowalny lipid – odpowiada za odpowiedź LNP na zmianę pH. LNP są stosunkowo stabilne w pH fizjologicznym, jednak w warunkach kwasowych panujących między innymi w endosomach ulegają jonizacji umożliwiając ucieczkę endosomalną.⁴⁵ Mimo że mechanizm ten nie jest do końca poznany, zakłada się, że LNP po sprotonowaniu ułatwiają oddziaływania elektrostatyczne i fuzję z ujemnie naładowaną błoną endosomu. Fuzja powoduje destabilizację struktury LNP i wyrzut kwasu nukleinowego do cytoplazmy.⁴⁶ Najnowsze doniesienia literaturowe oraz liczba raportowanych badań klinicznych nad LNP wskazują na wykorzystanie tych nośników w wydajnym dostarczaniu kwasów nukleinowych i ich znaczący potencjał aplikacyjny.⁴⁷

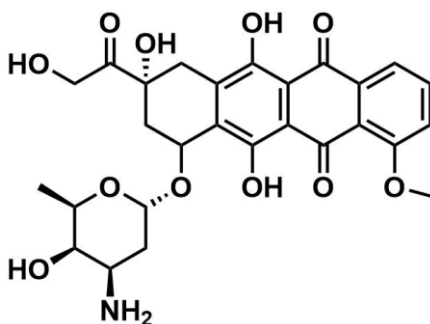


Rysunek 4. Schemat struktury nanocząstki lipidowej (LNP).

2. Terapie przeciwnowotworowe

Światowa Organizacja Zdrowia odnotowała w roku 2020 dziesięć milionów zgonów, których przyczyną były choroby nowotworowe.⁴⁸ Jest to znaczny wzrost w porównaniu do roku 2018, w którym zarejestrowano 9,4 milionów przypadków.⁴⁹ Dlatego istotne wydaje się lepsze zrozumienie podłoża genetycznego i mechanizmów molekularnych promujących kancerogenezę, co może przyczynić się do opracowania nowych metod leczenia chorób nowotworowych. Nowotwory pełnoobjawowe są łatwe do zdiagnozowania, jednak wykazują niski wskaźnik wyleczalności i nierzadko wymagają zastosowania kilku terapii, tzw. terapia skojarzona.⁵⁰ Wśród powszechnie stosowanych i łączonych ze sobą metod leczenia chorób nowotworowych wyróżnia się radioterapię, chemioterapię i leczenie chirurgiczne.⁵¹

Sztandarowym przykładem leku stosowanego w chemioterapii jest DOX, należąca do grupy antybiotyków antracyklinowych, wyizolowanych ponad 50 lat temu ze szczepu *Streptomyces percentus var. caesius*.⁵² DOX stosowana jest w leczeniu wielu typów nowotworów, tj. białaczki i chłoniaków Hodgkin'a, jak również w przypadku nowotworów litych piersi.⁵³ Złożony mechanizm działania przeciwnowotworowego DOX zdeterminowany jest poprzez jej strukturę chemiczną. DOX składa się aglikonu połączonego wiązaniem glikozydowym z daunozaminą (**Rys. 5**).⁵⁴ Jedną z propozycji wyjaśniających działanie DOX

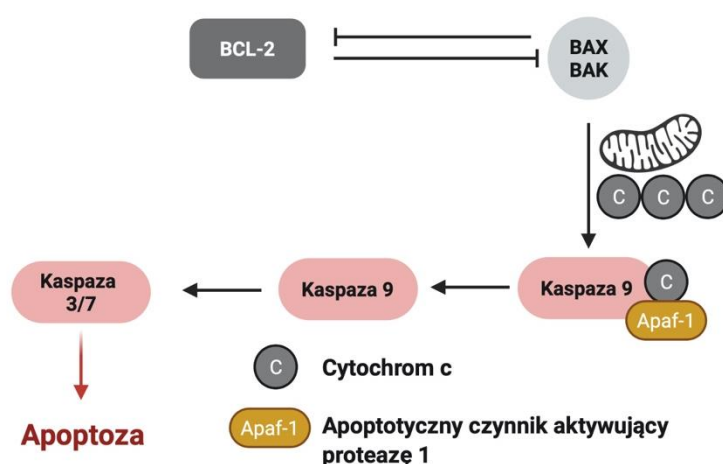


Rysunek 5. Struktura chemiczna doksorubicyny (DOX).

jest mechanizm oparty o interkalację części aglikonu do dwuniciowego DNA, co prowadzi do zahamowania procesów replikacyjnych i biosyntezy makromolekuł.⁵⁵ Dodatkowo, DOX może generować wolne rodniki, które powodują uszkodzenia DNA oraz utleniania lipidów, sieciować międzyłańcuchowo DNA i hamować działanie topoisomerazy II.^{56,57} Najsilniejsze działanie DOX obserwowane jest w fazie G₂/M cyklu komórkowego, prowadząc do apoptozy, czyli kontrolowanego procesu śmierci komórkowej. Pomimo skuteczności klinicznej, DOX wykazuje wiele skutków ubocznych, jak wysoka kardiotoxycywność, może wywierać niekorzystny wpływ na wątrobę i nerki oraz powodować martwicę tkanek ze względu na

dożylną/dotętniczną formę podawania cytostatyku.⁵⁸ Ponadto coraz częściej obserwowana jest wielolekowa oporność komórek nowotworowych (MDR, ang. *multiple drug resistance*) na cytostatyki poprzez hamowanie procesów apoptycznych, co skutkuje obniżeniem skuteczności działania chemioterapii pomimo zwiększania dawki leku lub zastosowania kombinacji różnych chemioterapeutyków.⁵⁹

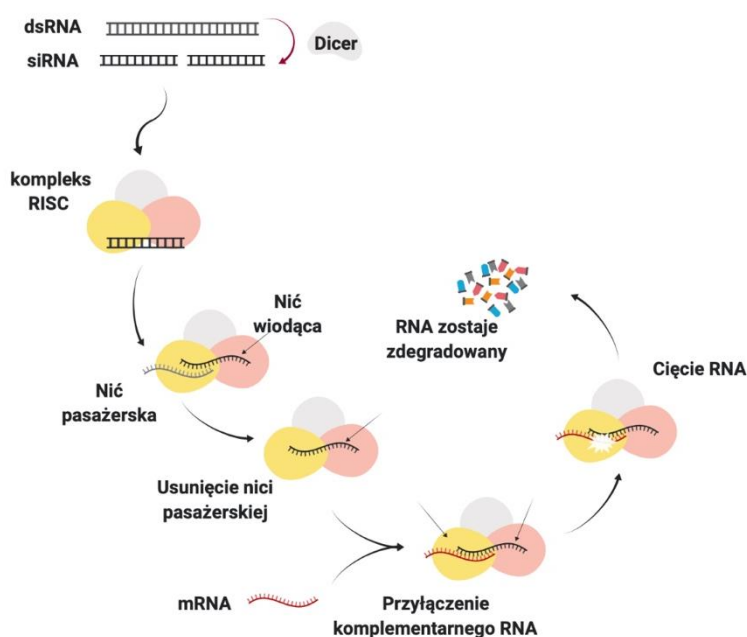
Dane literaturowe wskazują, że zjawisko oporności komórek nowotworowych na apoptozę zachodzi poprzez kilka mechanizmów, w tym przez mechanizmy naprawy DNA oraz nadekspresję białek antyapoptycznych.⁶⁰ Jednym z kluczowych czynników regulujących apoptozę są białka należące do rodziny Bcl-2 (ang. *B-cell leukemia/lymphoma-2*) odkryte ponad 30 lat temu w wyniku badań nad chłoniakami nieziarniczymi.⁶¹ Stwierdzono również, że w przypadku pacjentów leczonych według schematu CHOP (cyklofosfamid, winkrystyna, doksorubicyna i prednizon) ekspresja białka Bcl-2 wiąże się z gorszym rokowaniem.⁶² Białko Bcl-2 odpowiada za regulację mitochondrialnego szlaku apoptozy, hamując uwalnianie cytochromu c i szlaku kaspaz (**Rys. 6**).⁶³ Ze względu na ważną rolę białka Bcl-2



Rysunek 6. Schemat mitochondrialnego szlaku apoptozy regulowanego przez białko Bcl-2.

w szlakach apoptycznych zaczęto poszukiwać nowych strategii hamowania lub deregulacji ekspresji białka Bcl-2.⁶⁴ Dużym sukcesem okazało się zastosowanie antysensownych oligonukleotydów (ASO, ang. *antisense oligonucleotides*), np. Oblimersen, SPC2996 LNP czy PNT2258, testowanych klinicznie przeciwko szpiczakom mnogim i białaczkom.^{65,66} Działanie ASO opiera się na tworzeniu kompleksu z mRNA, aktywacji RNAzy H, a następnie enzymatycznemu pocięciu heterodupleksu, prowadzącemu do degradacji mRNA.⁶⁷ W roku 2016 otrzymano selektywny inhibitor białka Bcl-2 – wenetoklaks, który został zatwierdzony przez FDA do monoterapii w leczeniu przewlekłej białaczki limfocytowej.⁶⁸ Ze względu na

ograniczone korzyści wspomnianych monoterapii, coraz więcej trwających obecnie badań klinicznych łączy monoterapię z cytostatykami takimi jak DOX.^{69,70} Ekspresja antyapoptycznego białka Bcl-2 może jednak przeciwdziałać farmakologicznemu efektowi DOX. Dlatego w ostatnich latach skupiono się również na wykorzystaniu Bcl-2 siRNA i DOX w terapiach skojarzonych ukierunkowanych m. in. na raka jajnika czy glejaka.^{71,72} siRNA jest dwuniciowym fragmentem RNA o długości około 21-23 par zasad indukującym wyciszenie ekspresji wybranego genu.⁷³ Mechanizm wyciszania genów przy użyciu siRNA zachodzi kilkietapowo. W pierwszym etapie egzogenny dsRNA poddany zostaje hydrolizie przy udziale rybonukleazy Dicer, co skutkuje powstaniem siRNA. Następnie, siRNA wiąże się z efektorowym kompleksem białkowym RISC, w skład którego wchodzi białka AGO2, Dicer i TRBP (**Rys. 7**). W kolejnym etapie, z kompleksu usuwana jest tzw. nić pasażerska, a pozostawiona zostaje nić wiodąca, której koniec 5' wiąże się z obecnym w kompleksie białkiem AGO2. Pojedyncza nić siRNA włączona w kompleks RISC przyłącza komplementarne mRNA, powodując jego przecinanie, co skutkuje zahamowaniem ekspresji odpowiedniego transkryptu.⁷⁴



Rysunek 7. Sposób działania interferujących RNA (opis w tekście).

Na przestrzeni ostatnich lat poczyniono ogromny progres w badaniach nad zastosowaniem siRNA w leczeniu. Pierwszym lekiem opierającym swoje działanie na siRNA, który został dopuszczony przez FDA do użytku w sierpniu 2018 roku był *Onpattro*[®].⁷⁵ Wskazaniem do stosowania tego leku była dziedziczna amyloidoza transtyretynowa

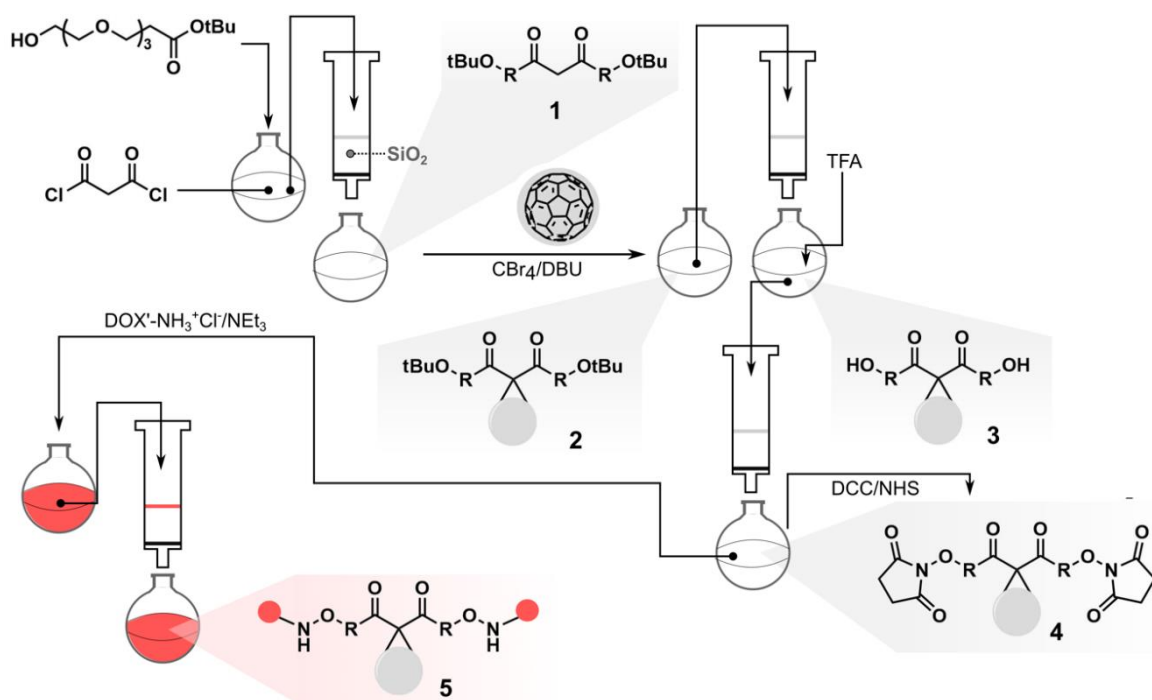
u pacjentów z polineuropatią. W listopadzie 2019 roku, FDA dopuściło do użytku *Givosiran*[®], jako drugi zaakceptowany lek na bazie siRNA i pierwszy używany w leczeniu ostrej porfirii wątrobowej.⁷⁶ Natomiast Komitet Europejskiej Agencji Leków dopuścił do obrotu *Givosiran*[®] w marcu 2020 roku. Jednak efekty terapeutyczne i sukces kliniczny stosowania RNA wymaga pokonania kilku głównych barier biologicznych, jak np. degradacja RNA w wyniku działania RNAz. Ponadto, egzogeny RNA charakteryzuje się silną immunogennością oraz może być łatwo wydalany przez nerki. Wyzwaniem jest również dostarczenie ujemnie naładowanego i stosunkowo dużego RNA przez hydrofobową błonę cytoplazmatyczną.⁷⁷

Badania kliniczne przeprowadzone w ciągu ostatnich kilku lat wskazują, że możliwe jest bezpieczne i skuteczne stosowanie siRNA w celu wyciszenia wybranego genu. Terapia ta jest potężnym i wszechstronnym narzędziem do walki z chorobami różnego pochodzenia, prowadzącym tym samym do polepszenia obecnych standardów leczenia. Faktycznie, liczba nowych leków RNA będących w trakcie opracowywania i poddanych badaniom klinicznym gwałtownie wzrosła, co jest spowodowane stopniowym rozwiązywaniem problemu stabilności, dostarczania i immunogenności RNA. Otrzymywanie zaawansowanych platform do transportu RNA w celu pokonania barier biologicznych wydaje się zatem obiecującym kierunkiem badań.

III. Badania własne

1. Dostarczanie doksorubicyny przy użyciu fulerenu C₆₀ jako nośnika [P1]

Na podstawie inspirujących doniesień literaturowych, postanowiłam otrzymać koniugat fulerenu C₆₀ z DOX (Ful-DOX), do stosowania w potencjalnej terapii przeciwnowotworowej (**Rys. 8** oraz **Schemat 1 w P1**). W pierwszym etapie prac badawczych otrzymałam malonian bis(14,14-dimetylo-12-oxo-3,6,9,13-tetraoxopentadekanowy) **1**, który stanowił łańcuch łączący fuleren C₆₀ z DOX. Struktura otrzymanego związku **1** została potwierdzona metodą spektrometrii mas (MALDI-TOF) oraz magnetycznego rezonansu jądrowego (NMR). Obecność w strukturze fulerenu C₆₀ atomów węgla związanych wiązaniem podwójnym czyni go podatnym na reakcję cykloaddycji. W celu sprzęgnięcia **1** z C₆₀ zastosowałam więc reakcję Bingela-Hirsha, która polega na cykloaddycji [2+1] przy udziale bromopochodnej kwasu malonowego w obecności zasady, np. DBU.⁷⁸ Tak otrzymany malonian-C₆₀ bis(14,14-dimetylo-12-oxo-3,6,9,13-tetraoxopentadekanowy) **2** poddałam hydrolizie przy użyciu TFA. Następnie, grupy karboksylowe produktu hydrolizy **3** aktywowałam stosując układ DCC/NHS. W kolejnym kroku ester aktywny **4** sprzęgałam z DOX, otrzymując produkt końcowy Ful-DOX **5**. Wszystkie produkty przejściowe **1-4** oraz ostateczny koniugat Ful-DOX **5** oczyściłam przy użyciu kolumnowej preparatywnej chromatografii cieczowej z wykorzystaniem DCM/MeOH jako eluentu i żelu krzemionkowego jako fazy stacjonarnej. Otrzymane związki zidentyfikowałam przy użyciu metody MALDI-TOF. Fachowa literatura sugeruje, iż, układy zawierające w swojej strukturze fuleren C₆₀ ulegają fragmentacji podczas jonizacji próbki, co również ma miejsce w przypadku związków zawierających cząsteczkę DOX.^{79,80} Rzeczywiście, na wszystkich zarejestrowanych widmach masowych obserwowałam szereg pików powstających w wyniku fragmentacji otrzymanych produktów, głównie na drodze utraty 1-oxy-2-hydroksyetylu lub daunozaminy.

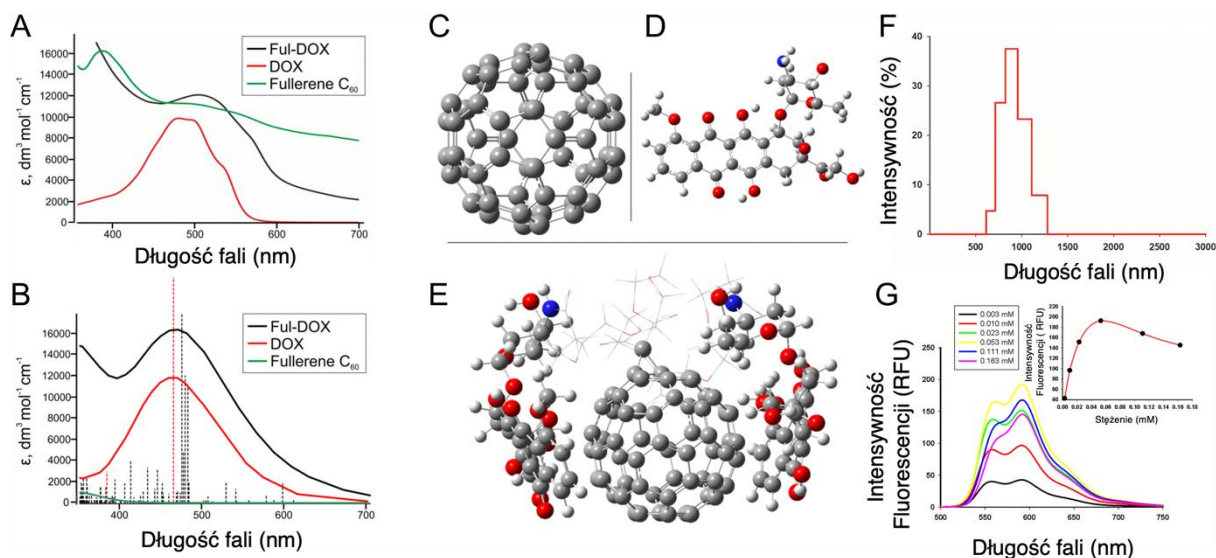


Rysunek 8. Schemat syntezy koniugatu Ful-DOX 5.

Otrzymany koniugat Ful-DOX scharakteryzowałam kilkoma metodami fizykochemicznymi, jak również przy użyciu obliczeń kwantowochemicznych DFT. Początkowo, za pomocą spektroskopii UV-vis porównałam widma absorpcyjne Ful-DOX, wolnej formy DOX oraz samego fulerenu (**Rys. 9A** oraz **Rys. 3A w P1**). Widmo zarejestrowane dla DOX przyjęło typowy dla tego związku kształt z maksimum absorpcji przy 484 nm. W przypadku fulerenu obserwowałam dwa charakterystyczne piki przy długości fal 387 nm oraz 493 nm. Widmo absorpcyjne Ful-DOX 5 wydaje się być nałożeniem obu wcześniej wspomnianych widm, co może świadczyć o udanym sprzęgnięciu fulerenu C₆₀ z DOX. Eksperymentalne dane spektralne pozostają w bardzo dobrej zgodności z wynikami obliczeń DFT, dodatkowo sugerując silne oddziaływania pomiędzy cząsteczką DOX a fulerem C₆₀ (**Rys. 9B-9E** oraz **Rys. 2A-2C** i **Rys. 3B w P1**).

Ponieważ cząsteczka DOX należy do molekuł fluoryzujących, zdecydowałam się na przeprowadzenie pomiarów intensywności fluorescencji w funkcji wzrastającego stężenia Ful-DOX. Eksperyment ten miał umożliwić zaobserwowanie agregacji koniugatu, możliwej ze względu na obecność hydrofobowej cząsteczki fulerenu w molekule Ful-DOX. Faktycznie, początkowo intensywność fluorescencji wzrastała liniowo, jednak po przekroczeniu stężenia 53 μM zaobserwowałam spadek jej intensywności i zmianę kształtu widma (**Rys. 9G** oraz **Rys.**

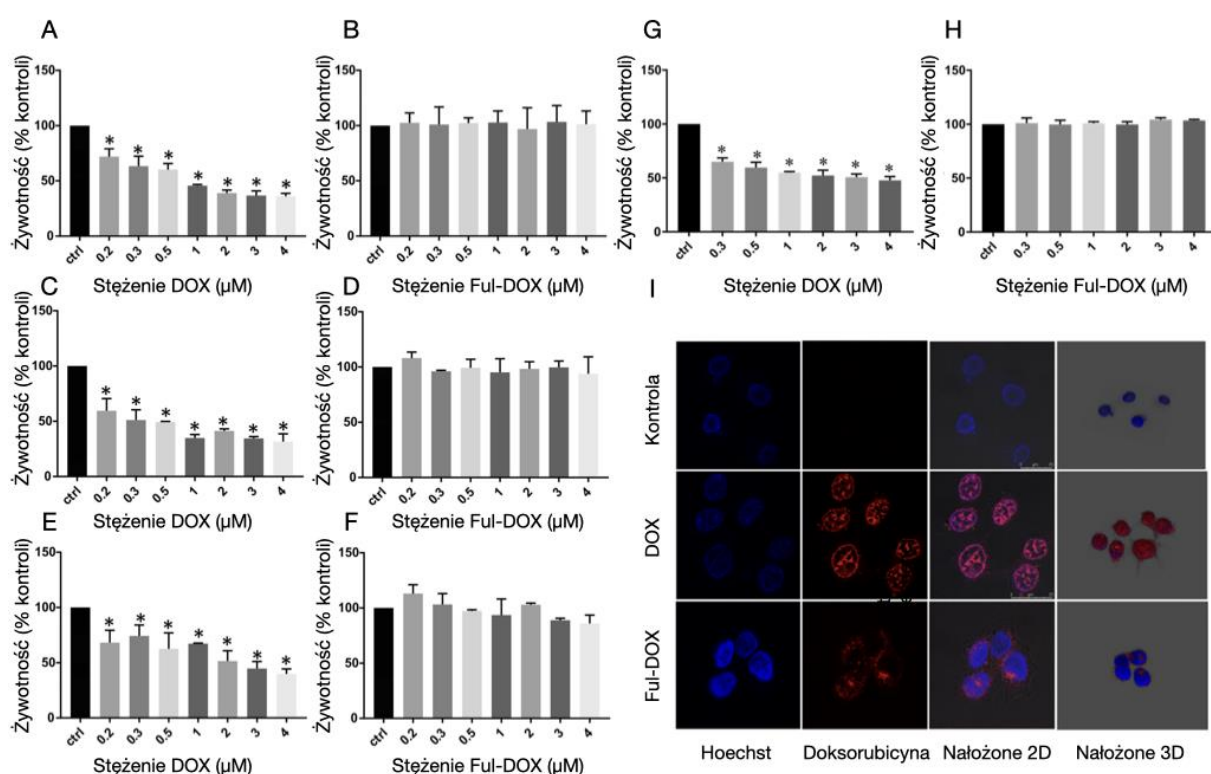
4 w P1). Wynik ten może sugerować powstawanie agregatów Ful-DOX skutkujących wygaszaniem fluorescencji. Obecność agregatów potwierdziłam dodatkowo przy użyciu techniki DLS. Wyniki eksperymentu dynamicznego rozpraszania światła wskazują, że w badanym roztworze najlepiej reprezentowane są agregaty o promieniu hydrodynamicznym około 800 nm (Rys. 9F oraz Rys. 5 w P1). Tak duży rozmiar Ful-DOX jest niekorzystny dla wychwytu komórkowego i może zaburzać działanie przeciwnowotworowe DOX.



Rysunek 9. Charakterystyka fizykochemiczna koniugatu Ful-DOX. **A.** Eksperymentalnie otrzymane widmo absorpcji dla DOX, fulerenu C_{60} oraz koniugatu Ful-DOX, zarejestrowane w zakresie długości fal 350-700 nm. **B.** Teoretyczne widmo absorpcji otrzymane dla DOX, fulerenu C_{60} oraz koniugatu Ful-DOX przy użyciu metod kwantowochemicznych DFT. **C.** Zoptymalizowana struktura fulerenu C_{60} PM6 **D.** Zoptymalizowana struktura DOX. **E.** Zoptymalizowana struktura koniugatu Ful-DOX. **F.** Rozkład średniego promienia hydrodynamicznego zarejestrowany dla koniugatu Ful-DOX. **G.** Widmo fluorescencji rejestrowane wraz ze wzrastającym stężeniem koniugatu Ful-DOX. Szczegółowy opis zaprezentowanych wyników znajduje się w publikacji P1.

Kolejnym celem projektu było wyjaśnienie czy pomimo dużego rozmiar koniugatu kowalencyjne związanie DOX ze stosunkowo nietoksycznym nośnikiem prowadzi do układu o właściwościach terapeutycznych. Badania *in vitro* przeprowadzono na różnych liniach komórkowych raka piersi (MCF-7, T47D i MDA MB 231) oraz raka prostaty (PC3) przy zastosowaniu dwóch testów cytotoxycznosci – SRB i WST-1 (Rys. 10A-H oraz Rys. 9A-F i Rys. 7 w P1). Wyniki otrzymane dla poszczególnych linii komórkowych sugerują brak aktywnosci przeciwnowotworowej koniugatu. Dla porównania, wolna forma DOX powodowała wyraźny spadek żywotności komórek wraz ze wzrostem stężenia. Przy najwyższym stosowanym stężeniu redukowala żywotność do około 40%. Natomiast w całym zakresie badanych stężeń Ful-DOX obserwowalam żywotność w zakresie 95–100% dla wszystkich użytych linii komórkowych. Przypuszczałam, iż może być to efekt powstających

agregatów. Aby to potwierdzić komórki linii MCF-7 inkubowałam z DOX oraz Ful-DOX, a następnie wizualizowałam stosując mikroskopię konfokalną (**Rys. 10I** oraz **Rys. 8 w P1**). Jak oczekiwałam, wolna forma DOX akumulowała się w jądrze komórkowym, czego nie obserwowałam w przypadku koniugatu Ful-DOX. Zarejestrowane obrazy mikroskopowe pokazują, iż koniugat Ful-DOX nie wnikał do jądra komórkowego, lecz agregował na błonie jądrowej, co pozostaje w zgodzie z faktem, iż rozmiar porów znajdujących się w błonie jądrowej nie przekracza 25 nm.⁸¹ Akumulacja Ful-DOX na błonie jądrowej i brak penetracji do wnętrza jądra komórkowego uniemożliwiają cytotoksyczne działanie DOX, jakim jest m. in. jej interkalacja pomiędzy pary zasad DNA. Dalsze badania i ewentualne modyfikacje koniugatu Ful-DOX zostały więc zaniechane.



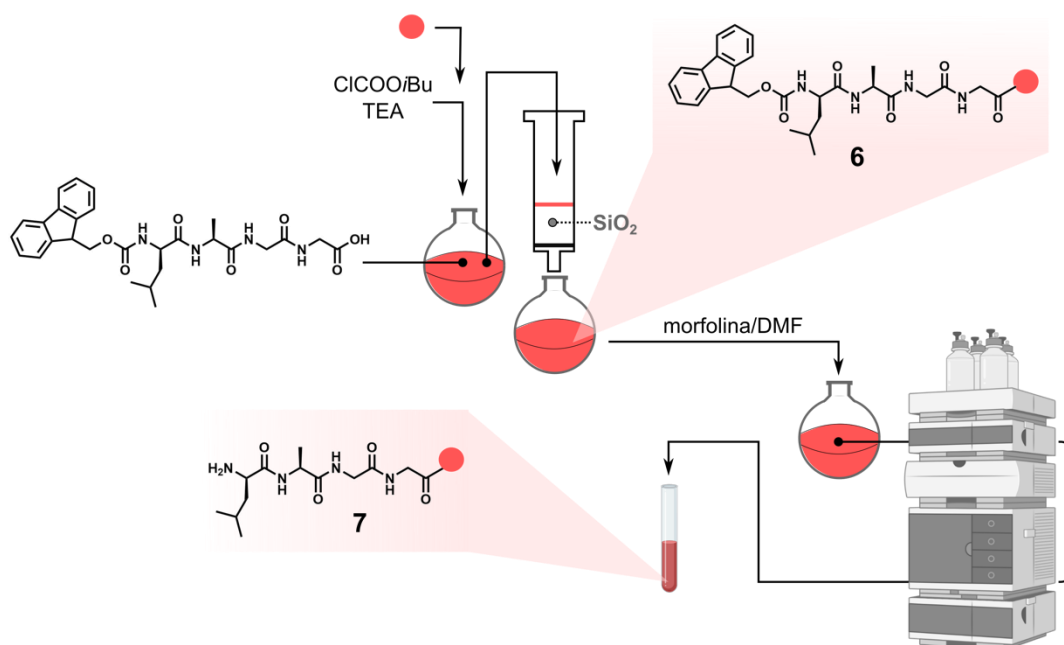
Rysunek 10. Analiza biologiczna in vitro koniugatu Ful-DOX. **A, B.** Żywność komórek MDA MB 231 inkubowanych przez 28 godzin wolną formą DOX (lewy panel) oraz koniugatem Ful-DOX (prawy panel) w zakresie stężeń od 0 do 4 µM. **C, D** Żywność komórek MCF-7 inkubowanych przez 28 godzin wolną formą DOX (lewy panel) oraz koniugatem Ful-DOX (prawy panel) w zakresie stężeń od 0 do 4 µM. **E, F** Żywność komórek T47D inkubowanych przez 28 godzin wolną formą DOX (lewy panel) oraz koniugatem Ful-DOX (prawy panel) w zakresie stężeń od 0 do 4 µM. **G, H** Żywność komórek PC3 inkubowanych przez 28 godzin wolną formą DOX (lewy panel) oraz koniugatem Ful-DOX (prawy panel) w zakresie stężeń od 0 do 4 µM. **I** Obrazy otrzymane przy wykorzystaniu mikroskopii konfokalnej dla komórek MCF-7 inkubowanych wolną formą DOX oraz koniugatem Ful-DOX. Jądro komórkowe zostało wybarwione przy użyciu Hoechst 33342. Szczegółowy opis zaprezentowanych wyników znajduje się w publikacji **P1**.

2. Dostarczanie doksorubicyny poprzez nośnik wrażliwy na działanie metaloproteinaz macierzy pozakomórkowej [P2, P3]

Wyniki otrzymane w pierwszym etapie projektu i opisane w pracy **P1** nadały nowy kierunek dalszym badaniom. W kolejny etapie postanowiłam wykorzystać nośnik wrażliwy na działanie wybranej klasy enzymów, których nadekspresja jest obserwowana w przypadku komórek nowotworowych. W tym celu wytypowałam MMP-2 oraz MMP-9 (MMP-2/-9) jako jedne z ciekawszych i dobrze opisanych markerów nowotworowych. Dane literaturowe proponują szereg sekwencji peptydowych specyficznych względem MMP-2/-9, których degradacja odbywa się dwuetapowo, prowadząc do uwolnienia transportowanego leku.^{82,83} Kratz i współpracownicy zaprezentowali szereg danych jakościowych i ilościowych, charakteryzując uwalnianie DOX w funkcji czasu z nośnika wrażliwego na MMP.⁸⁴ Początkowo obserwowany jest produkt pośredni jako wynik działania MMP na DDSs, a dopiero w drugim etapie następuje całkowite uwolnienie DOX. Produkt pośredni (powstający w pierwszym etapie trawienia) obserwowany jest nawet do 10 godzin po rozpoczęciu inkubacji z MMP. Obserwacje Kratza'ego skłoniły mnie do głębszych rozważań nad molekularnym mechanizmem działania produktu pośredniego na DNA.

Ponieważ jednym z głównych mechanizmów działania DOX jest jej interkalacja do dwuniciowego DNA postanowiłam zbadać zachodzenie tego procesu dla produktu pośredniego.⁸⁵ W tym celu, zaproponowałam oktapeptyd (8-pep) o sekwencji glicyna₁-prolina₂-leucyna₃-glicyna₄-leucyna₅-alanina₆-glicyna₇-glicyna₈, jako substrat ulegający hydrolizie w obecności MMP. W pierwszej kolejności zbadalam czy zaprojektowany 8-pep ulega hydrolizie w obecności MMP. Z punktu widzenia badań nad nośnikami wrażliwymi na działanie MMP istotne jest, aby substrat był wydajnie trawiony przez wybrany enzym. Dzięki wykorzystaniu wysokosprawnej chromatografii cieczonej (HPLC) i analizie MALDI-TOF wykazałam, iż hydroliza wiązania peptydowego zachodzi w pozycji ...-glicyna₄-leucyna₅-..... Dokładna analiza ilościowa potwierdziła, że zaproponowany 8-pep jest odpowiednim substratem do opracowania nośnika DOX wrażliwego na MMP. Po 12 godzinach inkubacji 8-pep z MMP obserwowałam mniej niż 20% substratu (**Rys. 12A,B** oraz **Rys. 2A,B** w **P2**). Aby scharakteryzować zachowanie produktu przejściowego przeprowadziłam jego dwuetapową syntezę (**Rys. 11** oraz **Rys. 3** w **P2**) stosując tetrapeptyd (4-pep) leucyna₅-alanina₆-glicyna₇-glicyna₈ (produkt trawienia 8-pep), posiadający dodatkowo osłonę Fmoc w celu tymczasowej ochrony grupy α-aminowej N-końcowego aminokwasu (Fmoc-4-pep).⁸⁶

W pierwszym etapie chroniony 4-pep sprzęgałam z DOX używając metody mieszanych bezwodników, która polegała na kondensacji chloromrówczanu isobutyłu (ClCOO*i*Bu) z *N*-chronionym 4-pep w obecności trietyloaminy (TEA) w DMF.⁸⁷ Następnie, do otrzymanej mieszaniny dodałam DOX otrzymaną w wyniku osobnej reakcji chlorowodoru DOX z TEA w DMF. Otrzymany produkt Fmoc-4-pep-DOX **6** oczyszczałam z wykorzystaniem kolumnowej preparatywnej chromatografii cieczowej. Drugim krokiem, była deprotekcja Fmoc-4-pep-DOX **6** przy zastosowaniu 50% roztworu morfoliny w DMF. Otrzymany produkt końcowy 4-pep-DOX **7** oczyszczałam za pomocą HPLC.



Rysunek 11. Schemat syntezy 4-pep-DOX.

Do scharakteryzowania oddziaływań 4-pep-DOX oraz wolnej formy DOX z fragmentem DNA o długości 20 par zasad zastosowałam szereg technik instrumentalnych, włączając w to spektrofotometrię UV-vis, spektrofluorymetrię, i izotermiczną kalorymetrię miareczkową (ITC, ang. *isothermal titration calorimetry*). Spektrofotometria UV-vis pozwoliła na zidentyfikowanie oddziaływań DOX i 4-pep-DOX z DNA poprzez porównanie widma ligandów (DOX i 4-pep-DOX) z widmem powstałego kompleksu ligand/DNA w trakcie miareczkowania ligandów wzrastającą ilością DNA (**Rys. 12C,D** oraz **Rys. 4A,B** w **P2**). Według literatury, cechą charakterystyczną powstawania kompleksów jest przesunięcie maksimum absorpcji kompleksu w kierunku fal dłuższych.⁸⁸ Faktycznie, w przypadku miareczkowania DOX wodnym roztworem DNA zaobserwowałam nieznaczne przesunięcie widma w tym kierunku. W przypadku spektrofluorymetrii, do badania wspomnianych wyżej

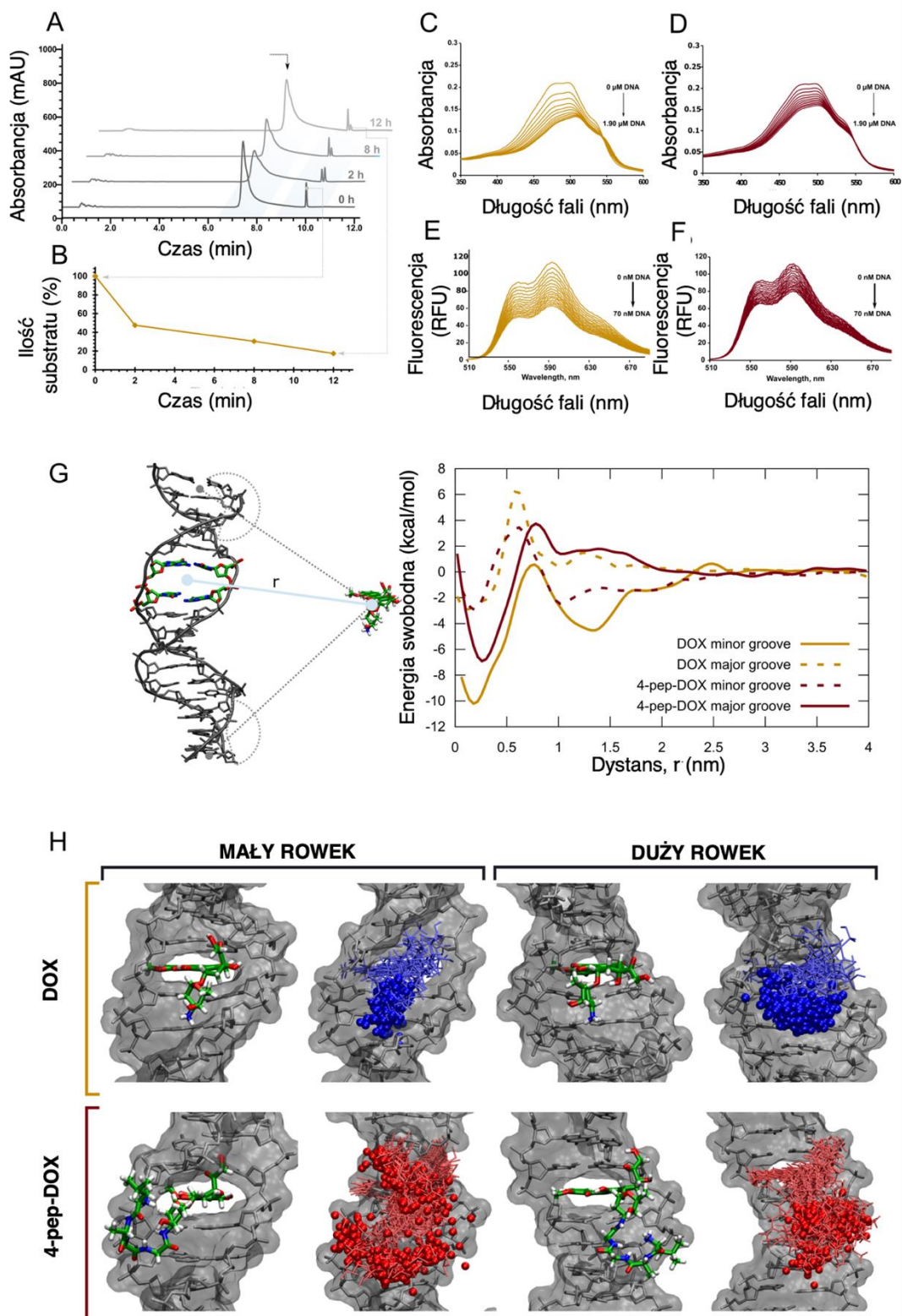
oddziaływań stosuje się miareczkowanie fluorescencyjne. Fluorofory, tutaj DOX i 4-pep-DOX były miareczkowane kolejnymi porcjami DNA, a następnie dokonywano pomiaru intensywności fluorescencji (**Rys. 12E,F** oraz **Rys. 5A,B** w **P2**). Unieruchomienie fluoroforów w kompleksie z DNA może powodować wygaszenie wraz ze wzrostem stężenia wygaszacza (DNA) w mieszaninie. Otrzymane dane jednoznacznie wskazują na mechanizm gaszenia statycznego, które w przeciwieństwie do gaszenia dynamicznego polega na natychmiastowym odebraniu energii wzbudzenia DOX i 4-pep-DOX przez DNA. Interesującą metodą pomiarową dającą informacje o pełnym profilu termodynamicznym reakcji oddziaływania liganda z DNA jest ITC.⁸⁹ Zachodzący proces wiązania liganda do DNA powoduje efekty cieplne – ciepło może być wydzielane lub pochłaniane w zależności od obserwowanego oddziaływania.

W każdym z powyższych eksperymentów wodne roztwory DOX oraz 4-pep-DOX miareczkowano roztworem DNA. Wykorzystując odpowiednie równania obliczono stałe wiązania/asocjacji (K_A) i dysocjacji (K_D) oraz energię swobodną (ΔG) procesu interkalacji DOX i 4-pep-DOX do DNA. Dodatkowe parametry termodynamiczne jak entalpia (ΔH) i entropia (ΔS) zostały wyznaczone na podstawie izoterm otrzymanych z pomiarów kalorymetrycznych. Uzyskane dane, pozwoliły stwierdzić, że produkt pośredni hydrolizy jest w stanie oddziaływać z DNA. Przykładowo, ΔG_{ITC} obliczona na podstawie danych kalorymetrycznych wynosi odpowiednio -8,26 kcal/mol dla układu DOX··DNA i -5.78 kcal/mol dla 4-pep-DOX. Ujemne wartości ΔG_{ITC} świadczą o spontanicznym zachodzeniu procesu interkalacji dla obu związków. Godnym podkreślenia jest fakt, że stałe termodynamiczne otrzymane eksperymentalnie, zarówno dla procesu interkalacji DOX, jak i 4-pep-DOX są porównywalne z danymi teoretycznymi. Stosując dynamikę molekularną, przeanalizowano profile energii swobodnej wiązania ligandów z DNA (ΔG), które dodatkowo ujawniły różne miejsca interkalacji wolnej formy DOX i 4-pep-DOX (**Rys. 12G** oraz **Rys. 10A,B** w **P2**). Może być to wynik modyfikacji DOX poprzez wprowadzenie do struktury łańcucha peptydowego, który ukierunkował wiązanie się 4-pep-DOX do DNA w dużym rowku, tak jak zachodzi to w przypadku większych molekuł (np. białka, **Rys. 12H** oraz **Rys. 11** w **P2**).⁹⁰ Oddziaływania tego typu nie obserwowano dla wolnej formy DOX, która interkaluje w małym rowku.⁹¹ Ponadto zgodnie z literaturą, DOX tworzy kompleksy interkalacyjne z DNA w miejscach zawierających sekwencję 5'-GC-3' i 5'-CG-3', co wpływa bezpośrednio na elastyczność podwójnej helisy, powodując jej relaksację.⁹² Dlatego wszystkie

opisane pomiary przeprowadziłam dla dwuniciowego oligonukleotydu zawierającego powtarzające się pary zasad 5'-CG-3'.

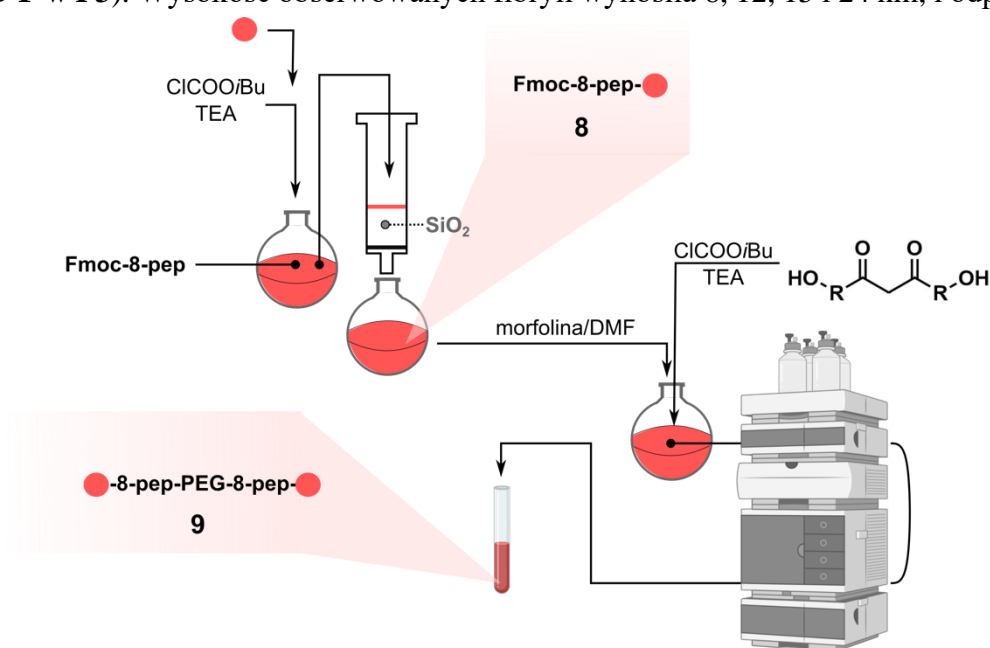
Na podstawie otrzymanych wyników można przypuszczać, że uwolnienie DOX z produktu przejściowego nie jest konieczne do efektywnego działania cytotoksycznego związku i już sam 4-pep-DOX może znacząco zaburzać procesy komórkowe. Dlatego w kolejnym etapie postanowiłam otrzymać nośnik wrażliwy na działanie MMPs, posługując się wcześniej opisanym 8-pep (PEG-8-pep-DOX, **P3**).

Po nieudanej próbie otrzymania aktywnego biologicznie nośnika Ful-DOX opisanego w publikacji **P1**, wykazującego tendencję do agregacji ze względu na obecność hydrofobowego fulerenu, zdecydowałam nie wykorzystywać go do dalszych modyfikacji łańcuchem peptydowym. Za nośnik posłużył natomiast wcześniej otrzymany ester aktywny **3** (nie zawierający w strukturze cząsteczki fulerenu C₆₀; **Rys. 8**). W celu otrzymania koniugatu PEG-8-pep-DOX przeprowadziłam trzyetapową syntezę (**Rys. 13** oraz **Rys. 1** w **P3**). Początkowo, oktapeptyd (8-pep) chroniony Fmoc sprzęgałam z DOX przy użyciu wcześniej opisanej metody mieszanych bezwodników. W drugim kroku, otrzymany Fmoc-8-pep-DOX **8** traktowałam 50% morfoliną w celu usunięcia osłony Fmoc, a następnie otrzymany 8-pep-DOX poddałam reakcji z estrem aktywnym **3**, otrzymując końcowy produkt PEG-8-pep-DOX **9**. Koniugat PEG-8-pep-DOX oczyszczałam przy użyciu metody HPLC. Ponadto, koniugat PEG-8-pep-DOX zidentyfikowałam za pomocą techniki MALDI-TOF. Otrzymane widmo MALDI-TOF było w dobrej zgodności z widmami obserwowanymi w przypadku fragmentacji koniugatu Ful-DOX **5** i rozpadem cząsteczki doksorubicyny.



Rysunek 12. Analiza fizykochemiczna oraz teoretyczna procesu interkalacji DOX i 4-pep-DOX do DNA. **A.** Chromatogramy HPLC zarejestrowane dla 8-pep inkubowanego z MMP w czasie 12 godzin. **B.** Wydajność trawienia 8-pep w funkcji czasu. **C.** Zmiany widma absorpcyjnego DOX w trakcie miareczkowania roztworem DNA zarejestrowane w zakresie długości fal 350-600 nm. **D.** Zmiany widma absorpcyjnego 4-pep-DOX w trakcie miareczkowania roztworem DNA zarejestrowane w zakresie długości fal 350-600 nm. **E.** Intensywność fluorescencji DOX miareczkowania roztworem DNA. **F.** Intensywność fluorescencji 4-pep-DOX miareczkowania roztworem DNA. **G.** Interkalacja DOX i 4-pep-DOX do DNA wraz z profilem energii swobodnej tworzenia kompleksu ligand/DOX. **H.** Miejsca interkalacji DOX i 4-pep-DOX do DNA. Szczegółowy opis zaprezentowanych wyników znajduje się w pracy P2.

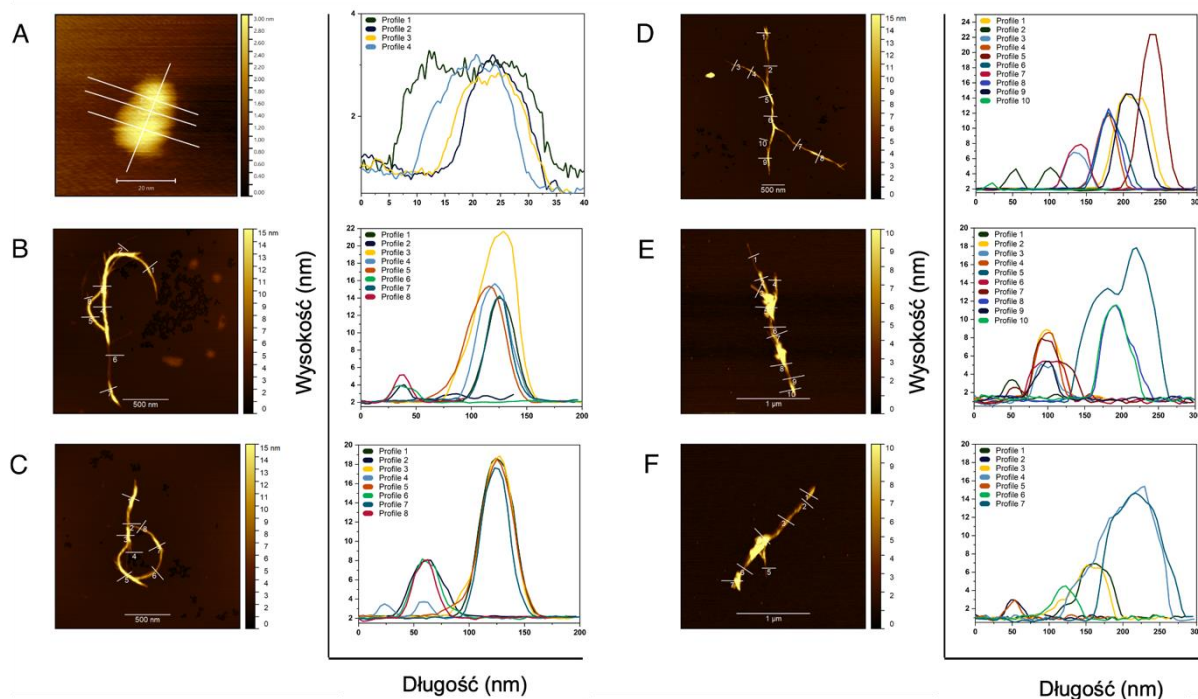
W celu scharakteryzowania koniugatu PEG–8–pep–DOX zdecydowałam się na pomiar potencjału zeta, który daje informację o ładunku powierzchniowym. Koniugat PEG–8–pep–DOX wykazywał ujemny ładunek, co może osłabiać wychwyty komórkowy ze względu na również ujemnie naładowaną błonę komórkową. Morfologię koniugatu scharakteryzowałam przy użyciu mikroskopii sił atomowych (AFM, ang. *atomic force microscopy*) Zarejestrowałam szereg obrazów AFM, przedstawiających agregaty o kształcie fibryli (**Rys. 14B-F** oraz **Rys. 3B-F w P3**). Wysokość obserwowanych fibryli wynosiła 6, 12, 15 i 24 nm, i odpowiadała



Rysunek 13. Schemat syntezy PEG–8–pep–DOX (oznaczonego jako DOX–8–pep–PEG–8–pep–DOX).

wielokrotności wysokości pojedynczej cząsteczki koniugatu wynoszącej około 3 nm (**Rys. 14A** oraz **Rys. 3A w P3**), co świadczy o silnych oddziaływaniach pomiędzy cząsteczkami koniugatu.⁹³ Obserwowana zdolność do agregacji sugeruje obniżoną aktywność biologiczną PEG–8–pep–DOX. Postanowiłam zatem zbadać mechanizm agregacji, tak aby określić czy wiązanie peptydowe ulegające hydrolizie w wyniku działania MMP jest dostępne dla enzymu pomimo tworzenia fibryli. W tym celu wykorzystałam symulacje dynamiki molekularnej dla monomeru, dimeru, tetrameru oraz oktameru PEG–8–pep–DOX (**Rys. 15A,B** oraz **Rys. 4** i **Rys. 5A-C w P3**). Wyniki obliczeń MD sugerują, że cząsteczki wykazują wysoką tendencję do tworzenia fibryli. Dla wszystkich układów wyznaczono procentowy udział fragmentu DOX, 8–pep i łańcucha PEG w zewnętrznej warstwie agregatów (**Rys. 15C** oraz **Rys. 6A,B w P3**). W przypadku DOX jest to około 39%, dla peptydu 37%, a fragment PEG to jedynie 24% powierzchni zewnętrznej fibryli. Taka struktura agregatów i eksponowanie fragmentu peptydowego może świadczyć o tym, że pomimo agregacji fragment peptydowy wrażliwy na działanie MMP jest dostępny dla efektywnego działania enzymu. W celu dokładniejszej analizy

mechanizmu agregacji zidentyfikowano fragmenty koniugatu mające największy udział podczas zachodzenia tego procesu. Analiza kontaktów wykazała, że proces ten zachodzi poprzez oddziaływania pomiędzy cząsteczkami DOX oraz fragmentu peptydowego z DOX.

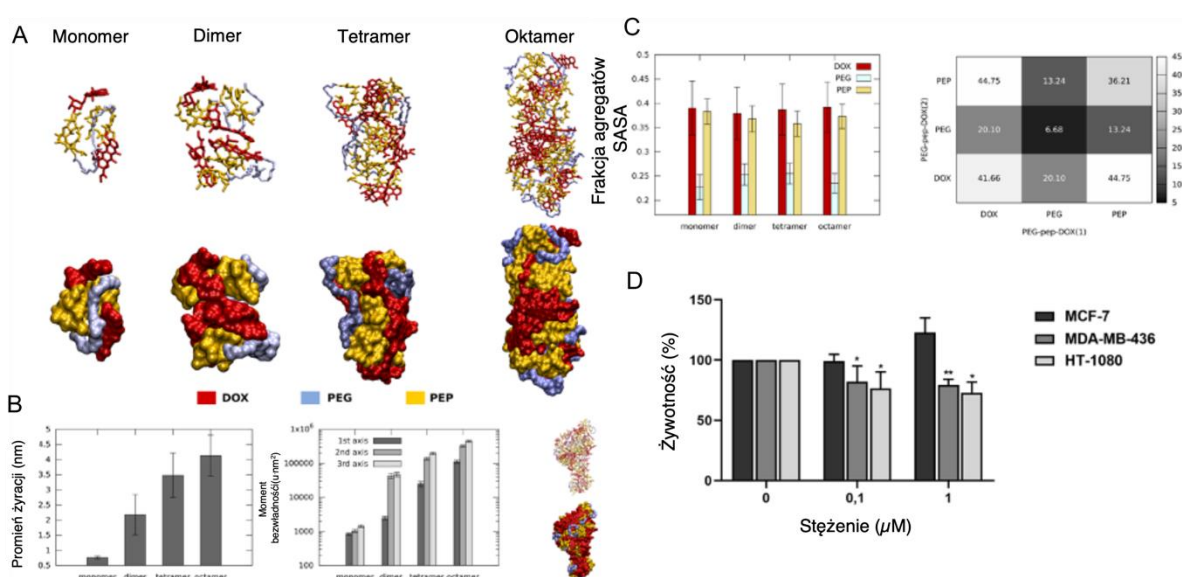


Rysunek 14. Analiza AFM koniugatu PEG-8-pep-DOX. **A.** Obraz pojedynczej cząsteczki koniugatu PEG-8-pep-DOX (lewy panel) wraz z przekrojem poprzecznym (prawy panel). **B-F.** Obrazy zarejestrowane dla obserwowanych fibryli (lewy panel). Wraz z ich przekrojami poprzecznymi (prawy panel). Szczegółowy opis zaprezentowanych wyników znajduje się w manuskrypcie P3.

Otrzymane wyniki sugerują, że pomimo agregacji koniugatu PEG-8-pep-DOX powinien on nadal być aktywny biologicznie, ze względu na ekspozycję wrażliwego na MMP fragmentu peptydowego. Zdecydowałam się więc na przeprowadzenie testu MTT, w celu określenia działania cytotoksycznego koniugatu w stężeniach 0, 0,1 i 1 μM (**Rys. 15D** oraz **Rys. 7** w **P3**). Test przeprowadziłam dla trzech wybranych linii komórek nowotworowych: włóknakiomięsaka HT-1080, raka piersi MDA-MB-436 (linia wykazujące wysoką ekspresję MMP) oraz raka piersi MCF-7 (linia komórkowa wykazująca niską ekspresję MMP). PEG-8-pep-DOX przejawiał właściwości cytotoksyczne względem linii HT-1080 i MDA-MB-436, skutkując obniżeniem żywotności o 25% dla najwyższego stężenia koniugatu. Efekt ten nie był obserwowany w przypadku linii MCF-7 (żywotność >100%), co może być bezpośrednio związane z brakiem wzmożonej ekspresji MMP. Dodatkowo, zaskakujący efekt wzrostu żywotności komórek MCF-7 można wytłumaczyć potencjalnym rozpoznawaniem peptydu przez inne receptory błony komórkowej, co skutkuje promowaniem wzrostu komórek. Wyniki te mogą wskazywać, iż koniugat redukuje wzrost komórek wykazujących nadekspresję MMP

i wykazuje tym samym selektywność, jednak efekt cytotoksyczny jest niższy niż spodziewany. Tak niski efekt można tłumaczyć niewystarczającym stężeniem enzymu w badanym układzie lub za krótkim czasem inkubacji.

Podsumowując, koniugat PEG-8-pep-DOX pomimo obserwowanej agregacji wykazuje umiarkowaną aktywność biologiczną względem linii komórkowych charakteryzujących się nadekspresją MMP. Doniesienia literaturowe oraz przeprowadzone przez mnie analizy sugerują, że DDSs wrażliwe na działanie MMP są interesującym i dynamicznie rozwijającym się kierunkiem badań, które w przyszłości mogą zaowocować nową grupą terapeutyków.^{94,95}

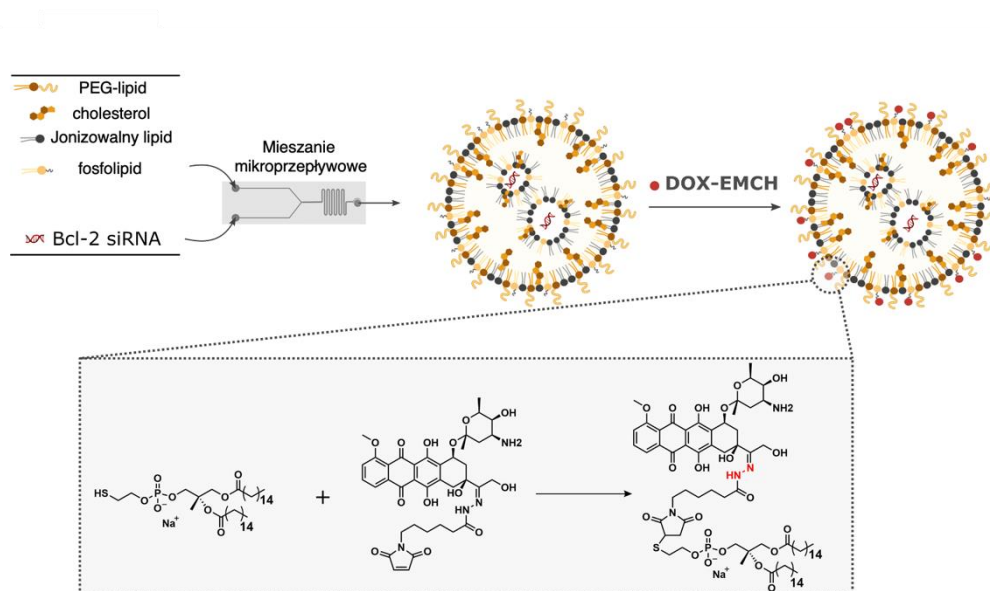


Rysunek 15. Analiza procesu agregacji koniugatu PEG-8-pep-DOX. *A.* Przykładowe struktury agregatów zawierające kolejno 2, 4 i 8 cząsteczek koniugatu PEP-8-pep-DOX. *B.* Średnia wartość promienia żyracji oraz moment bezwładności względem głównych osi wraz z przykładową strukturą agregatu dla 16 cząsteczek koniugatu PEP-8-pep-DOX. *C.* Pole powierzchni agregatów koniugatu PEP-8-pep-DOX dostępne dla rozpuszczalnika oraz liczba kontaktów pomiędzy DOX, PEG i 8-pep. *D.* Żywotność komórek MCF-7, MDA-MB-436 oraz HT-1080 inkubowanych koniugatem PEP-8-pep-DOX w czasie 72 godzin. Szczegółowy opis zaprezentowanych wyników znajduje się w manuskrypcie P3.

3. Dostarczanie doksorubicyny oraz siRNA za pomocą nanocząstek lipidowych [P4]

Nanocząstki lipidowe (LNP), posiadające dobrze zorganizowaną sferyczną strukturę i pożądane właściwości wymagane do wydajnego wychwytu komórkowego, są idealnymi systemami do dostarczania kwasów nukleinowych.^{96,97} Dodatkowe wprowadzenie do LNP zawierającego RNA (RNA-LNP) leku przeciwnowotworowego, np. DOX, może zaburzać

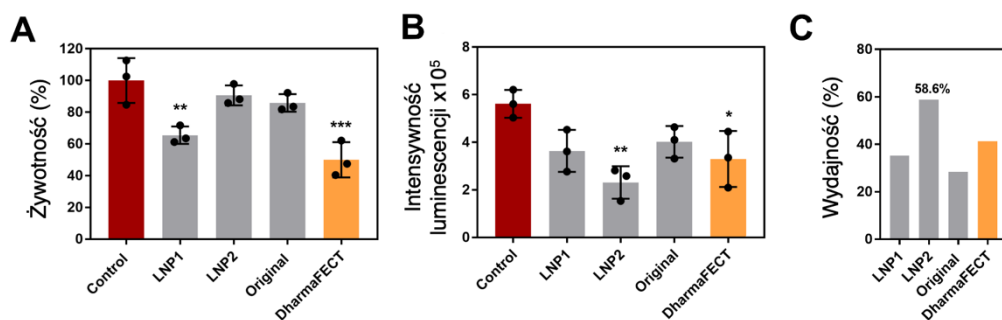
strukturę LNP i zmniejszać wydajność enkapsulacji RNA oraz bezpośrednio wpływać na destabilizację struktury.⁹⁸ W związku z powyższym zaproponowałam i otrzymałam RNA-LNP, która następnie została zmodyfikowana powierzchniowo poprzez wprowadzenie DOX. Ze względu na coraz częstszą oporność komórek nowotworowych na działanie chemioterapeutyków i na sukcesy terapii przy użyciu siRNA, zdecydowałam się na użycie siRNA powodującego represję genu *bcl-2* i deregulację ekspresji antyapoptycznego białka Bcl-2.



Rysunek 16. Schemat otrzymywania LNP2 oraz w dalszym etapie LNP2-DOX przy zastosowaniu mieszania mikroprzepływowego oraz reakcja addycji przy wykorzystaniu PTE i Aldorubicyny.

W pierwszym etapie badań zoptymalizowałam proces otrzymywania LNP, stosując siRNA wyciszający gen lucyferazy (siLuc). LNP otrzymałam przy użyciu techniki mieszania mikroprzepływowego, polegającej na połączeniu fazy wodnej zawierającej RNA z fazą etanolową w składzie: jonizowalny lipid (C12-200), fosfolipid posiadający grupę tiolową (PTE), cholesterol oraz PEG-lipid (C14-PEG2000).^{99,100} Mieszanie odbywało się przy użyciu systemu pomp podłączonych do jednokanałowej płytki wykonanej z poli(dimetylosiloksanu), posiadającej dwa wejścia, odpowiednio na fazę wodną i etanolową, oraz jedno wyjście umożliwiające zebranie utworzonej mieszaniny (**Rys. 16** oraz **Rys. 1A** w **P4**). Jednym z najistotniejszych parametrów podczas procesu otrzymywania LNP jest stosunek molowy jonizowalnego lipidu i siRNA, ponieważ wpływa on na wydajność enkapsulacji. Zastosowane przeze mnie stosunki molowe wytypowane zostały na podstawie danych literaturowych i wynosiły 5:1 (LNP1) oraz 15:1 (LNP2). Wszystkie LNP scharakteryzowałam przy użyciu DLS i pomiaru potencjału zeta. Średni promień hydrodynamiczny otrzymanych LNP mieścił

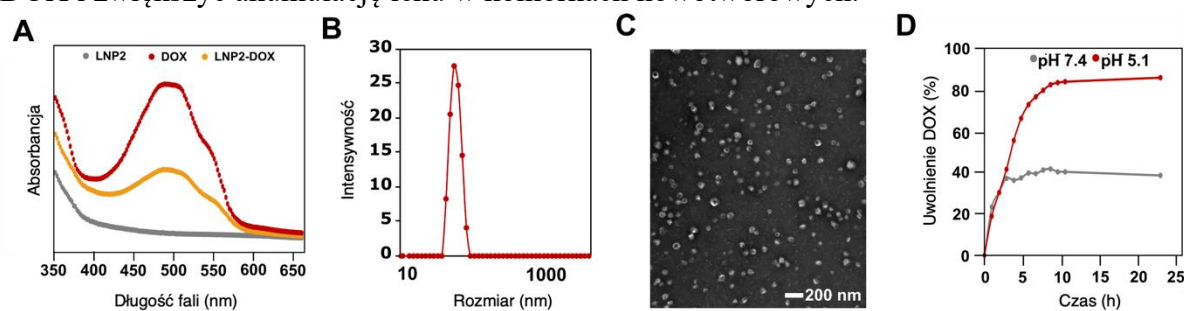
się w zakresie od 65 do 95 nm, a nanocząstki charakteryzowały się niewielkim ładunkiem ujemnym. Następnie zbadalam otrzymane LNP *in vitro*. Aby ocenić potencjalne efekty cytotoksyczne oraz wydajność wyciszania genu lucyferazy zastosowałam linię komórkową chłoniaka Burkitt'a (Raji) wykazującą wysoką aktywność genu reporterowego lucyferazy. Traktowanie komórek Raji LNP1 prowadziło do znaczącego spadku żywotności, jednak tego efektu nie obserwowałam dla nanocząstek LNP2 (**Rys. 17A** oraz **Rys. 2A** w **P4**). Zaprojektowane LNP wyciszały ekspresję lucyferazy w komórkach Raji (**Rys. 17B** oraz **Rys. 2B** w **P4**). W przypadku LNP1 obserwowałam nieznaczne obniżenie luminescencji natomiast dla LNP2 obniżenie intensywności fluorescencji wynosiło aż 58% względem kontroli (**Rys. 17C** oraz **Rys. 2C** w **P4**). Na podstawie powyższych wyników do dalszych badań wytypowałam LNP2 jako układ o najkorzystniejszych parametrach fizykochemicznych, nie wywołujący efektów cytotoksycznych oraz prowadzący do wydajnego wyciszania genu lucyferazy.



Rysunek 17. Analiza biologiczna *in vitro* zaprojektowanych LNP. **A.** Żywotność komórek Raji traktowanych otrzymanymi LNP w stężeniu 50 nM w czasie 48 godzin. **B.** Ekspresja lucyferazy obserwowana w komórkach Raji inkubowanych otrzymanymi LNP w stężeniu 50 nM. **C.** Wydajność wyciszania genu lucyferazy obliczona na podstawie intensywności luminescencji. Szczegółowy opis zaprezentowanych wyników znajduje się w manuskrypcie **P4**.

W celu przyłączenia DOX do powierzchni LNP2 użyłam klinicznie przebadanej Aldorubicyny, posiadającej w swojej strukturze grupę maleinową oraz wiązanie hydrazonowe, które może sprzyjać selektywnemu uwalnianiu DOX w obniżonym pH. Ze względu na obecność grupy maleinowej w strukturze Aldorubicyny zdecydowałam się na zastosowanie reakcji addycji typu Michaela. Reakcja Michaela polega na addycji nukleofilowej do α,β -nienasyconego wiązania C=C występującego, np. w grupie maleimidowej.¹⁰¹ Należy wspomnieć, iż nukleofilem w przypadku tej reakcji jest anion tiolowy powstały w wyniku odszczepienia atomu wodoru z grupy tiolowej.¹⁰² Dlatego w pierwszym kroku, otrzymaną wcześniej LNP2 zawierającą grupę tiolową (obecną w strukturze użytego PTE) traktowałam Aldorubicyną i inkubowałam przez 2 godziny (**Rys. 16** oraz **Rys. 1A** w **P4**). Następnie mieszaninę poddałam dializie w PBS

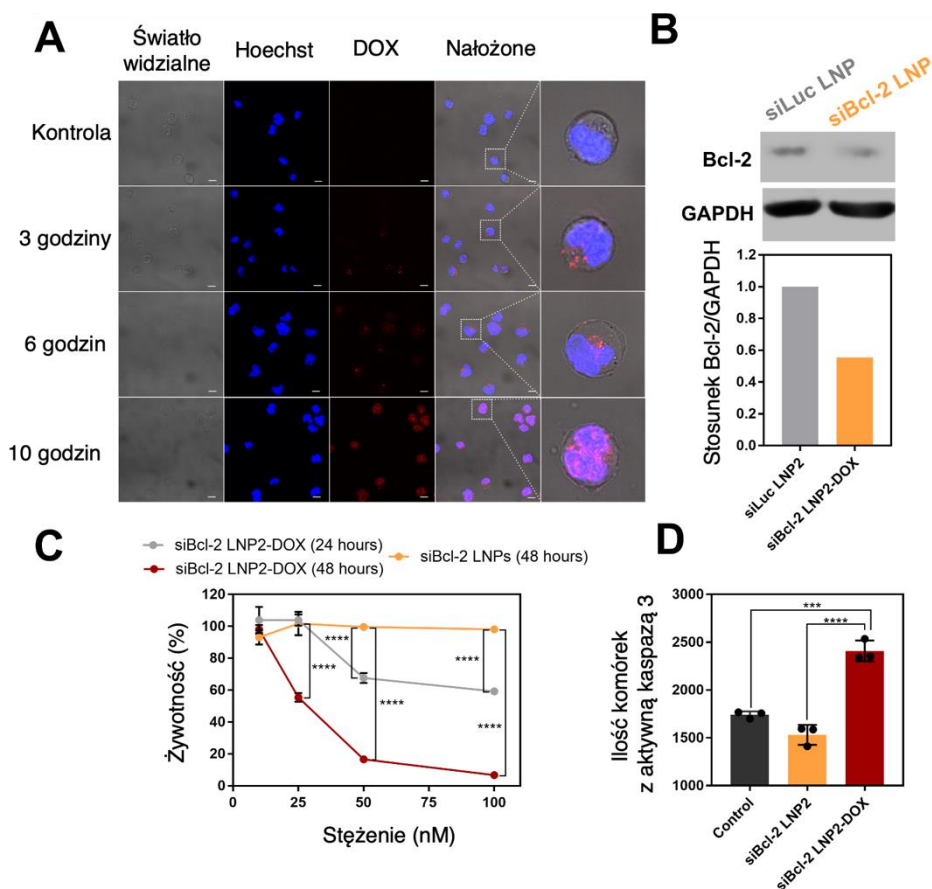
i przefiltrowałam przy użyciu filtrów strzykawkowych, otrzymując produkt końcowy LNP2–DOX. LNP2–DOX charakteryzował się zbliżonym promieniem hydrodynamicznym oraz zeta potencjałem do LNP2. Kolejnym etapem, była analiza widm absorpcyjnych LNP2, wolnej formy DOX oraz produktu końcowego LNP2–DOX (**Rys. 18A** oraz **Rys. 3A** w **P4**). Widmo absorpcyjne LNP2–DOX przypomina sumę widma LNP2 oraz DOX z ich charakterystycznymi maksimami, przy czym pasma te charakteryzują się obniżoną intensywnością w porównaniu do widm LNP2 i DOX. Wynik ten świadczy o udanej koniugacji LNP2 z Aldorubicyną. Oprócz pomiarów DLS zastosowałam również transmisyjną mikroskopię elektronową (TEM, ang. *transmission electron microscopy*) (**Rys. 18B** oraz **Rys. 3B** w **P4**). Obrazy TEM przedstawiały pojedyncze sferyczne struktury o średnim rozmiarze około 70 nm, co było w dobrej zgodności z wynikami DLS (**Rys. 18C** oraz **Rys. 3B** w **P4**). Ponieważ LNP2–DOX posiada w strukturze wiązanie hydrazonowe, wrażliwe na środowisko kwaśne zbadałam profil uwalniania DOX z LNP2–DOX w warunkach fizjologicznych oraz przy pH 5.1, które odpowiada pH obserwowanemu w endosomach lub późnych lizosomach. Tak jak oczekiwałam, profil uwalniania DOX z LNP2–DOX zależał od wartości pH buforu w którym się znajdował badany nośnik (**Rys. 18D** oraz **Rys. 3D** w **P4**). Wyniki eksperymentu dla pH 5.1 wskazały, że 80% DOX zostało uwolnione z nośnika już po 8 godzinach inkubacji, natomiast w przypadku pH fizjologicznego było to jedynie 40%. Otrzymane rezultaty badania uwalniania leku z LNP2–DOX, pozwalają przypuszczać, że LNP2–DOX może zredukować systemową toksycność DOX i zwiększyć akumulację leku w komórkach nowotworowych.



Rysunek 18. Charakterystyka fizykochemiczna LNP2. **A.** Widma absorpcyjne zarejestrowana dla LNP2, DOX oraz LNP2–DOX w zakresie długości fal 350-650 nm. **B.** Rozkład średniego promienia hydrodynamicznego dla LNP2–DOX. **C.** Obraz LNP2–DOX zestresowany przy użyciu TEM. Skala: 200 nm. **D.** Profil uwalniania DOX z LNP2–DOX w buforach o pH 5.1 oraz 7.4 zarejestrowany w czasie 24 godzin. Szczegółowy opis zaprezentowanych wyników znajduje się w manuskrypcie **P4**.

Ocenę wychwytu komórkowego i uwalniania DOX *in vitro* przeprowadziłam z wykorzystaniem mikroskopii konfokalnej (**Rys. 19A** oraz **Rys. 4A** w **P4**). Komórki Raji z wybarwionym jądrem komórkowym traktowałam LNP2–DOX w czasie 0, 3, 6 oraz 10 godzin. Uzyskane wyniki wskazują, iż po upływie 6 godzin DOX stopniowo akumuluje się w jądrze komórkowym, przy jednoczesnym pojawianiu się sygnału fluorescencji DOX

w cytoplazmie. Obrazy otrzymane po 10 godzinach inkubacji jednoznacznie wskazują na całkowitą akumulację DOX w jądrze komórkowym.



Rysunek 19. Analiza biologiczna in vitro LNP2–DOX. **A.** Wychwyty komórkowy i uwalnianie DOX w komórkach Raji inkubowanych LNP2–DOX w czasie 3, 6 i 10 godzin. Obrazy zarejestrowane przy użyciu mikroskopii konfokalnej. Skala: 10 μ m. **B.** Ilość białka Bcl-2 w komórkach Raji traktowanych siBcl2 LNP2 oraz siLuc LNP2 wyznaczona przy użyciu metody Western Blot. **C.** Żywność komórek Raji inkubowanych siBcl-2 LNP2 i siBcl-2 LNP2–DOX w zakresie stężeń od 0 do 100 nM w czasie 24 i 48 godzin. **D.** Wyznaczenie aktywności kaspazy 3 w komórkach Raji przy użyciu cytometrii przepływowej. Szczegółowy opis zaprezentowanych wyników znajduje się w pracy P4.

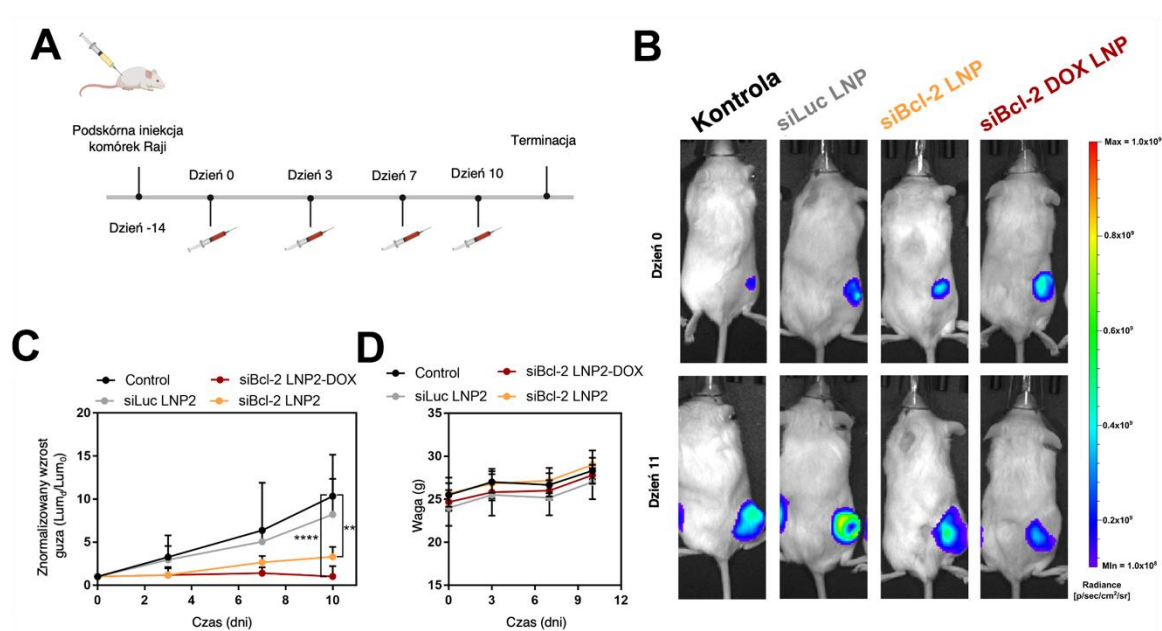
Ważną kwestią do rozważenia przy zastosowaniu LNP2–DOX jest zwiększenie cytotoksyczności DOX, gdy komórkowe antyapoptyczne mechanizmy są osłabione ze względu na wyciszenie genu bcl-2 poprzez wprowadzenie do komórki siRNA. Dlatego wymagane było potwierdzenie wygaszenia genu bcl-2, a tym samym obniżenie ekspresji białka Bcl-2. W tym celu zastosowałam metodę Western Blot. Zastosowanie tej metody pozwoliło mi na analizę ilościową ekspresji białka Bcl-2 w komórkach Raji traktowanych LNP2, które transportowały siRNA wyciszający gen bcl-2 (siBcl2 LNP2). Obserwowałam znaczące obniżenie poziomu ekspresji białka Bcl-2 wynoszące 55% w porównaniu do siLuc LNP2 (**Rys. 19B** oraz **Rys. 4B** w P4). Jednakże, wyciszenie genu bcl-2 było niewystarczające do osiągnięcia

efektów cytotoksycznych, co wykazały wyniki testu CellTiter-Glo (**Rys. 19C** oraz **Rys. 4C** w **P4**). siBcl2 LNP2 nawet po upływie 48 godzin nie hamowały proliferacji komórek Raji w całym spektrum użytych stężeń. Dopiero siBcl2 LNP2 z przyłączoną DOX (siBcl2 LNP2–DOX) przejawiały właściwości cytotoksyczne. siBcl2 LNP2–DOX po inkubacji z komórkami Raji przez dwie doby obniżały żywotność do 60% już przy stężeniu 25 nM. Spadek żywotności obserwowałam wraz ze wzrostem stężenia siBcl2 LNP2–DOX. Przy najwyższym użytym stężeniu nanocząstek żywotność komórek Raji wyniosła jedynie 6%.

Wcześniejsze doniesienia literaturowe wskazują, że DOX jest skutecznym czynnikiem proapoptycznym, inicjującym apoptozę komórek nowotworowych.¹⁰³ Kluczową rolę w tym procesie odgrywają kaspazy, w tym kaspaza 3, która indukuje apoptozę poprzez szlak mitochondrialny.¹⁰⁴ W celu oceny proapoptycznych właściwości siBcl2 LNP2 oraz siBcl2 LNP2–DOX zastosowałam cytometrię przepływową (**Rys. 19D** oraz **Rys. 4D** w **P4**). siBcl2 LNP2 nie powodowały istotnych statystycznie zmian aktywności kaspazy 3. Największe zmiany w aktywności kaspazy 3 obserwowałam w przypadku komórek traktowanych siBcl2 LNP2–DOX. Tutaj aktywność kaspazy 3 była 1,5 razy większa w porównaniu do pozostałych badanych grup. Otrzymane wyniki sugerują, iż siBcl2 LNP2–DOX może wpływać na aktywność kaspazy 3 i wywoływać apoptozę w linii komórkowej Raji.

Kluczowym etapem badań była analiza potencjału terapeutycznego siBcl2 LNP2–DOX na modelu mysim. Na przeprowadzenie badań uzyskano zgodę University of Pennsylvania Institution of Animal Care and Use Committee. W badaniach tych posłużyłam się dojrzałymi samcami myszy szczepu NSG (ang. *NOD scid gamma*) charakteryzującymi się niedoborem immunologicznym. Dwa tygodnie po podskórnej inokulacji w prawą kończynę miedniczną komórek linii nowotworowej Raji wykazującej aktywność genu reporterowego lucyferazy osobniki zostały podzielone na odpowiednie grupy: kontrola (podawano PBS), siLuc LNP2, siBcl2 LNP2 oraz siBcl2 LNP2–DOX. Badane związki, w ilości 1 µg/mysz, były wstrzykiwane bezpośrednio do guza co trzy dni (**Rys. 20A** oraz **Rys. 5A** w **P4**). Badania zakończono 11 dni po rozpoczęciu terapii. Wielkość guza przez cały okres trwania eksperymentu monitorowałam poprzez pomiar bioluminescencji, a następnie otrzymane dane znormalizowałam względem dnia 0 (**Rys. 20B** oraz **Rys. 5B** w **P4**). Otrzymane wyniki pokazują znaczący wzrost guza w grupie kontrolnej. Zarejestrowany ostatniego dnia badań sygnał luminescencji pochodzący z guza był 10-krotnie intensywniejszy w porównaniu do dnia 0 (**Rys. 20C** oraz **Rys. 5C** w **P4**). Grupa poddana terapii przy użyciu siLuc LNP2 wykazywała podobny trend w przyroście guza, co sugeruje brak aktywności przeciwnowotworowej. Interesującą obserwacją było spowolnienie

wzrostu guza w grupie poddanej terapii z siBcl2 LNP2. Wynik ten znacząco różni się od otrzymanych przeze mnie rezultatów badań *in vitro*. Przeprowadzona analiza *in vitro* nie wskazywała na jakiegokolwiek efekty cytotoksyczne względem linii komórkowej Raji, jednak efekt taki obserwowałam w przypadku badań *in vivo*. Ta jakże ciekawa obserwacja może być tłumaczona potencjalnym brakiem dodatkowych czynników proapoptycznych w badaniach *in vitro*, jak np. hipoksja.¹⁰⁵ Co istotne, po 11 dniach terapii z użyciem siBcl2 LNP2-DOX rozmiar guza nie wykazywał przyrostu, sugerując, iż terapia skojarzona z zastosowaniem siBcl-2 i DOX jest najefektywniejszą formą leczenia. Dodatkowo, podczas całego okresu trwania terapii nie zaobserwowałam spadku masy ciała osobników oraz żadnych niepokojących zmian w ich zachowaniu (Rys. 20D oraz Rys. 5D w P4).



Rysunek 20. Analiza biologiczna *in vivo* LNP2–DOX. **A.** Oś czasu zastosowana podczas badań *in vivo*. **B.** Przykładowe obrazy myszy NSG podczas pomiaru luminescencji na początku i końcu prowadzonej terapii. **C.** Krzywe wzrostu guza podczas 11 dni terapii. Dane znormalizowane względem dnia 0. **D.** Średnia masa osobników w trakcie trwania terapii. Szczegółowy opis zaprezentowanych wyników znajduje się w manuskrypcie P4.

Podsumowując, opracowany system siBcl2 LNP2–DOX, wykazujący silne efekty terapeutyczne poprzez zastosowanie terapii skojarzonej, w przyszłości może być obiecującym kandydatem w terapiach przeciwnowotworowych. Zaprojektowany układ może posłużyć do transportu innych rodzajów kwasu nukleinowego, jak również zostać ukierunkowany na inne geny.

IV. Podsumowanie

Tematyka przedłożonej rozprawy doktorskiej obejmuje zagadnienia związane z projektowaniem i otrzymaniem potencjalnych DDSs, służących do wydajnego dostarczenia DOX oraz siRNA. Podjęta tematyka badań wpisuje się w obecne trendy opisywane w literaturze. Przeprowadzone badania miały na celu wyselekcjonowanie DDSs, który wykazuje najlepsze właściwości fizykochemiczne, efekty terapeutyczne i potencjał aplikacyjny.

Uzyskane w toku badań wyniki wykazały, że:

- Badane DDSs charakteryzowały się różnorodną aktywnością biologiczną, wynikającą z ich struktury chemicznej i właściwości.
- Koniugat Ful–DOX cechował się wysoką tendencją do agregacji, co skutkowało jego akumulacją w błonie jądrowej i brakiem efektów cytotoksycznych względem badanych linii nowotworowych.
- Produkt przejściowy potencjalnego trawienia DDSs przez MMP (4–pep–DOX) posiada właściwości umożliwiające interkalację do DNA.
- Interkalacja 4–pep–DOX odbywa się w dużym rowku DNA, co jest charakterystyczne dla makromolekuł i odróżnia ten układ od wolnej formy DOX, interkalującej w małym rowku.
- Koniugat PEG–8–pep–DOX tworzy fibryle w wyniku agregacji zachodzącej poprzez oddziaływanie DOX z DOX oraz fragmentu peptydowego z DOX.
- Efekty cytotoksyczne dla koniugatu PEG–8–pep–DOX były obserwowane w przypadku linii komórkowej wykazującej wzmożoną ekspresję MMP.
- Uwalnianie DOX z LNP2–DOX zachodzi wydajniej w pH 5.1 niż w pH fizjologicznym, co może skutkować zwiększoną akumulacją leku w komórkach nowotworowych.
- siBcl-2 LNP2–DOX wykazuje znaczące efekty cytotoksyczne względem badanej linii komórkowej, nawet przy najniższym zastosowanym stężeniu.
- siBcl-2 LNP2–DOX hamuje ekspresję antyapoptycznego białka Bcl-2 oraz podwyższa aktywność kaspazy 3.
- Terapia skojarzona przy użyciu DOX i Bcl-2 silnie hamuje wzrost guza w modelu mysim chłoniaka Burkitt'a.

Podsumowując, przeprowadzone przeze mnie badania i uzyskane wyniki uzupełniają dotychczasowy stan wiedzy na temat DDSs stosowanych w transporcie DOX i siRNA. Ponadto stanowią one doskonały punkt wyjściowy do dalszych badań, zwłaszcza nad nośnikiem LNP2 opisanym w manuskrypcie **P4**, który charakteryzuje się znakomitymi właściwościami terapeutycznymi względem chłoniaka Burkitt's.

Zastosowanie DDSs w transporcie leków niesie za sobą wielki potencjał i w przyszłości platformy te zostaną zapewne wykorzystane jako skuteczna forma terapii przeciwnowotworowych.

V. Literatura

- ¹ Hoffman A. S. The origins and evolution of “controlled” drug delivery systems. *J. Control. Release* **2008**, 132: 153–163.
- ² Butowska K., Woziwodzka A., Borowik A., Piosik J. Polymeric nanocarriers: a transformation in doxorubicin therapies. *Materials* **2021**, 14:2135.
- ³ Feynman R. There’s plenty of room at the bottom. Caltech Institute Archives **1959**.
- ⁴ Folkman J., Long D. M., Rosenbaum R. A silicone rubber: a new diffusion property useful for general anesthesia. *Science* **1966**, 154:148–149.
- ⁵ Folkman J., Long D. M. The use of silicone rubber as a carrier for prolonged drug therapy. *J. Surg. Res.* **1964**, 4:139–142.
- ⁶ Stewart R. H., Novak S. Introduction of the ocuser ocular system to an ophthalmic practice. *Ann. Ophthalmol.* **1978**, 10:325–330.
- ⁷ Lähteenmäki P., Jukarainen H. Novel delivery systems in contraception. *Br. Med. Bull.* **2000**, 56:739–748.
- ⁸ Theeuwes F., Higuchi T. T. *US Patent* 3,845,770, **1974**.
- ⁹ Langer R., Folkman J. Polymers for the sustained release of proteins and other molecules. *Nature* **1976**, 263:797–800.
- ¹⁰ Kent J., Lewis D., Sanders L. *US Patent* 4,675,189, **1987**.
- ¹¹ Brem H., Langer R. Polymer-based delivery to the brain. *Sci. Med.* **1996**, 3:52–61.
- ¹² Abramović N., Mandić B., Savić-Radojević A., Simić T. Polymeric nanocarriers of drug delivery systems in cancer therapy. *Pharmaceutics* **2020**, 12:298.
- ¹³ Janssen M., Mihov G., Welting T., Thies J., Emanes P. Drugs and polymers for delivery systems OA joints: clinical needs and opportunities. *Polymers* **2014**, 6:799–819.
- ¹⁴ Janes K. A., Fresneasu M. P., Marazuela A., Fabra A., Alonso M. J. Chitosan nanoparticle as delivery systems for doxorubicin. *J. Control. Release* **2001**, 73:255–267.
- ¹⁵ Liu J., Xiao Y., Allen C. Polymer-drug compatibility: a guide to the development of delivery systems for the anticancer agent, ellipticine. *J. Pharm. Sci.* **2004**, 93:132–143.
- ¹⁶ Maeda H. Toward a full understanding of the EPR effect in the primary and metastatic tumors as well as issues related to its heterogeneity. *Adv. Drug Deliv. Rev.* **2015**, 91:3–6.
- ¹⁷ Guo X., Wang L., Wei Z., Zhou S., Polymer-based drug delivery systems for cancer treatment. *J. Polym. Sci. Part A Polym. Chem.* **2016**, 53:3525–3550.

- ¹⁸ Latchford K., Burt H. A., A review of the formation and classification of amphiphilic block copolymer nanoparticle structures: micelles, nanospheres, nanocapsules and polymersomes. *Eur. J. Pharm. Biopharm.* **2007**, 65:259–269.
- ¹⁹ Wu Q., Miao W. S., Zhang Y. D., Hao H. J., Hui D. Mechanical properties of nanomaterials. *Nanotechnol. Rev.* **2020**, 9:259–273.
- ²⁰ Kroto H. W., Heath J. R., O'Brien S. C. O., Curl R. F., Smalley R. E. C₆₀: Buckminsterfullerene. *Nature* **1985**, 318:162–163.
- ²¹ Johnson R. D., Bethune D. S., Yannoni C. S. Fullerene structure and dynamics: a magnetic resonance potpourri. *Acc. Chem. Res.* **1992**, 25:169–175.
- ²² Huang D. L., Dau P. D., Liu H. T., Wang L. S. High-resolution photoelectron imaging of cold C₆₀ anions and accurate determination of the electron affinity of C₆₀. *J. Chem. Phys.* **2014**, 140:224315.
- ²³ Hirsh A. Addition reactions of Buckminsterfullerene (C₆₀). *Synthesis* **1995**, 895–913.
- ²⁴ Lin C. M., Lu T. Y. C₆₀ fullerene derivatized nanoparticles and their application to therapeutics. *Recent Pat. Nanotechnol.* **2012**, 6:105–113.
- ²⁵ Zhao Z., Ukidve A., Kim J., Mitragoti S. Targeting strategies for tissue-specific drug delivery. *Cell* **2020**, 181:151–167.
- ²⁶ Yoo J., Park C., Yi G., Lee D., Koo H. Active targeting strategies using biological ligands for nanoparticles drug delivery systems. *Cancers* **2019**, 11:640.
- ²⁷ Nelson A. L., Dhimolea E., Reichert J. M. Development trends for human monoclonal antibody therapeutics. *Nat. Rev. Drug Discov.* **2010**, 9:767–774.
- ²⁸ Mitrus I., Szala S., Chemioterapia-główne przyczyny niepowodzeń. *Nowotwory* **2009**, 59:368–376.
- ²⁹ White K. A., Grillo-Hill B. K., Barber D. L. Cancer cell behaviors mediated by dysregulated pH dynamics at a glance. *J. Cell Sci.* **2017**, 130:663–669.
- ³⁰ Walker JA, Sorkin MR, Alabi CA. *Quantitative determination of intracellular bond cleavage*. In: Rosania GR, Thurber GM, editors. Quantitative analysis of cellular drug transport, disposition, and delivery. New York: Humana Press.; **2021**. p. 305–330.
- ³¹ Kratz F. Fichtner I., Zhu A., Craig A. INNO-206 (6-maleimidocaproyl hydrazone derivative of doxorubicin) shows superior antitumor efficacy compared to doxorubicin in different tumor xenograft models. *Mol. Cancer Ther.* **2007**, 6:A263.
- ³² Kratz F. DOXO-EMCH (INNO-206): the first albumin-binding prodrug of doxorubicin to enter clinical trials. *Expert Opin. Investig. Drugs* **2007**, 16: 855–866.

- ³³ Kwiatkowski P., Godlewski J., Śliwińska-Jawsiewicka A., Kmieć Z. Rola metaloproteinaz macierzy zewnątrzkomórkowej w procesie inwazji nowotworu. *Pol. Ann. Med.* **2008**, 15:43–50.
- ³⁴ Murphy G., Nagase H. Progress in matrix metalloproteinase research. *Mol. Aspects Med.* **2008**, 2:290–208.
- ³⁵ Lipka D., Boratyński J. Metaloproteinazy MMP. Struktura i funkcja. *Postępy Hig. Med. Dośw.* **2008**, 62:328–336.
- ³⁶ Vihinen P., Kähäri V. M. Matrix metalloproteinases in cancer: prognostic markers and therapeutic targets. *Int. J. Cancer.* **2002**, 99:157–166.
- ³⁷ You Y., Xu Z., Chen Y. Doxorubicin conjugated with trastuzumab epitope and an MMP-2 sensitive peptide linker for the treatment of HER2-positive cancer. *Drug Deliv.* **2018**, 25:448–460.
- ³⁸ Kratz F., Müller I. A., Ryppa C., Warnecke A. Prodrug strategies in anticancer therapies. *ChemMedChem* **2008**, 3:20–53.
- ³⁹ Bremer C., Tung C. H., Weissleder R. In vivo molecular target assessment of matrix metalloproteinase inhibition. *Nat. Med.* **2001**, 7:743–748.
- ⁴⁰ Andreadakis Z., Kumar A., Roman R. G., Tollefsen S., Saville M., Mayhew S. The COVID-19 vaccine development landscape. *Nat. Rev. Drug Discov.* **2020**; 19:305–306.
- ⁴¹ Barenholz Y. C. Doxil®-the first FDA-approved nano-drug: lessons learned. *J. Control. Release* **2021**, 160:117–134.
- ⁴² Akbarzadeh A., Rezaei-Sadabady R., Davaran S., Joo S. W., Zarghami N., Hanifepour Y., Samiei M., Kouhi M., Nejati-Koshiki K. Liposome: classification, preparation, and application. *Nanoscale Res. Lett.* **2013**, 102:1–9.
- ⁴³ Lv H., Zhang S., Wang B., Cui S., Yan J. Toxicity of cationic lipids and cationic polymers in gene delivery. *J. Control. Release* **2006**, 114:100–109.
- ⁴⁴ El-Mayta R., Zhang R., Shepherd S. J., Wang F., Billingsley M. M., Dudkin V., Klein D., Lu H. D., Mitchell M.J. A nanoparticle platform for accelerated in vivo oral delivery screening of nucleic acids. *Adv. Therap.* **2021**, 4:2000111.
- ⁴⁵ Mukalel A. J., Riley R. S., Zhang R., Mitchell M. J. Nanoparticles for nucleic acid delivery: applications in cancer immunotherapy. *Cancer Lett.* **2019**, 458:102–112.
- ⁴⁶ Hafez I. M., Maurer N., Cullis P. R. On the mechanism whereby cationic lipids promote intracellular delivery of polynucleic acids. *Gene Ther.* **2001**, 8:1188–1196.

- ⁴⁷ Thi T. T. H., Suys E. J. A., Lee J. S., Nguyen D. H., Park K. D., Truong N. P. Lipid-based nanoparticles in the clinic and clinical trials: from cancer nanomedicine to COVID-19 vaccines. *Vaccines* **2021**, 9:359.
- ⁴⁸ Sung H., Ferlay J., Siegel R. L., Laversanne M., Soerjomataram I., Jemal A., Bray F. Global Cancer Statistics 2020: GLOBOCAN estimates of incidence and mortality worldwide for 36 cancers in 185 countries. *CA: A Cancer J. Clin.* **2021**, 71: 209–249.
- ⁴⁹ Bray F., Ferlay J., Soerjomataram I., Siegel R. L., Torre L. A., Jemal A. Global Cancer Statistics 2018: GLOBOCAN estimates of incidence and mortality worldwide for 36 cancers in 185 countries. *CA: A Cancer J. Clin.* **2018**, 68: 394–424.
- ⁵⁰ Dyczka J., Jassem J., Fijuth J. (Ed.:R. Kordka), Onkologia. Podręcznik dla studentów i lekarzy. *Via Medica*, Gdańsk, **2007**, 67–70.
- ⁵¹ Chabner B., Roberts T. Chemotherapy and the war on cancer. *Nat. Rev. Cancer* **2005**, 5: 65–72.
- ⁵² Głogowska I., Dubiański, R., Skrzypczyk A., Pieńkowski T. Rola antracyklin w leczeniu zaawansowanego raka piersi-miejsce niepegylowanej doksorubicyny liposomalnej. *Onkol. Prak. Klin.* **2010**, A, A8–A17.
- ⁵³ Carvalho C., Santos R. X., Cardoso S., Correia S., Oliveira P. J., Santos M. S., Moreira P. I. Doxorubicin: the good, the bad and the ugly effect. *Curr. Med. Chem.* 2009, 16:3267–3285.
- ⁵⁴ Weiss R. B. The anthracyclines: will we ever find a better doxorubicin? *Semin. Oncol.* **1992**, 19:670–686.
- ⁵⁵ Goto S., Ihara Y., Urata Y., Izumi S., Abe K., Koji T., Kondo T. Doxorubicin-induced DNA intercalation and scavenging by nuclear glutathione S-transferase. *The FASEB J.* **2001**, 15:2702–2714.
- ⁵⁶ Szulawska A., Czyż M. Molekularne mechanizmy działania antracyklin. *Postępy Hig. Med. Dośw.* **2006**, 60:78–100.
- ⁵⁷ Feinstein E., Canaani E., Weiner L. M. Dependence of nucleic acid degradation on in situ free-radical production by Adriamycin. *Biochemistry* **1993**, 32:13156–13161.
- ⁵⁸ Singal P. K., Iliskovic N. Doxorubicin-induced cardiomyopathy. *N. Engl. J. Med.* **1998**, 339:900–905.
- ⁵⁹ Persidis A. Cancer multidrug resistance. *Nat. Biotech.* **1999**, 17:94–95.
- ⁶⁰ Gillet J. P., Gottesman M. M. Mechanism of multidrug resistance in cancer. In: Zhou J, editors. *Multi-drug resistance in cancer. Methods in molecular biology (methods and protocols)*. New York: Humana Press.; **2010**. p. 47–76.

- ⁶¹ Tsujimoto Y., Cossman J., Jaffe E., Croce C. Involvement of the Bcl-2 gene in human follicular lymphoma. *Science* **1985**, 228:1440–1443.
- ⁶² Mounier N., Briere J., Gisselbrecht C., Emile J. F., Lederlin P., Sebban C., Berger F., Bosly A., Morel P., Tilly H., Bouabdallah R., Reyes F., Gaulard P., Coiffier B. Rituximab plus CHOP (R-CHOP) overcomes bcl-2-associated resistance to chemotherapy in elderly patients with diffuse large B-cell lymphoma. *Blood* **2003**, 101:4279–4284.
- ⁶³ Brunelle J. K., Letai A. Control of mitochondrial apoptosis by the Bcl-2 family. *J. Cell Sci.* **2009**, 122:437–441.
- ⁶⁴ Adams C. M., Clark-Garvey S., Porcu P., Eischen C. M. Targeting the Bcl-2 family in B cell lymphoma. *Front. Oncol.* **2019**, 8:636.
- ⁶⁵ Wei Y., Cao Y., Sun R., Cheng L., Xiong X., Jin X., He X., Lu W., Zhao M. Targeting Bcl-2 proteins in acute myeloid Leukemia. *Front. Oncol.* **2020**, 10:2137.
- ⁶⁶ Xiong H., Veedu R. N., Diermeier S. D. Recent advances in oligonucleotide therapeutics in oncology. *Int. J. Mol. Sci.* **2021**, 22:3295.
- ⁶⁷ Kim R., Emi M., Tanabe K., Toge T. Therapeutic potential of antisense Bcl-2 as a chemosensitizer for cancer therapy. *Cancer* **2004**, 101:2491–2502.
- ⁶⁸ DiNardo C. D., Konopleva M. Y. A venetoclax bench-to-bedside story. *Nat. Cancer* **2021**, 2:3–5.
- ⁶⁹ Knox J. J., Chen X. E., Feld R., Nematollahi M., Cheiken R., Pond G., Zwiebel J. A., Gill S., Moore M. A phase I-II study of oblimersen sodium (G3139, Genasense) in combination with doxorubicin in advanced hepatocellular carcinoma (NCI #5798). *Invest. New Drugs* **2008**, 26:193–194.
- ⁷⁰ Walker A. R., Marcucci G., Yin J., Blum W., Stock W., Kohlschmidt J., Mrózek K., Carroll A. J., Eisfeld A. K., Wang E. S., Jacobson S., Kolitz J. E., Thakuri M., Sutamtewagul G., Vij R., Stuart R. K., Byrd J. C., Bloomfield C. D., Stone R. M., Larson R. A. Phase 3 randomized trial of chemotherapy with or without oblimersen in older ALM patients: CALGB 10201 (Alliance). *Blood Adv.* **2021**, 13:2775–2787.
- ⁷¹ Chen A. M., Zhang M., Wei D., Stueber D., Taratula O., Minko T., He H. Co-delivery of doxorubicin and Bcl-2 siRNA by mesoporous silica nanoparticles enhances the efficacy of chemotherapy in multidrug-resistant cancer cells. *Small* **2009**, 5:2673–2677.
- ⁷² Cheng D., Cao N., Chen J., Yu X., Shuai X. Multifunctional nanocarrier mediated co-delivery of doxorubicin and siRNA for synergistic enhancement of glioma apoptosis in rat. *Biomaterials* **2012**, 33:1170–1179.

- ⁷³ Wittrup A., Lieberman J. Knocking down disease: a progress report on siRNA therapeutics. *Nat. Rev. Genet.* **2015**, 16:543–552.
- ⁷⁴ Meister G., Landthaler M., Patkaniowska A., Dorsett Y., Teng G., Tuschl T. Human Argonaute2 mediated RNA cleavage targeted by miRNA and siRNA. *Mol. Cell* **2004**, 15:185–197.
- ⁷⁵ Akin A., Maier M. A., Manoharan M., Fitzgerald K., Jayaraman M., Barros S., Ansell S., Du X., Hope M. J., Madden T. D., Mui B. L., Semple S. C., Tam Y. K., Ciufolini M., Witzigmann D., Kulkarni J. A., van der Meel R., Cullis P. R. The Onpattro story and the clinical translation of nanomedicines containing nucleic acid-based drugs. *Nat. Nanotechnol.* **2019**, 14:1084–1087.
- ⁷⁶ Damase T. R., Sukhovshin R., Boada C., Tarabilli F., Pittigrew R. I., Cook J. P. The limitless future of RNA therapeutics. *Front. Bioeng. Biotechnol.* **2021**. 9:628137.
- ⁷⁷ Charbe N. B., Amnerkar N. D., Ramesh B., Tambuwala M. M., Bakshi H. A., Aljabali A. A. A., Khadse S. C., Satheeshkumar R., Satija S., Metha M., Chellappan D. K., Shrivastava G., Gupta G., Negi P., Dua K., Zacconi F. C. Small interfering RNA for cancer treatment: overcoming hurdles in delivery. *Acta Pharm. Sin. B* **2020**, 10:2075–2109.
- ⁷⁸ Bingel C. Cyclopropanierung von Fullerenen. *Chem. Ber.* **1993**, 126:1957–1959.
- ⁷⁹ Trimpin S., Keune S., RÄDER H. J., Müllen K. Solvent-free Maldi-MS:development improvements in the reliability and the potential of maldi in the analysis of synthetic polymers and giant organic molecules. *J. Am. Mass Spectrom.* **2006**, 17:667–671.
- ⁸⁰ Di Francesco R., Griggs J. J., Donnelly J., Di Cenzo R. Simultaneous analysis of cyclophosphamide, doxorubicin and doxorubicinol by liquid chromatography coupled to tandem mass spectrometry. *J. Chromatogr. B* **2007**, 852:545–553.
- ⁸¹ Stewart M. Nuclear pore structure and function. *Semin. Cell. Biol.* **1992**, 3:267–277.
- ⁸² Zhu L., Wang T., Perche F., Taigind A., Torchilin V. P. Enhanced anticancer activity of nanopreparation containing an MMP2-sensitive PEG-drug conjugate and cell-penetrating moiety. *Proc. Nat. Acad. Sci USA* **2013**, 110:17047–17052.
- ⁸³ Bacinello D., Garanger E., Taton D., Tam K. C., Lecommandoux S. Enzyme-degradable self-assembled nanostructures from polymer-peptide hybrids. *Biomacromolecules* **2014**, 15:1882–1888.
- ⁸⁴ Mansour A. M., Dreves J., Esser N., Hamada F. M., Badary O. A., Unger C., Fichtner I., Kratz F. A new approach for the treatment of malignant melanoma: enhanced antitumor efficacy of an albumin-binding doxorubicin prodrug that is cleaved by matrix metalloproteinase 2. *Cancer Res.* **2003**, 63: 4062–4066.

- ⁸⁵ Frederic C. A., Dean Williams L., Ughetto G., van der Marel G. A., van Boom H. J., Rich A., Wang A. H. J. Structural comparison of anticancer drug-DNA complexes: Adriamycin and daunomycin. *Biochemistry* **1990**, 29:2538–2549.
- ⁸⁶ Isidro-Llobet A., Álvarez M., Albericio F. Amino acid-protecting groups. *Chem. Rev.* **2009**, 109:2455–2504.
- ⁸⁷ Beyerman H. C., de Leer E. W. B., Floor J. On the repetitive excess mixed anhydride method for the synthesis of peptides. Synthesis of the sequence 1-10 of human growth hormone. *Recl. Trav. Chim. Pays-Bas* **1973**, 92:481–492.
- ⁸⁸ Dougherty G., Pigram W. J. Spectroscopy analysis of drug-nucleic acid interactions. *Critic Rev. Bioch.* **1982**, 103–132.
- ⁸⁹ Haq I., Landbury J. E., Chowdhry B. Z., Jenkins T. C., Chaires J. B. Specific binding of Hoechst 33259 to the d(CGCAAATTTGCG)₂ duplex: calorimetric and spectroscopic studies. *J. Mol. Bio.* **1997**, 271:244–257.
- ⁹⁰ Hamolton P. L., Arya D. P. Natural product DNA major groove binders. *Nat. Prod. Rep.* **2012**, 29:134–143.
- ⁹¹ Cullinane C., Cutts S. M., van Rosmalen A., Phillips D. R. Formation of Adriamycin-DNA adducts in vitro. *Nuc. Acid Res.* **1994**, 22:2296–2303.
- ⁹² Chaires J. B., Fox K. R., Herrera J. E., Britt M., Waring M. J. Site and sequence specificity of the daunomycin-DNA interaction. *Biochemistry* **1987**, 26:8227–8236.
- ⁹³ Hamley, I. W., Krysmann, M. J. Effect of PEG crystallization on the self-assembly of PEG/peptide copolymers containing amyloid peptide fragments. *Langmuir* **2008**, 24:8210–8214.
- ⁹⁴ Vaghasiya K., Ray E., Sharma A., Katare O. P., Verma R. K. Matrix metalloproteinase-responsive mesoporous silica nanoparticle cloaked with cleavable protein for “self-actuating” on-demand controlled drug delivery for cancer therapy. *ACS Appl. Bio Mater.* **2020**, 3:4987–4999.
- ⁹⁵ Kou L., Jiang X., Lin X., Huang H., Wang J., Yao Q., Chen R. Matrix metalloproteinase inspired therapeutic strategies for bone diseases. *Curr. Pharm. Biotechnol.* **2021**, 22:451–467.
- ⁹⁶ Evers M. J. W., Kulkarni J. A., van der Meel R., Cullis P. R., Vader P., Schiffelers R. M. State-of-the-art design and rapid-mixing production techniques of lipid nanoparticles for nucleic acid delivery. *Small Methods* **2018**, 2:1700375.
- ⁹⁷ Krohn-Grimberghe M., Mitchell M. J., Schloss M. J., Khan O. F., Courties G., Guimaraes P. P. G., Rohde D., Cremer S., Kowalski P. S., Sun Y., Tan M., Webster J., Wang K., Iwamoto Y., Schmidt S. P., Wojtkiewicz G. R., Nayar R., Frodermann V., Hulsmans M., Chung A.,

Hoyer F. F., Swirski F. K., Langer R., Anderson D. G., Nahrendorf M. Nanoparticle-encapsulated siRNA for gene silencing in the haematopoietic stem-cell niche. *Nat. Biomed. Eng.* **2020**, 4:1076–1089.

⁹⁸ Ickenstein L. M., Garidel P. Lipid-based nanoparticles formulations for small molecules and RNA drugs. *Expert Opin. Drug Deliv.* **2019**, 16:1205–1226.

⁹⁹ Billingsley MM, Singh N, Ravikumar P, Zhang R, June CH, Mitchell MJ. Ionizable lipid nanoparticle-mediated mRNA delivery for human CAR T engineering. *Nano Lett.* **2020**, 20:1578–1589.

¹⁰⁰ Shepherd S. J., Warzecha C. C., Yadavali S. Y., El-Mayta R., Alameh M. G., Wang L., Weissman D., Wilson J. M., Issadore D., Mitchell M. J. Scalable mRNA and siRNA lipid nanoparticle production using a parallelized microfluidic device. *Nano Lett.* **2021**, 21:5671–5680.

¹⁰¹ Korytkowska-Wałach A., Śmiga-Matuszowicz M., Łukaszczyk J. Układy polimerowe formowane in situ do zastosowań biomedycznych. Cz. II. Wstrzykiwalne układy hydrożelowe. *Polimery*, **2015**, 60:7–8.

¹⁰² Hoyle C. E., Bowman C. N. Thiol-ene click chemistry. *Angew. Chem.* **2010**, 49:1540–1573.

¹⁰³ Decaudin D., Geley S., Hirsch T., Castedo M., Marchetti P., Macho A., Kofler R., Kroemer G. Bcl-2 and Bcl-XL antagonize the mitochondrial dysfunction preceding nuclear apoptosis induced by chemotherapeutic agents *Cancer Res.* **1997**, 57:62–67.

¹⁰⁴ Porter A. G., Jänicke R. U. Emerging roles of caspase-3 in apoptosis. *Cell Death Differ.* **1999**, 6:99–104.

¹⁰⁵ Shimizu A., Eguchi Y., Kamiike W., Itoh Y., Hasegawa J., Yamabe K., Otsuki Y., Matsuda H., Tsujimoto Y. Induction of apoptosis as well as necrosis by hypoxia and predominant prevention of apoptosis by Bcl-2 and Bcl-X_L. *Cancer Res.* **1996**, 56:2161–2166.

VI. Wykaz rysunków i tabel

Rysunek 1. Historyczna oś czasu przedstawiająca zmiany zachodzące w dziedzinie DDSs wraz z przykładami komercyjnie dostępnych leków. **16**

Rysunek 2. Laureaci Nagrody Nobla w dziedzinie chemii nagrodzeni w 1996 roku za odkrycie fulerenów. **17**

Rysunek 3. Schemat dwuetapowego uwalniania leku z nośnika wrażliwego na działanie metaloproteinaz macierzy zewnątrzkomórkowej (MMP). **18**

Rysunek 4. Schemat struktury nanocząstki lipidowej (LNP). **19**

Rysunek 5. Struktura chemiczna doksorubicyny (DOX). **20**

Rysunek 6. Schemat mitochondrialnego szlaku apoptozy regulowanego przez białko Bcl-2. **21**

Rysunek 7. Szlak działania interferujących RNA (opis w tekście). **22**

Rysunek 8. Schemat syntezy koniugatu Ful-DOX 5. **25**

Rysunek 9. Charakterystyka fizykochemiczna koniugatu Ful-DOX. A. Eksperymentalnie otrzymane widmo absorbancji dla DOX, fulerenu C₆₀ oraz koniugatu Ful-DOX, zarejestrowane w zakresie długości fal 350-700 nm. B. Teoretyczne widmo absorbancji otrzymane dla DOX, fulerenu C₆₀ oraz koniugatu Ful-DOX przy użyciu metod kwantowochemicznych DFT. C. Zoptymalizowana struktura fulerenu C₆₀ PM6 D. Zoptymalizowana struktura DOX. E. Zoptymalizowana struktura koniugatu Ful-DOX. F. Rozkład średniego promienia hydrodynamicznego zarejestrowany dla koniugatu Ful-DOX. G. Widmo fluorescencji rejestrowane wraz ze wzrastającym stężeniem koniugatu Ful-DOX. Szczegółowy opis zaprezentowanych wyników znajduje się w publikacji P1. **26**

Rysunek 10. Analiza biologiczna in vitro koniugatu Ful-DOX. A, B. Żywotność komórek MDA MB 231 inkubowanych przez 28 godzin wolną formą DOX (lewy panel) oraz koniugatem Ful-DOX (prawy panel) w zakresie stężeń od 0 do 4 μM. C, D Żywotność komórek MCF-7 inkubowanych przez 28 godzin wolną formą DOX (lewy panel) oraz koniugatem Ful-DOX (prawy panel) w zakresie stężeń od 0 do 4 μM. E, F Żywotność komórek T47D inkubowanych przez 28 godzin wolną formą DOX (lewy panel) oraz koniugatem Ful-DOX (prawy panel) w zakresie stężeń od 0 do 4 μM. G, H Żywotność komórek PC3 inkubowanych przez 28 godzin wolną formą DOX (lewy panel) oraz koniugatem Ful-DOX (prawy panel) w zakresie stężeń od 0 do 4 μM. I Obrazy otrzymane przy wykorzystaniu mikroskopii konfokalnej dla komórek MCF-7 inkubowanych wolną formą DOX oraz koniugatem Ful-DOX. Jądro komórkowe zostało wybarwione przy użyciu Hoechst 33342. Szczegółowy opis zaprezentowanych wyników znajduje się w publikacji P1. **27**

Rysunek 11. Schemat syntezy 4-pep-DOX. **29**

Rysunek 12. A. Chromatogramy HPLC oktapeptydu inkubowanego z MMP w czasie 12 godzin. B. Wydajność trawienia oktapeptydu w czasie. Widma absorpcyjne DOX (C) i 4-pep-DOX (D) miareczkowanych wzrastającym stężeniem DNA. Intensywność fluorescencji DOX (E) i 4-pep-DOX (F) miareczkowanego wzrastającym stężeniem DNA. G. Interkalacja ligandów do DNA i profil energii swobodnej tworzenia kompleksu ligand.DNA. H. Miejsca interklacji ligandów do DNA w zależności od rowka DNA. Szczegółowy opis zaprezentowanych wyników znajduje się w publikacji P2. **32**

Rysunek 13. Schemat syntezy PEG-8-pep-DOX. **33**

Rysunek 14. Analiza AFM koniugatu PEG-8-pep-DOX. A. Obraz pojedynczej cząsteczki koniugatu PEG-8-pep-DOX (lewy panel) wraz z przekrojem poprzecznym (prawy panel). B-F. Obrazy zarejestrowane dla obserwowanych fibryli (lewy panel). Wraz z ich przekrojami poprzecznymi (prawy panel). Szczegółowy opis zaprezentowanych wyników znajduje się w manuskrypcie P3. **34**

Rysunek 15. Analiza teoretyczna procesu agregacji koniugatu PEG-8-pep-DOX. A. Przykładowe struktury agregatów zawierające kolejno 2, 4 i 8 cząsteczek koniugatu PEG-8-pep-DOX. B. Średnia wartość promienia żyracji oraz moment bezwładności względem głównych osi wraz z przykładową strukturą agregatu dla 16 cząsteczek koniugatu PEG-8-pep-DOX. C. Pole powierzchni agregatów koniugatu PEG-8-pep-DOX dostępne dla rozpuszczalnika oraz liczba kontaktów pomiędzy DOX, PEG i 8-pep. D. Żywołność komórek MCF-7, MDA-MB-436 oraz HT-1080 inkubowanych koniugatem PEG-8-pep-DOX w czasie 72 godzin. Szczegółowy opis zaprezentowanych wyników znajduje się w manuskrypcie P3. **35**

Rysunek 16. A. Schemat otrzymywania LNP2 oraz w dalszym etapie LNP2-DOX przy zastosowaniu mieszania mikroprzepływowego oraz reakcja addycji przy wykorzystaniu PTE i Aldorubicyny. **36**

Rysunek 17. Analiza biologiczna in vitro zaprojektowanych LNP. A. Żywołność komórek Raji traktowanych otrzymanych LNP w stężeniu 50 nM w czasie 48 godzin. B. Ekspresja lucyferazy obserwowana w komórkach Raji inkubowanych otrzymanymi LNP w stężeniu 50 nM. C. Wydajność wyciszenia genu lucyferazy obliczona na podstawie intensywności luminescencji. Szczegółowy opis zaprezentowanych wyników znajduje się w manuskrypcie P4. **37**

Rysunek 18. Charakterystyka fizykochemiczna LNP2. A. Widma absorpcyjne zarejestrowana dla LNP2, DOX oraz LNP2-DOX w zakresie długości fal 350-650 nm. B. Rozkład średniego promienia hydrodynamicznego dla LNP2-DOX. C. Obraz LNP2-DOX zestresowany przy użyciu TEM. Skala: 200 nm. D. Profil uwalniania DOX z LNP2-DOX w buforach o pH 5.1

oraz 7.4 zarejestrowany w czasie 24 godzin. Szczegółowy opis zaprezentowanych wyników znajduje się w manuskrypcie P4. **38**

Rysunek 19. Analiza biologiczna *in vitro* LNP2-DOX. A. Wychwyty komórkowy i uwalnianie DOX w komórkach Raji inkubowanych LNP2-DOX w czasie 3, 6 i 10 godzin. Obrazy zarejestrowane przy użyciu mikroskopii konfokalnej. Skala: 10 μ m. B. Ilość białka Bcl-2 w komórkach Raji traktowanych siBcl-2 LNP2 oraz siLuc LNP2 wyznaczona przy użyciu metody Western Blot. C. Żywotność komórek Raji inkubowanych siBcl-2 LNP2 i siBcl-2 LNP2-DOX w zakresie stężeń od 0 do 100 nM w czasie 24 i 48 godzin. D. Wyznaczenie aktywności kaspazy 3 w komórkach Raji przy użyciu cytometrii przepływowej. Szczegółowy opis zaprezentowanych wyników znajduje się w pracy P4. **39**

Rysunek 20. A. Analiza biologiczna *in vivo* LNP2-DOX. A. Oś czasu zastosowana podczas badań *in vivo*. B. Przykładowe obrazy myszy NSG podczas pomiaru luminescencji na początku i końcu prowadzonej terapii. C. Krzywe wzrostu guza podczas 11 dni terapii. Dane znormalizowane względem dnia 0. D. Średnia masa osobników w trakcie trwania terapii. Szczegółowy opis zaprezentowanych wyników znajduje się w manuskrypcie P4. **41**

VII. Kopie publikacji wchodzących w skład pracy doktorskiej

1. **K. Butowska**, W. Kozak, M. Zdrowowicz, S. Makurat, M. Rychłowski, A. Hać, A. Herman-Antosiewicz, J. Piosik, J. Rak, *Cytotoxicity of doxorubicin conjugated with C₆₀ fullerene. Structural and in vitro studies*. Structural Chemistry, **2019**, 30, 2327–2338. [P1]



Cytotoxicity of doxorubicin conjugated with C₆₀ fullerene. Structural and in vitro studies

Kamila Butowska^{1,2} · Witold Kozak² · Magdalena Zdrowowicz² · Samanta Makurat² · Michał Rychłowski³ · Aleksandra Hać⁴ · Anna Herman-Antosiewicz⁴ · Jacek Piosik¹ · Janusz Rak²

Received: 8 May 2019 / Accepted: 20 September 2019 / Published online: 22 October 2019

© The Author(s) 2019

Abstract

Conjugating an anticancer drug of high biological efficacy but large cytotoxicity with a “transporting” molecule of low toxicity constitutes a valuable approach to design safe drug delivery system. In the present study, doxorubicin (DOX) a drug of large cardiotoxicity was chemically conjugated to a C₆₀-fullerene. The synthesized molecule, a fullerene-doxorubicin conjugate (Ful-DOX), was characterized using the ¹H NMR and MALDI TOF mass spectrometry. The absorption and fluorescence spectra and dynamic light scattering of the conjugate were recorded in an aqueous solution, while the impact on viability of several cancer cell lines of the free DOX and the conjugate was compared using the SRB and WST-1 assays. A low antiproliferative activity of the conjugate as compared to the free DOX is a consequence of the presence of fullerene moiety in the former, which is also responsible for the conjugate aggregation in an aqueous solution. Unlike free DOX, these aggregates cannot pass through the nuclear membrane (as demonstrated by the confocal microscopy measurements), which makes them marginally cytotoxic.

Keywords Fullerene · Doxorubicin · Covalent conjugate · Drug delivery · Nanoparticle · Cancer cells

Introduction

Doxorubicin (DOX; for its chemical structure, see Fig. 1) is well known for its anticancer activity. Furthermore, it is commonly used in clinics against various types of cancer in adults

and children [1, 2]. Many studies have attributed DOX anticancer activity to intercalation into tumor cellular DNA, DNA cross-linking, binding to proteins involved in DNA replication and transcription, like topoisomerase II, as well as to generation of reactive oxygen species [3, 4]. Unfortunately, DOX cannot be applied at optimal doses mainly due to its cardiotoxic effects [5]. Although doxorubicin affects the brain, kidney, and liver, the heart seems to be the preferential target for its toxicity [6]. Actually, acute cardiotoxicity is observed in about 11% of patients exposed to DOX [7, 8], while the incidences of chronic myopathy are much less common and estimated to occur in ca 1.7% of cases [9].

Despite the fact that DOX-induced cardiotoxicity has been observed and studied for many years, the mechanism lying behind the toxic effect is still unclear [2]. Several models of cardiotoxicity have been proposed so far. Topoisomerase II, which is suppressed by DOX, was identified as a cardiotoxicity mediator [10]. On the other hand, oxidative stress, mediated by doxorubicin via enzymatic route employing intracellular or intramitochondrial oxidant enzymes, produces hydroxyl radicals that trigger DNA damage, protein modification, lipid peroxidation, and finally cell death by apoptosis or necrosis, which is considered as the main reason for DOX cardiotoxicity [2]. In the context of

Electronic supplementary material The online version of this article (<https://doi.org/10.1007/s11224-019-01428-4>) contains supplementary material, which is available to authorized users.

✉ Janusz Rak
janusz.rak@ug.edu.pl

Jacek Piosik
jacek.piosik@biotech.ug.edu.pl

¹ Laboratory of Biophysics, Intercollegiate Faculty of Biotechnology of the University of Gdańsk and Medical University of Gdańsk, Abrahamia 58, Gdańsk, 80-307, Poland

² Laboratory of Biological Sensitizers, Faculty of Chemistry, University of Gdańsk, Wita Stwosza 63, Gdańsk, 80-308, Poland

³ Department of Virus Molecular Biology, Intercollegiate Faculty of Biotechnology of the University of Gdańsk and Medical University of Gdańsk, Abrahamia 58, Gdańsk, 80-307, Poland

⁴ Department of Medical Biology and Genetics, Faculty of Biology, University of Gdańsk, Wita Stwosza 59, Gdańsk, 80-308, Poland

cardiotoxicity, the literature mentions also that DOX impaired Ca^{2+} handling [11], activated p53-dependent pathways [12], and cytochrome c mediated apoptosis via activation of caspase 9 and 3 [13].

As indicated above, the DOX-induced cardiotoxicity is coupled to an interaction between the anthracycline and a number of proteins. Therefore, a promising way of alleviating its toxic effects seems to be DOX binding into a sufficiently large molecule that would impair the protein-DOX interactions necessary to trigger the DOX toxicity. After accumulation in cancer cells, such a conjugate should release DOX, which only then could cause the lethal effects.

Fullerenes seem to be suitable drug carriers due to the stability of their cage and a relative ease to functionalization [14]. The literature shows that there were already several attempts to employ fullerenes as drug carriers [15]. Both van der Waals (vdW) complexes between the delivered drugs and a fullerene as well as fullerene-drug covalent conjugates were considered for this purpose. For instance, fullerene-DOX complexes, in which the release of DOX was pH-dependent, were prepared and characterized with capillary electrophoresis [16]. Similarly, a complex of fullerene-based carrier with cisplatin (well-known anticancer agents) was tested against lung cancer [17]. Eventually, the enhancement, as compared to the free drugs, of anticancer activity of DOX and cisplatin vdW complexes with a C_{60} -fullerene derivative, has been reported recently [18]. On the other hand, a C_{60} -fullerene-paclitaxel covalent conjugate was proposed as a slow release drug-delivery system [19]. Furthermore, a molecular system in which DOX is conjugated to the C_{60} fullerene via a reactive thioether linker sensitive to the reactive oxygen species (ROS) was tested on a mouse model [20]. The conjugate, of excellent stability in physiological environment, releases DOX due to the photoinduced generated ROS by the excited C_{60} -fullerene that in turn leads to the breakage of the linker. A conjugate strategy was also tested on poly(ethylene glycol) (PEG) connected to DOX and fullerene [21, 22].

Surprisingly, DOX coupled to C_{60} through a PEG spacer showed similar cytotoxicity against the MCF-7 cells as the

free DOX [20]. The observed effect was explained by different mode of action related to the free DOX and fullerene-DOX conjugate. The latter was claimed to be capable of inducing toxic effects in the cytoplasm; thus, in the light of ref. [21], the accumulation of DOX in nucleus might not be a prerequisite of the drug activity. These unexpected and anti-intuitive results prompted us to investigate the cytotoxicity of a similar fullerene-DOX conjugate. In the following, we describe a five-step chemical synthesis of a C_{60} -DOX conjugate coupled by a PEG linker. Using ^1H NMR spectroscopy and high-resolution MALDI-TOF mass spectrometry, we prove the identity of all intermediate products and the final conjugate. The structure of obtained conjugate is characterized physico-chemically with the help of several techniques like absorption and emission spectroscopy as well as dynamic light scattering. Furthermore, the toxicity of the obtained material is tested using two viability assays: SRB and WST-1. Finally, the distribution of the conjugate or the drug in the MCF-7 cells after 2-day incubation with the conjugate or DOX is shown by confocal microscopy. Our investigations unequivocally indicate that DOX covalently conjugated to C_{60} -fullerene is non-toxic in concentrations in which the free drug reduces cell viability by ca 50%.

Experimental and computational

Chemicals and reagents

t-Butyl 12-hydroxy-4,7,10-trioxadodecanoate, carbon tetrabromide, 1,8-diazabicyclo[5.4.0]undec-7-ene (DBU), dicyclohexylcarbodiimide (DCC), doxorubicin hydrochloride, fullerene- C_{60} , malonyl chloride, *N*-hydroxysuccinimide (NHS), trifluoroacetic acid (TFA), trimethylamine (TEA), and dimethyl sulfoxide (DMSO) were purchased from Sigma-Aldrich. Dichloromethane (DCM) was dried and distilled using standard procedures. Anhydrous *N,N*-dimethylformamide (DMF) and toluene were both available from Sigma-Aldrich. Column chromatography was performed using silica gel NORMASIL 60 (40–63 mesh, VWR Chemicals). Thin-layer chromatography was performed with silica gel plates, 60G, F254 (Sigma-Aldrich). RPMI cell culture medium, penicillin/streptomycin antibiotic mixture, and fetal bovine serum were purchased from Corning, while F12 medium in Kaingh modification (F12K) from Gibco. Hoechst 33342 was purchased from ThermoFisher Scientific.

Synthesis of bis(14,14-dimethyl-12-oxo-3,6,9,13-tetraoxapentadecyl) malonate 3 (for the structure see Scheme 1)

Malonyl chloride **1** (0.22 mL, 2.29 mmol) was added to the solution of *t*-butyl 12-hydroxy-4,7,10-trioxadodecanoate **2**

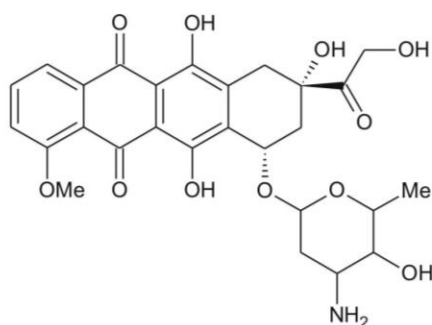


Fig. 1 Chemical structure of DOX

(1.34 g, 4.81 mmol) in dry DCM (10 mL). The mixture was cooled to 0 °C and TEA (0.80 mL, 5.73 mmol) was added. The solution was allowed to warm to room temperature and stirred for 72 h. The reaction was quenched with water (5 mL). The organic layer was separated and the remaining water phase was extracted with DCM (3 × 15 mL). Combined organic layers were dried over MgSO₄ and evaporated. The resulting residue was purified by column chromatography using DCM/MeOH 30/1 as an eluent to give the desired product as a yellowish oil in a 58% yield.

¹H NMR (Bruker AVANCE III, 500 MHz, CDCl₃), δ: 1.47 (s, 18H, CH₃), 2.52 (t, 4H, *J* = 6.6, CH₂), 3.47 (s, 2H) 3.62–3.69 (m, 16H, CH₂), 3.73 (t, 8H, *J* = 5.6, CH₂), 4.32 (t, 4H, *J* = 4.7, CH₂); HRMS (AB SCIEX MALDI TOF/TOF 5800), *m/z*: [M – H][−] calcd for C₂₉H₅₁O₁₄ 623.7140, found 623.2510 (see Figs. S1 and S2, Supplementary Information).

Synthesis of bis(14,14-dimethyl-12-oxo-3,6,9,13-tetraoxapentadecyl) C₆₀-malonate **4** (for the structure see Scheme 1)

To a solution of C₆₀-fullerene (50 mg, 0.069 mmol) in dry toluene (20 mL), malonic ester derivative **3** (37 mg, 0.059 mmol), CBr₄ (20 mg, 0.059 mmol), and DBU (10 μL, 0.066 mmol) were added. The mixture was stirred overnight at room temperature. After that, toluene was evaporated and the crude product was purified by column chromatography using toluene, to remove the unreacted fullerene-C₆₀, and then

DCM/MeOH 50/1 as an eluent to give the desired product as a brown solid in a 63% yield.

HRMS (AB SCIEX MALDI TOF/TOF 5800), *m/z*: [M – H][−] calcd for C₈₉H₄₉O₁₄ 1342.3412, found 1342.1563 (see Fig. S3, Supplementary Information).

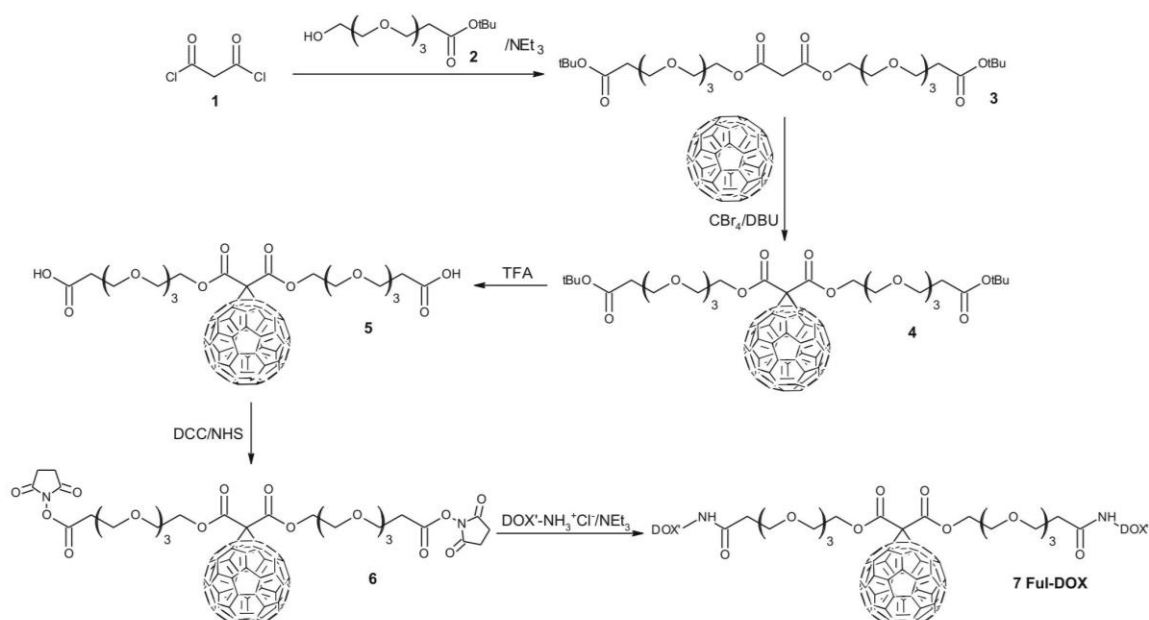
Synthesis of 15-C₆₀-14,16-dioxo-4,7,10,13,17,20,23,26-octaoxonacosane-1,29-dioic acid **5** (for the structure see Scheme 1)

The derivative **4** (50 mg, 0.037 mmol) was dissolved in DCM (15 mL) and TFA (15 mL) was added. The reaction was monitored by TLC analysis, and after the complete disappearance of the product (about 30 min), the mixture was evaporated and the crude product was purified by column chromatography using DCM/MeOH 30/1 as an eluent to give the desired compound as a brown solid in a quantitative yield.

HRMS (AB SCIEX MALDI TOF/TOF 5800), *m/z*: [M – H][−] calcd for C₈₁H₃₃O₁₄ 1230.1286, found 1230.1058 (Fig. S4, Supplementary Information).

Synthesis of bis(2-(2-(2-(3-((2,5-dioxopyrrolidin-1-yl)oxy)-3-oxopropoxy)ethoxy)ethoxy)ethyl) C₆₀-malonate **6** (for the structure see Scheme 1)

To a solution of the derivative **5** (50 mg, 0.041 mmol) in DCM (20 mL), NHS (21 mg, 0.180 mmol) and a solution of DCC (21 mg, 0.102 mmol) in DCM (5 mL) were added. The reaction mixture was left overnight. Then, the solvent was evaporated



Scheme 1 Reaction route for the synthesis of Ful-DOX conjugate 7

and the crude product was purified by column chromatography using DCM/MeOH 30/1. At this point, we eventually got a mixture of the desired product and DCU – a byproduct from the reaction of activation of carboxylic groups in **5**.

HRMS (AB SCIEX MALDI TOF/TOF 5800), m/z : $[M + Na]^+$ calcd for $C_{89}H_{40}N_2NaO_{18}$ 1448.2633, found 1447.1733 (see Fig. S5, Supplementary Information).

Synthesis of bis-doxorubicinyl amide of 15-C₆₀-14,16-dioxo-4,7,10,13,17,20,23,26-octaoxanonacosane-1,29-dioic acid 7 (Ful-DOX 7) (for the structure see Scheme 1)

The raw product **6** (50 mg, 0.035 mmol) was dissolved in dry DMF (2 mL). In the other flask, a solution of doxorubicin hydrochloride (41 mg, 0.070 mmol) in DMF (16 mL) was prepared. To the second mixture, TEA (10 μ L, 0.070 mmol) was added. After 2–3 min, the DOX solution was added dropwise to the DMF solution of **6**. After 48 h of stirring at room temperature, the reaction mixture was evaporated azeotropically with toluene. The final product was purified by column chromatography using as an eluent, at first DCM/MeOH 30/1 (to remove DCU from the activation procedure) and then DCM/MeOH 20/1.

HRMS (AB SCIEX MALDI TOF/TOF 5800), m/z : $[M - H]^-$ calcd for $C_{135}H_{87}N_2O_{34}$ 2281.1365, found 2280.7888 (see Fig. S6, Supplementary Information).

NMR and MS analyses

The NMR spectrum was recorded on a Bruker AVANCE III, 500 MHz spectrometer. Chemical shifts are reported in ppm relative to the residual solvent peak ($CDCl_3 = 7.28$ ppm for 1H). Coupling constants are given in Hertz. The MS measurements of the intermediates and final product were done with use of MALDI TOF/TOF 5800 (ABSciex, Germany). As a matrix, 2,5-dihydroxybenzoic acid (DHB, Sigma-Aldrich) was used. The measurements were done in reflectron negative ion mode with previous mass calibration with commercial standard (Sciex) for bis(14,14-dimethyl-12-oxo-3,6,9,13-tetraoxapentadecyl) malonate **3**, (14,14-dimethyl-12-oxo-3,6,9,13-tetraoxapentadecyl) C₆₀-malonate **4**, 15-C₆₀-14,16-dioxo-4,7,10,13,17,20,23,26-octaoxanonacosane-1,29-dioic acid **5** and bis-doxorubicinyl amide of the 15-C₆₀-14,16-dioxo-4,7,10,13,17,20,23,26-octaoxanonacosane-1,29-dioic acid **7**. For bis(2-(2-(2-(3-(2,5-dioxopyrrolidin-1-yl)oxy)-3-oxopropoxy)ethoxy)ethoxy)ethyl) C₆₀-malonate **6**, the measurement was done in reflectron positive ion mode. Samples were prepared using the dried droplet preparation method by mixing 0.6 mL of an analyte solution with 0.6 mL of matrix solution (directly on a plate). After air drying, the plate was introduced directly to the instrument. MS spectra were acquired from 499 to 2509 m/z for a total of 1000 laser shots

by a 1-kHz OptiBeam laser (ND-YAG). Laser intensity remained fixed for all the analyses. Registered spectra were analyzed with Data Explorer software.

Theoretical calculations

The molecular structures of DOX, Fullerene C₆₀, and Ful-DOX conjugate **7** (see Fig. 2) were optimized at the PM6-D3 [23, 24] level of theory. Next, for geometries obtained at the PM6-D3 level, the UV-Vis spectra were calculated using the TD-DFT/B3LYP-D3 [25] method with the Def2SVP [26, 27] basis set and the PCM [28, 29] model to account for water solvation. This combination of functional and basis set was successfully applied before for the prediction of UV-Vis spectra of fullerene conjugates [30]. For fullerene and DOX, 50 states were computed, while for the larger structure of Ful-DOX, we calculated 150 states. All calculations were performed using the Gaussian09 suite [31].

Spectrophotometric measurements

Visible absorption spectra were measured on SPECORD 50 PLUS spectrophotometer (Analytik Jena AG, Jena, Germany) with stabilized temperature (25 ± 0.1 °C) in the wavelength range of 350–700 nm with 0.5 nm intervals. Spectra were measured in a quartz cuvettes (1 cm light path) containing 2 mL of 0.2 M sodium phosphate buffer, pH 6.8, and an aqueous DMSO (DMSO concentration up to 10%) solution containing 0.036 mM DOX, 0.029 mM Ful-DOX conjugate **7**, and 0.029 mM C₆₀-fullerene.

Spectrofluorimetric measurements

All fluorescence measurements were carried out on a Jasco FP-8500 Spectrofluorometer equipped with a 150 W xenon lamp with stabilized temperature (25 ± 0.1 °C), using 1 cm quartz cuvettes in the wavelength range of 500–750 nm with 0.5 nm intervals. Experiments were done in 2 mL of 0.2 M sodium phosphate buffer, pH = 6.8. The Ful-DOX conjugate **7** fluorescence spectrum (excitation wavelength = 476 nm and emission wavelength = 548–650 nm) was measured (concentration range: 0.003–0.163 mM) and maximum fluorescence peak was observed at 593 nm. The obtained data are expressed in the mean relative fluorescence units (RFU).

Dynamic light scattering (DLS) characterization

DLS analysis was performed on Zetasizer Nano ZS (Malvern, Worcestershire, UK) by measuring the intensity of the scattered light for aqueous DMSO solution of 0.015 mM Ful-DOX conjugate **7**. DLS uses a 4-mW He-Ne 633 nm laser at a 173° scattering angle in 2.0-mL 0.2 M sodium phosphate buffer, pH = 6.8.

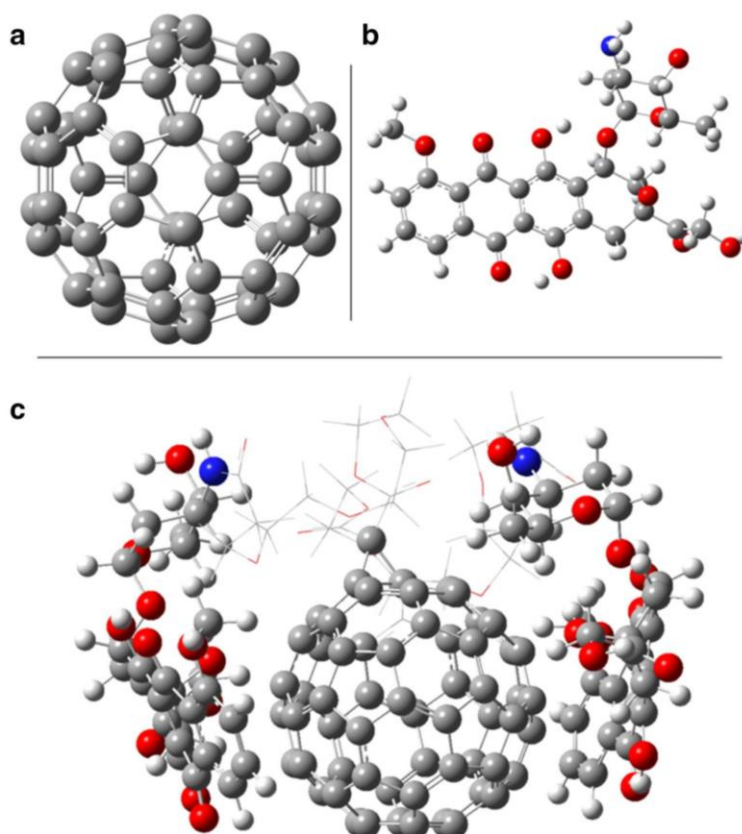
Cell culture

Monolayers of breast cancer cell lines: MDA-MB-231, T47D, and MCF-7 (purchased from CLS Cell Lines Service) were maintained in RPMI medium supplemented with 10% fetal bovine serum and 1% penicillin/streptomycin. Monolayers of the prostate cancer cell line – PC3 (purchased from American Type Culture Collection – ATCC) – were maintained in the F12K supplemented with 9% fetal bovine serum and antibiotics, as described in ref. [32]. Each cell line was maintained at 37 °C in a humidified atmosphere with 5% CO₂. Ful-DOX and DOX stock solutions in concentration of 1.3 mM and 1 mM, respectively, were prepared in DMSO (for molecular biology use). Control cells were treated with equal amount of pure vehicle (DMSO). The concentration of DMSO in each well was equal to 1%.

Confocal microscopy

MCF-7 cells were incubated with DOX (2 μM) and Ful-DOX conjugate **7** (2 μM) for 48 h at 37 °C. Nuclei were stained using Hoechst 33342 (10 μg/mL). Specimens were imaged using a confocal laser scanning microscope (LeicaSP8X equipped with an incubation chamber for the live analysis)

Fig. 2 Ball and stick representation of PM6-D3-optimized structures used for TD-DFT calculations: **a** fullerene, **b** DOX, **c** Ful-DOX conjugate **7** with the linker shown as lines for clarity



with a 63 × oil immersion lens (Leica, Germany). For DOX, the excitation wavelength was set to 476 nm and emission was detected at 548–650 nm and for Hoechst 33342–405 nm and 449–490 nm, respectively. 3D analyses were made using Leica Application Suite X.

Wst-1 (2-(4-iodophenyl)-3-(4-nitrophenyl)-5-(2,4-disulfophenyl)-2H tetrazolium monosodium salt) assay

Cells viability was determined by the WST-1 assay (in which the mitochondrial metabolic activity of cells is measured) as described previously [33]. A total of 4×10^3 cells per well were seeded at a 96-well plate and allowed to attach overnight. Cells were maintained at 37 °C in a humidified atmosphere with 5% CO₂. Next day, the medium was replaced with fresh one supplemented with the tested compounds (in concentration equal to 0.3, 0.5, 1, 2, 3, or 4 μM) or with the pure vehicle (DMSO). Then, the cells were incubated for 48 h. After this time, the WST-1 solution was added and cells were incubated for 3 h. The absorbance values in wells were measured at 440 nm (with the reference wavelength 660 nm) in an EnSpire (PerkinElmer) microplate reader. The viability of control was taken as 100%. Data were obtained from at least

two independent experiments, each treatment condition assayed in triplicate.

SRB (sulforhodamine B) assay

SRB assay was performed as described in [34]. Briefly, 4×10^3 cells/well were seeded at 96-well plate. Next day, cells were exposed to indicated concentrations of DOX, Ful-DOX, or pure vehicle (DMSO, control) for 48 h. After this time, medium was removed, and 100 μL /well of 10% trichloroacetic acid was added for 1 h in 4 °C. Afterwards, wells were washed with water, stained with 0.4% sulforhodamine B solution in 1% acetic acid for 15 min, and extensively washed with 1% acetic acid. After addition of 150 μL /well of 10 mM Tris base (pH 10.5), the absorbance was measured at 570 nm with a reference filter of 660 nm in a Victor microplate reader (PerkinElmer). The absorbance of control was taken as 100%. Data were obtained from two independent experiments, each treatment condition assayed in triplicate.

Statistical analysis of Wst-1 and SRB results

The results were analyzed with the use of GraphPad Prism software. The statistical evaluation of treated samples and untreated control was calculated using one-way analysis of variance (ANOVA) followed by Dunnett's multiple comparison test. The data were obtained from at least two independent experiments, and each treatment condition was assayed in triplicate. The differences were considered significant at $\alpha = 0.05$.

Results and discussion

Forming a covalent bond between DOX and fullerene should lead to the lowered cytotoxicity of the drug and its improved pharmacokinetics. Indeed, polymer-drug conjugates may increase tumor-specific download through their enhanced permeability and retention [35]. Moreover, a drug coupled to a polymer may possess increased solubility and resistance to proteolysis, which leads to a better control of pharmacokinetics, including the rate of drug release [36]. Hence, the main idea behind binding of an anticancer drug, which is usually extremely toxic toward healthy cells, to a biocompatible polymer is a safe transportation of the cytostatic to the tumor cells and releasing it only at the target site. However, despite the mentioned above, intuitively understandable idea, there are literature reports, which demonstrate that a doxorubicin conjugate with fullerene is equally toxic as the free DOX. Indeed, in ref. [20], it was demonstrated that the cytotoxicity, measured with the MTT assay using MCF-7 breast cancer cell line, of a fullerene conjugate and DOX was very similar. In order to verify this surprising finding and to reassess the suitability of

Ful-DOX conjugates in a possible anticancer therapy, we synthesized a very similar system and studied its physicochemical properties as well as cytotoxicity. Additionally, in order to determine cellular distribution of the studied conjugate, we carried out confocal microscopy analysis of the cells exposed to the conjugate or to the free drug. The results obtained using all methods employed in our study demonstrate that the properties of the conjugate and DOX itself are completely different. Moreover, our findings suggest that binding of DOX to C₆₀-fullerene dramatically lowers its antiproliferative activity. The reason which might explain all discrepancies between our and ref. [20] findings seems to be a considerable contamination of conjugate III [20] with the free DOX and its toxic derivatives.

Conjugate synthesis

There are many synthetic methods for the preparation of fullerene-containing compounds. Fullerene residue exhibits a negative induction effect, which is connected with their electrophilic propensities and possibility to react with different nucleophiles giving fullerene anion intermediates. These include a reaction with C-nucleophiles: (a) Bingel–Hirsch reaction [36] (a formed fullerene anion intermediate is stabilized by an internal addition reaction) and (b) with lithium- [37] or magnesium-organic compounds [38] (a formed fullerene anion intermediate is stabilized by the reaction with various electrophiles). The other example of the nucleophilic reaction with fullerenes is the addition of cyanides followed by the reaction with various nucleophiles [39]. Moreover, fullerenes act as dienophiles, which implicates their ability to undergo cycloaddition. Two types of the aforementioned process are distinguished in the chemical literature: cycloaddition [4+2], i.e., with cyclopentadiene [40], and [3+2], i.e., with diazomethane [41]. Furthermore, fullerenes can be aminated [42], halogenated [43], or hydrogenated [44].

In this study, we obtained a Ful-DOX 7 conjugate using a modified synthetic procedure described by Lu et al. [20]. For the whole synthetic route and chemical structures of all described compounds, see Scheme 1.

In the first step, we obtained a bis(14,14-dimethyl-12-oxo-3,6,9,13-tetraoxapentadecyl) malonate **3** via the reaction of malonyl chloride **1** with *t*-butyl 12-hydroxy-4,7,10-trioxadodecanoate **2** in dry DCM. **2** differs from a corresponding chain shown in ref. [20] by a single $-\text{CH}_2-$ group. We were not able to find a commercial substrate that would enable the synthesis of exactly the same structure as described in ref. [19]. Nevertheless, due to size of the system under consideration, two methylene groups (the end-product contains two poly(ethylene glycol) chains each differing by one methylene group from the conjugate described in ref. [20] difference should not influence considerably the physicochemical and/or biological properties of the conjugate.

After 24 h, the reaction was quenched with water, evaporated, and loaded onto the silica gel column. Compound **3** was detected on a TLC plate with the help of iodine to visualize it. Next, a direct functionalization of the malonyl ester derivative **3** was conducted with use of the Bingel–Hirsch reaction. Bis(14,14-dimethyl-12-oxo-3,6,9,13-tetraoxapentadecyl) C₆₀-malonate **4** was obtained by treating the derivative **3** with 1,8-diazabicyclo[5.4.0]undec-7-ene (DBU), carbon tetrabromide (CBr₄), and fullerene-C₆₀ in dry toluene. The *t*-butyl ester functions in derivative **4** were subsequently selectively hydrolyzed in the presence of primary esters with trifluoroacetic acid (TFA) [45]. The carboxylic groups present in such obtained 15-C₆₀-14,16-dioxo-4,7,10,13,17,20,23,26-octaoxonacosane-1,29-dioic acid **5** were then activated with dicyclohexylcarbodiimide (DCC)/*N*-hydroxysuccinimide (NHS) system to give bis(2-(2-(2-(3-((2,5-dioxopyrrolidin-1-yl)oxy)-3-oxopropoxy)ethoxy)ethoxy)ethyl) C₆₀-malonate **6**. At this point, 1,3-dicyclohexylurea (DCU) was obtained as a byproduct and it was impossible to separate it from the compound **6** due to the similarity in their chemical polarity. In the

next step, the contaminated active ester **6** was coupled with doxorubicin, freshly obtained via the reaction of doxorubicin hydrochloride with triethylamine in DMF, to give the final Ful-DOX conjugate **7**. At this stage, it was possible to remove DCU from the mixture, because compound **7** is more polar than DCU. The crude product was purified by column chromatography using as an eluent, at first DCM/MeOH 30/1 (to remove DCU from the activation procedure) and then DCM/MeOH 20/1. Initially, we tried to use the eluent suggested by Lu et al. [20] (CHCl₃/MeOH 19/1), but it resulted in getting the product **7** contaminated by DCU and other reddish byproducts, presumably derivatives of doxorubicin (for TLC from the last reaction step, see Fig. S7). The structures of compounds **3–7** were determined and confirmed by the MALDI-TOF analysis and, in case of compound **3** additionally by the ¹H NMR spectrum (see Figs. S1, S2, S3, S4, S5, and S6 in Supplementary Information). In the course of synthesis, it turned out that an electrospray ionization technique is unsuitable to study the structure of the conjugate **7** due to its very weak solubility in polar solvents. The usage of ionization mode employed by the MALDI method resolved the solubility problem. The chemical literature suggests that fullerene-containing compounds tend to fragment, while being irradiated by the laser beam during MALDI analysis [46]. Moreover, in the MALDI ionization source, the doxorubicin moiety can lose the daunosamine and the 1-oxo-2-hydroxyethyl fragment [47]. In consequence, beside a molecular ion peak, fragmentation signals are present on all MALDI spectra included in the supplementary information. The identities of fragments, formed along with their molecular masses, are depicted below particular spectra (see Electronic supplementary material).

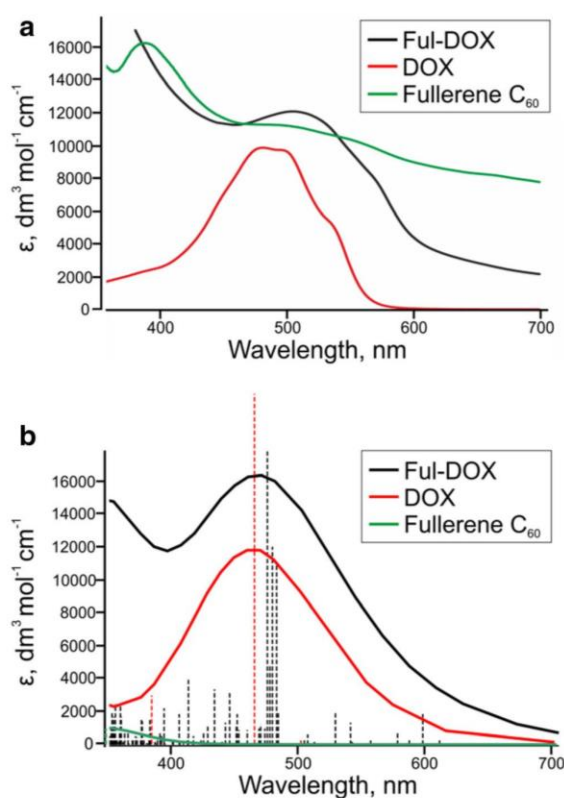


Fig. 3 UV–Vis spectra of DOX, fullerene C₆₀, and Ful-DOX: **a** measured in aqueous DMSO solution; **b** based on the TD-DFT calculations; the oscillator strengths indicated by dotted vertical lines. The scales of oscillator strengths differ for different compounds (cf. the height of vertical lines with the respective oscillator strengths in Table S1)

Physicochemical characteristics

In order to determine the structural features of the new material, aqueous solutions of conjugate **7** were studied by UV–Vis spectrophotometry, spectrofluorimetry, and dynamic light scattering (DLS). All these measurements were carried out using concentrations similar or somewhat larger than those used in biological assays which were primarily a consequence of sensitivity of specific technique. Thus, the UV–Vis spectra were recorded in a 30 μM buffered solution (Fig. 3), fluorescence was measured for Ful-DOX concentrations between 3 and 160 μM and DLS spectrum was obtained for a 15 μM solution of Ful-DOX. Here, it is also worth emphasizing that all the spectra were recorded for Ful-DOX solutions containing, besides buffer, certain amount of DMSO (up to 10%). In all biological tests, Ful-DOX was obtained from a DMSO stock solution and the cells were treated with media containing ca 1% (*v/v*) of DMSO.

The absorption spectra of Ful-DOX (29 μM) along with the spectrum of free DOX and C₆₀-fullerene are depicted in Fig. 3a. The experimental absorption maximum for DOX

occurs at 481 nm, while for the fullerene, two characteristic peaks at 387 nm and 493 nm are observed. Furthermore, the Ful-DOX spectrum seems to be a superposition of DOX and fullerene features (see Fig. 3a). The simulations of experimental spectra based on the TD-DFT calculations are shown in Fig. 3b and the most important electronic transitions along with their molecular orbitals are demonstrated in Electronic supplementary material (see Table S1 and Fig. S8).

In water, the fullerene forms aggregates and, due to interactions in the solid phase and light scattering, its UV–Vis spectrum is stronger, red-shifted, and broader than the spectra recorded in solvents in which C_{60} forms true solution [48]. The shape of the main long-wavelength absorption peak for Ful-DOX, red-shifted (with regard to DOX) to 506 nm, seems to be a superposition of doxorubicin and fullerene features. However, the maximum extinction coefficient of the conjugate is much smaller than the sum of C_{60} and DOX epsilons (see Fig. 3a). Interestingly, the noted above non-additive effect concerning the intensity of electronic transitions was not observed for the UV–Vis spectra published in ref. [20]. Actually, the maximum extinction coefficient of the conjugate (containing two DOX molecules) was ca. 2-fold bigger than that observed for DOX (an additive effect), which suggests lack of interactions between doxorubicin and the fullerene cage for the system studied by Lu et al. [20]. Contrary to their findings, our results indicate strong interactions between doxorubicin and the fullerene cage. Indeed, our quantum chemical calculations suggest that even in water, the conjugate possesses strong tendency to adopt a closed conformation, shown in Fig. 2, in which both DOX molecules interact via stacking with the delocalized π -electrons of the fullerene cage. The geometry optimization that started from the open conformation (both poly(ethylene glycol) chains extended) spontaneously

converged to the close one depicted in Fig. 2. Here, it is worth of emphasizing a very good correspondence between the measured and calculated spectra of DOX and Ful-DOX (although the shapes of measured and theoretical spectrum of C_{60} are similar (see Fig. 3), the latter is much weaker). This is a consequence of fullerene aggregation in water which results in strong scattering of incident light [49]). The main wavelength feature of DOX stems from the HOMO \rightarrow LUMO transition ($\pi\pi^*$ transition; see Table S1). Inspection of molecular orbitals involved in the electronic transitions shows that the HOMO \rightarrow LUMO transition in DOX corresponds to the one calculated at 480 nm in Ful-DOX (HOMO \rightarrow LUMO+4; see Table S1). Note, a large difference between the oscillator strengths calculated for DOX (0.29; Table S1) and for the transition involving the same orbitals in Ful-DOX (0.07; Table S1). The visible lowering of oscillator strength is a result of fullerene-DOX interaction. In the remaining transitions (476 and 484 nm) giving rise to the long wavelength feature of Ful-DOX (see Fig. 3b), the occupied orbitals with a considerable contribution from the fullerene are involved. All the above demonstrate strong fullerene-DOX interactions in the conjugate that justifies the non-additive effects observed in the measured absorption spectra.

For the Ful-DOX concentration of up to ca 30 μ M, fluorescence intensity increases almost linearly with the amount of conjugate (see the inset to Fig. 4). This suggests that also the number of fluorescing sites increases linearly, which implies, in turn, that the size of aggregates does not change substantially within the discussed concentration range. The presence of Ful-DOX aggregates in the studied aqueous DMSO solution was confirmed by DLS measurements (see Fig. 5). The spectrum presented in Fig. 5 shows that the average hydrodynamic radius for those clusters amount to as much as 838 nm. The maximum intensity of the fluorescence is observed for ca 60 μ M and then the fluorescence decreases with concentration. Change in the

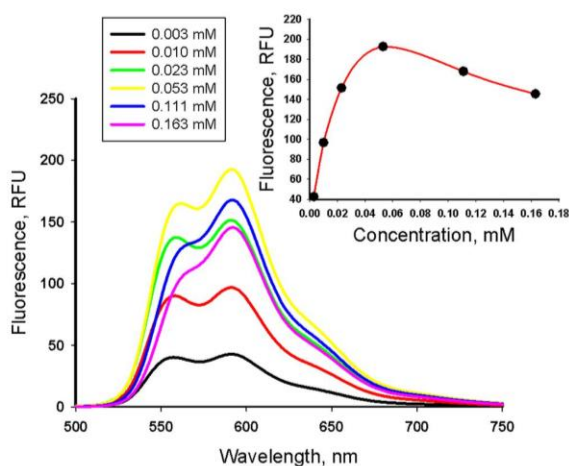


Fig. 4 Concentration effect on the fluorescence spectrum of Ful-DOX conjugate

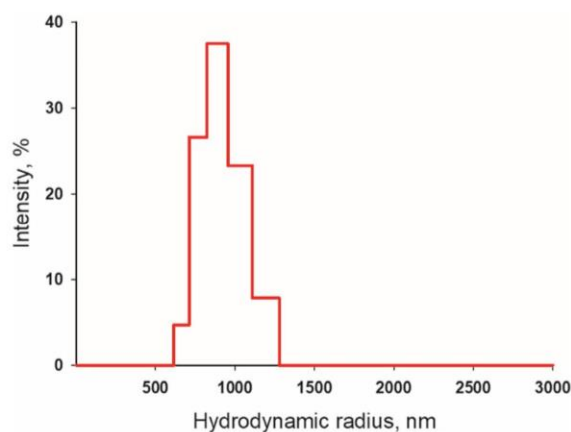


Fig. 5 Dynamic light scattering for an aqueous DMSO solution of Ful-DOX conjugate 7 ($c = 0.015$ mM); average hydrodynamic radius, $Z_{avg} = 838$ nm

shape of spectrum with increasing amount of Ful-DOX (see Fig. 4) suggests a trivial mechanism of quenching (reabsorption) [49]. Actually, the short-wavelength band of fluorescence gradually disappears for more concentrated solutions, which suggests reabsorption. Indeed, there is a strong overlap between the absorption and emission spectra of Ful-DOX in the range of 550–600 nm (cf. Figs. 3 and 4).

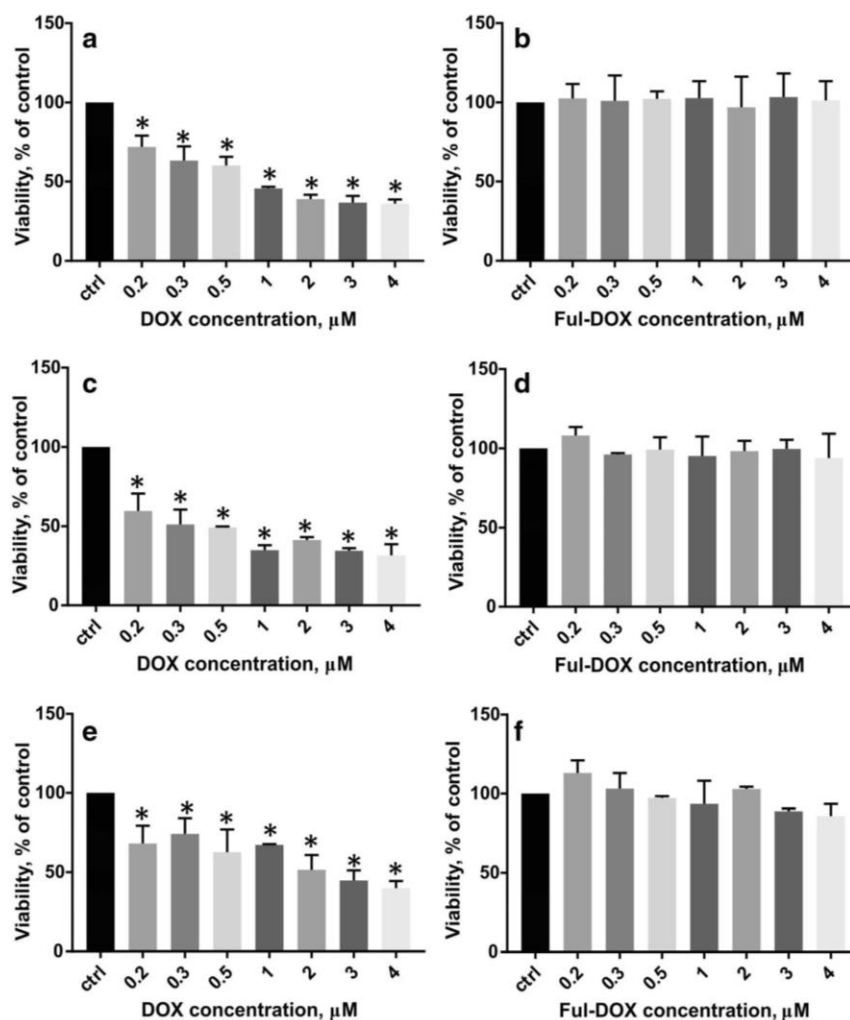
Impact of Ful-DOX on the viability of cancer cells

The main purpose of our study was to elucidate whether the binding of DOX to a non- or low-toxic carrier should alleviate the toxicity of doxorubicin. Actually, only then such construct might be used as a safe platform that enables toxic chemotherapeutics to be transported and released in the target cell. We compared viability of cells treated for 48 h with doxorubicin or Ful-DOX conjugate. To exclude that results might be cell

line specific, we used cancer cells derived from different organs, namely breast (MCF-7, T47D, and MDA MB 231 cell lines) and prostate (PC3 cell line). Breast cancer cells represent different molecular subtypes of this malignancy: MCF-7 and T47D cells are of luminal type characterized by the presence of estrogen receptor (ER) and progesterone receptor (PR) while MDA MB 231 cells are so called triple negative as they are negative for ER, PR, and human epithelial receptor 2 (HER2) and represent the most aggressive and one of the worst prognosis breast cancer subtype. Moreover, two types of viability assays have been used: SRB measuring total proteins in the cells and WST-1 which, similarly as MTT, indicates metabolically active cells.

As shown in Figs. 6 and 7, Ful-DOX in the studied range of concentrations demonstrates no or very low effect on viability of all tested cell lines, whereas free DOX reduces viability in a dose-dependent manner with IC₅₀ ca 1 (MDA MB 231 and

Fig. 6 The viability of MDA-MB-231 (a, b), MCF-7 (c, d), and T47D (e, f) cells after 48-h treatment with doxorubicin and Ful-DOX conjugate 7 in a range of concentrations from 0 (control; ctrl) to 4 μ M assessed by the SRB assay. Results are shown as mean \pm SD of two independent experiments performed in triplicate. *Statistically significant difference between the treated and control (untreated sample) at $\alpha = 0.05$



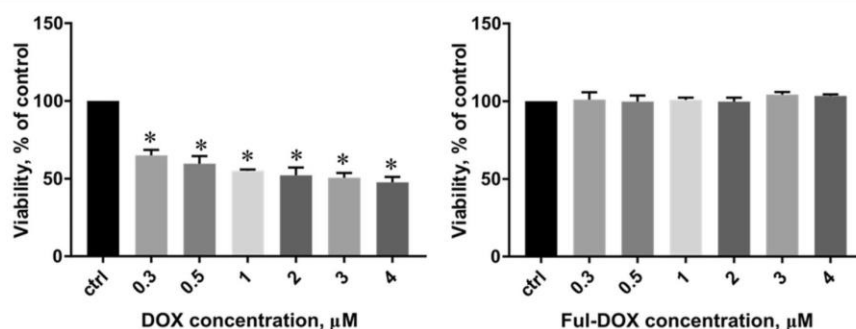


Fig. 7 The viability of PC3 cells after 48 h of treatment with doxorubicin and Ful-DOX conjugate 7 in a range of concentrations from 0 (control; ctrl) to 4 μ M determined by the WST-1 assay. Results are shown as mean \pm SD

of two independent experiments performed in triplicate. *Statistically significant difference is present between treated samples compared with control (untreated sample) at $\alpha = 0.05$

MCF-7 cells) or 2 μ M (T47D and PC-3 cells). It is worth noting that results of the WST-1 assay, which is much simpler than the SRB one (see the Methods section), show marginal standard deviations (see Fig. 7). Presented results remain in apparent discrepancy with those reported by Lu et al. [20]. They observed no difference between Dox and Ful-DOX activity towards MCF-7 cells as

assessed by MTT assay. Moreover, Ful-DOX at the concentration of 10 μ g/mL, which roughly corresponds to our 4 μ M, reduced viability of cells by about 40% compared with untreated controls after 24-h exposition. It contrasts with our results which indicate lack of toxicity of the conjugate, despite the fact that in our experiments, the cells were treated for longer time (48 h).

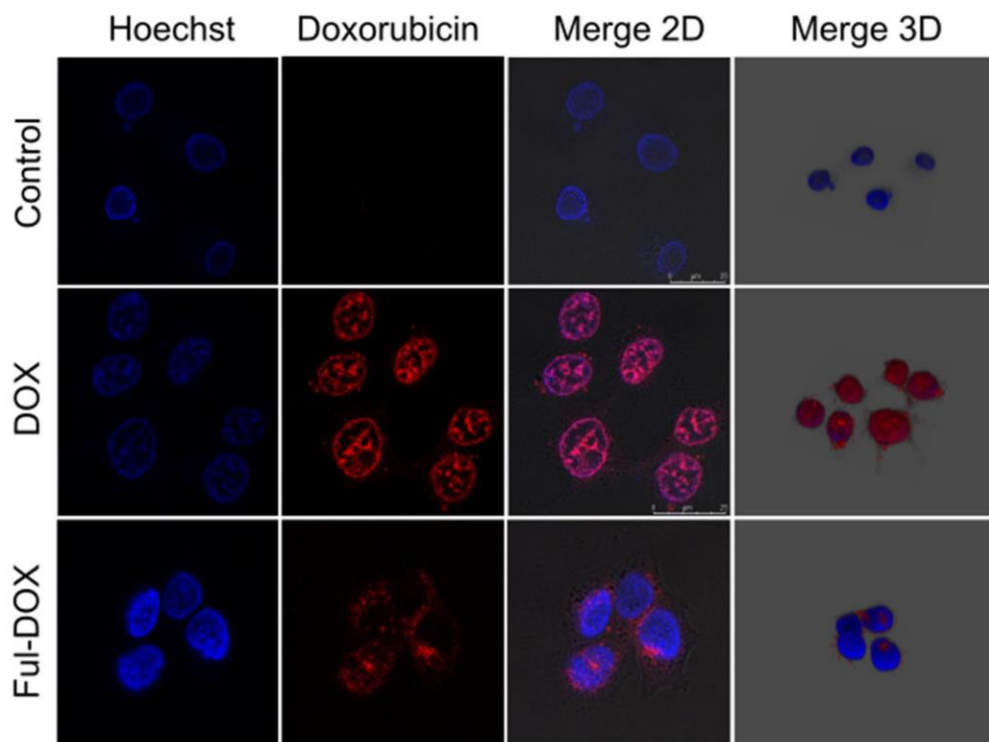


Fig. 8 Images from confocal microscope of MCF-7 cells treated with 2 μ M DOX and 2 μ M Ful-DOX conjugate 7. Nuclei are stained blue using Hoechst 33342, red color emitted by doxorubicin moieties, 2D and

3D merged images including the Hoechst dye and DOX or Ful-DOX 7 emission show cellular localization. The MCF-7 cells were incubated at with tested agents for 48 h. Scale bars are 25 μ m

Confocal microscopy

In order to verify our conclusions, we also carried out measurements concerning the distribution of free DOX and the conjugate in cells. Since DOX is a good fluorophore, we decided to employ confocal microscopy. Figure 8 gathers several confocal 2D and 3D images showing cellular distribution of DOX or full-DOX.

Cell nuclei are depicted by blue spots as they were stained with Hoechst 33342. On the other hand, DOX emits a red fluorescence. As indicated by the middle panel of Fig. 8, free DOX penetrates into the nuclei (DOX/Merge 2D, Fig. 8) as well as adsorbs on nuclear membrane (DOX/Merge 3D, Fig. 8). The behavior of Ful-DOX is quite different. It does not penetrate into the nuclei but accumulates on their membranes (Ful-DOX/Merge 2D and Ful-DOX/Merge 3D, Fig. 8). Taking into account the physicochemical properties of Ful-DOX, i.e., strong interactions between DOX and fullerene cage, chemically stable linker, as well as the size of hydrodynamic radius of nanoparticles which Ful-DOX forms in the buffered aqueous solution, one can expect that an efficient nucleus penetration, which seems to be indispensable for the DOX cytotoxic action, is reduced or abolished in case of the conjugate.

Conclusions

In this study, we synthesized a fullerene-DOX conjugate, measured its physicochemical characteristics, and determined its toxicity and the cellular distribution with the viability assays and confocal microscopy, respectively. The physicochemical characteristics indicate strong interactions between the fullerene cage and doxorubicin in the Ful-DOX as well as the formation of voluminous clusters of the conjugate under the conditions employed in the cellular studies. These explain the observed lack of cytotoxicity. Indeed, to be toxic, doxorubicin has to penetrate into the nucleus in order to directly interact with DNA or protein machinery dedicated to DNA processing. Being covalently bound to the fullerene-poly(ethylene glycol) moiety and additionally forming sizable clusters, DOX possibilities to interact with DNA are very limited. Moreover, a nuclear membrane does not support endocytosis and its pores are able to accommodate particles up to only about 25 nm diameter [50], while the synthesized Ful-DOX conjugate forms clusters with an average hydrodynamic radius of ca. 800 nm.

In summary, our study demonstrates that the studied conjugate has a potential to become a universal platform for safe transportation of toxic drugs into tumor cells. A quest for molecular modifications and implementation of DOX conjugates specifically releasing the drug is currently under way in our laboratories.

Funding information This work was supported by the Polish Ministry of Science and Higher Education under Grants Nos. DS 530-8227-D494-18 (J. R.) and DS 530-M045-D674-18 (J. P.). The calculations were performed in the Wrocław Center for Networking and Supercomputing, grant No. 209.

Compliance with ethical standards

Conflict of interest The authors declare that they have no conflicts of interest.

Open Access This article is distributed under the terms of the Creative Commons Attribution 4.0 International License (<http://creativecommons.org/licenses/by/4.0/>), which permits unrestricted use, distribution, and reproduction in any medium, provided you give appropriate credit to the original author(s) and the source, provide a link to the Creative Commons license, and indicate if changes were made.

References

1. Abushouk AI, Ismail A, Salem AMA, Afifi AM, Abdel-Daim MM (2017) Cardio protective mechanisms of phytochemicals against doxorubicin-induced cardiotoxicity. *Biomed Pharmacother* 90: 935–946
2. Mobaraki M, Faraji A, Zare M, Dolati P, Ataei M, Dehghan Manshadi HR (2017) Molecular mechanisms of cardiotoxicity: a review on the major side-effect of doxorubicin. *Indian J Pharm Sci* 79:335–344
3. Gewirtz DA (1999) A critical evaluation of the mechanisms of action proposed for the antitumor effects of the anthracycline antibiotics adriamycin and daunorubicin. *Biochem Pharmacol* 57:727–741
4. Box V (2007) The intercalation of DNA double helices with doxorubicin and nagalomycin. *J Mol Graph Mod* 26:14–19
5. Chatterjee K, Zhang J, Honbo N, Karliner JS (2010) Doxorubicin cardiomyopathy. *Cardiology* 115:155–162
6. Carvalho C, Santos RX, Cardoso S, Correia S, Oliveira PJ, Santos MS, Moreira PI (2009) Doxorubicin: The good, the bad and the ugly effect. *Curr Med Chem* 16:3267–3285
7. Takemura G, Fujiwara F (2007) Doxorubicin-induced cardiomyopathy: from the cardiotoxic mechanisms to management. *Prog Cardiovasc Dis* 49:330–352
8. Swain S, Whaley F, Ewer M (2003) Congestive heart failure in patients treated with doxorubicin. *Cancer* 97:2869–2879
9. von Hoff DD, Layard MW, Basa P, Davis HL, von Hoff AL, Rozenzweig M, Muggia FM (1979) Risk factors for doxorubicin-induced congestive heart failure. *Ann Intern Med* 91:710–717
10. Cirillo R, Sacco G, Venturella S, Brightwell J, Giachetti A, Manzini S (2000) comparison of doxorubicin – and MEN 10755 – induced long-term progressive cardiotoxicity in the rat. *J Cardiovasc Pharmacol* 35:100–108
11. Wallace KB (2007) Adriamycin-induced interference with cardiac mitochondrial calcium homeostasis. *Cardiovasc Toxicol* 7:101–107
12. Nousiainen T, Jantunen E, Vanninen E, Remes J, Vuolteenaho O, Hartikainen J (1999) Natriuretic peptides as markers of cardiotoxicity during doxorubicin treatment for non-Hodgkin's Lymphoma. *Eur J Haematol* 62:135–141
13. Chen B, Peng X, Pentassuglia L, Lim CC, Sawyer DB (2007) Molecular and cellular mechanisms of anthracycline cardiotoxicity. *Cardiovasc Toxicol* 7:114–121

14. Anilkumar P, Lu F, Cao L, Luo PG, Liu J-H, Sahu S, Tackett II KN, Wang Y, Sun Y-P (2011) Fullerenes for Applications in Biology and Medicine. *Curr Med Chem* 18:2045–2059
15. Zhang X, Cong H, Yu B, Chen Q (2019) Recent advances of water-soluble fullerene derivatives in biomedical applications. *Mini-Rev Org Chem* 16:92–99
16. Kepinska M, Kizek R, Milnerowicz H (2018) Fullerene as a doxorubicin nanotransporter for targeted breast cancer therapy: Capillary electrophoresis analysis. *Electrophoresis* 39:2370–2379
17. Chaudhuri P, Paraskar A, Soni S, Mashelkar RA, Sengupta S (2009) Fullereneol-cytotoxic conjugates for cancer chemotherapy. *ACS Nano* 3:2505–2514
18. Panchuk R, Prylutska S, Skorokhyd N, Lehka L, Skivka L, Hurmach V, Evstigneev M, Piosik J, Berger W, Prylutsky Y, Scharff P, Stoika R, Vari S. Enhancement of anticancer action of traditional (doxorubicin and cisplatin) and experimental (landomycin A) drugs by their delivery in vivo with novel C₆₀-fullerene-based nanocarrier possessing innate ROS-modulating activity. 11th Annual TechConnect World Innovation Conference and Expo, Washington, United States, 14.05–17.05.17
19. Zakharian TY, Seryshev A, Sitharaman B, Gilbert BE, Knight V, Wilson LJ (2005) A fullerene-paclitaxel chemotherapeutic: Synthesis, characterization, and study of biological activity in tissue culture. *J Am Chem Soc* 127:12508–12,509
20. Shi J, Wang B, Wang L, Lu T, Fu Y, Zhang H, Zhang Z (2016) Fullerene (C₆₀)-based tumor-targeting nanoparticles with “off-on” state for enhanced treatment of cancer. *J Contr Release* 235:245–258
21. Lu F, Haque SA, Yang S-T, Luo PG, Gu L, Kitaygorodskiy A, Li H, Lacher S, Sun Y-P (2009) Aqueous compatible fullerene-doxorubicin conjugates. *J Phys Chem C* 113:17768–17,773
22. Liu J-H, Cao L, Luo PG, Yang S-T, Lu F, Wang H, Meziani MJ, Haque AS, Liu Y, Lacher S, Sun Y-P (2010) Fullerene-conjugated doxorubicin in cells. *ACS Appl Mater Inter* 2:1384–1389
23. Stewart JJP (2007) Optimization of parameters for semiempirical methods. V. Modification of NDDO approximations and application to 70 elements. *J Mol Model* 13:1173–1213
24. Grimme S, Antony J, Ehrlich S, Krieg H (2010) A consistent and accurate ab initio parametrization of density functional dispersion correction (DFT-D) for the 94 elements H-Pu. *J Chem Phys* 132: 154104
25. Runge E, Gross EK (1984) Density-functional theory for time-dependent systems. *Phys Rev. Lett* 52:997–1000
26. Weigend F, Ahlrichs R (2005) Balanced basis sets of split valence, triple zeta valence and quadruple zeta valence quality for H to Rn: Design and assessment of accuracy. *Phys Chem Chem Phys* 7: 3297–3305
27. Weigend F (2006) Accurate coulomb-fitting basis sets for H to Rn. *Phys Chem Chem Phys* 8:1057–1065
28. Cossi M, Barone V, Cammi R, Tomasi J (1996) Ab initio study of solvated molecules: a new implementation of the polarizable continuum model. *Chem Phys Lett* 255:327–335
29. Miertuš S, Scrocco E, Tomasi J (1981) Electrostatic interaction of a solute with a continuum. A direct utilization of ab initio molecular potentials for the prevision of solvent effects. *J Chem Phys* 55:117–129
30. Kariminasab M, Tajbakhsh M, Ganji MD, Alinezhad H (2017) A theoretical investigation of the structural, electronic and UV-vis absorption spectra of fullerene derivatives based on PC61B-NHCS compound. *Mater Chem Phys* 199:597–608
31. Frisch MJ, Trucks GW, Schlegel HB, Scuseria GE, Robb MA, Cheeseman JR, Scalmani G, Barone V, Mennucci B, Petersson GA, et al. (2009) Gaussian 09 (Rev. D.01), Gaussian, Inc., Wallingford, CT
32. Hać A, Domachowska A, Narajczyk M, Cyske K, Pawlik A, Herman-Antosiewicz A (2015) S6K1 controls autophagosome maturation in autophagy induced by sulforaphane or serum deprivation. *Eur J Cell Biol* 94:470–481
33. Tominaga H, Ishiyama M, Ohseto F, Sasamoto K, Hamamoto T, Suzuki K, Watanabe M (1999) A water-soluble tetrazolium salt useful for colorimetric cell viability assay. *Anal Comm* 36:47–50
34. Pawlik A, Wała M, Hać A, Felczykowska A, Herman-Antosiewicz A (2017) Sulforaphane, an isothiocyanate present in radish plants, inhibits proliferation of human breast cancer cells. *Phytomedicine* 29:1–10
35. Veronese FM, Schiavon O, Pasut G, Mendichi R, Andersson L, Tsirk A, Ford J, Wu G, Kneller S, Davies J, Duncan R (2005) PEG-doxorubicin conjugates: influence of polymer structure on drug release, in vitro cytotoxicity, biodistribution, and antitumor activity. *Bioconjugate Chem* 16:775–784
36. Nakamura Y, Suzuki M, Imai Y, Nishimura J (2004) Synthesis of [60] fullerene adducts bearing carbazole moieties by Bingel reaction and their properties. *Org Lett* 6:2797–2799
37. Hirsch A, Brettreich M (2005) Fullerenes: chemistry and reactions, pp. 73–99, Wiley-VCH Verlag GmbH & Co. KGaA
38. Yan W, Seifermann SM, Pierrat P, Bräse S (2015) Synthesis of highly functionalized C₆₀ fullerene derivatives and their applications in material and life sciences. *Org Biomol Chem* 13:25–54
39. Komatsu K, Wang G-W, Murata Y, Tanaka T, Fujiwara K (1998) Mechanochemical synthesis and characterization of the fullerene dimer C₁₂₀. *J Org Chem* 63:9358–9366
40. Schlueter JA, Seaman JM, Taha S, Cohen H, Lykke KR, Wang HH, Williams JM (1993) Synthesis, purification, and characterization of the 1: 1 addition product of C₆₀ and anthracene. *J Chem Soc Chem Commun* 11:972–974
41. Prato M, Li QC, Wudl F, Lucchini V (1993) Addition of azides to fullerene C₆₀: synthesis of azafulleroids. *J Am Chem Soc* 115: 1148–1150
42. Hu X, Jiang Z, Jia Z, Huang S, Yang X, Li Y, Gan L, Zhang S, Zhu D (2007) Amination of [60]fullerene by ammonia and by primary and secondary aliphatic amines – preparation of amino[60]fullerene peroxides. *Chem Eur J* 13:1129–1141
43. Olah GA, Bucsi I, Lambert C, Aniszfeld R, Trivedi NJ, Sensharma DK, Prakash GKS (1991) Chlorination and bromination of fullerenes. Nucleophilic methoxylation of polychlorofullerenes and their aluminum trichloride catalyzed friedel-crafts reaction with aromatics to polyarylfullerenes. *J Am Chem Soc* 113:9385–9387
44. Monakov YB, Zaikov GE (2006) Molecular and high molecular chemistry: theory and practice. Science publishers, Nova, pp 1–47
45. Greene TW, Wuts PGM (1999) Protective groups in organic synthesis, vol 65–67. Wiley, New York, pp 404–408
46. Trimpin S, Keune S, Räder HJ, Müllen K (2006) Solvent-free Maldi-MS: developmental improvements in the reliability and the potential of maldi in the analysis of synthetic polymers and giant organic molecules. *J Am Soc Mass Spectrom* 17:667–671
47. Di Francesco R, Griggs JJ, Donnelly J, Di Cenzo R (2007) Simultaneous analysis of cyclophosphamide, doxorubicin and doxorubicinol by liquid chromatography coupled to tandem mass spectrometry. *J Chromatogr B* 852:545–553
48. Chang X, Vikesland PJ (2011) UV-vis Spectroscopic properties of nC₆₀ produced via extended mixing. *Environ Sci Technol* 45:9967–9974
49. Bowen EJ (1968) Luminescence in chemistry. D. Van Nostrand Reinhold Ltd., Princeton, p 154
50. Stewart M (1992) Nuclear pore structure and function. *Semin Cell Biol* 3:267–277

Publisher's note Springer Nature remains neutral with regard to jurisdictional claims in published maps and institutional affiliations.

Electronic supplementary material

Cytotoxicity of doxorubicin conjugated with C₆₀ fullerene. Structural and *in vitro* studies

Kamila Butowska^{1,2} Witold Kozak² Magdalena Zdrowowicz² Samanta Makurat² Michał Rychłowski⁴ Aleksandra Hać³ Anna Herman-Antosiewicz³ Jacek Piosik¹ Janusz Rak²

¹Laboratory of Biophysics, Intercollegiate Faculty of Biotechnology of the University of Gdańsk and Medical University of Gdańsk, Abrahama 58, 80-307 Gdańsk, Poland

²Laboratory of Biological Sensitizers, Faculty of Chemistry, University of Gdańsk, Wita Stwosza 63, 80-308 Gdańsk, Poland

³Department of Medical Biology and Genetics, Faculty of Biology, University of Gdańsk, Wita Stwosza 59, 80-308 Gdańsk

⁴Department of Virus Molecular Biology, Intercollegiate Faculty of Biotechnology of the University of Gdańsk and Medical University of Gdańsk, Abrahama 58, 80-307 Gdańsk, Poland

Corresponding Authors: Janusz Rak, e-mail: janusz.rak@ug.edu.pl; Jacek Piosik, e-mail: jacek.piosik@biotech.ug.edu.pl

1. ^1H NMR and MS analysis.....2-11

2. TLC analysis 12

3. TD-DFT calculations 13

1. ^1H NMR and MS analysis

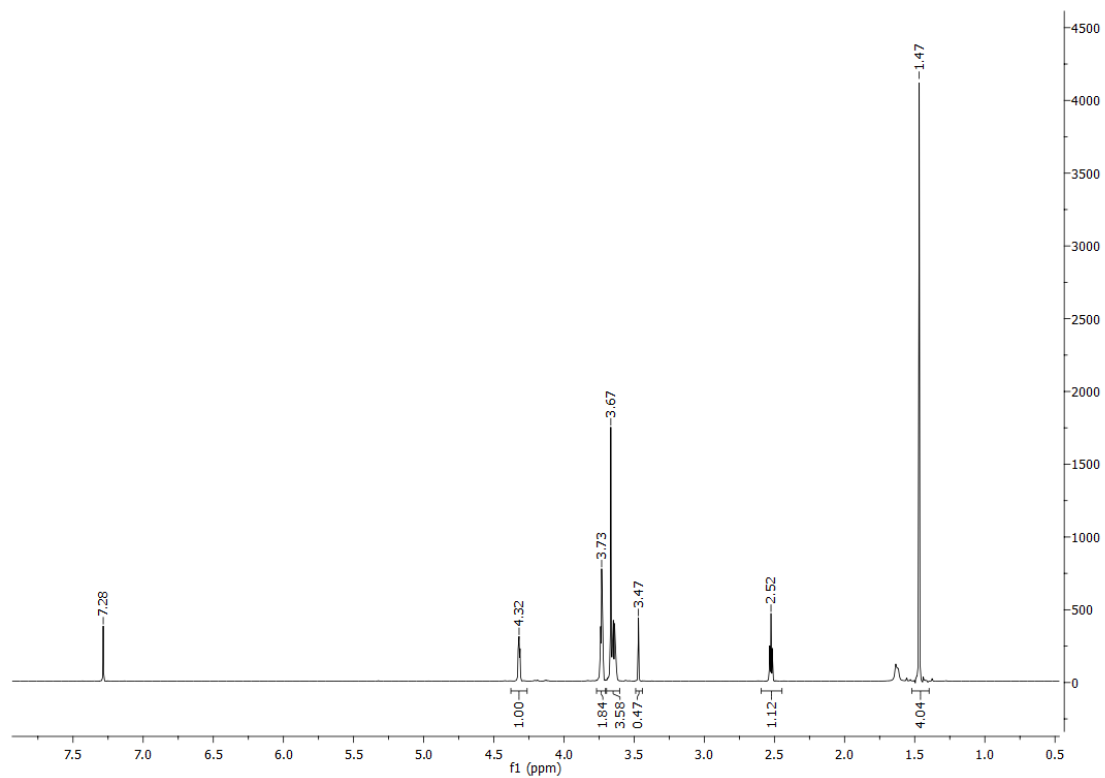


Fig. S1 ^1H NMR spectrum of compound 3

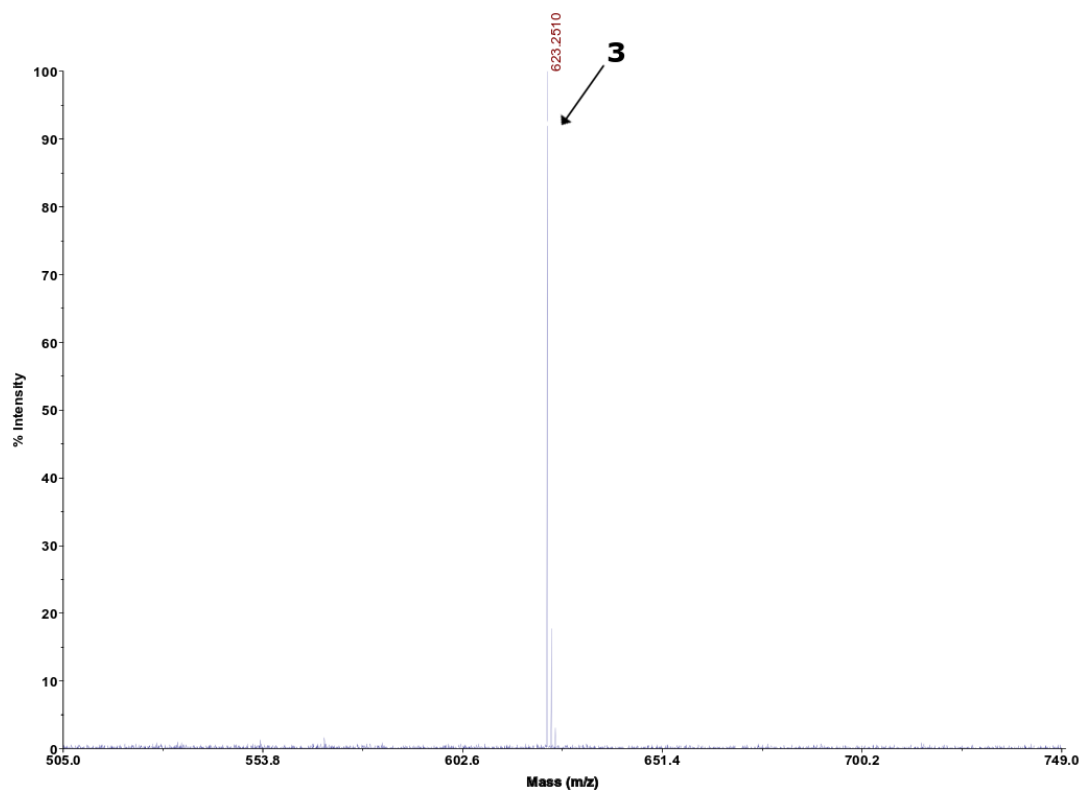


Fig. S2 MALDI-TOF mass spectrum of compound **3** in negative ionization mode; for ion identities see the table below

Compound	Chemical structure
3	<p data-bbox="842 1451 1066 1491">[M-H⁻] = 623.2510</p>

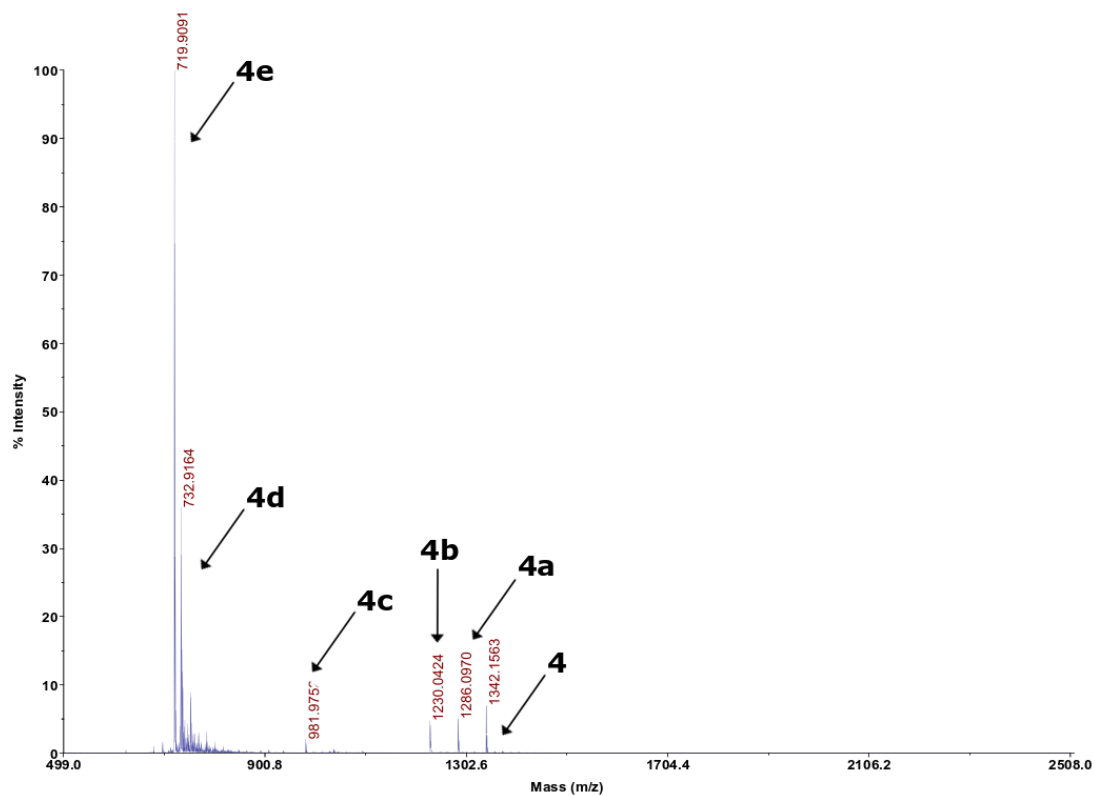
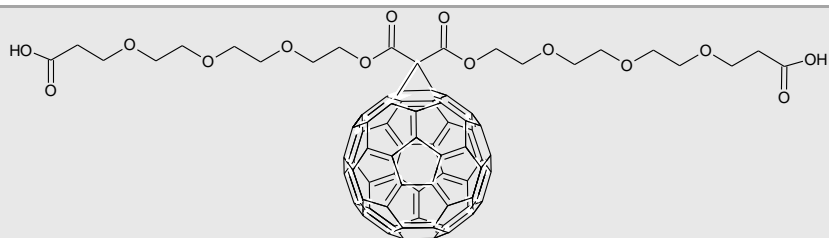


Fig. S3 MALDI-TOF mass spectrum of compound **4** in negative ionization mode; for ion identities see the table below

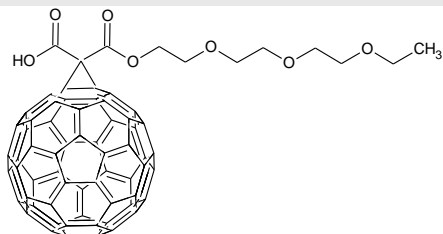
Compound	Chemical structure
4	<p>$[M-H^-] = 1342.1563$</p>
4a	<p>$[M-H^-] = 1286.0970$</p>

4b



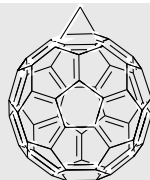
$[M-H^-] = 1230.0424$

4c



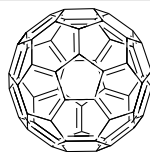
$[M-H^-] = 981.9752$

4d



$[M-H^-] = 732.9164$

4e



$[M-H^-] = 720.9091$

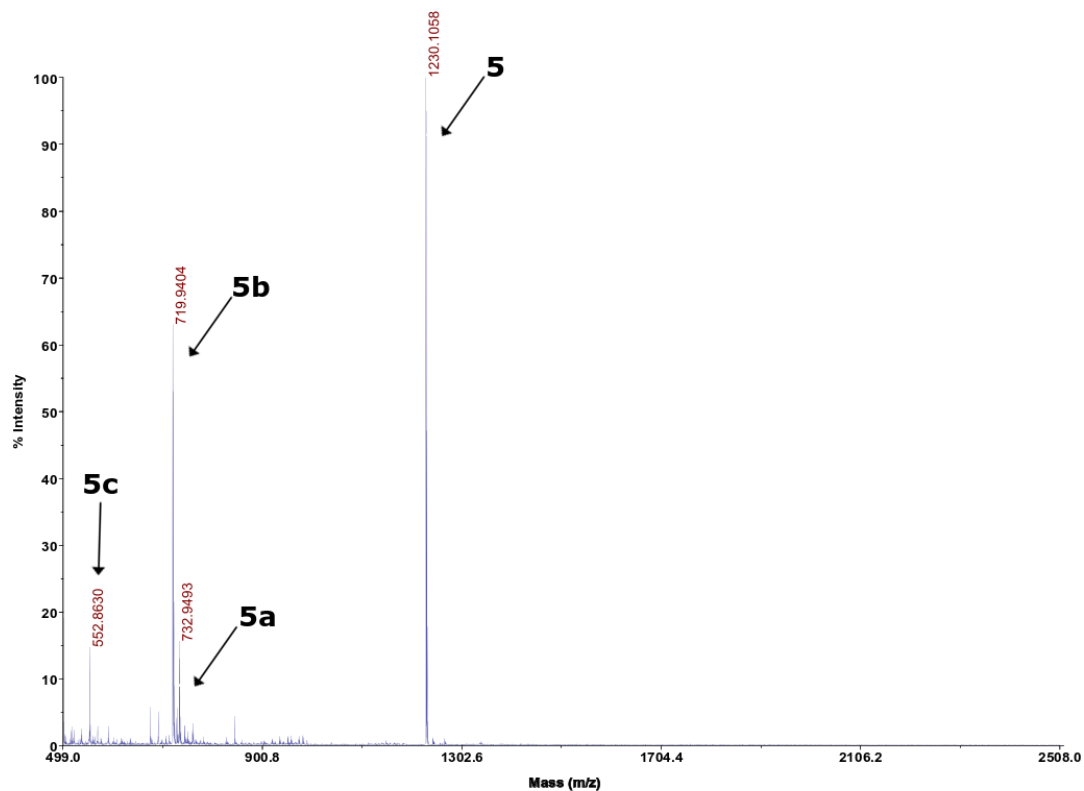


Fig. S4 MALDI-TOF mass spectrum of compound **5** in negative ionization mode; for ion identities see the table below

Compound	Chemical structure
5	<p>$[M-H^-] = 1230.1058$</p>
5a	<p>$[M-H^-] = 732.9493$</p>
5b	<p>$[M-H^-] = 719.9404$</p>

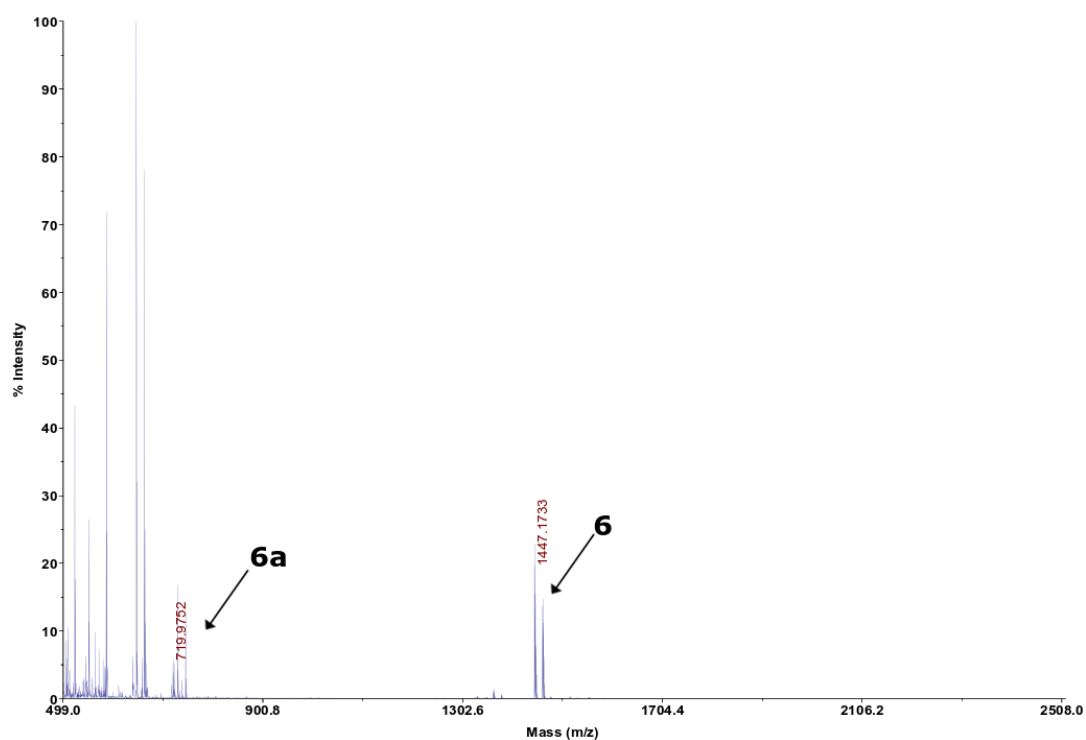
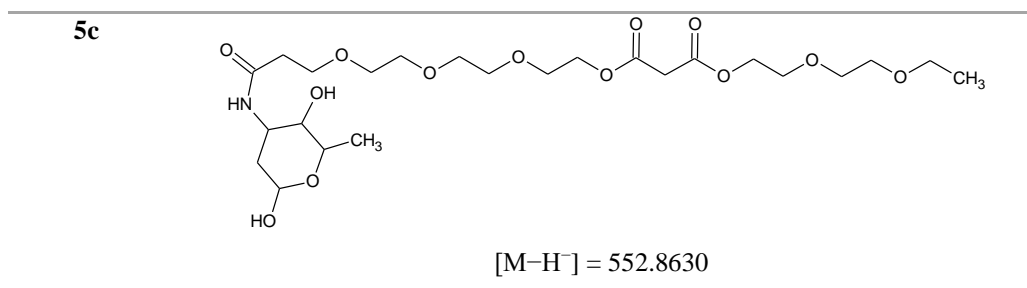
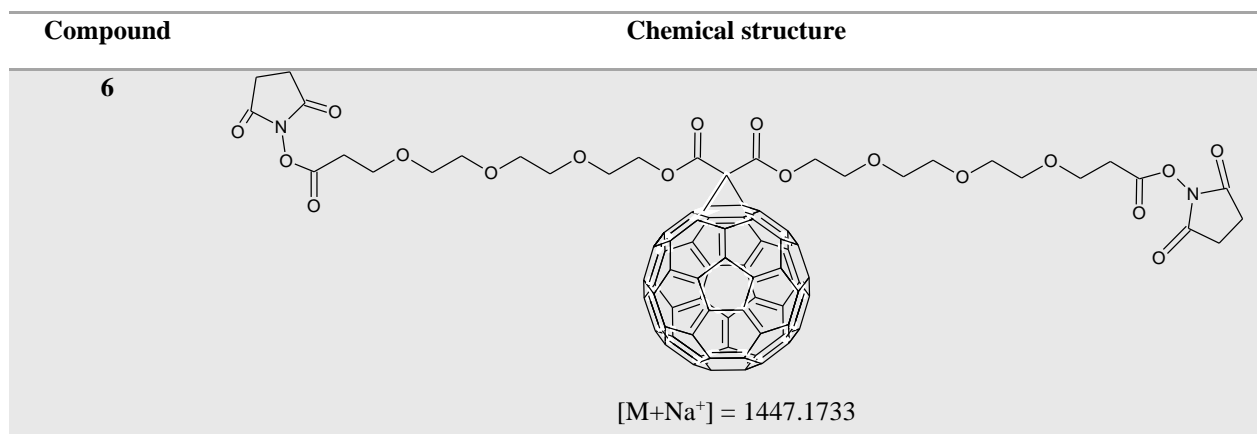
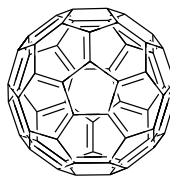


Fig. S5 MALDI-TOF mass spectrum of compound **6** in positive ionization mode; for ion identities see the table below



6a



M = 719.9752

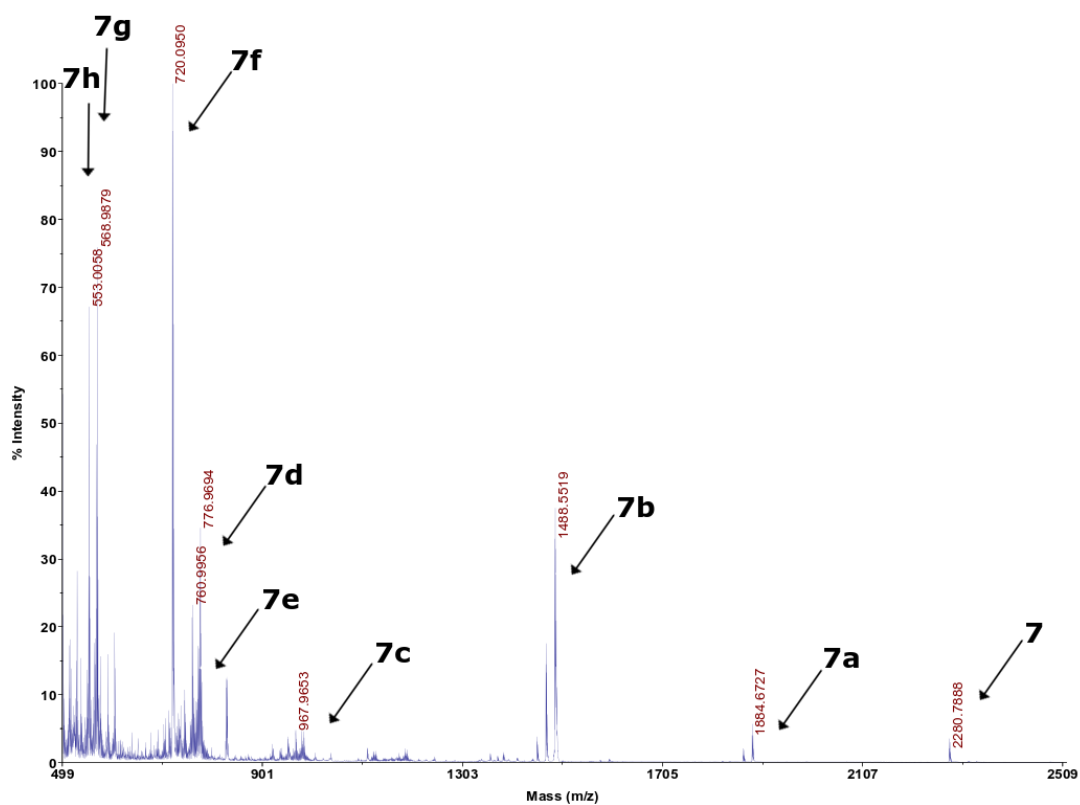
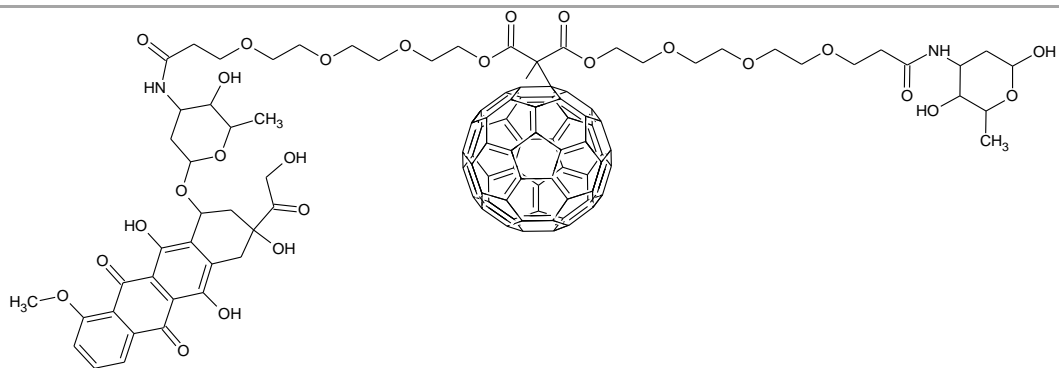


Fig. S6 MALDI-TOF mass spectrum of compound 7 in negative ionization mode; for ion identities see the table below

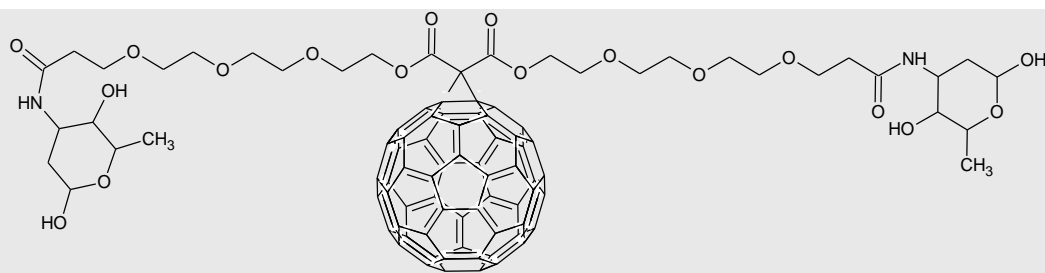
Compound	Chemical structure
7	<p>[M-H]⁻ = 2280.7888</p>

7a



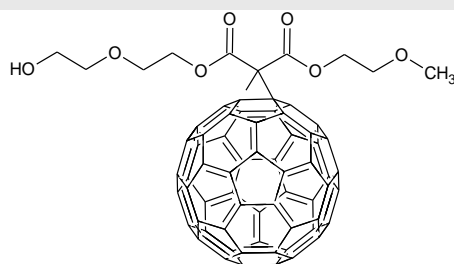
$[M-H^-] = 1884.6727$

7b



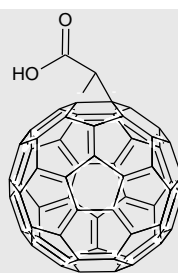
$[M-H^-] = 1488.5519$

7c



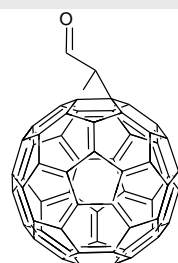
$[M-H^-] = 967.9653$

7d

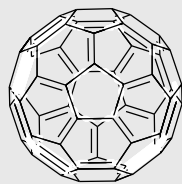
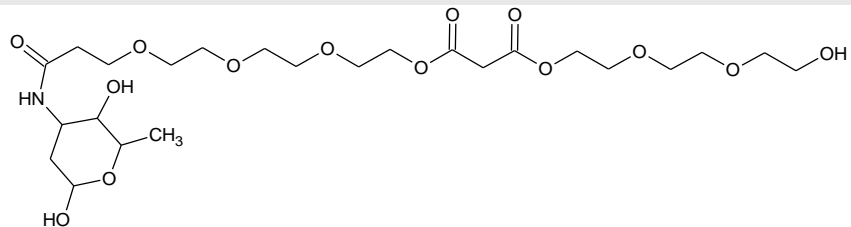
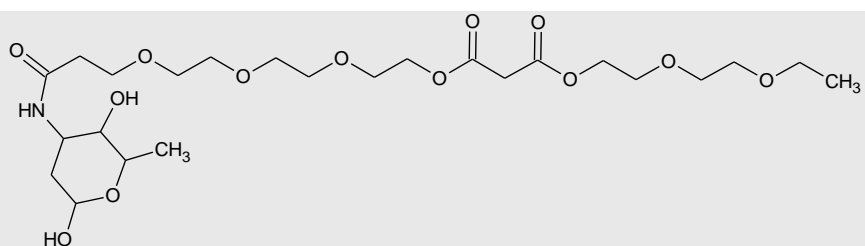


$[M-H^-] = 776.9694$

7e



$[M-H^-] = 760.9956$

7f $M = 720.0950$ **7g** $[M-H^-] = 568.9879$ **7h** $[M-H^-] = 553.0058$

2. TLC analysis

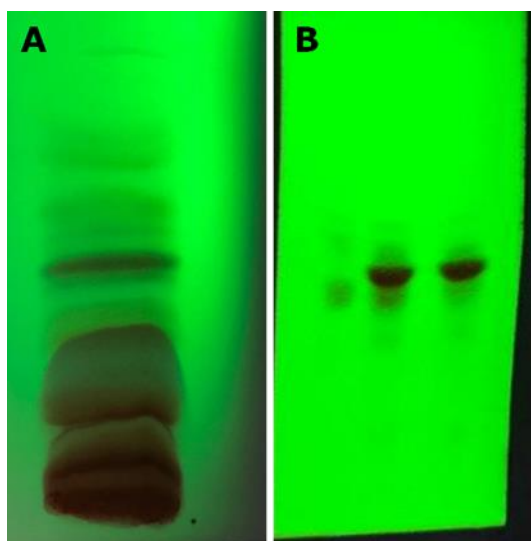


Fig. S7 TLC plates visualized with UV light. A) the preparative TLC plate from the coupling reaction between compound 6 and doxorubicin (after 24 h), B) purified compound 7 (right lane), the mixture before purification (middle lane) unidentified contamination (the left lane).

3. TD-DFT calculations

Table S1 Most important (oscillator strength > 0.05) electronic transitions as calculated by the TD-DFT/B3LYP/def2-SVP method

Compound	Wavelength [nm]	Energy [eV]	Oscillator strength	Main contribution
DOX	465.67	2.6624	0.29	HOMO → LUMO
FUL-DOX	483.56	2.564	0.06	HOMO → LUMO+4
	480.52	2.5802	0.07	HOMO-1 → LUMO+3
				HOMO → LUMO+4
				HOMO-2 → LUMO+3
	476.07	2.6043	0.10	HOMO-2 → LUMO+3
			HOMO-1 → LUMO+3	
Fullerene	-	-	-	-

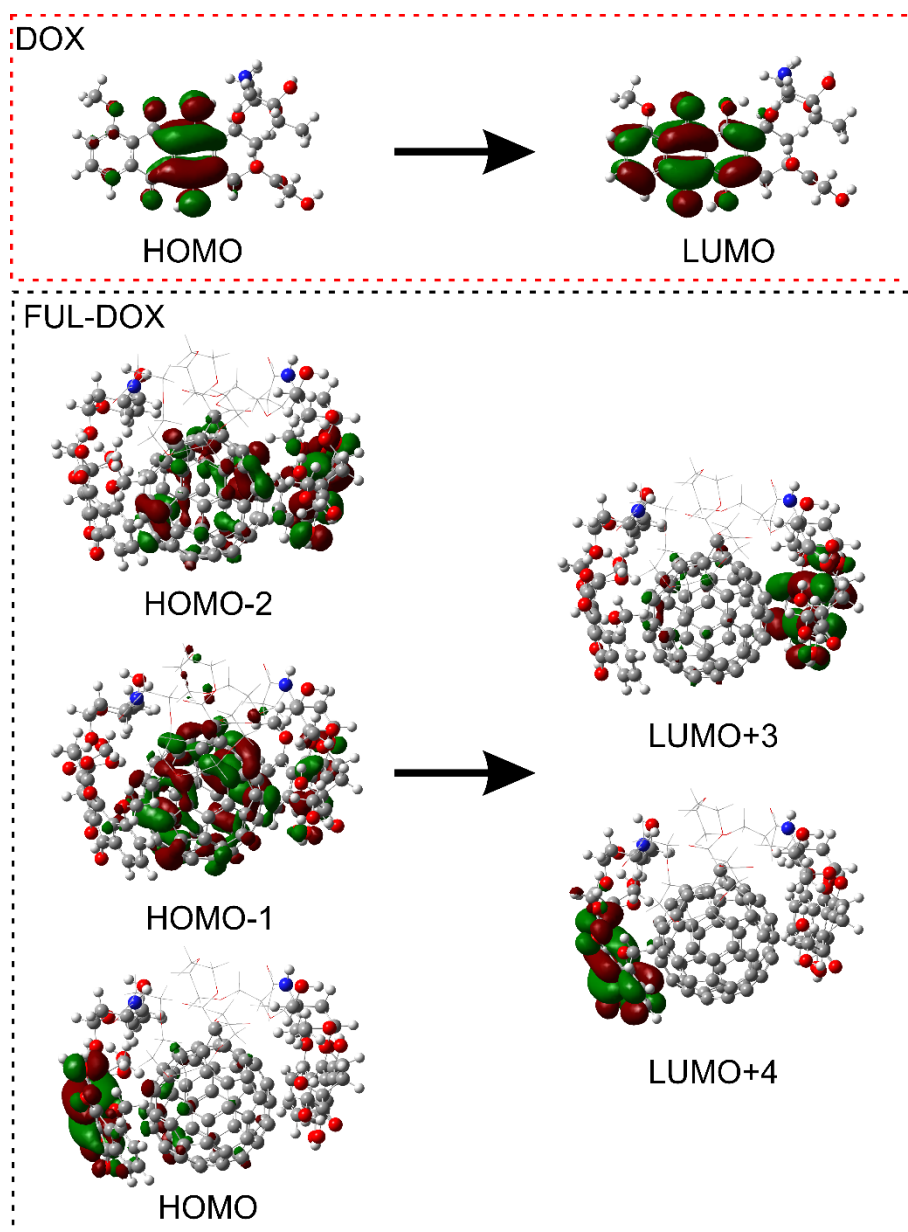


Fig. S8 The most important molecular orbitals taking part in the electronic transitions for DOX and Ful-DOX as calculated by the TD-DFT/B3LYP/def2-SVP methods (isosurface value equal to $0.02 \text{ a.u.}^{-3/2}$)

2. **K. Butowska**, K. Żamojć, M. Kogut, W. Kozak, D. Wyrzykowski, W. Wiczak, J. Czub, J. Piosik, J. Rak, *The product of matrix metalloproteinase cleavage of doxorubicin conjugate for anticancer drug delivery: calorimetric, spectroscopic, and molecular dynamic studies on peptide-doxorubicin binding to DNA*. International Journal of Molecular Sciences, **2020**, 21, 6923. [P2]



Article

The Product of Matrix Metalloproteinase Cleavage of Doxorubicin Conjugate for Anticancer Drug Delivery: Calorimetric, Spectroscopic, and Molecular Dynamics Studies on Peptide–Doxorubicin Binding to DNA

Kamila Butowska ^{1,2,*}, Krzysztof Żamojć ³, Mateusz Kogut ⁴, Witold Kozak ²,
Dariusz Wyrzykowski ³, Wiesław Wiczak ⁵, Jacek Czub ⁴, Jacek Piosik ¹ and Janusz Rak ²

¹ Laboratory of Biophysics, Intercollegiate Faculty of Biotechnology University of Gdańsk and Medical University of Gdańsk, Abrahama 58, 80-307 Gdańsk, Poland; jacek.piosik@biotech.ug.edu.pl

² Department of Physical Chemistry, Faculty of Chemistry, University of Gdańsk, Wita Stwosza 63, 80-308 Gdańsk, Poland; davelombardo@wp.pl (W.K.); janusz.rak@ug.edu.pl (J.R.)

³ Department of General and Inorganic Chemistry, Faculty of Chemistry, University of Gdańsk, Wita Stwosza 63, 80-308 Gdańsk, Poland; krzysztof.zamojc@ug.edu.pl (K.Ż.);
dariusz.wyrzykowski@ug.edu.pl (D.W.)

⁴ Department of Physical Chemistry, Faculty of Chemistry, Gdańsk University of Technology, Narutowicza 11/12, 80-233 Gdańsk, Poland; giggsmk@op.pl (M.K.); jacek.czub@pg.edu.pl (J.C.)

⁵ Department of Biomedical Chemistry, Faculty of Chemistry, University of Gdańsk, Wita Stwosza 63, 80-308 Gdańsk, Poland; wieslaw.wiczak@ug.edu.pl

* Correspondence: kamila.butowska@phdstud.ug.edu.pl; Tel.: +48-58-523-6310

Received: 29 July 2020; Accepted: 18 September 2020; Published: 21 September 2020



Abstract: Matrix metalloproteinases (MMPs) are extracellular matrix degradation factors, promoting cancer progression. Hence, they could provide an enzyme-assisted delivery of doxorubicin (DOX) in cancer treatment. In the current study, the intercalation process of DOX and tetrapeptide–DOX, the product of the MMPs' cleavage of carrier-linked DOX, into dsDNA was investigated using stationary and time-resolved fluorescence spectroscopy, UV-Vis spectrophotometry and isothermal titration calorimetry (ITC). The molecular dynamics (MD) simulations on the same tetrapeptide–DOX ··· DNA and DOX ··· DNA systems were also performed. The undertaken studies indicate that DOX and tetrapeptide–DOX can effectively bond with dsDNA through the intercalation mode; however, tetrapeptide–DOX forms less stable complexes than free DOX. Moreover, the obtained results demonstrate that the differences in DNA affinity of both forms of DOX can be attributed to different intercalation modes. Tetrapeptide–DOX shows a preference to intercalate into DNA through the major groove, whereas DOX does it through the minor one. In summary, we can conclude that the tetrapeptide–DOX intercalation to DNA is significant and that even the lack of non-specific proteases releasing DOX from the tetrapeptide conjugate, the presence of which is suggested by the literature for the efficient release of DOX, should not prevent the cytostatic action of the anthracycline.

Keywords: doxorubicin; matrix metalloproteinases; intercalation; DNA; cleavable peptide; drug delivery

1. Introduction

Cancer—the second leading cause of death worldwide—can be treated by several modalities, of which chemotherapy represents 36% of the treatment options [1,2]. Anthracyclines are one of the most widely used chemotherapeutic drugs for the treatment of various types of cancer including leukemia, melanoma, Kaposi's sarcoma, and solid tumors, e.g., breast or prostate [3,4]. Doxorubicin (DOX) is one

of the well-known anthracycline antibiotics, which was isolated in the 1960s from a mutated variant of *Streptomyces peucetius* (var. *S. caesioides*) [5]. It is an important chemotherapeutic agent with a wide spectrum of activity [3,6,7]. The mechanism of DOX action is related to its intercalation into cellular DNA leading to the inhibition of the synthesis of macromolecules, DNA cross-linking, and alkylation, as well as the generation of free radicals and the inhibition of topoisomerase II [8–10]. Despite its clinical efficacy, it has severe disadvantages, including cardiotoxicity and myelosuppression [11,12]. Moreover, DOX can lead to several side effects that mainly affect the brain, kidneys, and liver [13].

One of the strategies to increase therapeutic efficiency, with high binding specificity and reduced toxic effects of a drug, is to conjugate it with polymers, lipid nanoparticles, or antibody–drug conjugates [14–16]. Such an approach can lead to a system characterized by enhanced solubility, permeability, and retention in body plasma that triggers drug release in cancer cells [17]. A variety of polymers, including polymer–drug conjugates (PDCs), polymer–protein/peptide, polymer–DNA, and their hybrids, have been developed in the past decades as selective therapeutic agents. Several examples of PDCs have been observed to couple a hydrophobic drug with hydrophilic polymers such as poly(lactic-co-glycolic acid) (PLGA) and poly(ethylene glycol) (PEG) [18,19]. However, PDCs with increased stability, solubility, and lower toxicity would not be suitable for cancer therapy if they did not release an anticancer component at the target place. To overcome this problem, PDCs release a drug using a peptide fragment selectively cleaved by enzymes, or under specific conditions [20]. Matrix metalloproteinases (MMPs) are a group of over 20 proteolytic enzymes characterized by their ability to remodel and degrade the extracellular matrix [21]. MMPs are overexpressed in newly formed tumor tissues, thereby promoting angiogenesis, and are involved in cancer progression; MMP-2 and MMP-9, in particular, play a critical role in this process [22,23]. Therefore, MMPs could constitute a promising strategy for targeted therapeutic agent delivery via an enzyme-triggered release mechanism [24]. According to the literature, there are a series of substrate peptide sequences degradable in the presence of MMPs, e.g., Gly–Pro–Leu–Gly–Ile–Ala–Gly–Gln, Pro–Val–Gly–Leu–Ile–Gly, or Pro–Leu–Gly–Val–Arg, where cleavage occurs between leucine (Leu) and glycine (Gly) [25–27]. Using this approach, new polymer–drug conjugates with a selective peptide sequence between the carrier (polymer) and the cargo (drug) have been designed [28]. The drug release from enzymatically cleavable prodrugs occurs within a two-step mechanism: (1) a prodrug is cleaved by MMPs and is (2) further cleaved or hydrolyzed to the desired drug [29]. Hence, some reports suggest that additional proteases are important for liberating a free drug from intermediate cleavage products [30].

In this study, we present the synthesis of a tetrapeptide–DOX conjugate (Leu–Ala–Gly–Gly–DOX, i.e., 4-pep–DOX), as a potential result of MMPs' action on the substrate peptide sequence (Figure 1). The selected MMP-2/-9-cleavable peptide, containing the Leu–Gly sequence, was expanded to Gly–Pro–Leu–Gly–Leu–Ala–Gly–Gly, which is cleavable by the chosen MMPs' domain [31]. We demonstrated the impact of the presence of the tetrapeptide fragment in 4-pep–DOX on its intercalating properties to dsDNA, and compared the tetrapeptide–DOX ··· dsDNA complex with free doxorubicin, namely DOX ··· dsDNA. The characteristics of the dsDNA complex with 4-pep–DOX and DOX were studied by spectrophotometric titration, steady-state, and time-resolved fluorescence spectroscopy, as well as isothermal titration calorimetry (ITC). Furthermore, molecular dynamics (MD) simulations were carried out to determine the preferred binding sites to dsDNA. To the best of our knowledge, this is the first report where an MMP-cleavable product (Leu–Ala–Gly–Gly–DOX) has been characterized at the molecular level.

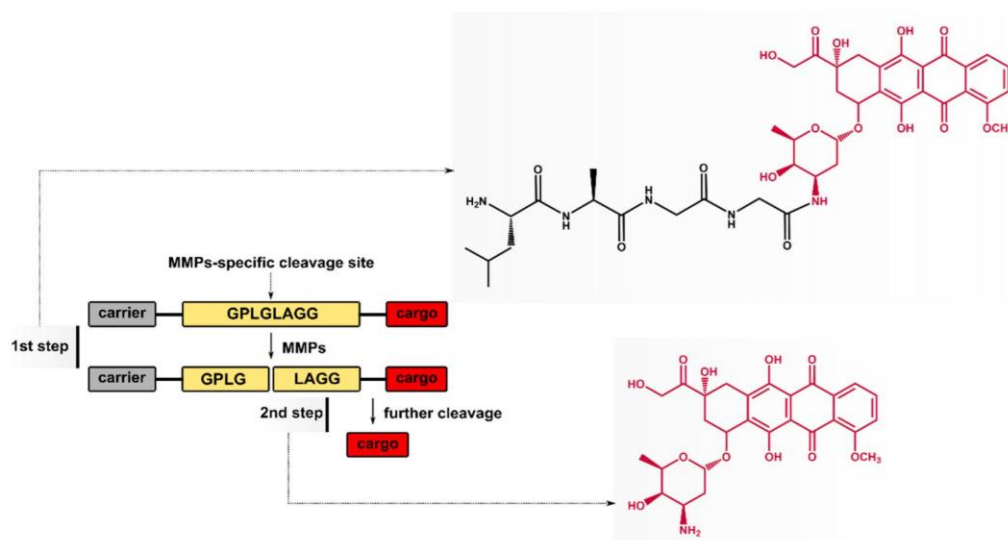


Figure 1. Doxorubicin (DOX) release strategies for matrix metalloproteinase (MMP)-cleavable prodrugs.

2. Results and Discussion

2.1. Cleavage of Peptide by MMPs

The MMP-2/-9-cleavable peptide was degraded by collagenase IV (containing MMP-2/-9) in a time-dependent manner. The MMPs' substrate specificity, revealed by the MS analysis, is consistent with that reported previously and indicates that the proposed octapeptide can be responsive to MMPs [32,33]. The MALDI TOF spectrum proved that the octapeptide was cleaved between leucine (Leu) and glycine (Gly), yielding two products, namely Fmoc-Gly-Pro-Leu-Gly and Leu-Ala-Gly-Gly (see Figure S1, Supplementary Materials). Consistently, the HPLC chromatogram (Figure 2A) shows two peaks from the enzymatic digestion—the substrate, Fmoc-Gly-Pro-Leu-Gly-Leu-Ala-Gly-Gly, and the product, Fmoc-Gly-Pro-Leu-Gly, at 10.30 and 10.04 min, respectively. During incubation, the Fmoc-Gly-Pro-Leu-Gly peak significantly increased, whereas the octapeptide peak disappeared. After 12 h of incubation, 17.43% of the substrate and 82.42% of the MMP-2/-9 cleaved product were observed. In order to investigate how fast the octapeptide cleaved, the aliquots were removed after 2, 8, and 12 h. After 2 h of incubation, 52.54% of Fmoc-Gly-Pro-Leu-Gly was detected and after 8 h it increased to 69.53% (Figure 2B). The efficiency of the enzymatic digestion reached 82.42% after 12 h of incubation. The results proved that the octapeptide can be cleaved by collagenase IV and that the amount of product formed increases with the incubation time.

2.2. Synthesis of Tetrapeptide-DOX

In order to synthesize the desired conjugate, we performed a two-step procedure (Figure 3). First, Fmoc-Leu-Ala-Gly-Gly was coupled with DOX using the mixed anhydride method. For this purpose, Fmoc-Leu-Ala-Gly-Gly was treated with isobutyl chloroformate in the presence of triethylamine in DMF, followed by the addition of DOX (obtained independently by the reaction of DOX hydrochloride with TEA in DMF). The so-obtained raw Fmoc-Leu-Ala-Gly-Gly-DOX was purified by preparative column chromatography. In the second step, Fmoc-Leu-Ala-Gly-Gly-DOX was deprotected with a 50% morpholine solution in DMF, furnishing raw Leu-Ala-Gly-Gly-DOX, which was finally isolated with the HPLC system and proved by MALDI TOF/TOF (see Figure S2, Supplementary Materials). It is worth mentioning that we had tested two different deprotection methods with 1,8-diazabicyclo[5.4.0]undec-7-ene (DBU) and piperidine, respectively. In both cases, we struggled through some difficulties. As far as DBU is concerned, dibenzofulvene is released during the reaction,

which readily reacts, as an electrophile, with N-terminal amino acid residue leading to undesired by-products [34]. When it came to piperidine, we obtained the desired product in a very poor yield, which could be due to the presumed dealkylation properties of piperidine (DOX possesses a methoxyl function in its constitution) [35].

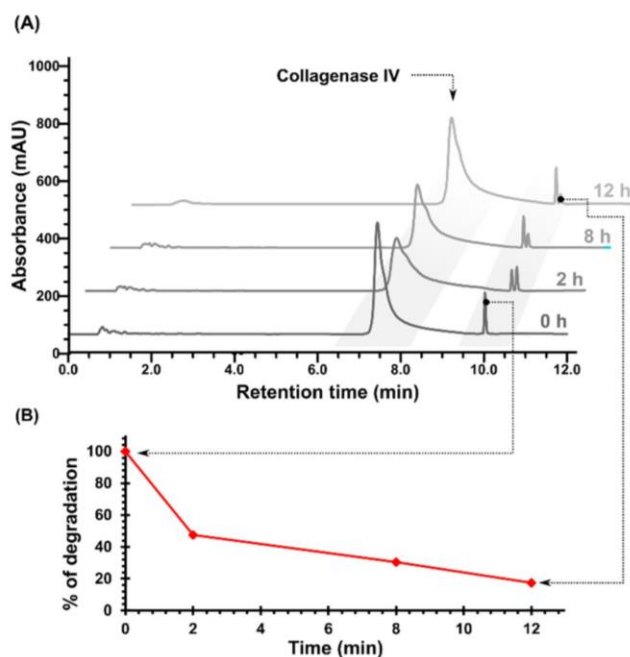


Figure 2. (A) HPLC chromatograms of the MMP-2/-9-cleavable peptide after 2, 8, and 12 h of incubation with collagenase IV. (B) The curves depicting the efficacy of enzymatic cleavage, triggered in a time-dependent manner.

2.3. Spectrophotometric Titrations

In order to evaluate the binding strength of DOX and 4-pep-DOX to dsDNA, the binding/association constants (K_A) of the resulting complexes were determined from the changes in absorbance of DOX and 4-pep-DOX bands with increasing amounts of dsDNA (Figure 4). The intrinsic association constants (K_A) of the complexes were calculated according to the Benesi-Hildebrand equation:

$$\frac{A_0}{A - A_0} = \frac{\epsilon_f}{\epsilon_b - \epsilon_f} + \frac{\epsilon_f}{\epsilon_b - \epsilon_f} \cdot \frac{1}{K_A [DNA]}, \quad (1)$$

where A_0 and A are the absorbances of DOX/4-pep-DOX in the absence and presence of dsDNA in the solution, respectively, ϵ_f and ϵ_b correspond to the extinction coefficients of free and bound ligands, respectively, while $[DNA]$ is the concentration of dsDNA. The ligand-dsDNA binding constants were calculated from the ratio of the intercept to the slope of the linear equation of the plot of $\frac{A_0}{A - A_0}$ (measured at 480 nm) to $\frac{1}{[DNA]}$, and were determined to be $K_{A \text{ DOX} \cdots \text{dsDNA}} = 1.10 \times 10^6 \text{ M}^{-1}$ and $K_{A \text{ 4-pep-DOX} \cdots \text{dsDNA}} = 0.54 \times 10^6 \text{ M}^{-1}$. The free energies of the binding (ΔG) were calculated using the standard thermodynamic relationship, $\Delta G = -RT \ln K_A$, and were determined to be $\Delta G_{\text{DOX} \cdots \text{dsDNA}} = -8.23 \text{ kcal/mol}$ and $\Delta G_{\text{4-pep-DOX} \cdots \text{dsDNA}} = -7.81 \text{ kcal/mol}$.

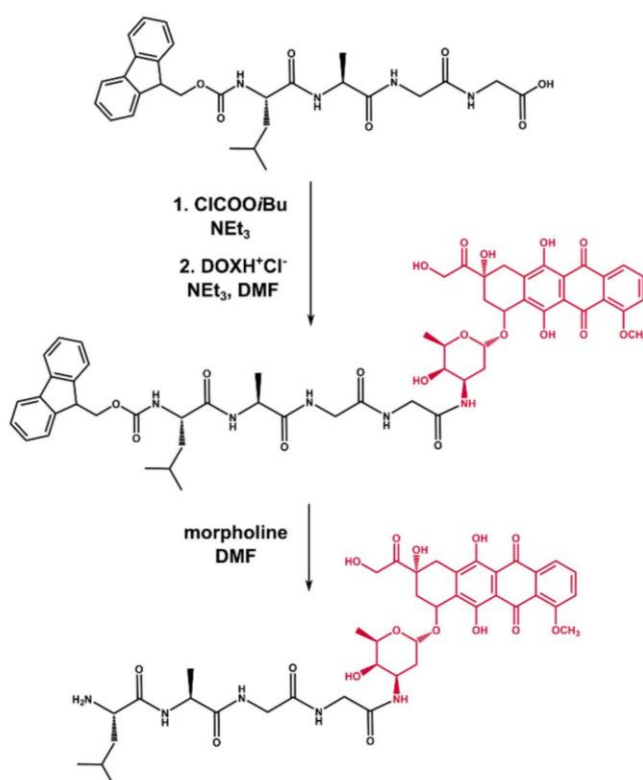


Figure 3. Synthesis scheme of the Leu–Ala–Gly–Gly–DOX conjugate.

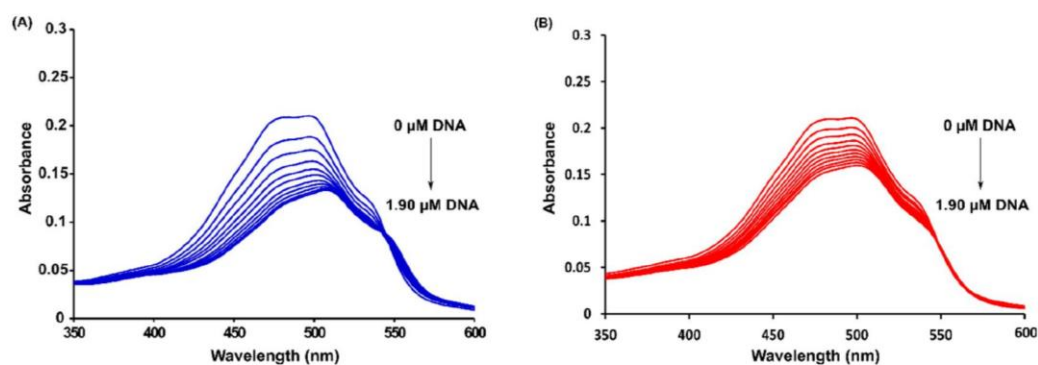


Figure 4. UV-Vis absorption spectra of DOX (A) and 4-pep–DOX (B) in the presence of dsDNA at various concentrations in 10 mM Tris–HCl buffer (pH 7.2) at 25 °C (the initial concentration of DOX and 4-pep–DOX = 18 μM).

2.4. Steady-State and Time-Resolved Spectroscopy

Figure 5 shows the fluorescence emission spectra of DOX and 4-pep–DOX recorded in the presence of various dsDNA concentrations, using drug excitation at 490 nm. It can be observed that the fluorescence intensity of both drugs decreases regularly with the increasing concentration of dsDNA, which may result from a variety of processes such as excited state reactions, ground-state complex formations, or collisional processes.

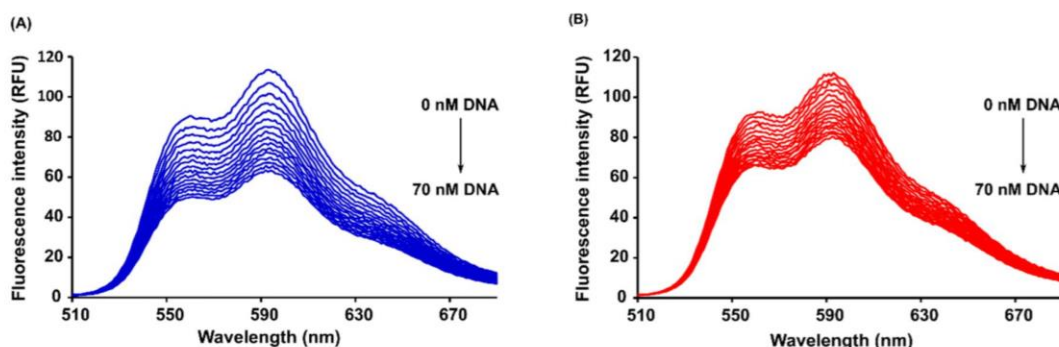


Figure 5. Fluorescence emission spectra of DOX (A) and 4-pep-DOX (B) in the presence of dsDNA at various concentrations in 10 mM Tris-HCl buffer (pH 7.2) at 25 °C (the initial concentration of DOX and 4-pep-DOX = 1.94 μ M).

In order to confirm the quenching mechanism, the fluorescence quenching was analyzed according to the Stern–Volmer equation:

$$\frac{F_0}{F} = 1 + K_{SV}[Q] = 1 + k_q\tau_0[Q], \quad (2)$$

where F_0 and F are the fluorescence intensities in the absence and presence of quencher, $[Q]$ is the quencher concentration, K_{SV} is the Stern–Volmer quenching constant, k_q is the bimolecular quenching rate constant, while τ_0 is the lifetime of the fluorophore in the absence of quencher [36]. The graphs of $\frac{F_0}{F}$ versus $[Q]$ plotted according to the Stern–Volmer equation are shown in Figure 6. It can be observed that straight lines were obtained for both drug–DNA complexes, indicating that, in the investigated range of concentrations, the quenching is purely static or dynamic. Since the τ_0 values for free DOX and 4-pep-DOX around neutral pH were determined to be 1.057 ns and 1.076 ns, respectively (see below), the values of the bimolecular quenching rate constants (k_q) are $9.37 \times 10^{15} \text{ M}^{-1} \text{ s}^{-1}$ for DOX \cdots dsDNA and $5.20 \times 10^{15} \text{ M}^{-1} \text{ s}^{-1}$ for 4-pep-DOX \cdots dsDNA complexes. As these values are much larger than the maximum scatter collision quenching constant ($2.0 \times 10^{10} \text{ M}^{-1} \text{ s}^{-1}$) [37], this indicates that the fluorescence quenching effects of DOX and 4-pep-DOX by dsDNA are not initiated by dynamic collisions, but rather caused by the formation of ground-state complexes.

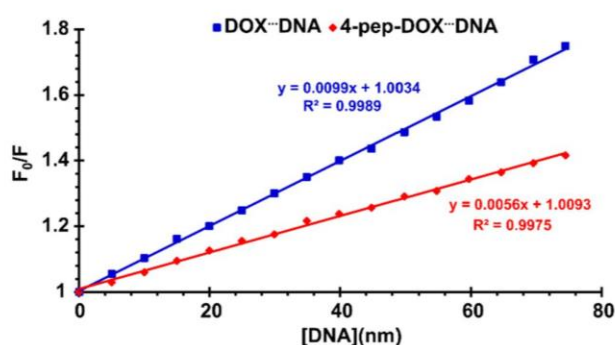


Figure 6. Stern–Volmer plots for the DOX \cdots dsDNA and 4-pep-DOX \cdots dsDNA systems in 10 mM Tris-HCl buffer (pH 7.2) at 25 °C.

Given that the fluorescence quenching of both DOX and 4-pep-DOX by dsDNA is static, the dissociation constants (K_D) of the newly formed complexes can be determined by the Lineweaver–Burk formula [38]:

$$\frac{1}{F_0 - F} = \frac{1}{F_0} + \frac{K_D}{F_0[0]} \quad (3)$$

The Lineweaver–Burk double-reciprocal plots were constructed based on the relationship of $\frac{F_0}{F_0-F}$ vs. $\frac{1}{[DNA]}$ (Figure 7).

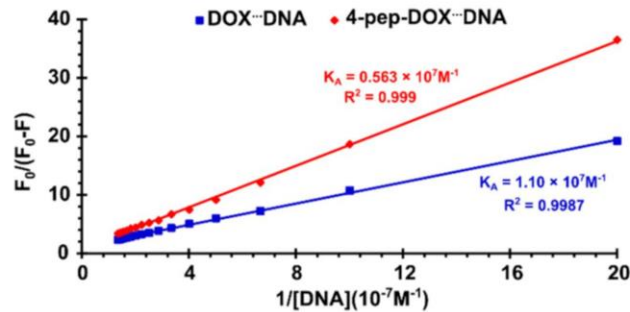


Figure 7. Lineweaver–Burk double-reciprocal curves of $\frac{F_0}{F_0-F}$ vs. $\frac{1}{[DNA]}$ for the DOX ··· dsDNA and 4-pep–DOX ··· dsDNA systems in 10 mM Tris–HCl buffer (pH 7.2) at 25 °C.

From the regression analysis, the association constants ($K_A = K_D^{-1}$) between dsDNA and both studied drugs were determined to be $K_{A \text{ DOX} \cdots \text{dsDNA}} = 1.10 \times 10^7 \text{ M}^{-1}$ and $K_{A \text{ 4-pep-DOX} \cdots \text{dsDNA}} = 0.56 \times 10^7 \text{ M}^{-1}$ (as the averages of two independent experiments), respectively. The observed discrepancies between the K_A values obtained from spectrophotometric and spectrofluorometric titrations may result from the specificity of each method, as well as from differences in the experimental conditions (i.e., concentrations). By comparing the measured association constants, it is clear that both DOX and 4-pep–DOX show a high affinity to dsDNA; however, the complexes formed by DOX are slightly more stable compared to those of 4-pep–DOX. When small molecules bind independently to a set of equivalent sites on a macromolecule, the number of binding sites (n) can be found from the following Scatchard equation [39]:

$$\log\left[\frac{F_0-F}{F}\right] = \log K_A + n \log[Q], \quad (4)$$

The plots of $\log\left[\frac{F_0-F}{F}\right]$ vs. $\log[Q]$ for both DOX and 4-pep–DOX are shown in Figure 8. It can be observed that the n values, determined as the slopes of the straight-line plots, were found to be approximately 1.0 for both ligands that are bound per dsDNA molecule. Furthermore, the association constants estimated by this method are basically in accordance with those obtained by the Lineweaver–Burk equation ($K_{A \text{ DOX} \cdots \text{dsDNA}} > K_{A \text{ 4-pep-DOX} \cdots \text{dsDNA}}$).

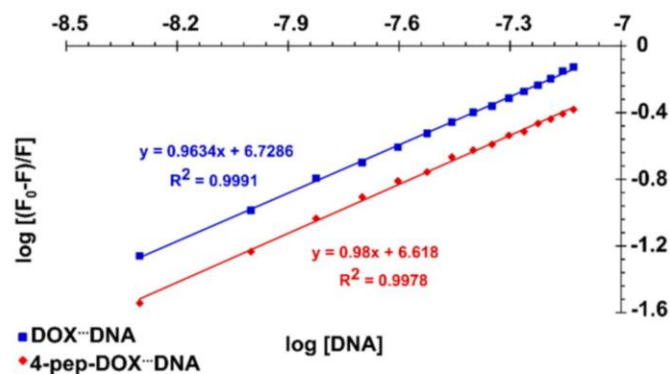


Figure 8. Plots of $\log\left[\frac{F_0-F}{F}\right]$ vs. $\log[DNA]$ for the DOX ··· dsDNA and 4-pep–DOX ··· dsDNA systems in 10 mM Tris–HCl buffer (pH 7.2) at 25 °C.

The determination of fluorescence lifetimes was carried out to confirm that the static quenching is the sole reason for the observed fluorescence quenching. According to the performed time-resolved experiments, the fluorescence lifetimes of DOX and 4-pep-DOX were constant, regardless of the dsDNA concentration, and equal to 1.057 ± 0.022 ns for DOX (the value is in good agreement with literature data [40]) and 1.076 ± 0.006 ns for 4-pep-DOX. Therefore, $\tau_0/\tau = 1$, which is characteristic for pure static quenching. This is in a good agreement with the results presented in Figure 4, since the formation of a complex is often reflected in a change of the absorption spectrum of the fluorophore.

2.5. Isothermal Titration Calorimetry

The ITC method was applied to determine the binding constants (K_{ITC}) and the thermodynamic parameters (ΔG_{ITC} , ΔH_{ITC} , ΔS_{ITC}) for the interactions of DOX and 4-pep-DOX with dsDNA. Representative binding isotherms for the interactions under study are shown in Figure 9, and the thermodynamic parameters are summarized in Table 1. The molar ratios of the resulting complexes were estimated based on ITC data and they are $7.29 (\pm 0.09)$ and $7.98 (\pm 1.23)$ for DOX to dsDNA and 4-pep-DOX to dsDNA, respectively. The binding constants of the resulting complexes, as well as the binding enthalpies, were obtained directly from the calorimetric experiments by fitting binding isotherms (a nonlinear least-squares procedure) to a model that assumes a single set of identical binding sites.

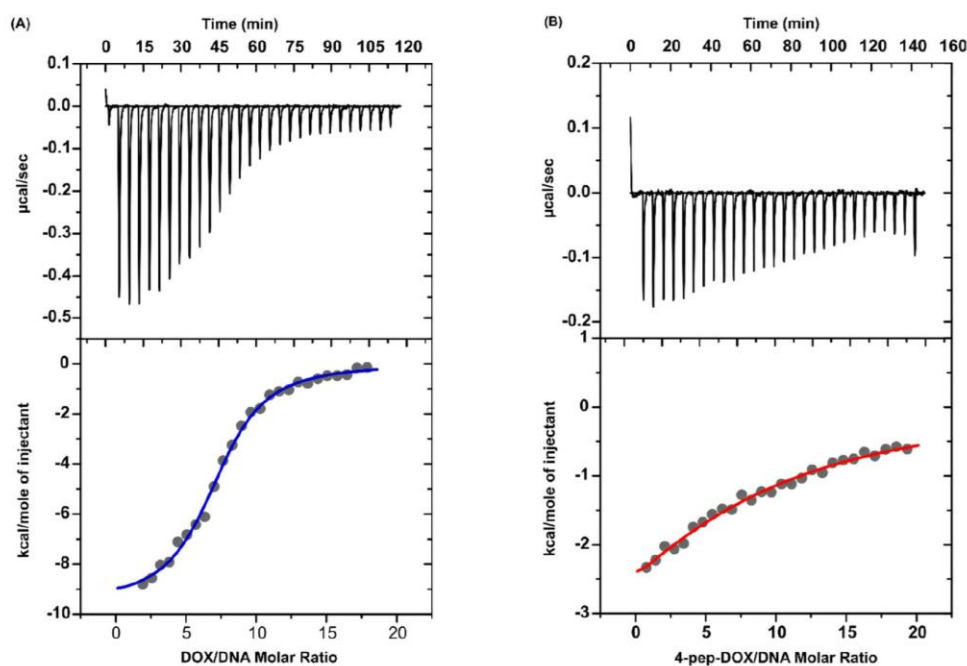


Figure 9. Calorimetric titration isotherms of the binding interaction between (A) DOX and dsDNA and between (B) 4-pep-DOX and dsDNA in 10 mM Tris-HCl buffer (pH 7.2, 25 °C).

Table 1. Thermodynamic parameters of DOX and 4-pep-DOX bound to dsDNA in 10 mM Tris-HCl buffer (pH 7.2) at 25 °C (standard deviation values in parentheses). ITC, isothermal titration calorimetry.

Parameter	DOX ··· dsDNA	4-pep-DOX ··· dsDNA
$\log K_{ITC}$	6.03 (± 0.04)	4.24 (± 0.09)
ΔH_{ITC} [kcal/mol]	-9.52 (± 0.17)	-5.84 (± 1.27)
$T\Delta S_{ITC}$ [kcal/mol]	-1.3	-0.05
ΔG_{ITC} [kcal/mol]	-8.26 (± 0.05)	-5.78 (± 0.12)

The standard thermodynamic relationships, namely $\Delta G_{ITC} = -RT \ln K_{ITC} = \Delta H_{ITC} - T\Delta S_{ITC}$, were used to calculate the free energy of binding (ΔG_{ITC}) and the entropy change ($T\Delta S_{ITC}$). The formation of the investigated dsDNA complexes is an enthalpy-driven process (Table 1). The negative values of the binding enthalpy and small entropic contribution correspond to the intercalative nature of the tetracyclic core of the low-molecular ligands. The modification of the DOX structure with a Leu-Ala-Gly-Gly tetrapeptide results in a decreasing strength of interaction. This phenomenon is reflected in the values of the binding constant $\log K_{ITC}(\text{DOX-dsDNA}) > \log K_{ITC}(\text{4-pep-DOX-dsDNA})$ and remains in agreement with the results obtained from the spectroscopic measurements. In contrast to DOX, the presence of the hydrophobic peptide chain in the structure of 4-pep-DOX hinders the intercalating interactions of the modified ligand with dsDNA, and weakens its ability to form hydrogen-bonding and electrostatic interactions, which are typical for groove binders [41]. According to the general rule, the more new bonds are formed and the stronger they are, the more energy (heat) is released. Thus, the difference in the binding enthalpy results from the different mode of the DOX-dsDNA and 4-pep-DOX-dsDNA interactions. This phenomenon probably is the most important factor responsible for the release of a larger amount of energy in the case of DOX binding to dsDNA.

2.6. Molecular Dynamics Simulations

To provide a molecular-level understanding of the differences in the stability of the intercalation complexes formed by DOX and 4-pep-DOX with dsDNA, we computed the free energy profiles for the two different intercalation modes in which the amino sugar moiety is extended into either the minor or major groove. As a collective coordinate describing the intercalation process, we used the separation distance between the centers of mass of the two base pairs forming the intercalation site and the planar chromophore of DOX and 4-pep-DOX (see Figure 10A).

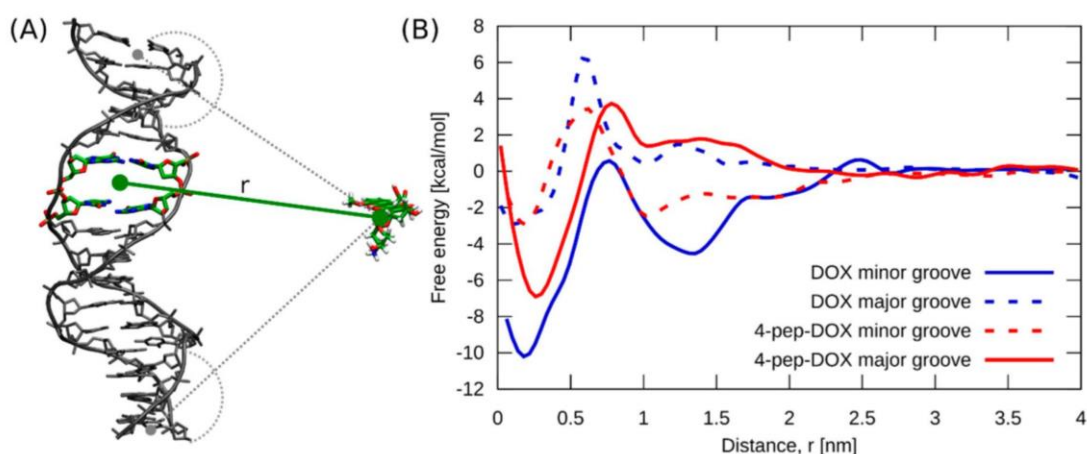


Figure 10. (A) Intercalation of DOX and 4-pep-DOX into dsDNA in the simulation was studied using the coordinate defined as the separation distance between the centers of mass of the two base pairs forming the intercalation site, and the planar chromophore of the ligand (green solid line). In addition, one-sided harmonic potentials were used to prevent association of the ligands at the dsDNA ends (see Methods section, grey dashed lines.) (B) Free energy profiles for the formation of the intercalation complexes of DOX and 4-pep-DOX with dsDNA as a function of the separation distance between them (r), in two intercalation modes (minor/major groove).

Comparison of the two free energy profiles obtained for the DOX ··· dsDNA system (blue lines in Figure 10B) strongly suggests that the highly stable DOX intercalation complex, observed in spectrophotometric titrations and ITC, corresponds to the minor-groove binding mode. Indeed, the intercalation of DOX from the major-groove side is 7.5 kcal/mol less favorable. This conclusion is further supported by a very good agreement between the depth of the main free energy minimum

computed for DOX intercalating from the minor groove (-9.8 kcal/mol at ~ 0.2 nm) and the measured binding free energies. The free energy simulations further revealed that the intercalation of DOX is preceded by its relatively strong binding to the dsDNA surface (-4.5 kcal/mol) with a clear kinetic barrier to overcome. In contrast, 4-pep-DOX (red lines in Figure 10B) shows a 3.7 kcal/mol preference for intercalation from the major groove. The predicted absolute binding free energy in this case (-6.7 kcal/mol) is consistent with our ITC results and, to a lesser extent, the spectrophotometric values, supporting the conclusion that the stable intercalation complexes of 4-pep-DOX observed in our experiments are in fact characterized by the major-groove binding mode.

To structurally compare the four intercalation complexes considered in Figure 10B, we performed a cluster analysis of the MD-generated unbiased ensembles. This was done using the hybrid k-centers k-medoids clustering algorithm for all heavy atoms of DOX and 4-pep-DOX, with a root mean square deviation (RMSD) cut-off of 0.3 nm. Before clustering, the structures were superimposed by minimizing a heavy-atom RMSD for the two dsDNA base pairs forming the intercalation site [42].

Figure 11 shows, separately, the most likely structures of DOX \cdots dsDNA and 4-pep-DOX \cdots dsDNA complexes identified by our cluster analysis for each of the four intercalation cases considered. As expected, the energetically most favorable DOX \cdots dsDNA complex in the minor-groove mode is characterized by a well-defined structure with one preferred arrangement of the ligand with respect to the dsDNA duplex (85% of the bound ensemble). This is also manifested by the limited structural fluctuations of the ligand within the intercalation site, and by strong interactions between the positively charged amino group of DOX with dsDNA phosphate groups, with the mean distance to the closest phosphate being 0.62 nm. By comparison, intercalation of DOX from the major-groove side does not allow for a favorable electrostatic contact between the amino group and the dsDNA backbone (the mean distance to the closest phosphate is 1.06 nm), resulting in a substantially reduced stability of the complex.

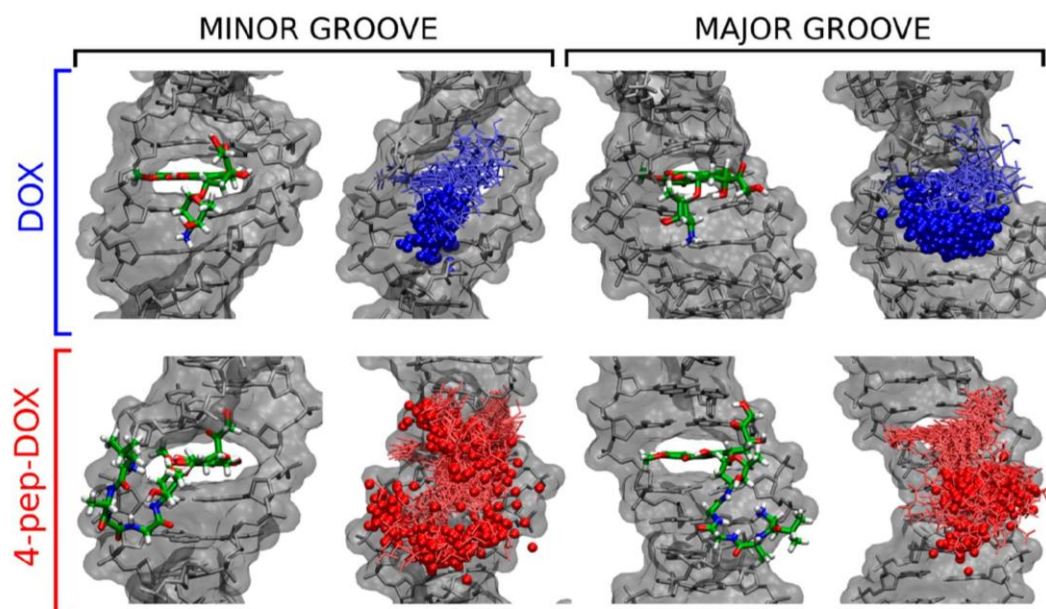


Figure 11. The most likely structures (left) and the range of ligand fluctuations (right) in the two considered intercalation modes (minor/major groove) of the DOX \cdots dsDNA and 4-pep-DOX \cdots dsDNA complexes. In addition, 100 overlaid representative positions of the protonated amino group (in the amino sugar of DOX or at the N-terminus of the tetrapeptide of 4-pep-DOX) are marked with spheres.

In contrast to the DOX case, the most likely arrangement of 4-pep-DOX intercalated into dsDNA from the minor groove accounts for only 35% of the ensemble (Figure 11). In this position,

the tetrapeptide fragment resides outside the minor groove, not interacting specifically with the dsDNA chain despite a relatively small average distance to the closest phosphate group (0.76 nm). Notably, DOX and 4-pep-DOX intercalated via the minor groove differ substantially in the orientation of their planar chromophore relative to the flanking base pairs. In particular, the 4-pep-DOX core is rotated by 33° resulting in a decreased stacking overlap with the flanking nucleobases, as compared to DOX (see Figure S3, Supplementary Materials).

In its more stable major-groove intercalation mode, 4-pep-DOX exhibits one well-defined structure (74% of the ensemble, Figure 11), in which the tetrapeptide interacts largely with one dsDNA strand, with the mean distance of the amino group to the closest phosphate equal to 0.45 nm. This suggests that effective stabilization of the intercalation complex requires accommodation of the flexible peptide substituent in the wider and more accessible major groove.

3. Materials and Methods

3.1. Materials

Fmoc-Leu-Ala-Gly-Gly and Fmoc-Gly-Pro-Leu-Gly-Leu-Ala-Gly-Gly peptides were purchased from Lipopharm.pl (Zblewo, Poland). Oligonucleotides 5'-CGT ACG CGT ACG CGT ACG CG-3' and 5'-CGC GTA CGC GTA CGC GTA CG-3' were purchased from Future Synthesis (Poznań, Poland). Collagenase IV and Hank's Balanced Salt Solution (HBSS), with calcium and magnesium, were purchased from ThermoFisher Scientific (Waltham, MA, USA). Acetonitrile (ACN), 4-aminophenylmercuric acetate (APMA), dichloromethane (DCM), 2,5-dihydroxybenzoic acid (DHB), N,N-dimethylformamide (DMF), doxorubicin hydrochloride, formic acid, isobutyl chloroformate, methanol, sodium hydroxide, tetrahydrofuran (THF), triethylamine (TEA), and Tris-HCl were purchased from Sigma-Aldrich (St. Louis, MO, USA). Column chromatography was performed using silica gel NORMASIL 60 (40–63 mesh, VWR Chemicals, Radnor, PA, USA). Thin-layer chromatography was performed using silica plates, 60G, F₂₅₄ (Sigma-Aldrich, St. Louis, MO, USA).

3.2. Methods

3.2.1. Assembly of dsDNA

Two oligonucleotides of 20 base pairs, 5'-CGT ACG CGT ACG CGT ACG CG-3' and 5'-CGC GTA CGC GTA CGC GTA CG-3', were mixed at concentrations of 10 μM each, in 10 mM Tris-HCl buffer (pH 7.2). The mixtures were submitted to the annealing procedure at 95 °C for 5 min, 50 °C for 30 min, and cooled to 4 °C in 20 min using a Mastercycler gradient from Eppendorf (Hamburg, Germany). The formation of double-stranded DNA was confirmed by the HPLC Dionex Ultimate 3000 System (Waltham, MA, USA; data not shown). The analysis was performed on the XBridge OST C18 column (2.5 μm, 4.6 × 50 mm; Waters, Milford, MA, USA) at 20 °C. The flow was set at 1 mL/min with a mobile phase consisting of solvent A (1% ACN with 50 mM triethylamine acetate) and solvent B (80% ACN). The gradient was 0–20% of solvent B in 20 min.

3.2.2. Enzymatic Cleavage of Peptide by MMPs

The MMP-2/-9-cleavable octapeptide Fmoc-Gly-Pro-Leu-Gly-Leu-Ala-Gly-Gly was evaluated by enzymatic digestion with the use of collagenase IV (containing MMP-2/-9). In the first step, 1 mL of HBSS was added to 1 g of collagenase IV (205 u/mg) and mixed to complete dissolution. Activation of collagenase IV was performed using 1 mM APMA in 0.15 M NaOH for 1.5 h at 37 °C [24,43]. The octapeptide stock solution was added to activated 1 mM collagenase IV and incubated at 37 °C. The aliquots were removed and analyzed by HPLC, between 2 and 12 h. The HPLC Dionex Ultimate 3000 (Waltham, MA, USA) was equipped with a bioZen Intact XB-C8 column (3.6 μm, 2.1 × 150 mm; Phenomenex, Aschaffenburg, Germany). The flow rate was set at 0.5 mL/min with a mobile phase consisting of solvent A (0.1% TFA) and solvent B (100% ACN). The gradient was as follows: 0–5 min,

0% of solvent B; 5–8 min, 0–30% of solvent B. The hydrolysis product was detected by MALDI TOF/TOF 5800 mass spectrometry (AB Sciex, Darmstadt, Germany).

3.2.3. Synthesis of Fmoc–Leu–Ala–Gly–Gly–DOX

Isobutyl chloroformate (9.6 μL , 74.3 μmol) and TEA (10.4 μL , 74.3 μmol) were added to the solution of Fmoc–Leu–Ala–Gly–Gly (40 mg, 74.3 μmol) in DMF (1 mL) cooled to $-10\text{ }^{\circ}\text{C}$. After 20 min of vigorous stirring, a solution of DOX (obtained by treating DOX hydrochloride (43 mg, 74.3 μmol) in DMF with TEA (10.4 μL , 74.3 μmol)) in DMF (0.5 mL) was added to the reaction mixture. After 1 h at RT, DMF was evaporated, azeotropically, with toluene on a rotary evaporator (Heidolph Hei-VAP Gold 3, Heidolph, Schwabach, Germany). The raw Fmoc–Leu–Ala–Gly–Gly–DOX was purified by preparative column chromatography, using CHCl_3 : MeOH 30: 1 as an eluent, to give the desired product (59 mg) in a 75% yield.

3.2.4. Synthesis of Leu–Ala–Gly–Gly–DOX

Morpholine (0.5 mL) was added to a stirred solution of Fmoc–Leu–Ala–Gly–Gly–DOX (50 mg, 47 μmol) in DMF (0.5 mL), and the stirring was carried on for a further 2 h. Afterward, the mixture was neutralized with trifluoroacetic acid (0.6 mL). The raw product was isolated on a semi-preparative HPLC System (Shimadzu, LC 20AD, Shimadzu, Canby, OR, USA) using a Gemini NX Column (5.0 μm , $10 \times 150\text{ mm}$) to give 24 mg in a 61% yield. The flow rate was set at 4.0 mL/min with the mobile phase consisting of solvent A (0.1% formic acid) and solvent B (100% ACN). The gradient was as follows: 0–15 min, 10–90% of solvent B; 15–20 min, 90% of solvent B. The chemical structure of the product was confirmed using MALDI TOF/TOF 5800 mass spectrometry (AB Sciex, Darmstadt, Germany). As a matrix, 2,5-dihydroxybenzoic acid was used. The measurement was done in reflector positive ion mode. Samples were prepared using the dried droplet preparation method by mixing 0.8 mL of an analyte solution with 0.8 mL of the matrix solution (directly on a plate). MS spectra were acquired from 789 to 961 m/z for a total of 1000 laser shots by a 1 kHz OptiBeam laser (AB Sciex, Darmstadt, Germany).

3.2.5. Spectrophotometric Titrations

The concentrations of the studied compounds (DOX and 4-pep–DOX) were confirmed spectrophotometrically based on the absorbance and the value of the molar extinction coefficient determined at 480 nm ($\epsilon_{480} = 11500\text{ M}^{-1}\text{ cm}^{-1}$) [44]. UV-Vis spectrophotometric experiments were carried out in 10 mM Tris-HCl buffer (pH 7.2) at $25\text{ }^{\circ}\text{C}$ using a PerkinElmer Lambda 650 UV/Vis spectrophotometer (Waltham, MA, USA). UV-Vis absorption spectra of DOX and 4-pep–DOX (18.0 μM) were recorded in the absence and presence of increasing concentrations of dsDNA, up to 1.90 μM . In the performed spectrophotometric experiments, 2 mL of DOX and 4-pep–DOX at 18.0 μM were titrated with ten 10 μL aliquots of dsDNA solution at 40 μM .

3.2.6. Steady-State and Time-Resolved Fluorescence Spectroscopy

Steady-state fluorescence experiments were carried out at $25\text{ }^{\circ}\text{C}$ using a Cary Eclipse Varian spectrofluorometer (Agilent, St. Clara, CA, USA) equipped with a temperature controller and a 1.0 cm quartz multicell holder. The fluorescence emission spectra ($\lambda_{\text{ex}} = 490\text{ nm}$) of DOX and 4-pep–DOX (1.94 μM) were recorded from 510 to 690 nm in the absence and presence of increasing concentrations of dsDNA, up to 75 nM. In the performed fluorescence titration experiments, 2 mL of DOX and 4-pep–DOX at 1.94 μM were titrated with fifteen 1 μL aliquots of dsDNA solution at 10 μM . The intensity of the band at 594 nm (corresponding to the maximum emission of both, DOX and its analogue 4-pep–DOX) was used to calculate the association constants (K_A) and other parameters. Time-resolved fluorescence measurements were performed with a FluoTime 300 high performance fluorescence lifetime spectrometer (PicoQuant, Berlin, Germany) at $20\text{ }^{\circ}\text{C}$. The excitation source was a pulsed LED of the PLS series ($\lambda_{\text{ex}} = 420\text{ nm}$). The fluorescence lifetimes of both DOX and 4-pep–DOX (5 μM) were measured in the absence and presence of variable concentrations of dsDNA (0.05 μM ,

0.10 μM , 0.15 μM , 0.20 μM , and 0.25 μM). After each added portion of dsDNA, the studied solution was gently stirred, and the fluorescence lifetime was measured at the wavelength corresponding to the maximum of the fluorophore emission ($\lambda_{\text{em}} = 594 \text{ nm}$).

3.2.7. Isothermal Titration Calorimetry

All ITC experiments were performed at 25 °C using an AutoITC isothermal titration calorimeter (MicroCal Inc. GE Healthcare, Northampton, MA, USA). The details of the measuring devices and experimental setup have been described previously [45]. The reagents (DOX, 4-pep-DOX, and dsDNA) were dissolved directly in 10 mM Tris-HCl buffer solution (pH 7.2). The experiment comprised injections of 10.02 μL (29 injections, 2 μL for the first injection only) of the buffered solution of DOX (0.174 mM) or 4-pep-DOX (0.470 mM) into the reaction cell, which initially contained the buffered solution of dsDNA (0.002 mM or 0.005 mM, respectively). For each experiment, a blank was performed by injecting the titrant solution into the cell filled with the buffer only. This blank was subtracted from the corresponding titration to account for the heat of dilution. All solutions were degassed prior to the titration. The titrant was injected at approximately 4 min intervals to ensure that the titration peak returned to the baseline before the next injection. Each injection lasted 20 s. To ensure a homogeneous mixing in the cell, the stirrer speed was kept constant at 300 rpm. Calibration of the AutoITC calorimeter was carried out using electrically generated heat pulses. The CaCl_2 -EDTA titration was performed to check the apparatus and the results (n -stoichiometry, K , ΔH) were compared with those obtained for the same samples (a test kit) at MicroCal Inc./Malvern Instruments (Malvern, UK).

3.2.8. Molecular Dynamics Simulations

All simulated systems were built on the basis of the crystal structure of the doxorubicin-dsDNA complex (PDB id 1D12) [46]. Initial coordinates of a 20-bp long dsDNA helix with 5'-CGT ACG CGT ACG CGT ACG CG-3' sequence were generated by removing the two base pairs at the 3'-end of dsDNA in the crystal structure, and then the appropriate extension of the structure at the 5' and 3' ends by using the X3DNA program [47]. The obtained dsDNA-drug complexes were solvated with 13,947 TIP3P water molecules in a dodecahedral box with a cell vector length of 8.5 nm, at physiological ionic strength (150 mM NaCl) [48]. The Amber parmbsc1 force field was used for dsDNA and ions [49]. The force field parameters for DOX and the tetrapeptide fragment of 4-pep-DOX were taken from the General Amber Force Field (GAFF) and directly from Amber, respectively [50]. Partial charges for both ligands were obtained from HF calculations in Gaussian via Merz-Kollman ESP fitting, using the 6-31G* basis set [51]. The MD simulations were performed using Gromacs 5.0.4 in the NPT ensemble, with the temperature kept at 25 °C and using the v-rescale thermostat with the pressure kept at 1 bar using a Parrinello-Rahman barostat [52–54]. Periodic boundary conditions were applied in 3D, and the electrostatic interactions were calculated using the particle mesh Ewald (PME) method with a real-space cut-off of 1.2 nm and a Fourier grid spacing of 0.12 nm [55]. A cut-off of 1.2 nm was used for Lennard-Jones interactions. All bond lengths were constrained using P-LINCS for dsDNA and SETTLE for water [56,57]. The equations of motion were integrated using the leap-frog algorithm with a 2 fs time step.

To study the relative stability of the complexes formed by DOX and 4-pep-DOX with dsDNA duplex in two different intercalation modes (with the amino sugar extending into either the minor or major groove), we calculated the corresponding free energy profiles using replica-exchange umbrella sampling (REUS). The calculations were carried out using the PLUMED 2.0 plugin coupled to Gromacs [58]. To generate the initial configurations for the REUS simulations, we first performed short equilibrium simulations (150 ns) of the DOX and 4-pep-DOX, initially intercalated at a CpG step of dsDNA, in either a minor- or major-groove mode. In the former case, the initial configuration of the DOX \cdots dsDNA intercalation complex was taken directly from the crystal structure and the 4-pep-DOX \cdots dsDNA complex was then obtained by attaching the tetrapeptide moiety to the amino group of DOX. In the latter case, the orientation of both intercalators was manually inverted within the

same intercalation site. To obtain the dissociated states for the so-prepared four systems, we ran steered MD (SMD) simulations, in which the ligands were pulled away from dsDNA during 100 ns using a moving harmonic potential with a force constant of 286.1 kcal/(mol·nm²) applied to the coordinate, defined as the separation distance between the centers of mass of the two base pairs forming the intercalation site and the planar chromophore of DOX and 4-pep-DOX (*r* vector in Figure 10A).

Next, from SMD trajectories, we generated 21 uniformly distributed 0.2 nm separated REUS windows. In each of these windows, the systems were simulated for 0.5 μs using the harmonic potential with a force constant of 143.05 kcal/(mol·nm²) to restrain the system along the reaction coordinate *r*. In addition, we used one-sided harmonic potentials with a force constant of 286.1 kcal/(mol·nm²), turning on below 1.2 nm to prevent ligands binding at the dsDNA ends (grey dashed lines in Figure 10A). The exchanges between neighboring windows were attempted every 2 ps, and the acceptance rate turned out to be 19 %. The free energy profiles were determined from the last 450 ns of the thus obtained trajectories using the standard weighted histogram analysis method [59]. All molecular images were created using VMD 1.9.2 (University of Illinois, Urbana, IL, USA) [60].

4. Conclusions

In this work, we successfully synthesized the tetrapeptide-DOX (4-pep-DOX) adduct as a product of octapeptide cleavage by MMPs, for extensive investigation of the parameters that are critical in forming a 4-pep-DOX ··· dsDNA complex. The experimental and theoretical studies demonstrated that the presence of tetrapeptide does not affect the overall tendency of DOX to intercalate into dsDNA, but rather changes its binding mode. While the main mode of action of DOX has been attributed to its intercalation from the minor groove of dsDNA, the binding of 4-pep-DOX primarily occurs from the major groove. Multifaceted binding modes for DOX and 4-pep-DOX highlight the important role of electrostatic and hydrophobic interactions between the negatively charged phosphate group on the groove surface and the peptide chain of 4-pep-DOX. Hence, these results demonstrate that the release of a free DOX from the MMP-cleaved intermediate product by intracellular non-specific proteases is probably not vital to the cytostatic action of the drug. We believe that the presented detailed explanation of the intercalation mechanism of 4-pep-DOX adduct can be useful for paving the way for the future design of peptide-DOX prodrugs.

Supplementary Materials: Supplementary materials can be found at <http://www.mdpi.com/1422-0067/21/18/6923/s1>.

Author Contributions: Conceptualization, K.B., J.R. and J.P.; Formal Analysis, K.B., K.Ż., M.K., W.K., D.W., W.W., J.R., J.C. and J.P.; Investigation, K.B., K.Ż., M.K., W.K. and D.W.; Funding acquisition, J.R. and J.P.; Writing—original draft, K.B., K.Ż., M.K., W.K. and D.W.; Writing—review and editing, J.R., J.C. and J.P.; Supervision, J.R. and J.P.; Project administration, K.B. All authors have read and agreed to the published version of the manuscript.

Funding: This work was supported by the Polish Ministry of Science and Higher Education under Grant Nos. DS 531-T080-D494-20 (J.R.) and DS 531-M045-D788-19 (J.P.). This research was supported in part by PL-Grid Infrastructure.

Acknowledgments: We wish to thank the Academic Computer Centre in Gdańsk, Poland, for granting CPU time. This research was supported in part by PL-Grid Infrastructure.

Conflicts of Interest: The authors declare no conflict of interest.

Abbreviations

DOX	Doxorubicin
MMPs	Matrix metalloproteinases
MD	Molecular dynamics
ITC	Isothermal titration calorimetry

References

- Bray, F.; Ferlay, J.; Soerjomataram, I.; Siegel, R.L.; Torre, L.A.; Jemal, A. Global cancer statistics 2018: GLOBOCAN estimates of incidence and mortality worldwide for 36 cancers in 185 countries. *CA Cancer J. Clin.* **2018**, *68*, 394–424. [[CrossRef](#)] [[PubMed](#)]
- Tavan, H.; Azadi, A.; Veisani, Y. Return to work in cancer patients: A systematic review and meta-analysis. *Indian J. Palliat. Care* **2019**, *25*, 147–152. [[PubMed](#)]
- Gewirtz, D.A. A critical evaluation of the mechanisms of action proposed for the antitumor effects of the anthracycline antibiotics adriamycin and daunorubicin. *Biochem. Pharm.* **1999**, *57*, 727–741. [[CrossRef](#)]
- Petrioli, R.; Fiaschi, A.I.; Francini, E.; Pascucci, A.; Francini, G. The role of doxorubicin and epirubicin in the treatment of patients with metastatic hormone-refractory prostate cancer. *Cancer Treat. Rev.* **2008**, *34*, 710–718. [[CrossRef](#)] [[PubMed](#)]
- Arcamone, F. *Doxorubicin: Anticancer Antibiotics*; Academic Press: New York, NY, USA, 1981.
- Minotti, G.; Menna, P.; Salvatorelli, E.; Cairo, G.; Gianni, L. Anthracyclines: Molecular advances and pharmacology developments in antitumor activity and cardiotoxicity. *Pharm. Rev.* **2004**, *56*, 185–229. [[CrossRef](#)] [[PubMed](#)]
- Binaschi, M.; Capranico, G.; Dal Bo, L.; Zunino, F. Relationship between lethal effects and topoisomerase II-mediated double-stranded DNA breaks produced by anthracyclines with different sequence specificity. *Mol. Pharm.* **1997**, *51*, 1053–1059. [[CrossRef](#)]
- Feinstein, E.; Canaani, E.; Weiner, L.M. Dependence of nucleic acid degradation on in situ free-radical production by adriamycin. *Biochemistry* **1993**, *32*, 13156–13161. [[CrossRef](#)]
- Tewey, K.M.; Rowe, T.C.; Yang, L.; Halligan, B.D.; Liu, L.F. Adriamycin-induced DNA damage mediated by mammalian DNA topoisomerase II. *Science* **1984**, *226*, 466–468. [[CrossRef](#)]
- Cutts, S.M.; Parsons, P.G.; Sturm, R.A.; Phillips, D.R. Adriamycin-induced DNA adducts inhibit the DNA interactions of transcription factors and RNA polymerase. *J. Biol. Chem.* **1996**, *271*, 5422–5429. [[CrossRef](#)]
- Swain, S.M.; Whaley, F.S.; Ewer, M.S. Congestive heart failure in patients treated with doxorubicin: A retrospective analysis of three trials. *Cancer* **2003**, *97*, 2869–2879. [[CrossRef](#)]
- Bally, M.B.; Nayar, R.; Masin, D.; Cullis, P.R.; Mayer, L.D. Studies on the myelosuppressive activity of doxorubicin entrapped in liposomes. *Cancer Chemother. Pharm.* **1990**, *27*, 13–19. [[CrossRef](#)] [[PubMed](#)]
- Carvalho, C.; Santos, R.; Cardoso, S.; Correia, S.; Oliveira, P.; Santos, M.; Moreira, P. Doxorubicin: The good, the bad and the ugly effect. *Curr. Med. Chem.* **2009**, *16*, 3267–3285. [[CrossRef](#)] [[PubMed](#)]
- Kalepu, S.; Nekkanti, V. Insoluble drug delivery strategies: Review of recent advances and business prospects. *Acta Pharm. Sin. B* **2015**, *5*, 442–453. [[CrossRef](#)] [[PubMed](#)]
- Singh, S.K.; Singh, S.; Willard, J.; Singh, R. Drug delivery approaches for breast cancer. *Int. J. Nanomed.* **2017**, *12*, 6205–6218. [[CrossRef](#)] [[PubMed](#)]
- Rudra, A.; Li, J.; Shakur, R.; Bhagchandani, S.; Langer, R. Trends in therapeutic conjugates: Bench to clinic. *Bioconjug. Chem.* **2020**, *31*, 462–473. [[CrossRef](#)]
- Janssen, M.; Mihov, G.; Welting, T.; Thies, J.; Emans, P. Drugs and polymers for delivery systems in OA joints: Clinical needs and opportunities. *Polymers* **2014**, *6*, 799–819. [[CrossRef](#)]
- Milton Harris, J.; Chess, R.B. Effect of pegylation on pharmaceuticals. *Nat. Rev. Drug Discov.* **2003**, *2*, 214–221. [[CrossRef](#)]
- Yoo, H.S.; Park, T.G. Biodegradable polymeric micelles composed of doxorubicin conjugated PLGA-PEG block copolymer. *J. Control. Release* **2001**, *70*, 63–70. [[CrossRef](#)]
- Maeda, H.; Khatami, M. Analyses of repeated failures in cancer therapy for solid tumors: Poor tumor-selective drug delivery, low therapeutic efficacy and unsustainable costs. *Clin. Transl. Med.* **2018**, *7*, 1–20. [[CrossRef](#)]
- Cathcart, J.; Pulkoski-Gross, A.; Cao, J. Targeting matrix metalloproteinases in cancer: Bringing new life to old ideas. *Genes Dis.* **2015**, *2*, 26–34. [[CrossRef](#)]
- Vihinen, P.; Kähäri, V.M. Matrix metalloproteinases in cancer: Prognostic markers and therapeutic targets. *Int. J. Cancer* **2002**, *99*, 157–166. [[CrossRef](#)] [[PubMed](#)]
- Egeblad, M.; Werb, Z. New functions for the matrix metalloproteinases in cancer progression. *Nat. Rev. Cancer* **2002**, *2*, 161–174. [[CrossRef](#)] [[PubMed](#)]
- You, Y.; Xu, Z.; Chen, Y. Doxorubicin conjugated with a trastuzumab epitope and an MMP-2 sensitive peptide linker for the treatment of HER2-positive breast cancer. *Drug Deliv.* **2018**, *25*, 448–460. [[CrossRef](#)] [[PubMed](#)]

25. Zhu, L.; Wang, T.; Perche, F.; Taigind, A.; Torchilin, V.P. Enhanced anticancer activity of nanopreparation containing an MMP2-sensitive PEG-drug conjugate and cell-penetrating moiety. *Proc. Natl. Acad. Sci. USA* **2013**, *110*, 17047–17052. [[CrossRef](#)]
26. Zhang, J.; Yuan, Z.F.; Wang, Y.; Chen, W.H.; Luo, G.F.; Cheng, S.X.; Zhuo, R.X.; Zhang, X.Z. Multifunctional envelope-type mesoporous silica nanoparticles for tumor-triggered targeting drug delivery. *J. Am. Chem. Soc.* **2013**, *135*, 5068–5073. [[CrossRef](#)]
27. Bacinello, D.; Garanger, E.; Taton, D.; Tam, K.C.; Lecommandoux, S. Enzyme-degradable self-assembled nanostructures from polymer-peptide hybrids. *Biomacromolecules* **2014**, *15*, 1882–1888. [[CrossRef](#)]
28. Lee, G.Y.; Park, K.; Kim, S.Y.; Byun, Y. MMPs-specific PEGylated peptide-DOX conjugate micelles that can contain free doxorubicin. *Eur. J. Pharm. Biopharm.* **2007**, *67*, 646–654. [[CrossRef](#)]
29. Kratz, F.; Müller, I.A.; Ryppa, C.; Warnecke, A. Prodrug strategies in anticancer chemotherapy. *ChemMedChem* **2008**, *3*, 20–53. [[CrossRef](#)]
30. Mansour, A.M.; Dreves, J.; Esser, N.; Hamada, F.M.; Badary, O.A.; Unger, C.; Fichtner, I.; Kratz, F. A new approach for the treatment of malignant melanoma: Enhanced antitumor efficacy of an albumin-binding doxorubicin prodrug that is cleaved by matrix metalloproteinase 2. *Cancer Res.* **2003**, *63*, 4062–4066.
31. Guarnieri, D.; Biondi, M.; Yu, H.; Belli, V.; Falanga, A.P.; Cantisani, M.; Galdiero, S.; Netti, P.A. Tumor-activated prodrug (TAP)-conjugated nanoparticles with cleavable domains for safe doxorubicin delivery. *Biotechnol. Bioeng.* **2015**, *112*, 601–611. [[CrossRef](#)]
32. Jiang, T.; Olson, E.S.; Nguyen, Q.T.; Roy, M.; Jennings, P.A.; Tsien, R.Y. Tumor imaging by means of proteolytic activation of cell-penetrating peptides. *Proc. Natl. Acad. Sci. USA* **2004**, *101*, 17867–17872. [[CrossRef](#)] [[PubMed](#)]
33. Wang, H.X.; Yang, X.Z.; Sun, C.Y.; Mao, C.Q.; Zhu, Y.H.; Wang, J. Matrix metalloproteinase 2-responsive micelle for siRNA delivery. *Biomaterials* **2014**, *35*, 7622–7634. [[CrossRef](#)] [[PubMed](#)]
34. Ralhan, K.; KrishnaKumar, V.G.; Gupta, S. Piperazine and DBU: A safer alternative for rapid and efficient Fmoc deprotection in solid phase peptide synthesis. *RSC Adv.* **2015**, *5*, 104417–104425. [[CrossRef](#)]
35. Fields, G.B. Methods for removing the Fmoc group. *Methods Mol. Biol.* **1994**, *35*, 17–27. [[PubMed](#)]
36. Eftink, M.R.; Ghiron, C.A. Fluorescence quenching studies with proteins. *Anal. Biochem.* **1981**, *114*, 199–227. [[CrossRef](#)]
37. Ware, W.R. Oxygen quenching of fluorescence in solution: An experimental study of the diffusion process. *J. Phys. Chem.* **1962**, *66*, 455–458. [[CrossRef](#)]
38. Xiang, G.; Tong, C.; Lin, H. Nitroaniline isomers interaction with bovine serum albumin and toxicological implications. *J. Fluoresc.* **2007**, *17*, 512–521. [[CrossRef](#)]
39. Congdon, R.W.; Muth, G.W.; Splittgerber, A.G. The binding interaction of coomassie blue with proteins. *Anal. Biochem.* **1993**, *213*, 407–413. [[CrossRef](#)]
40. Dai, X.; Yue, Z.; Eccleston, M.E.; Swartling, J.; Slater, N.K.H.; Kaminski, C.F. Fluorescence intensity and lifetime imaging of free and micellar-encapsulated doxorubicin in living cells. *Nanomed. Nanotechnol. Biol. Med.* **2008**, *4*, 49–56. [[CrossRef](#)]
41. Chaires, J.B. A thermodynamic signature for drug-DNA binding mode. *Arch. Biochem. Biophys.* **2006**, *453*, 26–31. [[CrossRef](#)]
42. Beauchamp, K.A.; Bowman, G.R.; Lane, T.J.; Maibaum, L.; Haque, I.S.; Pande, V.S. MSMBuilder2: Modelling conformational dynamics on the picosecond to millisecond scale. *J. Chem. Theory Comput.* **2011**, *7*, 3412–3419. [[CrossRef](#)] [[PubMed](#)]
43. Shi, N.Q.; Gao, W.; Xiang, B.; Qi, X.R. Enhancing cellular uptake of activable cell-penetrating peptide-doxorubicin conjugate by enzymatic cleavage. *Int. J. Nanomed.* **2012**, *7*, 1613–1621.
44. Munnier, E.; Cohen-Jonathan, S.; Linassier, C.; Douziech-Eyrolles, L.; Marchais, H.; Soucé, M.; Hervé, K.; Dubois, P.; Chourpa, I. Novel method of doxorubicin-SPION reversible association for magnetic drug targeting. *Int. J. Pharm.* **2008**, *363*, 170–176. [[CrossRef](#)] [[PubMed](#)]
45. Panuszko, A.; Bruździak, P.; Zielkiewicz, J.; Wyrzykowski, D.; Stangret, J. Effects of urea and trimethylamine-N-oxide on the properties of water and the secondary structure of hen egg white lysozyme. *J. Phys. Chem. B* **2009**, *113*, 14797–14809. [[CrossRef](#)] [[PubMed](#)]
46. Frederick, C.A.; Dean Williams, L.; Ughetto, G.; van der Marel, G.A.; van Boom, H.-J.; Rich, A.; Wang, A.H.-J. Structural comparison of anticancer drug-DNA complexes: Adriamycin and daunomycin. *Biochemistry* **1990**, *29*, 2538–2549. [[CrossRef](#)]

47. Lu, X.-J.; Olson, W.K. 3DNA: A software package for the analysis, rebuilding and visualisation of three-dimensional nucleic acid structures. *Nucl. Acids Res.* **2003**, *31*, 5108–5121. [[CrossRef](#)] [[PubMed](#)]
48. Jorgensen, W.L.; Chandrasekhar, J.; Madura, J.D.; Impey, R.W.; Klein, M.L. Comparison of simple potential functions for simulating liquid water. *J. Chem. Phys.* **1983**, *79*, 926–935. [[CrossRef](#)]
49. Ivani, I.; Dans, P.D.; Noy, A.; Pérez, A.; Faustino, I.; Hospital, A.; Walther, J.; Andrio, P.; Goñi, R.; Balaceanu, A.; et al. Parmbsc1: A refined force field for DNA simulations. *Nat. Methods* **2015**, *13*, 55–58. [[CrossRef](#)]
50. Wang, J.; Wang, W.; Kollman, P.A.; Case, D.A. Automatic atom type and bond type perception in molecular mechanical calculations. *J. Mol. Graph. Model.* **2006**, *25*, 247–260. [[CrossRef](#)]
51. Frisch, M.J.; Trucks, G.W.; Schlegel, H.B.; Scuseria, G.E.; Robb, M.A.; Cheeseman, J.R.; Scalmani, G.; Barone, V.; Petersson, G.A.; Nakatsuji, H.; et al. *Gaussian 09*; Software for Calculation; Gaussian, Inc.: Wallingford, CT, USA, 2016.
52. Hess, B.; Kutzner, C.; Van Der Spoel, D.; Lindahl, E. GROMACS 4: Algorithms for highly efficient, load-balanced, and scalable molecular simulation. *J. Chem. Theory Comput.* **2008**, *4*, 435–447. [[CrossRef](#)]
53. Parrinello, M.; Rahman, A. Polymorphic transitions in single crystals: A new molecular dynamics method. *J. Appl. Phys.* **1981**, *52*, 7182–7190. [[CrossRef](#)]
54. Bussi, G.; Donadio, D.; Parrinello, M. Canonical sampling through velocity rescaling. *J. Chem. Phys.* **2007**, *126*, 014101. [[CrossRef](#)] [[PubMed](#)]
55. Darden, T.; York, D.; Pedersen, L. Particle mesh Ewald: An N-log(N) method for Ewald sums in large systems. *J. Chem. Phys.* **1993**, *98*, 10089–10092. [[CrossRef](#)]
56. Hess, B. P-LINCS: A parallel linear constraint solver for molecular simulation. *J. Chem. Theory Comput.* **2008**, *4*, 116–122. [[CrossRef](#)] [[PubMed](#)]
57. Miyamoto, S.; Kollman, P.A. Settle: An analytical version of the SHAKE and RATTLE algorithm for rigid water models. *J. Comput. Chem.* **1992**, *13*, 952–962. [[CrossRef](#)]
58. Bonomi, M.; Branduardi, D.; Bussi, G.; Camilloni, C.; Provasi, D.; Raiteri, P.; Donadio, D.; Marinelli, F.; Pietrucci, F.; Broglia, R.A.; et al. PLUMED: A portable plugin for free-energy calculations with molecular dynamics. *Comput. Phys. Commun.* **2009**, *180*, 1961–1972. [[CrossRef](#)]
59. Kumar, S.; Rosenberg, J.M.; Bouzida, D.; Swendsen, R.H.; Kollman, P.A. Multidimensional free-energy calculations using the weighted histogram analysis method. *J. Comput. Chem.* **1995**, *16*, 1339–1350. [[CrossRef](#)]
60. Humphrey, W.; Dalke, A.; Schulten, K. VMD: Visual molecular dynamics. *J. Mol. Graph.* **1996**, *14*, 33–38. [[CrossRef](#)]



© 2020 by the authors. Licensee MDPI, Basel, Switzerland. This article is an open access article distributed under the terms and conditions of the Creative Commons Attribution (CC BY) license (<http://creativecommons.org/licenses/by/4.0/>).

The product of matrix metalloproteinase cleavage of doxorubicin conjugate for anticancer drug delivery. Calorimetric, spectroscopic and molecular dynamics studies on peptide–doxorubicin binding to DNA

Kamila Butowska ^{1,2,*}, Krzysztof Żamojć ³, Mateusz Kogut ⁴, Witold Kozak ², Dariusz Wyrzykowski ³, Wiesław Wiczek ⁵, Jacek Czub ⁴, Jacek Piosik ¹ and Janusz Rak ²

¹ Laboratory of Biophysics, Intercollegiate Faculty of Biotechnology University of Gdańsk and Medical University of Gdańsk, Abrahama 58, 80-307 Gdańsk; kamila.butowska@phdstud.ug.edu.pl (K.B.); jacek.piosik@biotech.ug.edu.pl (J.P.)

² Department of Physical Chemistry, Faculty of Chemistry, University of Gdańsk, Wita Stwosza 63, 80-308 Gdańsk; davelombardo@wp.pl (W.K.); janusz.rak@ug.edu.pl (J.R.)

³ Department on General and Inorganic Chemistry, Faculty of Chemistry, University of Gdańsk, Wita Stwosza 63, 80-308 Gdańsk; krzysztof.zamojc@ug.edu.pl (K.Z.); dariusz.wyrzykowski@ug.edu.pl (D.W.)

⁴ Department of Physical Chemistry, Faculty of Chemistry, Gdańsk University of Technology, Narutowicza 11/12, 80-233 Gdańsk; giggsmk@op.pl (M.K.); jacek.czub@pg.edu.pl (J.C.)

⁵ Department of Biomedical Chemistry, Faculty of Chemistry, University of Gdańsk, Wita Stwosza 63, 80-308 Gdańsk; wieslaw.wiczek@ug.edu.pl (W.W.)

* Correspondence: kamila.butowska@phdstud.ug.edu.pl; Tel.: +48 58 523 6310

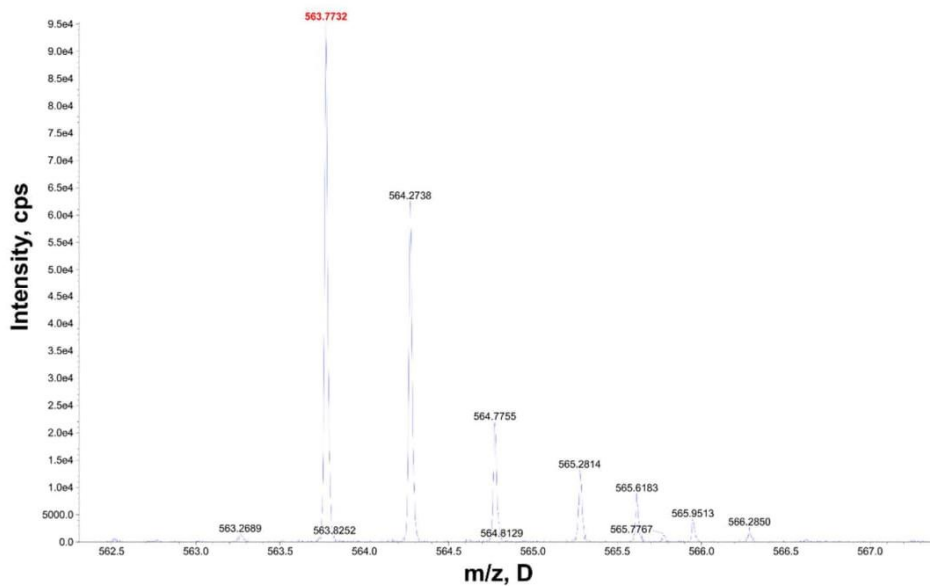


Figure S1. MALDI-TOF mass spectrum of Fmoc-Gly-Pro-Leu-Gly in a positive mode (m/z 563.7732).

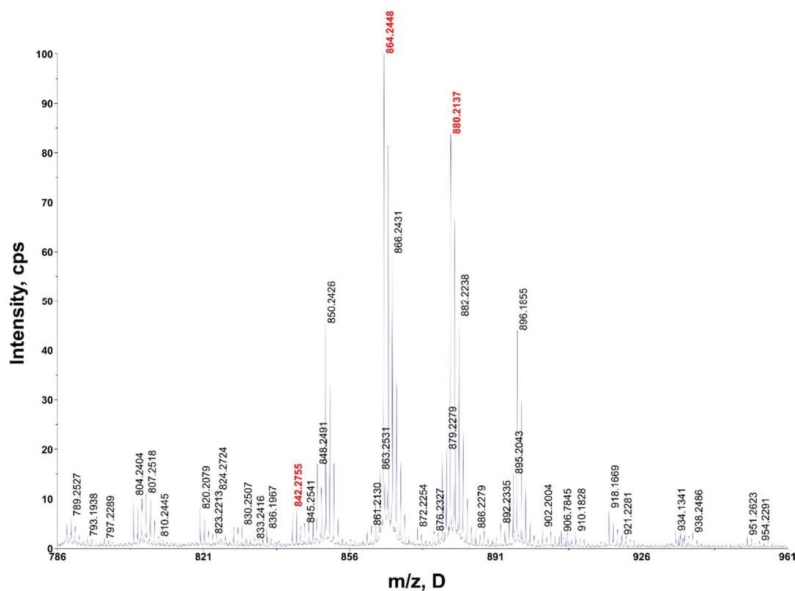


Figure S2. MALDI-TOF spectrum of Leu-Ala-Gly-Gly-DOX in a positive mode [(Leu-Ala-Gly-Gly-DOX + H⁺) m/z 842.2755; (Leu-Ala-Gly-Gly-DOX + Na⁺) m/z 864.2448; (Leu-Ala-Gly-Gly-DOX + K⁺) m/z 880.2137].

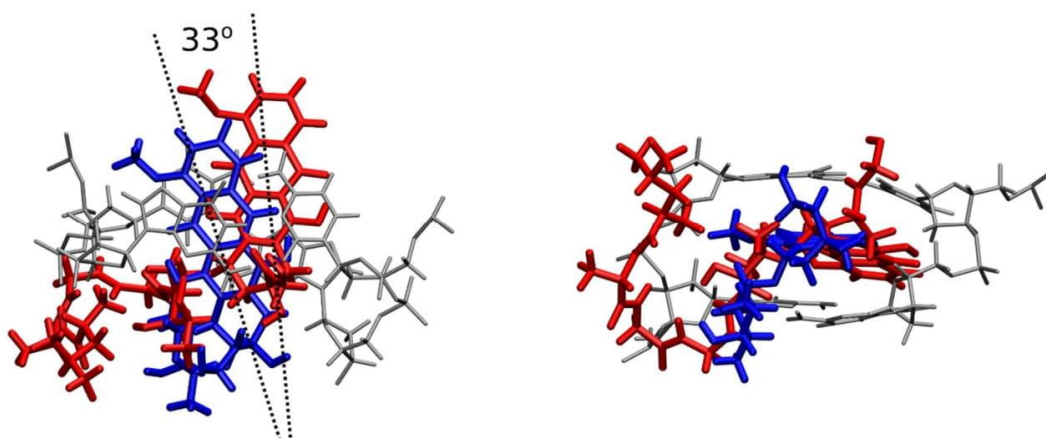


Figure S3. Comparison of the minor groove intercalation modes of DOX (blue) and 4-pep-DOX (red) – top view (left), side view (right). When intercalated from the minor groove, 4-pep-DOX is rotated by ca. 33deg with respect to the flanking base pairs, compared to DOX.

3. **K. Butowska**, W. Kozak, M. Kogut, Z. Pietralik-Molińska, A. Moliński, K. Kitowska, M. Kozak, J. Czub, R. Sądej, J. Rak, J. Piosik, *MMPs-sensitive release of doxorubicin as a strategy for cancer targeted therapy*. *Materials*, **2021** [P3]

MMPs-sensitive release of doxorubicin as a strategy for cancer targeted therapy

Kamila Butowska,^{*1,2} Witold Kozak,² Mateusz Kogut,³ Zuzanna Pietralik-Molińska,⁴ Augustyn Moliński,^{4,7} Kamila Kitowska,⁵ Maciej Kozak,⁴ Jacek Czub,⁶ Rafał Sądej,⁵ Janusz Rak,² and Jacek Piosik^{*1}

- ¹ Laboratory of Biophysics, Intercollegiate Faculty of Biotechnology, University of Gdańsk and Medical University of Gdańsk, Abrahamowa 58, 80-307 Gdańsk, Poland; kamila.butowska@phdstud.ug.edu.pl (K.B.); jacek.piosik@biotech.ug.edu.pl (J.P.)
- ² Department of Physical Chemistry, Faculty of Chemistry, University of Gdańsk, Wita Stwosza 63, 80-308 Gdańsk, Poland; davelombardo@wp.pl (W.K.); janusz.rak@ug.edu.pl (J.R.)
- ³ Institute of Physics, Polish Academy of Sciences, Al. Lotników 32/46, 02-668 Warsaw, Poland
- ⁴ Department of Macromolecular Physics, Faculty of Physics, Adam Mickiewicz University in Poznań, Uniwersytetu Poznańskiego 2, 61-614 Poznań, Poland; zuzannap@amu.edu.pl (Z. P.-M.); augmol@amu.edu.pl (A. M.); mkozak@amu.edu.pl (M. K.)
- ⁵ Department of Molecular Enzymology and Oncology, Intercollegiate Faculty of Biotechnology, University of Gdańsk and Medical University of Gdańsk, Dębinki 1, 80-211, Gdańsk, Poland; kkitowska@gumed.edu.pl (K. K.); rafal.sadej@gumed.edu.pl (R. S.)
- ⁶ Department of Physical Chemistry, Faculty of Chemistry, Gdańsk University of Technology, Narutowicza 11/12, 80-233 Gdańsk, Poland; giggsmk@op.pl (M.K.); jacek.czub@pg.edu.pl (J.C.)
- ⁷ NanoBioMedical Centre, Adam Mickiewicz University in Poznań, Wszechnicy Pastowskiej 3, 61-614 Poznań, Poland

* Correspondence: jacek.piosik@biotech.ug.edu.pl; kamila.butowska@phdstud.ug.edu.pl;

Citation: Lastname, F.; Lastname, F.; Lastname, F. Title. *Pharmaceutics* **2021**, *13*, x. <https://doi.org/10.3390/xxxxx>

Academic Editor: Firstname Lastname

Received: date
Accepted: date
Published: date

Publisher's Note: MDPI stays neutral with regard to jurisdictional claims in published maps and institutional affiliations.



Copyright: © 2021 by the authors. Submitted for possible open access publication under the terms and conditions of the Creative Commons Attribution (CC BY) license (<https://creativecommons.org/licenses/by/4.0/>).

Abstract: Doxorubicin (DOX) exhibits an exceptional therapeutic effect in different cancer therapies, but severe side effects, like cardiomyopathy or nephropathy still limit the usage of this anthracycline. In the last few decades increasing attention has been paid to solve these problems, as well as to improve the specificity of DOX by targeted drug delivery. One of the approaches is the enzyme-sensitive release strategy to enhance DOX delivery into cancer cells which overexpressed specific enzymes, e.g., matrix metalloproteinases (MMPs). In the present study, a PEG-pep-DOX carrier has been synthesized using poly(ethylene glycol) (PEG) and the MMPs-sensitive octapeptide moiety (pep) conjugated with DOX. Using atomic force microscopy and molecular dynamics simulation, the PEG-pep-DOX conjugate were found to create fibril-like aggregates. The theoretical results indicate that the dimer, tetramer, and octamer of the conjugate have a tendency to form linear structures, as a result of favorable octapeptide-DOX and octapeptide-octapeptide interactions. *In vitro* studies demonstrate that PEG-pep-DOX exhibits moderate toxicity against the cell lines with MMPs overexpression compared to the cell line that does not overexpress the enzyme. Based on these findings, we suggest thus that it is possible to use the PEG-pep-DOX carrier to deliver DOX despite its aggregation effects. However, for efficient drug release, the concentration of MMPs has to be higher than in our *in vitro* studies.

Keywords: doxorubicin; matrix metalloproteinases; drug delivery

1. Introduction

Over the past decades, stimuli-responsive polymers and nanoparticles have been widely investigated as potential drug delivery systems (DDSs) [1,2]. Indeed, DDSs in response to a specific stimulus (light, temperature or pH change) may release drug in

desired target [3,4]. Additionally, DDSs can be modified by a substrate motif recognized by enzymes, like phospholipases, glycosidases and proteases [5-7]. The improvements achieved by incorporating substrate peptide sequence into nanoparticles or by conjugating it with different polymers are desirable for the delivery of known but toxic drugs [8]. This concept is called a prodrug approach, and uses inert precursors (e.g., DDSs) which undergo enzymatic degradation in the targeted site and release a pharmacologically active drug or generate it by structural transformation [9,10].

Numerous studies have shown that dendrimers, micelles and liposomes, polymersomes and polymer-drug conjugates can be used as effective enzyme-sensitive DDSs [11-14]. Comparing to free drug molecules, DDSs can enhance permeability and retention effect, therefore avoiding non-specific drug administration in healthy tissues [15]. Moreover, their biocompatibility and improved pharmacokinetics prompted the approval of some DDSs by US Food and Drug Administration (FDA) while many are under evaluation in clinical trials [16,17]. There is many responsive DDSs, which have been transitioned from preclinical animal studies to clinical trials [18]. For example, the ThermoDOxs undergoing Phase III clinical trial against different types of cancer, such as breast or liver cancer, as a thermo-sensitive liposome for efficient DOX release [19]. Moreover, a promising and the most advance enzyme-activated polymeric nanoparticle, called Opaxio, have entered Phase III clinical trial in the treatment of ovarian cancer and non-small lung cancer [20]. As mentioned above, responsive DDSs have shown great potential in a broad range clinical trials and further applications. Nowadays, studies of DDSs are well documented, it is also well acknowledged that proteases are extremely useful to improve prodrug potency and selectivity [21,22].

One of the most extensively investigated proteases are matrix metalloproteinases (MMPs) that belong to zinc-dependent endopeptidases and are involved in various pathological processes including cancer progression and metastasis [23-25]. The overexpression of MMPs is observed in many types of human carcinomas like breast, head and neck cancers, or fibrosarcoma. The major members of the MMPs family are MMP-2 and MMP-9 (gelatinase A and gelatinase B, respectively), known from their ability to remodel extracellular matrix, basement membrane degradation and angiogenesis [26-28]. Commonly, cancer patients are treated with many different drugs like mitotic inhibitors (paclitaxel), alkylating agents (streptozocin) or DNA-intercalating agents (doxorubicin, DOX) [29]. DOX has proven successful in the treatment of hematological malignancies, including Kaposi's sarcoma, lymphomas, as well as solid tumors, e.g., ovarian and breast cancers. Despite its clinical application, DOX exhibited many side effects, such as cardiomyopathy, bone marrow aplasia and hepatotoxicity [30]. In order to reduce those toxic effects and achieve targetability and better tumor penetration, DOX has been incorporated in a wide spectrum of DDSs sensitive to MMPs [31-35].

The objective of the present work was to develop an MMP-2/-9 sensitive poly(ethylene glycol) (PEG) carrier for a controlled DOX release. The Gly-Pro-Leu-Gly-Leu-Ala-Gly-Gly (GPLGLAGG) octapeptide sequence was selected as an MMP-2/-9-sensitive moiety. In our previous study, we showed that the proposed octapeptide is recognized by MMP-2/-9 and is cleaved between glycine and leucine in a time-dependent manner [36]. Herein, the GPLGLAGG peptide was conjugated with DOX and PEG through the mixed anhydride coupling reaction, giving a symmetric carrier (PEG-pep-DOX). Next, PEG-pep-DOX was characterized using zeta-potential (ζ potential) measurements and atomic force microscopy (AFM). The AFM images showed individual particles with a height of 3 nm, and many fibrillar aggregates. The cross-section profiles analysis of the aggregates has suggested that the height values of fibrils were the multiple of the height of a single molecule. To determine the formation mechanism of the observed PEG-pep-DOX aggregates, we performed molecular dynamics (MD) simulations. Additionally, the biological activity and cellular uptake of PEG-pep-DOX were investigated using the 3-[4,5-dimethylthiazole-2-yl]-2,5-diphenyltetrazolium bromide (MTT) assay. These proof-of-concept studies provided that PEG-pep-DOX biological effects despite its aggregation. Further work to

develop an efficient DOX delivery via MMPs-sensitive symmetric carriers is however required.

2. Materials and Methods

2.1. Materials

Fmoc-Gly-Pro-Leu-Gly-Leu-Ala-Gly-Gly peptide were obtained on solid support using Fmoc strategy was purchased from Lipopharm.pl (Zblewo, Poland). Acetonitrile (ACN), 4,6-diamidino-2-phenylindole 3-(4,5-Dimethylthiazol-2-yl)-2,5-diphenyltetrazolium bromide (MTT), dichloromethane (DCM), *N,N*-dimethylformamide (DMF), dimethyl sulfoxide (DMSO), doxorubicin hydrochloride (DOX), ethanol, formic acid, isobutyl chloroformate (ClCOO*i*Bu), methanol, morpholine, tetrahydrofuran (THF), toluene, triethylamine (TEA), trifluoroacetic acid (TFA) were purchased from Sigma-Aldrich (St. Louis, MO, USA). Column chromatography was performed using silica gel NORMASIL 60 (40–63 mesh, VWR Chemicals, Radnor, PA, USA). Thin-layer chromatography was performed using silica plates, 60G, F254 (Sigma-Aldrich, St. Louis, MO, USA).

2.2. Cells

The human fibrosarcoma HT-1080, triple negative breast cancer MDA-MB-436, and luminal A breast cancer MCF-7 cell lines were purchased from American Type Culture Collection (ATCC, Manassas, VA, USA). Each cell line was maintained at 37 °C in a humidified atmosphere with 5% CO₂, passaged for a maximum of 3–4 months post resuscitation, and regularly tested for mycoplasma contamination. HT-1080, MDA-MB-436 and MCF-7 cell lines were cultured in DMEM medium (Corning, NY, USA) supplemented with 10% (v/v) fetal bovine serum (FBS) and 100 U/mL/100 µg/mL penicillin/streptomycin.

2.3. Synthesis of Fmoc-Gly-Pro-Leu-Gly-Leu-Ala-Gly-Gly-DOX 5

The solution of Fmoc-Gly-Pro-Leu-Gly-Leu-Ala-Gly-Gly (40 mg, 46.4 µmol) in DMF (4 mL) was prepared at room temperature (RT) and then cooled to –10 °C. After, isobutyl chloroformate (6.0 µL, 46.4 µmol) and TEA (6.5 µL, 46.4 µmol) were added and stirred for an additional 20 min. Next, a solution of DOX (obtained in an independent reaction of DOX hydrochloride (26.8 mg, 46.4 µmol) with TEA (6.5 µL, 46.4 µmol)) in DMF (1 mL)) was added to the reaction mixture. After 1 h of stirring at RT, DMF was evaporated azeotropically with toluene on a rotary evaporator (Heidolph Hei-VAP Gold 3, Heidolph, Schwabach, Germany). The raw Fmoc-Gly-Pro-Leu-Gly-Leu-Ala-Gly-Gly-DOX 6 was purified by preparative column chromatography, using CHCl₃: MeOH 15: 1 as an eluent, furnishing the desired product (57 mg) in an 88.6% yield.

2.4. Synthesis of Gly-Pro-Leu-Gly-Leu-Ala-Gly-Gly-DOX 7

To a stirred solution of Fmoc-Gly-Pro-Leu-Gly-Leu-Ala-Gly-Gly-DOX (57 mg, 41.1 µmol) in DMF (0.5 mL), morpholine (0.5 mL) was added. After 2 h of stirring, the mixture was neutralized with TFA (0.6 mL). Isolation of the raw product was performed on a semi-preparative HPLC System (Shimadzu, LC 20AD, Shimadzu, Canby, OR, USA) using a Gemini NX Column (5.0 µm, 10 × 150 mm) giving a crystalline solid (22 mg) in a 46% yield. The flow rate was set at 4.0 mL/min with the mobile phase consisting of solvent A (0.1% formic acid) and solvent B (100% ACN). The gradient was as follows: 0–15 min, 10–90% of solvent B; 15–20 min, 90% of solvent B.

2.5. Synthesis of PEG-pep-DOX 8

Isobutyl chloroformate (2.34 µL, 18.1 µmol) and TEA (2.54 µL, 18.1 µmol) were added to the cooled to –10 °C solution of 14,16-dioxo-4,7,10,13,17,20,23,26-octaoxonacosane-1,29-

dioic acid (4.4 mg, 8.6 μmol ; obtained in an independent synthesis, by treating bis(14,14-dimethyl-12-oxo-3,6,9,13-tetraoxapentadecyl malonate with TFA in DCM [37]) in DMF (3.1 mL). After 20 min of stirring, a DMF (0.5 mL) solution of Gly-Pro-Leu-Gly-Leu-Ala-Gly-Gly-DOX (20 mg, 17.2 μmol) was added to the reaction mixture and further stirred for 1 h at RT. DMF was evaporated azeotropically with toluene in a similar manner as the synthesis of compound. A semi-preparative HPLC System (Shimadzu, LC 20AD, Shimadzu, Canby, OR, USA) with a Gemini NX Column (5.0 μm , 10 \times 150 mm) was used to isolate the desired product (3 mg) in a 12.4% yield.

2.6. Mass spectrometry

MALDI-TOF/TOF mass spectrometry (MALDI TOF/TOF 5800, AB Sciex, Darmstadt, Germany) was used to confirm the chemical structure of the final compound **8**. The measurement was performed in a reflector positive ion mode using 2,5-dihydroxybenzoic acid as the MALDI matrix. Samples were prepared directly on a plate using a dried droplet preparation method (0.8 mL of an analyte solution was mixed with 0.8 mL of the matrix solution). MS spectra were acquired from 99 to 3008 m/z for a total of 1000 laser shots by a 1 kHz OptiBeam laser (AB Sciex, Darmstadt, Germany).

2.7. Zeta Potential

The zeta potential (ζ) of PEG-pep-DOX **8** was evaluated utilizing the Litesizer 500 particle size analyser (Anton Paar GmbH, Graz, Austria), with a semiconductor laser diode (40 mW, 658 nm). In this system, zeta potential measurements are based on Electrophoretic Light Scattering (ELS) with cmPALS technology. Zeta potential was calculated using relation of the measured electrophoretic mobility (μ_e) to the Smoluchowski equation: $\zeta = \mu_e \eta (\epsilon_{\text{rel}} \times \epsilon_0)^{-1}$, where ϵ_0 is a dielectric constant of vacuum (the vacuum permittivity), ϵ_{rel} and η are relative permittivity and viscosity of the studied solution sample, respectively. The PEG-pep-DOX stock solution was diluted with ethanol to a final volume of 1 mL and concentration of 50 mM. The sample measurements were performed in Omega Cuvettes (Anton Paar GmbH, Graz, Austria), in triplicate at RT.

2.8 Atomic Force Microscopy

Atomic force microscopy (AFM) measurements were performed using the NanoWizard IV AFM system (JPK Instruments, Berlin, Germany). PEG-pep-DOX samples were diluted at 1:10 and 1:100 using double-distilled water. 10 μL of sample solution was then deposited on a freshly cleaved mica surface, flushed with water, and slowly dried before visualization. AFM imaging was carried out in the air contact mode using a Tap150AI-G Soft Tapping Mode AFM silicon cantilevers with aluminum reflective coating (150 kHz, 5 N/m) (BudgetSensors®, Innovative Solutions Bulgaria Ltd., Sofia, Bulgaria). AFM images were visualized and analyzed using the Gwyddion software package (version 2.56) [38].

2.9. Molecular Dynamics Simulations

The study included simulations of four systems containing 1, 2, 4 and 8 molecules of PEG-pep-DOX. The initial structures of PEG-pep-DOX **8** were generated by Avogadro [39] and then uniformly placed in the simulation box using PACKMOL [41] to avoid close contacts. PEG-pep-DOX **8** molecules were solvated with TIP3P water [41] in a dodecahedral box (see details of systems in Tab S1), at physiological ionic strength (150 mM NaCl). The Amber force field was used for PEG-pep-DOX **8** and ions [42]. The force field parameters for the DOX and octapeptide moieties were taken from our previous studies [36] and directly from the Amber99sb, respectively [43]. Force field parameters for the poly(ethylene glycol) fragment were obtained from the General Amber Force Field (GAFF). Partial charges

for PEG and its connection to the peptide were calculated at the HF/6-31G* level of theory via Merz–Kollman ESP fitting, using Gaussian [44], consistently with the standard Amber procedure. All molecular dynamics (MD) simulations were performed using Gromacs 2018 package [45] in the NPT ensemble using the v-rescale thermostat [46], a reference temperature of 25 °C, and the Parrinello–Rahman barostat [47] while maintaining pressure at 1 bar. Periodic boundary conditions were applied in 3D. The particle mesh Ewald (PME) method [48] with a real-space cutoff of 1.2 nm and a Fourier grid spacing of 0.12 nm were used to account for long-range electrostatics. A cut-off of 1.2 nm was used for Lennard-Jones interactions. During the simulations, all bond lengths were constrained using the P-LINCS algorithm [49] for PEG-pep-DOX and SETTLE algorithm for water [50]. The equations of motion were integrated using the leap-frog algorithm with a 2 fs time step. For each of the four systems, we ran 5 independent 500 ns equilibrium simulations (with a total simulation time of 10 μ s).

2.10. Cytotoxicity assay

Cell viability was determined by the MTT colorimetric assay. HT-1080, MCF-7 and MDA-MB-436 cells were seeded in 96-well plates in triplicate at 2×10^3 cell/well (HT-1080 cell line), 10×10^3 cell/well (MDA MB 436) and 7×10^3 cell/well (MCF-7 cell line) with a final volume of 100 μ L of suitable medium and incubated overnight in a humidified atmosphere at 37 °C and 5% CO₂. The next day, cells were exposed to indicated concentrations of free DOX or PEG-pep-DOX **8** (concentrations equal to 0.1 and 1 μ M) for a period of 72 h. Concentrated stock solutions of tested compounds were prepared in DMSO/sterile water solution (< 0.5% of DMSO). Then, MTT stock solution was added to each well so that the final concentration of MTT in the medium was 0.5 mg/mL and incubated for 2 h. Afterwards, the medium was discarded and replaced by 100 μ L of DMSO to dissolve the formed crystals. Absorbance was measured at 590 nm using a microplate reader. The MTT assay was performed in triplicate for each cell line. Results were analyzed with the use of GraphPad Prism 5 software (San Diego, CA, USA). The statistical evaluation of treated samples was calculated using one-way analysis of variance (ANOVA) followed by Dunnett's multiple comparison test. Differences were considered significant at $\alpha < p$, $p = 0.05$.

3. Results

3.1. Synthesis

In order to synthesize the studied conjugate, we performed a three-step synthetic procedure (Fig. 1). In a first step, a Fmoc-protected peptide (no. 5 in Fig. 1) was coupled to a doxorubicin molecule in its neutral form (no. 2 in Fig. 1) in the presence of ClCO₂iBu and TEA by a mixed anhydride approach. A such obtained compound (no. 6 in Fig. 1) was subsequently deprotected in the presence of morpholine. Finally, a peptide-DOX conjugate (no. 7 in Fig. 1) was treated with 14,16-dioxo-4,7,10,13,17,20,23,26 octaoxonacosane-1,29-dioic (no. 4 in Fig. 1, obtained in an independent synthesis by treating bis(14,14-dimethyl-12-oxo-3,6,9,13-tetraoxapentadecyl) malonate with TFA in DCM [37]) using the mixed anhydride procedure again. PEG-pep-DOX (no. 8 in Fig. 1) was successfully isolated by HPLC in a low yield and identified by mass spectrometry. As was reported previously, in the MALDI ionization source, the doxorubicin moiety can lose the daunosamine, as well as the 1-oxo-2-hydroxyethyl fragment [51,52]. The identities of fragments are depicted below MALDI spectrum (Fig. S1 in Supplementary Information). The molecular ion A [$M + H^+ + Na^+$] of low intensity was observed (Fig. S1). Taking into account fragments B, C and D (Fig. S1), one can state that the molecule contains a doxorubicin moiety as well as the octapeptide and PEG fragments.

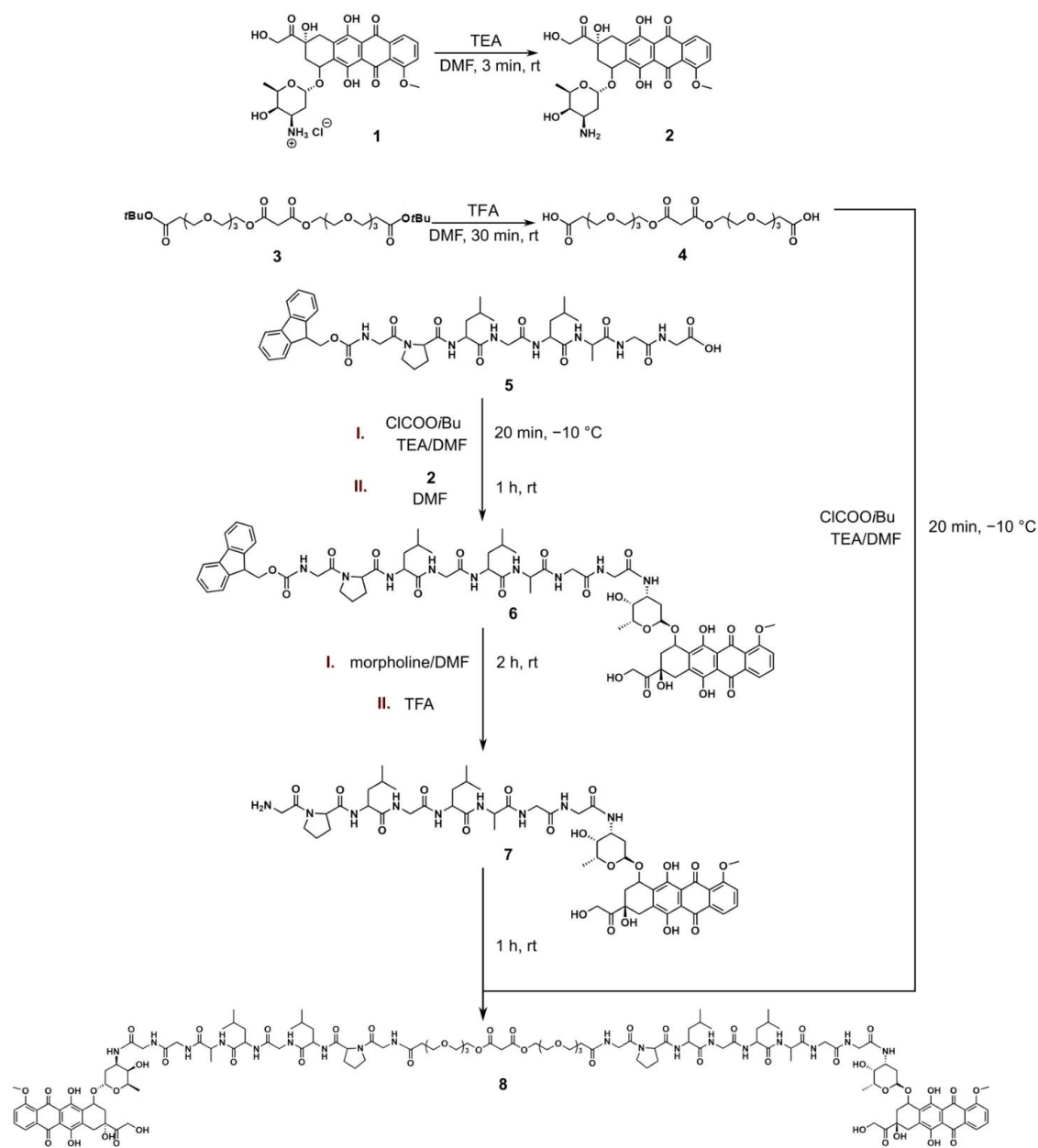


Figure 1 . Synthesis route of PEG-pep-DOX conjugate.

3.2. Zeta potential

Zeta potential provides information about the external surface charge of dispersed particles, which is related to the stability of their suspensions. The value of the potential of PEG-pep-DOX was estimated at -20.4 ± 0.9 mV (Fig. 2). In this range, e.g., 10-20 mV,

253

254

255

256

257

dispersion is considered to be rather stable [53], whereas higher values (> 30 mV) indicate monodisperse solution. Based on the AFM measurements we established that for the PEG-pep-DOX conjugate aggregates are formed. It was also confirmed by the DLS measurements (data not shown because of high level of polydispersity). However, the negative zeta potential can be an advantage because of the increased cellular uptake, and its moderate value is considered beneficial for interactions with biological cells which have similar zeta values [54].

258
259
260
261
262
263
264
265
266

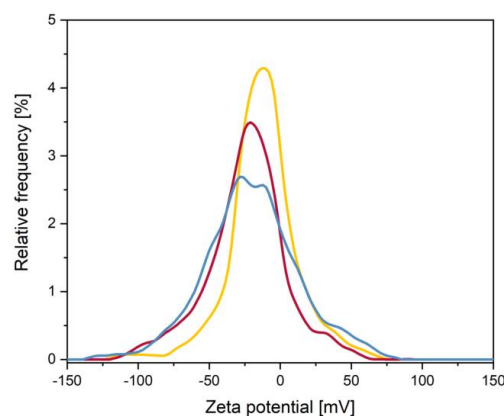


Figure 2. Three independent measurements of Zeta potential distribution of PEG-pep-DOX conjugate.

3.3. Atomic Force Microscopy

The AFM was used to visualize the PEG-pep-DOX conjugate to confirm its morphology. Singular objects were observed with a height of 3 nm, and XY dimensions around $15 \text{ nm} \times 25\text{--}30 \text{ nm}$ (Fig. 3A.). The registered shape of the PEG-pep-DOX molecule is rather oval which indicates the more flexible peptide fragment and PEG moiety are compactly packed. It should be emphasized that Z-dimension is the most accurate, because of the characteristic of scanning probe and basics of the technique itself; the XY dimensions are only estimative. Many fibrillar structures were observed with lengths from several hundred nanometers to dozens micrometers (Fig. 3B-3F). Their most common height values were 3, 6, 12, 15 and 24 nm. One can see that the above-mentioned values are a multiplication of the value of the height of the smallest objects observed, thus it can be concluded that the investigated singular items are in fact the synthesized constructs, and observed fibrils are built of multiple molecules. Therefore, we hypothesized that the resultant fibrils are composed of a self-assemble layered individual conjugate. When looking for similar, self-organizing PEG-pep hybrid structures, it is worth noting that for copolymers of PEG with short peptide fragments, based on $A\beta(16\text{--}20)$ sequence, Hamley and Krysmann observed an evidence for chain folding of PEG (crystallization) and fibril formation in these PEG/peptide conjugates [55].

267
268
269
270
271
272
273
274
275
276
277
278
279
280
281
282
283
284
285
286

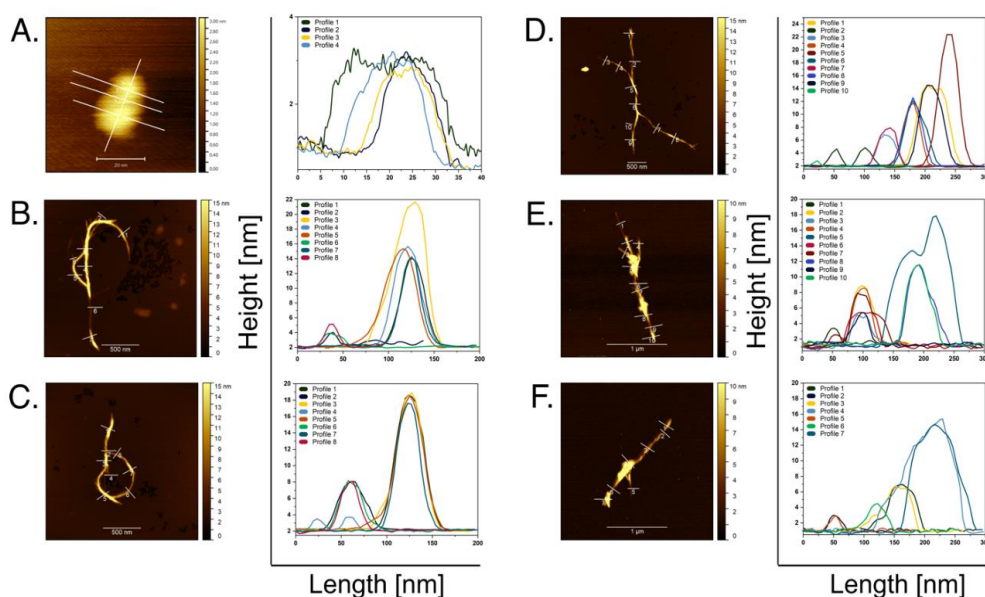


Figure 3. Representative AFM topography images (left panel) and cross-section profiles (right panel) of individual molecule of PEG-pep-DOX (A) and its aggregates (B-F). The cross-section profiles correspond the white lines.

287

288

289

3.3. Molecular Dynamic Simulations

To confirm the aggregation of PEG-pep-DOX in aqueous solution suggested by the zeta potential and AFM imaging, we determined the fraction of simulation frames in which at least 50% of the molecules in the simulation box are bound to any other (form at least two intermolecular contacts with a cut-off of 0.6 nm). In the system containing 2, 4 and 8 molecules of PEG-pep-DOX, aggregation defined in this way is observed in 88, 92 and 80% of the simulation time, respectively. These results suggest a substantial propensity of PEG-pep-DOX to aggregate in aqueous solution, even on a relatively short time scale of a few hundreds of nanoseconds sampled in our simulations. To further characterize aggregation process, for subsequent analysis we selected only those MD frames in which all PEG-pep-DOX present in a given system formed a single oligomer (~42% of all frames).

To compare and characterize structurally the PEG-pep-DOX aggregates as a function of the number of monomers, we performed a cluster analysis of the MD-generated ensembles. This was done using the hybrid k-centers k-medoids clustering algorithm for all heavy atoms of PEG-pep-DOX, with a root mean square deviation (RMSD) cut-off of 0.8 nm. Before clustering, the structures were superimposed by minimizing a heavy-atom RMSD for all PEG-pep-DOX molecules considering their permutations. Figure 4 shows, the most likely structures of the PEG-pep-DOX oligomers identified by our cluster analysis for each of the four considered systems. As can be seen, the simulated PEG-pep-DOX oligomers (2-8 molecules) exhibit an extended shape and tend to grow in one direction, which agrees with the fibrillar structures observed on mica by AFM. To characterize in detail the size and shape of the PEG-pep-DOX monomers and oligomers, we calculated their radius of gyration (R_g) and moments of inertia (MOI) with respect to the principal

290

291

292

293

294

295

296

297

298

299

300

301

302

303

304

305

306

307

308

309

310

311

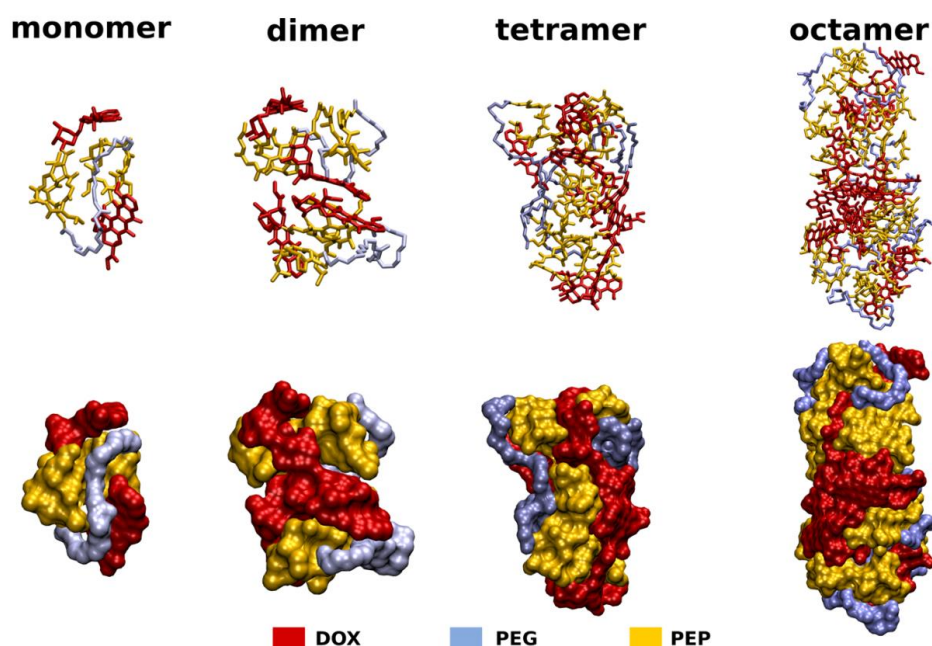


Figure 4. Representative structures of the PEG-pep-DOX monomers and oligomers containing either 2, 4 or 8 associated molecules, determined by the cluster analysis (hydrogen atoms have been omitted for clarity). DOX, PEP and PEG moieties are indicated in red, yellow, and gray, respectively. The bottom row shows the surface representation of the oligomers using the same color code.

axes, as well as the center-of-mass distances between the DOX fragments in a given molecule, LDOX-DOX (Fig. 5). Comparison of the average radius of gyration of PEG-pep-DOX monomers (0.79 ± 0.02 nm) with the size of a maximally extended molecule (10 nm) indicates that in aqueous solution they adopt very compact structures. The average diameter of the PEG-pep-DOX monomer estimated from R_g (assuming a spherical shape [56]) is equal to 2.04 nm and agrees well with the values obtained from AFM (3 nm). The values

312
313
314
315
316
317

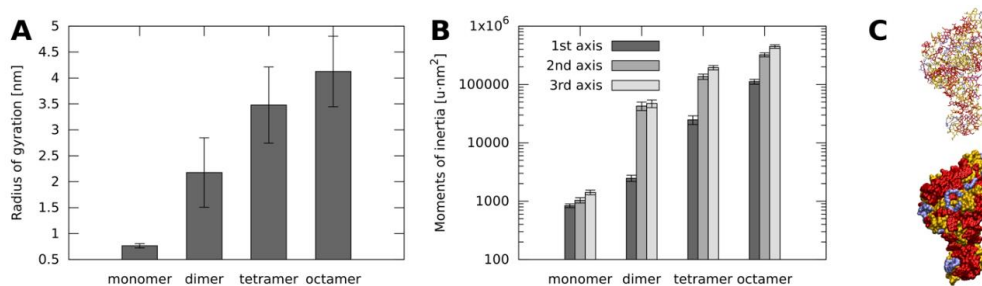


Figure 5. Average values of the radius of gyration (A) and the moment of inertia with respect to the principal axes (B) calculated for the PEG-pep-DOX monomers and oligomers containing either 2, 4 or 8 associated molecules (C) Representative structures of the PEG-pep-DOX oligomer containing 16 associated molecules. The same color code as in Fig. 4 was used.

of Rg of the oligomers systematically increase with the number of monomers involved in aggregate formation, but faster than expected for isotropic growth (e.g., for a sphere, where N is a number of molecules), suggesting anisotropic growth of the aggregates. Indeed, since the MOI with respect to the 1st axis is in all cases significantly smaller than for the two remaining ones with (see Figure 5B), this indicates that aggregates prefer to adopt elongated shapes with one dominant growth axis. To strengthen this conclusion, we also simulated the system containing 16 molecules of PEG-pep-DOX, which confirmed our earlier observation (see Fig. 5C). Relatively large separation distances between the two DOX moieties in a given monomer (1.21 ± 0.23 nm) compared to the effective diameter of the molecule (d) indicate that these fragments do not tend to form intra-monomer contacts (see DOX fragment highlighted in red in Fig. 4).

Next, to test whether enzyme-sensitive peptide fragments are directly accessible for MMPs-2/-9- on the surface of the aggregates, we calculated the fraction of their total solvent accessible surface area (SASA) corresponding to the DOX, PEP, and PEG moieties. Figure 6A shows that the largest surface areas are formed by DOX (~39%) and PEP (~37%) fragments, while PEG fragments on average contribute to the remaining 24% of the total surface. Notably, the contributions from each of these moieties do not depend largely on

the oligomer stoichiometry. This shows that the peptide is always well exposed to the water solution and therefore the efficiency of the MMPs-2/-9-mediated cleavage should not be markedly affected by the aggregation. To examine how PEG-pep-DOX molecules interact with each other to form aggregates, we calculated the number of intermolecular contacts between their DOX, PEG and PEP moieties, for all oligomers considered (Figure 6B). As can be seen from the calculated pairwise contacts between the moieties, the aggregation process is mediated largely by mutual interactions between the DOX moieties and by DOX-PEP interactions, while the involvement of PEG in stabilization of aggregates is much less.

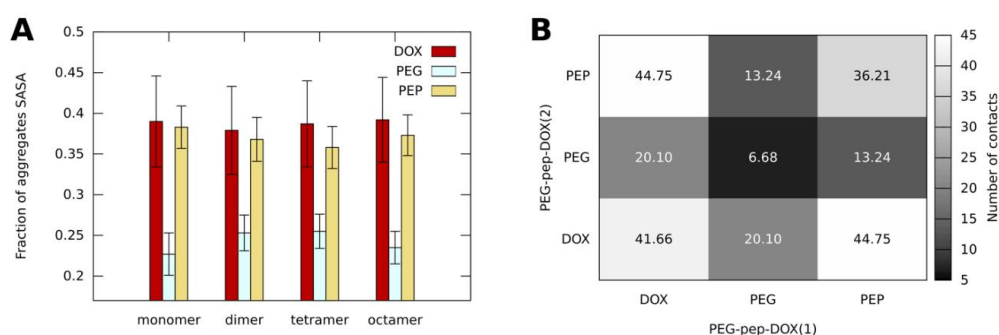


Figure 6. Solvent accessible surface area (SASA) of PEG-pep-DOX monomers and oligomers containing either 2, 4 or 8 associated molecules. (A) Average number of intermolecular contacts between DOX, PEG and PEP moieties of within the PEG-pep-DOX oligomers. (B) A contact is defined when a pair of atoms is in contact. The number of contacts were averaged over all oligomers and all pairs of moieties that form at least two contacts with each other.

3.4. Cytotoxicity assay

Evaluation of DOX and free DOX cytotoxic activity was conducted in HT-1080, MCF-7 and MDA-MB-436 cell lines treated for 72 h. The HT-1080 cell line, which has been demonstrated to overexpress MMPs, was compared with MMPs low-expressing MCF-7 cells (negative control) [57]. Additionally, MDA-MB-436 cells were chosen as a model for the

346

347

348

349

350

351

most aggressive subtype of breast cancer with a poor prognosis and lack of targeted therapy [58]. As illustrated in Fig. 7, it was found that incubation of HT-1080 and MDA-MB-436 but not MCF-7 cells with PEG-pep-DOX resulted in modest (20-25%), but statistically significant growth inhibition. The results confirmed that PEG-pep-DOX affected the growth of but, to our surprise, with moderately lower efficiency than expected. The observed PEG-pep-DOX cytotoxicity can be rationalized by time lag needed to degrade the peptide linker or the concentration of MMPs which is not sufficient for sustained releasing of DOX from the carrier. Nevertheless, our results indicate that PEG-pep-DOX exhibits higher potency in the cells expressing elevated level of MMPs. Additionally, the cytotoxicity results for free DOX (Fig. S3 in Supplementary Information) show that its activity is concentration dependent, and the compound is highly toxic against all tested cell lines without any MMPs-related specificity.

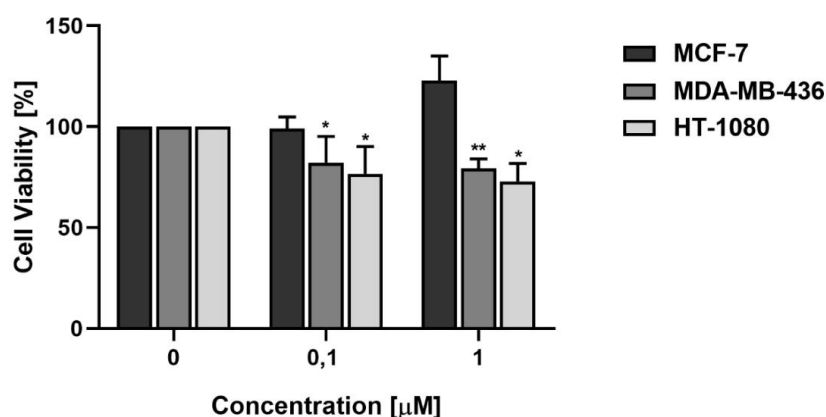


Figure 7. Viability of MCF-7, MDA-MB-436 and HT-1080 cell lines incubated for 72 h with PEG-pep-DOX (0,1 µM and 1 µM). Results are shown as the mean \pm SD of at least three independent experiments performed in triplicate. Growth of cells in the presence of PEG-pep-DOX was compared to control – untreated conditions, * $p < 0,1$, ** $p < 0,01$.

5. Conclusions

In summary, using few-steps synthesis route we obtained PEG-pep-DOX conjugate used for potentially targeted DOX delivery. From the AFM images, as well as zeta potential and DLS studies we hypothesized that PEG-pep-DOX has a high affinity to create fibril-like aggregates. Our molecular dynamics simulations confirmed this finding and showed that aggregation of PEG-pep-DOX occurs *via* DOX-DOX and DOX-peptide interactions. Notably, we also found that the peptide fragment is well exposed even in the aggregated state, such that aggregation should not affect MMP-2/-9 cleavage efficiency. The significant cytotoxic effects of PEG-pep-DOX were expected in the MMPs overexpressing cell line compared with cells that do not express those enzymes. However, we observed only a moderate cell growth-inhibiting activity of the conjugate, which may be the result of relatively low MMPs concentration or aggregation of PEG-pep-DOX at elevated concentrations. We also found that PEG-pep-DOX gently induced proliferation of MMPs-negative MCF-7 cells. This surprising effect might be explained by recognition of the peptide by other cell membrane receptors which results in cell growth promotion. In the broader

context, further studies will be required to demonstrate the efficacy of PEG-pep-DOX in the future.

Supplementary Materials: The following are available online at www.mdpi.com/xxx/s1, Figure S1: MALDI-TOF mass spectrum of compound 8, Figure S2: AFM images of representative large scan area (10x10 µm) of PEG-pep-DOX, Figure S3: Viability of MDA MB 436, MCF-7 AND HT 1080 cell lines incubated with free DOX Table S1: Details of simulates systems.

Author Contributions: Conceptualization, K.B., J.R., J.P.; Formal Analysis, K.B., W.K., M.K., Z.P-M., A.M., K.K., M.K, R.S., J.R., J.C., J.P.; Investigation, K.B., W.K., M.K., Z.P-M., A.M., K.K.; Funding acquisition, J.R., J.P.; Writing—original draft, K.B., W.K., M.K., Z.P-M., A.M.; Writing—review and editing, K.K, M.K, R.S., J.R., J.C., J.P.; Supervision, J.R., J.P.; Project administration, K.B. All authors have read and agreed to the published version of the manuscript.

Acknowledgments: This work was supported by the Polish Ministry of Science and Higher Education under Grant Nos. DS 531-T080-D494-21 (J.R.) and DS 531-M045-D788-19 (J.P.). This research was supported in part by PL-Grid Infrastructure. We wish to thank the Academic Computer Centre in Gdańsk, Poland, for granting CPU time. The research performed by M.K., Z.P-M. and A.M. was supported by OPUS research grant from National Science Centre (Grant No: 2017/27/B/ST4/00485).

Conflicts of Interest: The authors declare no conflict of interest

References

- Q. Yin, J. Shen, Z. Zhang, H. Yu, Y. Li, *Advanced Drug Delivery Reviews*, 2013, **65**, 1699-1715.
- S. S. Das, P. Bharadwaj, M. Bilal, M. Barani, A. Rahdar, P. Taboada, S. Bungau, G. Z. Kyzas, *Polymers*, 2020, **12**, 1397.
- S. Mura, J. Nicolas, P. Couvreur, *Nature Materials*, 2013, **12**, 991-1003.
- A. Gulzar, S. Gai, P. Yang, C. Li, M. B. Ansari, J. Lin, *Journal of Materials Chemistry B*, 2015, **3**, 8599-8622.
- R. De La Rica, D. Aili, M. M. Stevens, *Advanced Drug Delivery Reviews*, 2012, **64**, 967-978.
- Q. Hu, P. S. Katti, Z. Gu, *Nanoscale*, 2014, **6**, 12273-12286.
- M. Shahriari, M. Zahiri, K. Abnous, S. M. Taghdisi, M. Ramezani, M. Alibolandi, *Journal of Controlled Release*, 2019, **308**, 172-189.
- F. Kratz, I. A. Müller, C. Ryppe, A. Warnecke, *ChemMedChem: Chemistry Enabling Drug Discovery*, 2008, **3**, 20-53.
- K. M. Huttunen, H. Raunio, J. Rautio, *Pharmacological Reviews*, 2011, **63**, 750-771.
- J. Rautio, H. Kumpulainen, T. Heimbach, R. Oliyai, D. Oh, T. Järvinen, J. Savolainen, *Nature Reviews Drug Discovery*, 2008, **7**, 255-270.
- M. Han, M. Y. Huang-Fu, W. W. Guo, N. N. Guo, J. Chen, H. N. Liu, Z. Q. Xie, M. T. Lin, Q. C. Wei, J. Q. Gao, *ACS Applied Materials & Interfaces*, 2017, **9**, 42459-42470.
- W. Ke, J. Li, K. Zhao, Z. Zha, Y. Han, Y. Wang, W. Yin, P. Zhang, Z. Ge, *Biomacromolecules*, 2016, **17**, 3268-3276.
- J. Li, S. Xiao, Y. Xu, S. Zuo, Z. Zha, W. Ke, C. He, Z. Ge, *ACS Applied Materials & Interfaces*, 2017, **9**, 17727-17735.
- M. Olsman, V. Sereti, K. Andreassen, S. Snipstad, A. van Wamel, R. Eliassen, S. Berg, A. J. Urquhart, T. L. Andresen, C. de Lange Davies, *Journal of Controlled Release*, 2020, **325**, 121-134.
- H. Maeda, J. Wu, T. Sawa, Y. Matsumura, K. Hori, *Journal of Controlled Release*, 2000, **65**, 271-284.
- A. A. D. Jones III, G. Mi, T. J. Webster, *Trends in Biotechnology*, 2019, **37**, 117-120.
- D. Bobo, K. J. Robinson, J. Islam, K. J. Thurecht, S. R. Corrie, *Pharmaceutical Research*, 2016, **33**, 2373-2387.
- C. Alvarez-Lorenzo, A. Concheiro, *Chemical Communications*, 2014, **50**, 7743-7765.
- Paul C. Lyon, L. F. Griffiths, J. Lee, D. Chung, R. Carlisle, F. Wu, M. R. Middleton, F. V. Gleeson, C. C. Coussios, *Journal of Therapeutic Ultrasound*, 2017, **5**, 28.
- S. D. Chipman, F. B. Oldam, G. Pezzoni, J. W. Singer, *International Journal of Nanomedicine*, 2006, **1**, 375.
- M. Poreba, M. *The FEBS Journal*, 2020, **287**, 1936-1969.
- Y. J. Zhong, L. H. Shao, Y. A. N. Li, *International Journal of Oncology*, 2013, **42**, 373-383.
- S. Curran, G. I. Murray, *European Journal of Cancer*, 2000, **36**, 1621-1630.
- K. Kessenbrock, V. Plaks, Z. Werb, *Cell*, 2010, **141**, 52-67.
- C. Gialeli, A. D. Theocharis, N. K. Karamanos, *The FEBS Journal*, 2011, **278**, 16-27.
- A. Jabłońska-Trypuć, M. Matejczyk, S. Rosochacki, S. *Journal of Enzyme Inhibition and Medicinal Chemistry*, 2016, **31**, 177-183.
- M. Egeblad, Z. Werb, *Nature Reviews Cancer*, 2002, **2**, 161-174.
- S. Quintero-Fabián, R. Arreola, E. Becerril-Villanueva, J. C. Torres-Romero, V. E. Arana-Argáez, J. Lara-Riegos, M. A. Ramirez-Camacho, M. E. Alvarez Sanchez, *Frontiers in Oncology*, 2019, **9**, 1370.
- B. A. Chabner, T. G. Roberts, *Nature Reviews Cancer*, 2005, **5**, 65-72.

30. C. Carvalho, R. X. Santos, S. Cardoso, S., Correia, P. J. Oliveira, M. S. Santos, P. I. Moreira, *Current Medicinal Chemistry*, 2009, **16**, 3267-3285. 434
435
31. F. Kratz, A. Warnecke, B. Schmid, B., D. E. Chung, M. Gitzel, *Current Medicinal Chemistry*, 2006, **13**, 477-523. 436
32. K. Vaghasiya, E. Ray, A. Sharma, O. P. Katare, R. K. Verma, *ACS Applied Bio Materials*, 2020, **3**, 4987-4999. 437
33. S. Ruan, Q. He, H. Gao, *Nanoscale*, 2015, **7**, 9487-9496. 438
34. H. H. Wang, Z. G. Fu, W. Li, Y. X. Li, L. S. Zhao, L. Wen, J. J. Zhang, N. Wen, *International Journal of Nanomedicine*, 2019, **14**, 623. 439
35. J. Li, B. Zhang, C. Yue, J. Wu, L. Zhao, D. Sun, R. Wang, *Journal of Drug Targeting*, 2018, **26**, 9-26. 440
36. K. Butowska, K., Żamojć, M. Kogut, W. Kozak, D. Wyrzykowski, W. Wiczak, J. Czub, J. Piosik, J. Rak, *International Journal of Molecular Sciences*, 2020, **21**, 6923. 441
442
37. T. W. Greene, P. G. M. Wuts, *Protective groups in organic synthesis*. Wiley, New York, 1999, **65-67**, 404-408. 443
38. D. Nečas, P. Klapetek, *Central European Journal of Physics*, 2012, **10**, 181-188. 444
39. M. D. Hanwell, D. E. Curtis, D. C. Lonie, T. Vandermeersch, E. Zurek, G. R. Hutchison, *Journal of Cheminformatics*, 2012, **4**, 1-17. 445
40. L. Martínez, R. Andrade, E. G. Birgin, J. M. Martínez, *Journal of computational chemistry*, 2009, **30**, 2157-2164. 446
41. W. L. Jorgensen, J. Chandrasekhar, J. D. Madura, R. W. Impey, M. L. Klein, *The Journal of chemical physics*, 1983, **79**, 926-935. 447
42. I. Ivani, P. D. Dans, A. Noy, A. Pérez, I. Faustino, A. Hospital, J. Walther, P. Andrio, R. Goñi, A. Balaceanu, *Nature Methods*, 2015, **13**, 55-58. 448
449
43. J. Wang, R. M. Wolf, J. W. Caldwell, P. A. Kollman, D. A. Case, *Journal of Computational Chemistry*, 2004, **25**, 1157-1174. 450
44. M. J. Frisch, G. W. Trucks, H. B. Schlegel, G. E. Scuseria, M. A. Robb, J. R. Cheeseman, H. Nakatsuji, Gaussian 09; Software for Calculation; Gaussian, Inc. Wallingford, CT, USA. 2016 451
452
45. M. J. Abraham, T. Murtola, R. Schulz, S. Páll, J. C. Hess, E. Lindhal, *SoftwareX*, 2015, **1**, 19-25. 453
46. G. Bussi, D. Donadio, M. Parrinello, *The Journal of Chemical Physics*, 2007, **126**, 014101. 454
47. M. Parrinello, A. Rahman, *Journal of Applied Physics*, 1981, **52**, 7182-7190. 455
48. T. Darden, D. York, L. Pedersen, *The Journal of Chemical Physics*, 1993, **98**, 10089-10092. 456
49. B. Hess, *Journal of Chemical Theory and Computation*, 2008, **4**, 116-122. 457
50. S. Miyamoto, P. A. Kollman, *Journal of Computational Chemistry*, 1992, **13**, 952-962. 458
51. K. Butowska, W. Kozak, M. Zdrowowicz, S. Makurt, M. Rychłowski, A. Hać, A. Herman-Antosiewicz, J. Piosik, J. Rak, *Structural Chemistry*, 2019, **30**, 2327-2338. 459
460
52. R. DiFrancesco, J. J. Griggs, J. Donnelly, R. DiCenzo, *Journal of Chromatography B*, 2007, **852**, 545-553. 461
53. V. R. Patel, Y. K. Agrawal, *Journal of Advanced Pharmaceutical Technology & Research*, 2011, **2**, 81-87. 462
54. S. Honary, F. Zahir, *Tropical Journal of Pharmaceutical Research*, 2013, **12**, 255-264. 463
55. I. W. Hamley, M. J. Krysmann, *Langmuir*, 2008, **24**, 8210-8214. 464
56. R. A. Meyers, *Encyclopedia of Physical Science and Technology*. 1987, Academic Press. 465
57. J. E. Bartsch, B. S. Edgar, D. Staren, H. E. Appert, *Journal of Surgical Research*, 2003, **110**, 383-392. 466
58. E. M. Yousef, M. R. Tahir, Y. St-Pierre, L. A. Gaboury, *BMC Cancer*, 2014, **14**, 609. 467
468

SUPPLEMENTARY INFORMATION

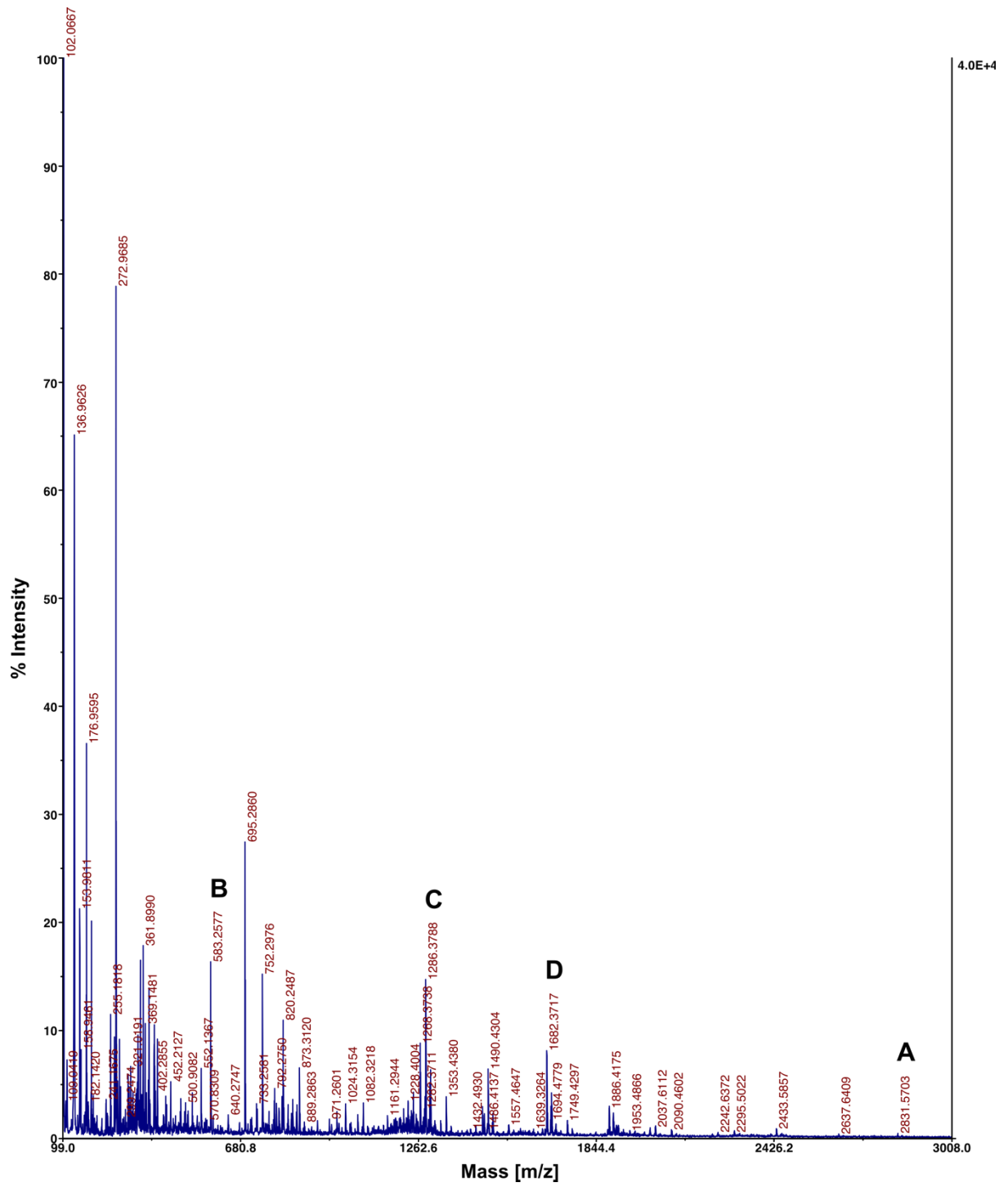
MMPs-sensitive release of doxorubicin as a strategy for cancer targeted therapy

Kamila Butowska,^{*1,2} Witold Kozak,² Mateusz Kogut,³ Zuzanna Pietralik-Molińska,⁴ Augustyn Moliński,^{4,7} Kamila Kitowska,⁵ Maciej Kozak,⁴ Jacek Czub,⁶ Rafał Sądej,⁵ Janusz Rak,² and Jacek Piosik^{*1}

- 1 Laboratory of Biophysics, Intercollegiate Faculty of Biotechnology, University of Gdańsk and Medical University of Gdańsk, Abrahama 58, 80-307 Gdańsk, Poland; kamila.butowska@phdstud.ug.edu.pl (K.B.); jacek.piosik@biotech.ug.edu.pl (J.P.)
- 2 Department of Physical Chemistry, Faculty of Chemistry, University of Gdańsk, Wita Stwosza 63, 80-308 Gdańsk, Poland; davelombardo@wp.pl (W.K.); janusz.rak@ug.edu.pl (J.R.)
- 3 Institute of Physics, Polish Academy of Sciences, Al. Lotników 32/46, 02-668 Warsaw, Poland
- 4 Department of Macromolecular Physics, Faculty of Physics, Adam Mickiewicz University in Poznań, Uniwersytetu Poznańskiego 2, 61-614 Poznań, Poland; zuzanna.p@amu.edu.pl (Z. P.-M.); augmol@amu.edu.pl (A. M.); mkozak@amu.edu.pl (M. K.)
- 5 Department of Molecular Enzymology and Oncology, Intercollegiate Faculty of Biotechnology, University of Gdańsk and Medical University of Gdańsk, Dębinki 1, 80-211, Gdańsk, Poland; kkitowska@gumed.edu.pl (K. K.); rafal.sadej@ug.edu.pl (R. S.)
- 6 Department of Physical Chemistry, Faculty of Chemistry, Gdańsk University of Technology, Narutowicza 11/12, 80-233 Gdańsk, Poland; giggsmk@op.pl (M.K.); jacek.czub@pg.edu.pl (J.C.)
- 7 NanoBioMedical Centre, Adam Mickiewicz University in Poznań, Wszechnicy Pastowskiej 3, 61-614 Poznań, Poland

* Correspondence: kamila.butowska@phdstud.ug.edu.pl; Tel.: +48-58-523-6310

E-mail: jacek.piosik@biotech.ug.edu.pl; kamila.butowska@phdstud.ug.edu.pl



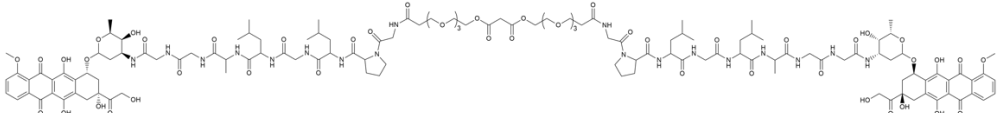
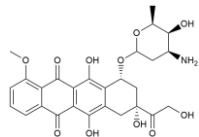
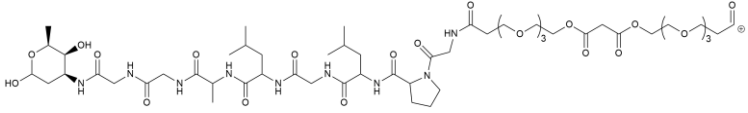
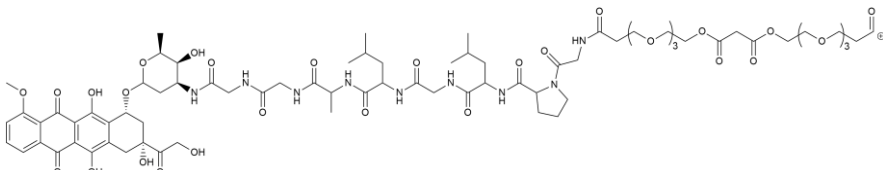
Compound	Chemical structure
A	 <p data-bbox="630 376 1157 405">[M + Na⁺]_{exp} = 2831.5730; [M + Na⁺]_{the} = 2831.94</p>
B	 <p data-bbox="654 604 1125 638">[M + K⁺]_{exp} = 583.2577; [M + K⁺]_{the} = 583.54</p>
C	 <p data-bbox="646 813 1141 846">[M + K⁺]_{exp} = 1286.3788; [M + K⁺]_{the} = 1286.37</p>
D	 <p data-bbox="646 1048 1141 1081">[M + K⁺]_{exp} = 1682.3717; [M + K⁺]_{the} = 1682.72</p>

Figure S1. MALDI-TOF mass spectrum of compound **8** in positive ionization mode and ion identities (*exp*-experimental mass; *the*-theoretical mass).

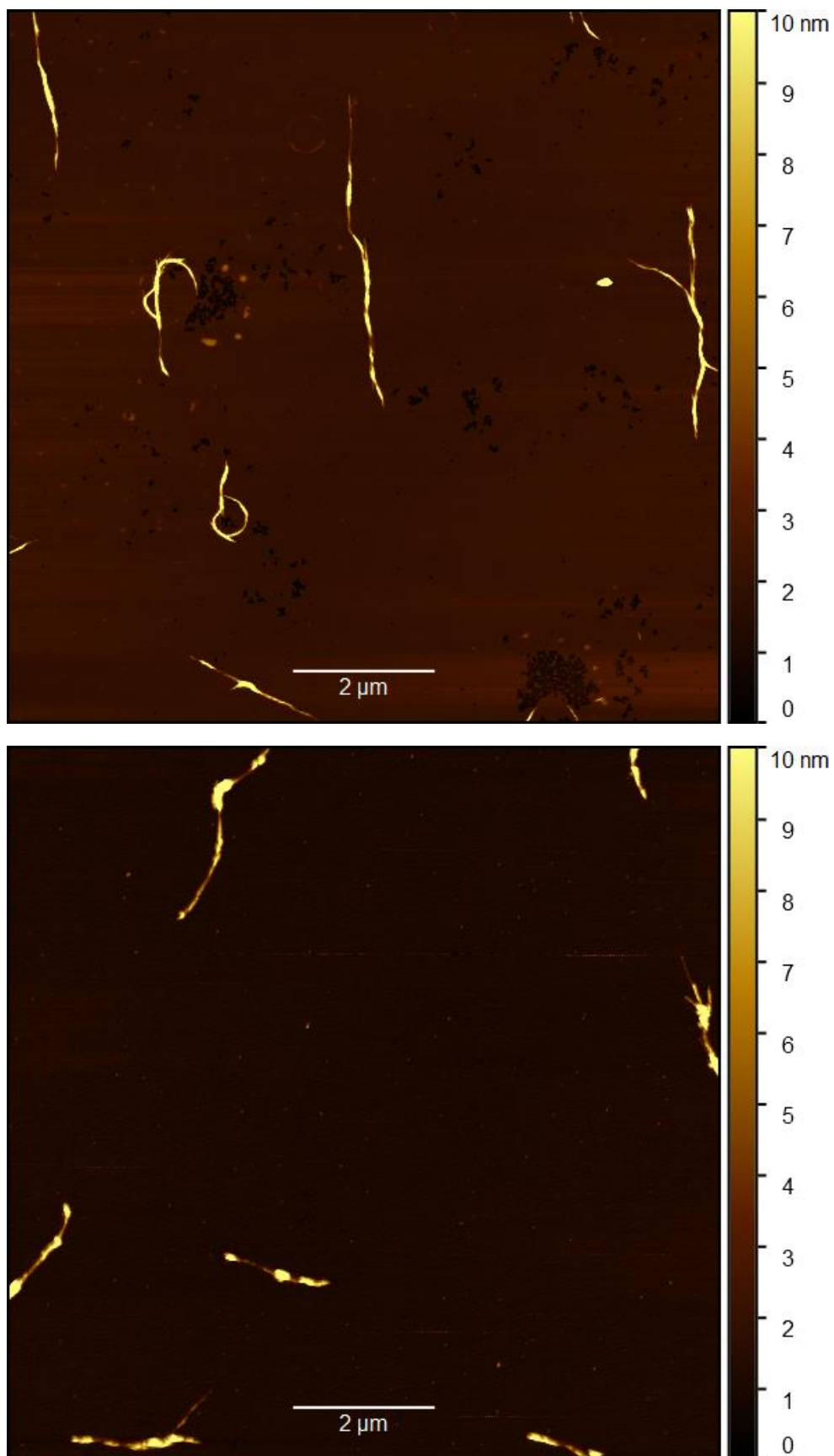


Figure S2. AFM images of representative large scan area (10x10 μm) of PEG-pep-DOX deposited on mica surface, presenting structures formed by this conjugate; both aggregated, fibrillar forms and small, singular objects.

Table S1. Details of simulated systems.

No. of PEG-pep-DOX	No. of water molecule	Ions	Unit cell len. (a × b × c) [nm]
1	17655	K ⁺ : 43 Cl ⁻ : 43	9.22 × 9.22 × 6.28
2	28079	K ⁺ : 68 Cl ⁻ : 68	10.69 × 10.69 × 7.56
4	31137	K ⁺ : 76 Cl ⁻ : 76	11.12 × 11.12 × 7.86
8	54028	K ⁺ : 132 Cl ⁻ : 132	13.32 × 13.32 × 9.42
16	67965	K ⁺ : 168 Cl ⁻ : 168	14.45 × 14.45 × 10.22

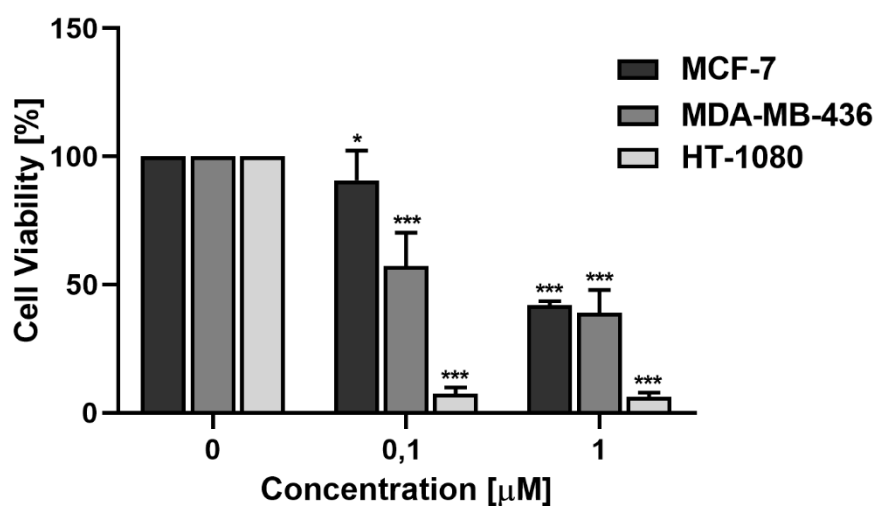


Figure S3. Viability of MCF-7, MDA-MB-436 and HT-1080 cell lines incubated for 72 h with free DOX (0,1 and 1 µM). Results are shown as the mean ± SD of at least three independent experiments performed in triplicate. Effect of DOX for cell growth was compared to control – untreated conditions, * p < 0,1, ** p < 0,01, *** p < 0,001.

4. **K. Butowska**, X. Han, N. Gong, R. El-Mayta, R. M. Haley, W. Zhong, W. Guo, M. J. Mitchell, *Doxorubicin-conjugated siRNA lipid nanoparticles for combination cancer therapy*. *Acta Pharmacologica Sinica B*, **2021** [P4]

Original article

Doxorubicin-conjugated siRNA lipid nanoparticles for combination cancer therapy

Kamila Butowska^{a,b,†}, Xuexiang Han^{a,†}, Ningqiang Gong^a, Rakan El-Mayta^a, Rebecca M. Haley^a, Wenqun Zhong^c, Wei Guo^c, Michael J. Mitchell^{a,d,e,f,g*}

^a*Department of Bioengineering, University of Pennsylvania, Philadelphia, PA, 19104, USA*

^b*Intercollegiate Faculty of Biotechnology, University of Gdańsk & Medical Gdańsk, Gdańk, 80-307, Poland*

^c*Department of Biology, University of Pennsylvania, Philadelphia, PA, 19104, USA*

^d*Abramson Cancer Center, Perelman School of Medicine, University of Pennsylvania, Philadelphia, PA, 19104, USA*

^e*Institute for Immunology, Perelman School of Medicine, University of Pennsylvania, Philadelphia, PA, 19104, USA*

^f*Cardiovascular Institute, Perelman School of Medicine, University of Pennsylvania, Philadelphia, PA, 19104, USA*

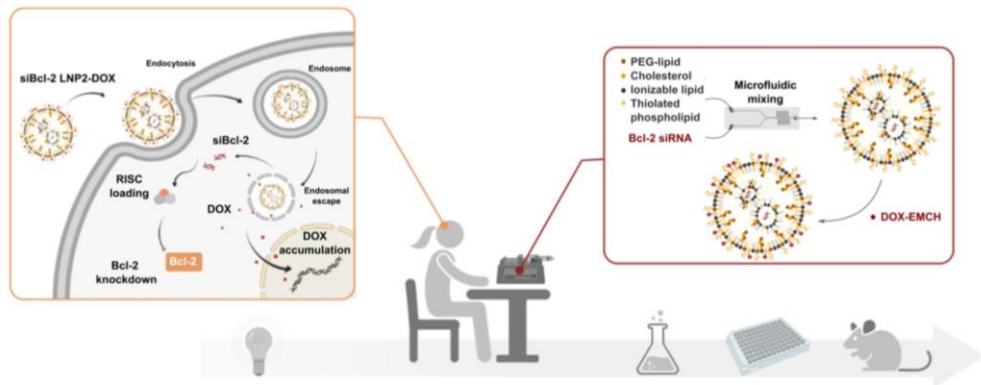
^g*Institute for Regenerative Medicine, Perelman School of Medicine, University of Pennsylvania, Philadelphia, PA, 19104, USA*

*Corresponding author. Tel.: +1 215 898 0882; E-mail address: mjmitch@seas.upenn.edu.

†These authors made equal contributions to this work.

Running title: Doxorubicin-conjugated siRNA lipid nanoparticles for lymphoma therapy

Graphical



Lipid nanoparticles have been shown to efficiently encapsulate siRNA and enable potent intracellular delivery for gene knockdown. In this work, we engineered doxorubicin-conjugated siRNA lipid nanoparticles to achieve potent chemo- and RNA interference (RNAi) therapy.

Doxorubicin-conjugated siRNA lipid nanoparticles for combination cancer therapy

Abstract

Evasion of apoptosis is a hallmark of cancer, attributed in part to the overexpression of the anti-apoptotic protein B-cell lymphoma 2 (Bcl-2). Bcl-2 is overexpressed in a variety of cancer types, including lymphoma. Therapeutic targeting of Bcl-2 has demonstrated efficacy in the clinic and is the subject of extensive clinical testing in combination with chemotherapy. Therefore, the development of co-delivery systems for Bcl-2 targeting agents, such as small interfering RNA (siRNA), and chemotherapeutics, such as doxorubicin (DOX), holds promise for enabling combination cancer therapies. Lipid nanoparticles (LNPs) are a clinically advanced nucleic acid delivery system with a compact structure that is suitable for siRNA encapsulation and delivery. Inspired by ongoing clinical trials of albumin-hitchhiking doxorubicin prodrugs, here we developed a DOX-siRNA co-delivery strategy via conjugation of doxorubicin to the surface of siRNA-loaded LNPs. Our optimized LNPs enabled potent knockdown of Bcl-2 and efficient delivery of DOX into the nucleus of Burkitt's lymphoma (Raji) cells, leading to effective inhibition of tumor growth in a mouse model of lymphoma. Based on these results, our LNPs may provide a platform for the co-delivery of various nucleic acids and DOX for the development of new combination cancer therapies.

KEY WORDS Lipid nanoparticles; Doxorubicin; Bcl-2; siRNA delivery; Chemotherapy; Lymphoma

1. Introduction

The World Health Organization estimated that 10 million cancer deaths occurred worldwide in 2020, an increase from 9.4 million cancer-related cases in 2018^{1,2}. Cancer treatment typically involves the use of systemically administered therapies, such as chemotherapy and immune therapy, or localized therapies (e.g., surgery) used separately or in combination³. For patients with non-Hodgkin's lymphoma, chemotherapy is a major treatment option⁴. However, many cancer patients do not respond to chemotherapy or lose responsiveness over time, in part due to cancer cell resistance to apoptosis⁵.

Recent studies have indicated that evasion of apoptosis occurs through several mechanisms, including the enhancement of DNA repair by nonhomologous end-joining proteins or the overexpression of anti-apoptotic proteins, which can act individually or synergistically⁶. One of the major anti-apoptotic factors is the B cell lymphoma-2 (Bcl-2) family of proteins, discovered almost 30 years ago in non-Hodgkin's lymphoma^{7,8}. Bcl-2 protein is incorporated into the membranes of mitochondria and endoplasmic reticulum, which can prevent the release of apoptosis-inducing factor and cytochrome c, inhibiting caspase-mediated cell apoptosis⁹. Due to the important role of Bcl-2 in the apoptotic pathway, several therapeutic strategies have been developed to inhibit or downregulate the Bcl-2 protein¹⁰. For example, Bcl-2-targeting antisense oligonucleotides (ASOs)—such as Oblimersen, SPC2996 LNA gapmer, or PNT2258—were developed and tested in clinical trials against various types of cancers including multiple myeloma and leukemia^{11,12}. In 2016, a small molecule inhibitor of Bcl-2, Venetoclax, was approved as a monotherapy by the Food and Drug Administration (FDA) for treating patients with chronic lymphocytic leukemia¹³. However, due to the limited benefit of this monotherapy, many clinical trials are currently ongoing to evaluate combination therapies with various chemotherapeutics, such as doxorubicin (DOX)¹⁴. DOX acts as a pro-apoptotic drug which can cause cell death. However, the overexpression of Bcl-2 by cancer cells can largely counteract the pharmacological effect of DOX. Therefore, development of a clinically advanced platform to co-deliver Bcl-2-targeting therapeutics and DOX holds promise in the development of combination cancer therapies^{15,16}.

In recent years, efforts have been made to co-deliver Bcl-2 siRNA (siBcl-2) and DOX for combination cancer therapies against ovarian cancer, glioma, and other cancer types.^{17,18,19} So far, biomaterials are the most widely used carriers for these applications due to their multi-functionality and ability to either encapsulate or conjugate drugs. However, most of these delivery systems suffer from non-degradability, complexity, and insufficient biological activity. Lipid nanoparticles (LNPs) are a promising platform for the co-delivery of Bcl-2 siRNA and DOX, as they are a clinically advanced delivery system shown to effectively encapsulate siRNA and facilitate its intracellular delivery²⁰. The success of LNPs lies in their ability to remain stable at physiologically relevant neutral pH but become ionized under acidic conditions—such as the endosomal compartment of the cell—which enables LNPs to escape from the endosome and release siRNA into the cytosol. Over the last two decades, significant progress in the development of LNP-based nucleic acid delivery systems has been achieved²¹. The first LNP-based siRNA therapeutic, Onpatro, was approved by the FDA in 2018 for the treatment of hereditary transthyretin-mediated polyneuropathy²². More recently, two LNP-based COVID-19 mRNA vaccines received emergency use authorization^{23,24}.

Unlike liposomes, such as those used in the FDA-approved liposomal doxorubicin drug Doxil, LNPs have a compact spherical structure and are highly optimized for siRNA delivery^{25,26}. Therefore, incorporation of chemotherapeutic drugs into siRNA-LNPs by physical encapsulation may interrupt the highly organized structure and cause potential issues, such as low encapsulation or destabilization of spherical shape due to accumulation in the lipid bilayer²⁷. To circumvent these issues, we developed a strategy to conjugate doxorubicin directly to LNPs. We modified formulated siRNA-LNPs using a thiol-maleimide Michael addition click reaction to conjugate a (6-maleimidocaproyl)hydrazone derivative of DOX (DOX-EMCH) to the LNP surface. DOX-EMCH is a clinical prodrug of DOX possessing a maleimide group and an acid-cleavable hydrazone bond, which can bind to albumin following intravenous injection to prolong its circulation half-life and release parental drug in an acidic environment²⁸. Inspired by this process, we formulated a thiolated LNP with a sulfur-containing phospholipid to conjugate DOX-EMCH to the surface of LNPs. Our optimized LNP formulation, siBcl-2 LNP2-DOX, achieved potent knockdown of Bcl-2 in Burkitt's lymphoma (Raji) cells while also successfully delivering DOX to the cell nucleus. We also provide *in vivo* evidence that siBcl-2 LNP2-DOX can effectively inhibit tumor growth in a NSG mouse model of lymphoma. These results suggest that our LNPs may provide a platform for the co-delivery of various nucleic acids and DOX, which could be used to develop combination therapies for a wide range of cancers.

2. Materials and methods

2.1. Materials

Aldoxorubicin (DOX-EMCH) was purchased from MedChem Express (Monmouth Junction, NJ, USA). Cholesterol and dimethyl sulfoxide (DMSO) were purchased from SigmaAldrich (St. Louis, MO, USA). 1,2-dimyristoyl-*sn*-glycero-3-phosphoethanolamine-*N*-[methoxy(polyethylene glycol)-2000] (ammonium salt, C14-PEG2000), 1,2-dipalmitoyl-*sn*-glycero-3-phosphoethanol (sodium salt, PTE) and 1,2-distearoyl-*sn*-glycero-3-phosphocholine (DSPC) were purchased from Avanti (Alabaster, AL, USA). The ionizable lipid 1,1'-((2-(4-(2-((bis(2-hydroxydodecyl)amino)ethyl) (2 hydroxydodecyl) amino)ethyl)piperazin-1-yl)ethyl)azanediy)bis(dodecan-2-ol) (C12-200) was synthesized as previously described²⁹.

2.2. Formulation of LNPs

The ionizable lipid C12-200 was diluted in ethanol with cholesterol, DSPC or PTE, and C14-PEG-2000 at a 50:38.5:10:1.5 molar ratio in a total volume of 100 μ L. Luciferase (siLuc) or Bcl-2 (siBcl-2) siRNA was dissolved in 10 mM citrate buffer (pH 3.0) at weight ratios of 5:1 or 15:1 (ionizable lipid:siRNA), in a total volume of 300 μ L. The aqueous and ethanol phases were combined via mixing in a microfluidic device at a volume ratio of 3:1 (citrate buffer:ethanol, v/v)³⁰. Two LNPs with different ionizable lipid:siRNA weight ratios (LNP1 - 5:1 and LNP2 - 15:1) were prepared. LNPs were dialyzed against 1X PBS for 2 hours before sterile filtration via 0.22 μ m syringe filters (Genesee Scientific, El Cajon, CA, USA). Next, DOX-EMCH (1.2 mmol) was added to LNPs (1 mmol PTE) and incubated with shaking (250 rpm) for 2 hours. Afterwards, the mixture was dialyzed against 1X PBS for 2 hours, sterilized through 0.22 μ m syringe filters, and kept at 4 °C. A modified Quant-iT RiboGreen assay (ThermoFisher, Waltham, MA, USA) was used to obtain the concentration and encapsulation efficiency of siRNA in LNPs by comparing fluorescence intensity (λ_{ex} =490 nm, λ_{em} =530 nm) in the presence and absence of Triton X-100³¹.

2.3. Physicochemical characterization of LNPs

20 μ l of LNP solution was combined with 780 μ l of H₂O in 4 mL disposable cuvettes or zeta cuvettes for dynamic light scattering (DLS) and zeta potential (ζ) measurements. Measurements were performed using a Zetasizer Nano (Malvern Instruments, Malvern, UK) in triplicate, and reported as average diameter (z-average) \pm SD and polydispersity index (PDI) from three runs. Light absorption spectra were obtained in a wide wavelength range of 350–650 nm with 2 nm intervals at 24°C using an Infinite M Plex (Tecan, Morrisville, NC, USA) absorbance plate reader. Measurements were done in 100 μ L of 1X PBS (pH 7.4) containing the same concentration of LNP2, DOX, and LNP2 conjugated with DOX (LNP2-DOX) using a transparent 96-well plate.

2.4. Transmission electron microscopy (TEM)

A JEOL 1010 electron microscope system (Jeol, Tokyo, Japan) was used to collect the transmission electron microscopy (TEM) images. Typically, 10 μ L of LNP2-DOX suspension was deposited on thin carbon films supported by copper grids (Ted Pella Inc., Redding, CA, USA) and was dried at 37 °C. The sample was then stained with 2% uranyl acetate (Electron Microscopy Sciences, Hatfield, PA, USA) for 10 min. TEM was operated under an 80 KV voltage mode.

2.5. Doxorubicin release profile

To assess DOX release in a physiological and slightly acidic environment, LNP2-DOX was suspended in 150 μ L of 1X PBS buffer solution adjusted to pH 7.4 or 5.1. The suspensions were placed into dialysis cassettes (MWCO: 20 kDa), and subsequently placed into a beaker with 100 mL of PBS buffer at the same pH values at 37 °C. Beakers were constantly stirred in the dark at 250 rpm for 24 hours. 10 μ L of the solution inside the dialysis cassettes was collected at the indicated time points and fluorescence (λ_{ex} =470 nm, λ_{em} =595 nm) of the samples was detected using an Infinite M Plex (Tecan, Morrisville, NC, USA) fluorescence plate reader to determine the amount of DOX released.

2.6. Cell culture

The human Burkitt lymphoma Raji cell line and luciferase-expressing Raji cell line (Raji Luc+) were purchased from American Type Culture Collection (ATCC, Manassas, VA, USA). Both cell lines were cultured in RPMI medium (ThermoFisher, Waltham, MA, USA) supplemented with 10% (v/v) fetal bovine serum (FBS) and 100 U/mL/100 µg/mL penicillin/streptomycin. Cells were maintained at 37°C in a humidified atmosphere with 5% CO₂. Cells were passaged every 2–3 days after reaching 70% confluence.

2.7. *In vitro* cytotoxicity and luciferase knockdown assays

Luc+ Raji cells were plated at 10,000 cells per well in 96-well plates in 100 µL of RPMI media. Cells were then treated with LNPs at a siRNA dose of 50 nM diluted in RPMI. For dose-dependent cytotoxicity analysis, cells were treated with LNPs at concentrations ranging from 10 to 100 nM of siRNA. DharmaFECT 1 Transfection Reagent (Horizon, Cambridge, UK) was used as a positive control of knockdown according to the manufacturer's protocol. Cell viability was measured using CellTiter-Glo Luminescent Cell Viability assay according to the manufacturer's protocol. Luciferase expression was measured using Luciferase1000 according to the manufacturer's protocol. Cell luminescence was quantified using an Infinite M Plex plate reader (Tecan, Morrisville, NC, USA) and normalized to untreated cells. IC₅₀ for siRNA knockdown was determined on GraphPad Prism 8 software through non-linear regression.

2.8. Confocal microscopy

Raji cells were plated at 5×10⁵ cells per well in a 6-well plate in 1 mL of RPMI media and incubated with 50 nM of LNP2-DOX for 3, 6, and 10 hours at 37 °C. Nuclei were stained using Hoechst 33342 (10 µg/mL). Cells were transferred into glass-bottom chambers and imaged using a confocal laser scanning microscope Zeiss LSM 710 (Zeiss, White Plains, NY, USA) with a 63x oil immersion lens. For siBcl-2-DOX-LNPs, the excitation wavelength was set to 479 nm and emission was detected at 595 nm.

2.9. Western blot

Raji cells were plated at 5×10⁵ cells per well in a 6-well plate in 1 mL of RPMI media and incubated with 50 nM of Bcl-2 siRNA-encapsulating LNP2 (siBcl-2-LNP2) and Luc siRNA-encapsulating LNP2 (siLuc-LNP2) for 48 hours at 37 °C. Cells were then collected, and total cell protein was extracted. Cells were lysed using lysis buffer, and the concentrations of total protein were measured using a BCA assay (Thermo Scientific). 40 µg of protein was then separated using 10% SDS-polyacrylamide gel electrophoresis (SDS-PAGE), and protein was then transferred to PVDF membranes. After blocking with 5% nonfat milk, the blots were incubated overnight with anti-Bcl-2 primary antibodies (R&D Systems) at 4°C. After repeated washing, the blots were incubated with secondary antibodies at room temperature for 1 hour. Protein expression was detected using an enhanced chemiluminescence reagent (Thermo Scientific). GAPDH was used as an internal control.

2.10. Caspase-3 assay

Caspase-3 activity in Raji cells was measured using a Caspase-3 Assay Kit (ab39401, Abcam, Waltham, MA, USA). Raji cells were seeded in a 6-well plate (5×10⁵ cells/well) and then treated with 50 nM of siBcl-2-LNP2 or siBcl-2-LNP2-DOX for

6 hours. Raji cells were collected and incubated at 37 °C in the dark for 1 hour with a fluorescein isothiocyanate conjugate of caspase inhibitor FITC-DEVD-FMK. Caspase-3 signal was quantified using flow cytometry according to the manufacturer's protocol.

2.11. Animal experiments

All animal use was in accordance with the guidelines and approval from the University of Pennsylvania Institution of Animal Care and Use Committee. Male NSG mice aged 6–8 weeks were inoculated with 2×10^6 Raji Luc+ cells per mouse by subcutaneous injection. After two weeks, mice were separated randomly into the following treatment groups: PBS, siLuc-LNP2, siBcl-2-LNP2, and siBcl-2-LNP2-DOX treatment ($n = 5$). PBS and LNP formulations were administered via intratumoral injection every three or four days for 11 days. Mice were treated with LNPs at an siRNA dose of 1 $\mu\text{g}/\text{mouse}$ (DOX concentration equal 80 $\mu\text{g}/\text{mL}$). Tumor growth curves were plotted based on normalized luminescence intensity to day 0 ($\text{Lum}_t/\text{Lum}_0$). Bioluminescence imaging was performed using an IVIS Spectrum Imaging system (Caliper Life Sciences, Waltham, MA, USA) after mice were injected with 150 mg/kg of D-luciferin potassium salt.

2.12. Statistical analysis

Data represent the mean \pm SD for triplicate measurements in each experiment. The results were evaluated statistically with GraphPad Prism 8 software. One-way variance analysis (ANOVA) followed by the post-hoc RIR Tukey's test was applied. Significance level was established at $P < 0.05$.

3. Results and discussion

3.1. Formulation of LNPs encapsulating siRNA

In this study, LNPs were chosen for the co-delivery of siRNA and DOX to lymphoma cells due to their physicochemical properties and *in vivo* potency. We first formulated two siRNA-encapsulating LNPs (LNP1 and LNP2) consisting of four components: a gold standard ionizable lipid (C12-200), cholesterol, a thiolated phospholipid (PTE), and a lipid-anchored polyethylene glycol (PEG) conjugate (C14-PEG-2000)^{32,33}. The ionizable lipid to siRNA weight ratios were 5:1 and 15:1 for LNP1 and LNP2, respectively (Table 1). The LNPs were formulated by microfluidic mixing at a component molar ratio of 50:38.5:10:1.5 (Fig. 1A)³⁴. These molar ratios were selected based on previously optimized data for efficient siRNA delivery³⁵. The original C12-200 LNP incorporating DSPC was also formulated to serve as a positive control. Resulting LNPs were 65–95 nm in z-average diameter with siLuc encapsulation efficiencies between 48% and 72% (Table 1). Additionally, PDIs of the original C12-200 LNP and LNP2 were low (0.032 and 0.078, respectively), while the PDI of LNP1 was equal to 1.0. These PDI values suggested that the original C12-200 LNP and LNP2 formulations were monodisperse. The high PDI value for LNP1 indicated the formulation was polydisperse, and thus suggested that these LNPs had a broad size distribution. All LNPs were neutral or slightly negatively charged, which is consistent with previous studies³⁶. All three LNPs loaded with siRNA against luciferase (siLuc) were then evaluated for their *in vitro* toxicity and ability to knockdown luciferase in a Raji Luc+ cell line. After treatment with LNP1 and DharmaFECT (a commercial siRNA transfection reagent), cell viability was significantly reduced compared to control samples (untreated group, Fig. 2A). By contrast, LNP2 and the original LNP induced minimal

toxic effects at the same concentration. Furthermore, treatment with LNPs led to a decrease in luminescence signal intensity in all groups. However, LNP1, DharmaFECT, and the original LNP were less effective than LNP2 at silencing luciferase expression (Fig. 2B). LNP2 was the most effective formulation, with approximately 60% luciferase silencing efficacy (Fig. 2C). Collectively, these results suggested that LNP2 was the optimal formulation for siRNA knockdown, and thus was selected for subsequent DOX conjugation.

3.2. Synthesis and characterization of DOX-conjugated siRNA LNPs

After the initial screening, DOXO-EMCH, a clinically tested maleimide-containing prodrug, was chosen for conjugation to LNPs. DOXO-EMCH contains a pH-sensitive hydrazone bond, which is relatively stable in blood plasma, but cleavable under slightly acidic conditions such as those in the endosome³⁷. To synthesize LNP2-DOX, we utilized a well-known click chemistry reaction between thiol and maleimide groups that results in a thiosuccinimide product (Fig. 1A)³⁸. DOXO-EMCH was incubated with LNP2 containing free thiol groups. The reaction product was then dialyzed against 1X PBS, sterilized using syringe filters, and characterized. DOX conjugation was examined by absorbance spectroscopy. The UV/Vis absorption spectrum of free DOX along with the spectra of LNP2 and LNP2-DOX are depicted in Fig. 3A. The LNP2-DOX spectrum demonstrated the characteristic shape of the DOX spectrum, indicating a successful conjugation. Importantly, the reaction with DOXO-EMCH was shown to not affect encapsulation efficiency of siRNA in LNPs (Table 1.).

We then measured z-average diameter and PDI of LNP2-DOX, and no significant changes in z-average diameter or PDI were observed compared to LNP2 (Fig. 3B). Additionally, the surface charge of LNP2-DOX was similar to that of unconjugated LNP2. Next, the size of LNP2-DOX and its morphology were confirmed by TEM. The TEM image of LNP2-DOX showed a monodisperse spherical structure with an average size of ~70 nm, which was comparable with DLS results (Fig. 3C). Since the DOXO-EMCH used for LNP2-DOX synthesis is an acid-sensitive prodrug, we investigated the DOX release from LNP2-DOX via hydrolysis of the hydrazone bond³⁹. We performed a drug release experiment in 1X PBS buffer solution adjusted to pH 5.1, which corresponds to the pH of the late endosome/lysosome (Fig. 3C)⁴⁰. At pH 5.1, 80% of DOX was released within 8 hours, and reached almost 90% at 24 hours. In comparison, only 40% of DOX was released from LNP2-DOX at pH 7.4 within 8 hours. These results suggest that DOX can successfully be conjugated to the LNP2 formulation and achieve drug release under acidic conditions.

3.3. Bcl-2 knockdown and DOX cytotoxicity in vitro

A key aspect of siRNA and DOX action is cellular uptake and release into cancer cells (Fig. 1B). To investigate the intracellular distribution of LNP2-DOX, LNP-treated Raji cells were assessed using confocal microscopy. After 3 hours of incubation, strong punctate signals indicative of DOX fluorescence appeared in the cytoplasm (Fig. 4A), indicating that LNP2-DOX was taken up through the endocytic pathway and trapped initially in endosomal compartments, similar to other LNPs reported previously⁴¹. Based on pH-dependent drug release results, it was expected that accelerated DOX release can be achieved in the acidic endosome. After 6 hours of incubation, a weak red fluorescence signal appeared in the nucleus, suggesting that DOX can be successfully released from LNP2-DOX and accumulate in the nucleus. At 10 hours post LNP2-DOX treatment, the DOX fluorescence signal was predominantly localized in the nucleus, where DOX can intercalate within DNA and induce cell apoptosis⁴².

An important consideration for the combination of DOX and Bcl-2 knockdown is to enhance cytotoxicity when cellular anti-apoptotic defense is dampened. First, knockdown of anti-apoptotic Bcl-2 protein by siBcl-2 LNP was confirmed by western blotting. The results showed that after treatment with siBcl-2 LNP2, the level of Bcl-2 protein was down-regulated to 55% of the level of the control group (Fig. 4B). However, based on viability measurements of siBcl-2 LNP2-treated cells, knockdown of Bcl-2 alone was unable to trigger cell death after 48 hours at siRNA doses ranging from 10 to 100 nM (Fig. 4C). These results motivated us to explore the cytotoxicity of siBcl-2 LNP2-DOX. Raji cells incubated with a high dose of siBcl-2 LNP2-DOX for 24 hours showed a significant reduction in cell viability, but no obvious toxicity was observed in low dose-treated cells. This is most likely due to insufficient Bcl-2 knockdown and DOX accumulation at this short incubation time point. To determine this, we measured cell viability at 48 hours post-treatment. As expected, siBcl-2 LNP2-DOX exhibited toxic effects at the lowest tested concentration (25 nM), and reduced cell viability to 60%. The percentage of live cells was further reduced to 20% when cells were treated with 50 nM of siBcl-2 LNP2-DOX and reduced further to 6% at the highest dose (100 nM). Based on these results, the half-maximal inhibitory concentration (IC_{50}) of siBcl-2 LNP2-DOX at 48 hours was calculated to be 25.64 nM. Prior investigations have shown that DOX is a pro-apoptotic anticancer drug.⁴³ Therefore, we measured caspase-3 activity—a crucial mediator of apoptosis—to examine apoptotic pathways⁴⁴. Cells treated with siBcl-2 LNP2 showed a low level of caspase-3 activity comparable to the control group (Fig. 4D and S1), further suggesting that knockdown of Bcl-2 alone is not enough to trigger caspase 3-mediated apoptosis. However, caspase-3 activity was significantly higher in cells treated with Bcl-2 LNP2-DOX than other groups. Collectively, these results indicate that treatment with siBcl-2 LNP2-DOX can activate caspase-3 in Raji cells to induce apoptosis.

3.4. Tumor growth inhibition by siBcl-2 and DOX co-delivered LNPs

To evaluate the therapeutic potential of siBcl-2 LNP2-DOX, we performed an *in vivo* experiment in Raji Luc+ tumor-bearing NSG mice. As a proof-of-concept, different LNP formulations (siLuc LNP2, siBcl-2 LNP2, and siBcl-2 LNP2-DOX) were intratumorally administered to mice at a dose of 1 μ g of siRNA (Fig. 5A). Tumor growth was measured every 3 days by bioluminescence imaging (Fig. 5B). Results showed that tumors in the non-treated control group grew rapidly, causing the tumor luminescence signal on day 11 to be 10 times higher than the tumor luminescence signal on day 0 (Fig. 5C). The second control group, treated with siLuc LNP2, exhibited a similar trend in tumor growth, demonstrating that siLuc LNP2 exhibited no anti-tumor activity. Interestingly, the tumor growth for the siBcl-2 LNP2 treatment group was slowed significantly. While no cytotoxic effect for siBcl-2 LNP2 was observed *in vitro*—potentially due to the lack of pro-apoptotic triggers—such significant *in vivo* anti-tumor activity may be ascribed to existing intrinsic pro-apoptotic pressures such as hypoxia and nutrient shortage⁴⁵. Importantly, tumor growth was inhibited completely after treatment with siBcl-2 LNP2-DOX. After 11 days, tumors had no significant increase in size, suggesting that a combination of siBcl-2 siRNA and DOX was the most effective treatment. In addition to tumor growth examination, body weight was monitored to studying the potential toxic effects of various treatment regimens. As shown in Figure 5D, all groups exhibited no significant weight loss within the 11 days of treatment, and no abnormal changes in mice behavior was observed. Together, these results suggest that DOX-conjugated siBcl-2 LNP2 can serve as a promising regimen for enhanced LNP-based combination chemo- and RNAi therapy.

4. Conclusions

In summary, we have developed a DOX-conjugated siRNA LNP platform for combination chemo- and RNAi therapy. The optimized LNP achieved efficient Bcl-2 silencing while also delivering DOX in a controlled manner. This dual delivery system exhibits strong toxicity in lymphoma cells, due to increased apoptosis. Finally, we demonstrate that introducing DOX into LNPs enhanced Bcl-2-targeted RNAi therapy, and inhibited tumor growth in a mouse model of lymphoma. Therefore, our DOX conjugation strategy holds great promise in augmenting the anti-tumor efficacy of LNP-based siRNA therapy. Together, these results suggest that DOX-conjugated LNPs are a promising candidate for combination cancer therapies, and in the future could be used in the treatment of many types of cancer.

Acknowledgments

M.J.M. acknowledges support from a US National Institutes of Health (NIH) Director's New Innovator Award (DP2 TR002776), a Burroughs Wellcome Fund Career Award at the Scientific Interface (CASI), a grant from the American Cancer Society (129784-IRG-16-188-38-IRG), and the National Institutes of Health (NCI R01 CA241661, NCI R37 CA244911, and NIDDK R01 DK123049). K.B. acknowledges support from Polish National Agency for Academic Exchange (No. PNN/IWA/2019/00057, Poland). R.M.H. was supported by the National Science Foundation Graduate Research Fellowship Program (NSF-GRFP) under Grant No. DGE-1845298. Any opinions, finding, and conclusions or recommendations expressed in this material are those of the authors and do not necessarily reflect the views of the NSF.

Author contributions

K.B. and X.H. contributed equally to this work. K.B., X.H., and M.J.M. conceived the project and designed the experiments. The experiments were performed by K.B., X.H., N.G., and W.Z. and interpreted by all authors. K.B., X.H., and M.J.M. wrote the manuscript. K.B. designed and prepared the figures. All authors edited the manuscript and figures and approved the final version for submission.

Conflicts of interest

The authors declare no conflicts of interest.

References

1. Bray F, Ferlay J, Soerjomataram I, Siegel RL, Torre LA, Jemal A. Global Cancer Statistics 2018: GLOBOCAN estimates of incidence and mortality worldwide for 36 cancers in 185 countries. *CA: A Cancer J Clin* 2018; **68**: 394-424.
2. Sung H, Ferlay J, Siegel RL, Laversanne M, Soerjomataram I, Jemal A, Bray F. Global Cancer Statistics 2020: GLOBOCAN estimates of incidence and mortality worldwide for 36 cancers in 185 countries. *CA: A Cancer J Clin* 2021; **71**: 209-249.
3. Tavan H, Azadi A, Veisani Y. Return to work in cancer patients: A systematic review and meta-analysis. *Indian J Palliat Care* 2019; **25**: 147-152.

4. American Cancer Society. *Cancer Treatment & Survivorship Facts & Figures 2019-2021*. Atlanta: American Cancer Society; 2019.
5. Lage H. An overview of cancer multidrug resistance: a still unsolved problem. *Cell Mol Life Sci* 2008; **65**:3145-3167.
6. Gillet JP, Gottesman MM. Mechanism of multidrug resistance in cancer. In: Zhou J, editors. *Multi-drug resistance in cancer. Methods in molecular biology (methods and protocols)*. New York: Humana Press.; 2010. p. 47-76.
7. Tsujimoto Y, Cossman J, Jaffe E, Croce C. Involvement of the Bcl-2 gene in human follicular lymphoma. *Science* 1985; **228**: 1440–1443.
8. Yip KW, Reed JC. Bcl-2 family proteins and cancer. *Oncogene* 2008; **27**:6398-6406.
9. Brunelle JK, Letai A. Control of mitochondrial apoptosis by the Bcl-2 family. *J Cell Sci* 2009; **122**:437-441.
10. Adams CM, Clark-Garvey S, Porcu P, Eischen CM. Targeting the Bcl-2 family in B cell lymphoma. *Front Oncol* 2019; **8**:636.
11. Wei Y, Cao Y, Sun R, Cheng L, Xiong X, Jin X, He X, Lu W, Zhao M. Targeting Bcl-2 proteins in acute myeloid Leukemia. *Front Oncol* 2020; **10**:2137.
12. Xiong H, Veedu RN, Diermeier SD. Recent advances in oligonucleotide therapeutics in oncology. *Int J Mol Sci* 2021; **22**:3295.
13. DiNardo CD, Konopleva MY. A venetoclax bench-to-bedside story. *Nat Cancer* 2021; **2**:3-5.
14. Knox JJ, Chen XE, Feld R, Nematollahi M, Cheiken R, Pond G, Zwiebel JA, Gill S, Moore M. A phase I-II study of oblimersen sodium (G3139, Genasense) in combination with doxorubicin in advanced hepatocellular carcinoma (NCI #5798). *Invest New Drugs* 2008; **26**:193-194.
15. Marcucci G, Byrd JC, Dai G, Klisovic MI, Kourlas PJ, Young DC, Cataland SR, Fisher DB, Lucas D, Chan KK, Porcu P, Lin ZP, Farag SF, Frankel SR, Zwiebel JA, Kraut EH, Balcerzak SP, Bloomfield CD, Grever MR, Caligiuri. Phase 1 and pharmacodynamic studies of G3139, a Bcl-2 antisense oligonucleotide, in combination with chemotherapy in refractory or relapsed acute leukemia. *Blood* 2003; **101**:425:432.
16. Walker AR, Marcucci G, Yin J, Blum W, Stock W, Kohlschmidt J, Mrózek K, Carroll AJ, Eisfeld AK, Wang ES, Jacobson S, Kolitz JE, Thakuri M, Sutamtewagul G, Vij R, Stuart RK, Byrd JC, Bloomfield CD, Stone RM, Larson RA. Phase 3 randomized trial of chemotherapy with or without oblimersen in older ALM patients: CALGB 10201 (Alliance). *Blood Adv* 2021; **13**:2775-2787.
17. Chen AM, Zhang M, Wei D, Stueber D, Taratula O, Minko T, He H. Co-delivery of doxorubicin and Bcl-2 siRNA by mesoporous silica nanoparticles enhances the efficacy of chemotherapy in multidrug-resistant cancer cells. *Small* 2009; **5**:2673-2677.
18. Cheng D, Cao N, Chen J, Yu X, Shuai X. Multifunctional nanocarrier mediated co-delivery of doxorubicin and siRNA for synergistic enhancement of glioma apoptosis in rat. *Biomaterials* 2012; **33**:1170-1179.

19. Sun W, Chen X, Xie C, Wang Y, Lin L, Zhu K, Shuai X. Co-delivery of doxorubicin and anti-BCL-2 siRNA by pH-responsive polymeric vector to overcome drug resistance in in vitro and in vivo HepG2 hepatoma model. *Biomacromolecules* 2018; **19**:2248-2256.
20. Hou X, Zaks T, Langer R, Dong Y. Lipid nanoparticle for mRNA delivery. *Nat Rev Mater* 2021; **170**: 83-112.
21. Thi TTH, Suys EJ, Lee JS, Nguyen DH, Park KD, Truong NP. Lipid-based nanoparticle in the clinic and clinical trials: from cancer nanomedicine to COVID-19 vaccines. *Vaccines* 2021; **9**:359.
22. Akin A, Maier MA, Manoharan M, Fitzgerald K, Jayaraman M, Barros S, Ansell S, Du X, Hope MJ, Madden TD, Mui BL, Semple SC, Tam YK, Ciufolini M, Witzigmann D, Kulkarni JA, van der Meel R, Cullis PR. The Onpattro story and the clinical translation of nanomedicines containing nucleic acid-based drugs. *Nat Nanotechnol* 2019; **14**:1084-1087.
23. Andreadakis Z, Kumar A, Roman RG, Tollefsen S, Saville M, Mayhew S. The COVID-19 vaccine development landscape. *Nat Rev Drug Discov* 2020; **19**:305-306.
24. Baden LR, El Sahly HM, Essink B, Kotloff K, Frey S, Novak R, Diemert D, Spector SA, Rouphael N, Creech B, McGettigan J, Khetan S, Segall N, Solis J, Brosz A, Fierro C, Schwartz H, Neuzil K, Corey L, Gilbert P, Janes H, Follmann D, Marovich M, Mascola J, Polakowski L, Ledgerwood J, Graham BS, Bennett H, Pajon R, Knightly C, Leav B, Deng W, Zhou H, Han S, Ivarsson M, Miller J, Zaks T. Efficacy and safety of the mRNA-1273 SARS-CoV-2 vaccine. *N Engl J Med* 2021; **384**:403-416.
25. Evers MJW, Kulkarni JA, van der Meel R, Cullis PR, Vader P, Schiffelers RM. State-of-the-art design and rapid-mixing production techniques of lipid nanoparticles for nucleic acid delivery. *Small Methods* 2018; **2**:1700375.
26. Krohn-Grimberghe M, Mitchell MJ, Schloss MJ, Khan OF, Courties G, Guimaraes PPG, Rohde D, Cremer S, Kowalski PS, Sun Y, Tan M, Webster J, Wang K, Iwamoto Y, Schmidt SP, Wojtkiewicz GR, Nayar R, Frodermann V, Hulsmans M, Chung A, Hoyer FF, Swirski FK, Langer R, Anderson DG, Nahrendorf M. Nanoparticle-encapsulated siRNA for gene silencing in the haematopoietic stem-cell niche. *Nat Biomed Eng* 2020; **4**:1076-1089.
27. Ickenstein LM, Garidel P. Lipid-based nanoparticles formulations for small molecules and RNA drugs. *Expert Opin Drug Deliv* 2019; **16**:1205-1226.
28. Kratz F. DOXO-EMCH (INNO-206): the first albumin-binding prodrug of doxorubicin to enter clinical trials. *Expert Opin Investig Drugs* 2007; **16**: 855-866.
29. Billingsley MM, Singh N, Ravikumar P, Zhang R, June CH, Mitchell MJ. Ionizable lipid nanoparticle-mediated mRNA delivery for human CAR T engineering. *Nano Lett* 2020; **20**:1578-1589.
30. Shepherd SJ, Warzecha CC, Yadavali SY, El-Mayta R, Alameh MG, Wang L, Weissman D, Wilson JM, Issadore D, Mitchell MJ. Scalable mRNA and siRNA lipid nanoparticle production using a parallelized microfluidic device. *Nano Lett* 2021; **21**:5671-5680.

31. Riley RS, Kashyap MV, Billingsley MM, White B, Alameh MG, Bose SK, Zoltick PW, Li H, Zhang R, Cheng AY, Weissman D, Peranteau WH, Mitchell MJ. Ionizable lipid nanoparticle for in utero mRNA delivery. *Sci Adv* 2021; **7**: eaba1028.
32. El-Mayta R, Zhang R, Shepherd SJ, Wang F, Billingsley MM, Dudkin V, Klein D, Lu HD, Mitchell MJ. A nanoparticle platform for accelerated in vivo oral delivery screening of nucleic acids. *Adv Therap* 2021; **4**:2000111.
33. Zhang R, El-Mayta R, Murdoch TJ, Warzecha CC, Billingsley MM, Shepherd SJ, Gong N, Wang L, Wilson JM, Lee D, Mitchell MJ. Helper lipid structure influences protein adsorption and delivery of lipid nanoparticles to spleen and liver. *Biomater Sci* 2021; **9**:1449-1463.
34. Guimaraes PPG, Zhang R, Spektor R, Tan M, Chung A, Billingsley MM, El-Mayta R, Riley RS, Wang L, Wilson JM, Mitchell MJ. Ionizable lipid nanoparticles encapsulating barcoded mRNA for accelerated in vivo delivery screening. *J Control Release* 2019; **316**:404-417.
35. Whitehead KA, Dorkin JR, Vegas AJ, Chang PH, Veiseh O, Matthews J, Fenton OS, Zhang Y, Olejnik KT, Yesilyurt V, Chen D, Barros S, Klebanov B, Novobrantseva T, Langer R, Anderson DG. Degradable lipid nanoparticles with predictable in vivo siRNA delivery activity. *Nat Comm* 2014; **5**:4277.
36. Whitehead KA, Matthews J, Chang PH, Niroui F, Dorkin JR, Severgnini M, Anderson DG. In vitro-in vivo translation of lipid nanoparticles for hepatocellular siRNA delivery. *ACS Nano* 2012; **6**:6922-6929.
37. Walker JA, Sorkin MR, Alabi CA. *Quantitative determination of intracellular bond cleavage*. In: Rosania GR, Thurber GM, editors. Quantitative analysis of cellular drug transport, disposition, and delivery. New York: Humana Press.; 2021. p. 305-330.
38. Northrop BH, Frayne SH, Choudhary U. Thiol-maleimide “click” chemistry: evaluation of the influence of solvent, initiator, and thiol on the reaction mechanism, kinetics, and selectivity. *Polym Chem* 2015; **6**:3415-3430.
39. Butowska K, Woziwodzka A, Borowik A, Piosik J. Polymeric nanocarriers: a transformation in doxorubicin therapies. *Materials* 2021; **14**:2135.
40. White KA, Grillo-Hill BK, Barber DL. Cancer cell behaviors mediated by dysregulated pH dynamics at a glance. *J Cell Sci* 2017; **130**:663-669.
41. Yu B, Wang X, Zhou C, Teng L, Ren W, Yang Z, Shih CH, Wang T, Lee RJ, Tang S, Lee LJ. Insight into mechanism of cellular uptake of lipid nanoparticles and intracellular release of small RNAs. *Pharm Res* 2014; **31**:2685-2695.
42. Patel AG, Kaufmann SH. Cancer: how does doxorubicin work? *eLife* 2012; **1**:e00387.
43. Decaudin D, Geley S, Hirsch T, Castedo M, Marchetti P, Macho A, Kofler R, Kroemer G. Bcl-2 and Bcl-XL antagonize the mitochondrial dysfunction preceding nuclear apoptosis induced by chemotherapeutic agents. *Cancer Res* 1997; **57**:62-67.
44. Porter AG, Jänicke RU. Emerging roles of caspase-3 in apoptosis. *Cell Death Differ* 1999; **6**:99-104.

45. Shimizu A, Eguchi Y, Kamiike W, Itoh Y, Hasegawa J, Yamabe K, Otsuki Y, Matsuda H, Tsujimoto Y. Induction of apoptosis as well as necrosis by hypoxia and predominant prevention of apoptosis by Bcl-2 and Bcl-X_L. *Cancer Res* 1996; **56**:2161-2166.

Figure captions

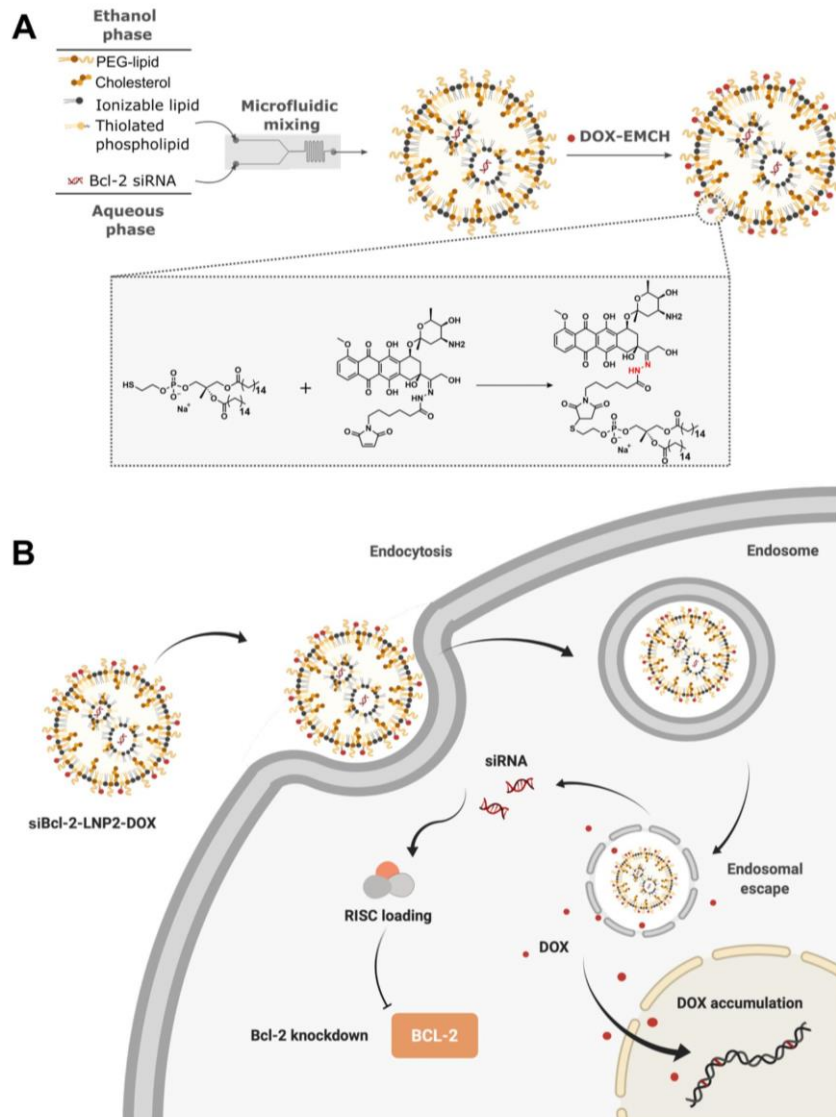


Figure 1. (A) A schematic illustrating the preparation of doxorubicin-conjugated Bcl-2 siRNA loaded lipid nanoparticles (siBcl-2 LNP2-DOX). LNPs were formulated by microfluidic mixing, followed by conjugation with DOX through a thiol-maleimide Michael addition click reaction between DOXO-EMCH and thiolated phospholipid PET. (B) Schematic diagram of intracellular co-delivery of siBcl2 and DOX enabled by siBcl-2 LNP2-DOX.

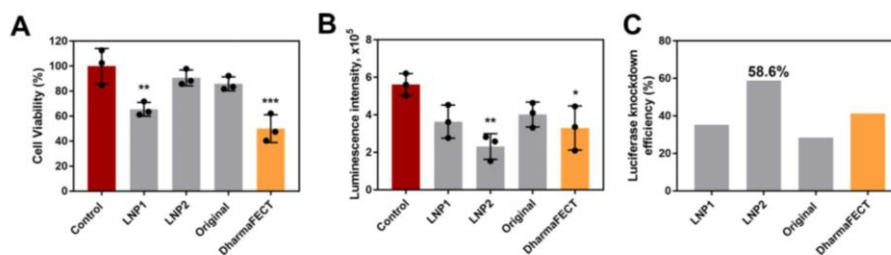


Figure 2. LNP-mediated luciferase knockdown in vitro. (A) Viability of Raji cells treated with 50 nM siRNA for 48 hours using different LNP formulations. Data are plotted as mean \pm SD, $n=3$; * $P<0.05$, vs. Control; (B) Luciferase expression in Raji cells after treatment with different LNP formulations for 48 hours at a dose of 50 nM siRNA. Data are plotted as mean \pm SD, $n=3$; * $P<0.05$, vs. Control; (C) Luciferase knockdown efficiency in Raji cells. Data are plotted as average mean * $P<0.05$, vs. Control.

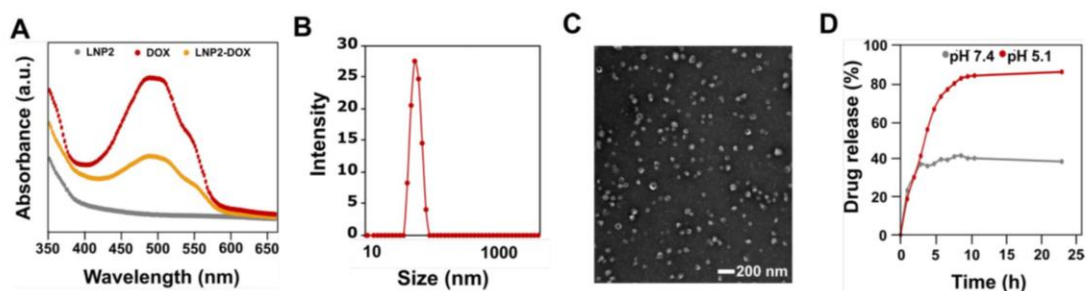


Figure 3. Physicochemical characterization of DOX-conjugated siRNA LNPs. (A) UV-vis spectra of LNP2, DOX, and LNP2-DOX in PBS; (B) The size (z-average) distribution of a representative sample of siBcl-2 LNP2-DOX, revealing a diameter of 70 nm using DLS (C) TEM image of siBcl-2 LNP2-DOX. Scale bar = 200 nm; (D) The time-dependent release profiles of DOX from Bcl-2 LNP2-DOX at pH 5.1 and pH 7.4.

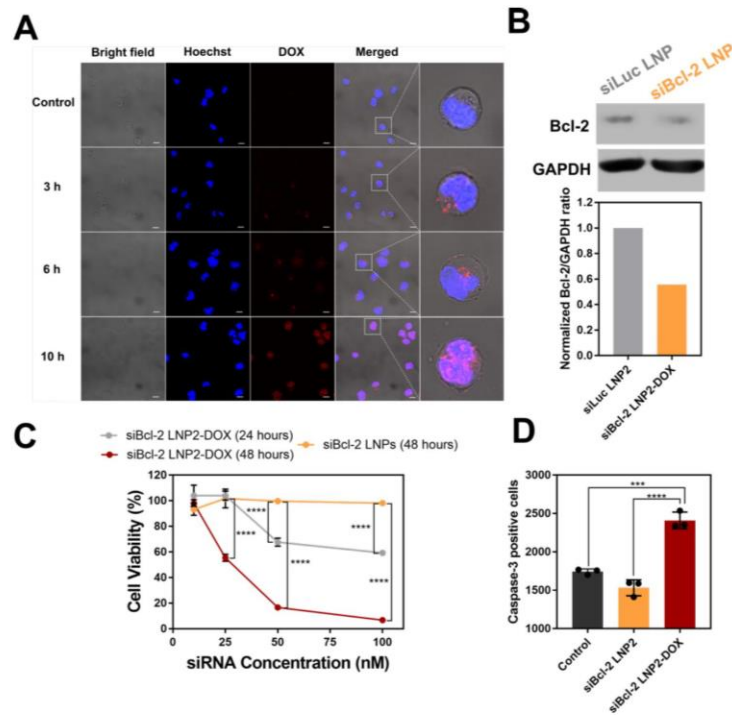


Figure 4. Intracellular delivery, Bcl-2 knockdown, and caspase-3 activity *in vitro* using DOX-conjugated siRNA LNPs. (A) Confocal microscopy images of Raji cancer cells. Cells were incubated with siBcl-2 LNP2-DOX for 3, 6, and 10 hours. Scale bar = 10 μm .; (B) Detection of Bcl-2 knockdown by Western blotting; (C) Viability of Raji cells treated at a range of concentrations (0-100 nM) for 24 or 48 hours using different LNP formulations. Data are plotted as mean \pm SD, $n=3$; * $P<0.05$, vs. Control.; (D) Caspase-3 activity assessed by a FITC-DEVD-FMK probe after 6 hours of incubation with 50 nM of Bcl-2 LNP and Bcl-2 LNP2-DOX. Data are plotted as mean \pm SD, $n=3$; * $P<0.05$.

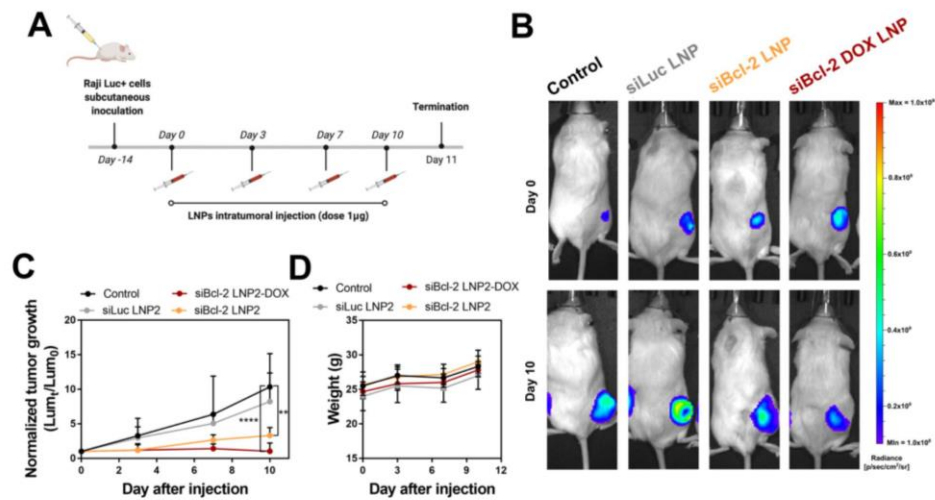


Figure 5. *In vivo* delivery of DOX-conjugated siRNA LNPs to treat a mouse model of lymphoma. (A) Drug treatment schedules for *in vivo* experiments. The treatment doses for Bcl-2 siRNA and DOX were 1 μg and 0.1 μg per mouse, respectively.; (B) Representative bioluminescence images of tumor-bearing mice; (C) Tumor growth curves for different treatment groups. All data is normalized to bioluminescence radiant efficiency (photons/sec/cm²/sr) on day 0. Data are plotted as mean \pm SD, $n=5$; * $P<0.05$ vs. Control. (D) Average body weight of different treatment groups during the treatment schedule.

Table 1 LNP characterization data consisting of hydrodynamic diameter, polydispersity index (PDI), encapsulation efficiency (EE), and zeta potential of each LNP formulation (\pm standard deviation).

LNP	Phospholipid	EE (%)	Ionizable lipid: siRNA (wt:wt)	Size (nm)	PDI	Zeta potential (mV)
Original	DSPC	71.80	5:1	65.59 \pm 1.85	0.032	-4.96 \pm 1.13
LNP1	PTE	48.25	5:1	95.06 \pm 5.29	1.000	-13.83 \pm 3.73
LNP2	PTE	65.06	15:1	69.88 \pm 4.16	0.078	-5.02 \pm 1.68
LNP2-DOX	PTE	65.00	15:1	72.60 \pm 1.49	0.120	-6.42 \pm 0.27

Supporting Information

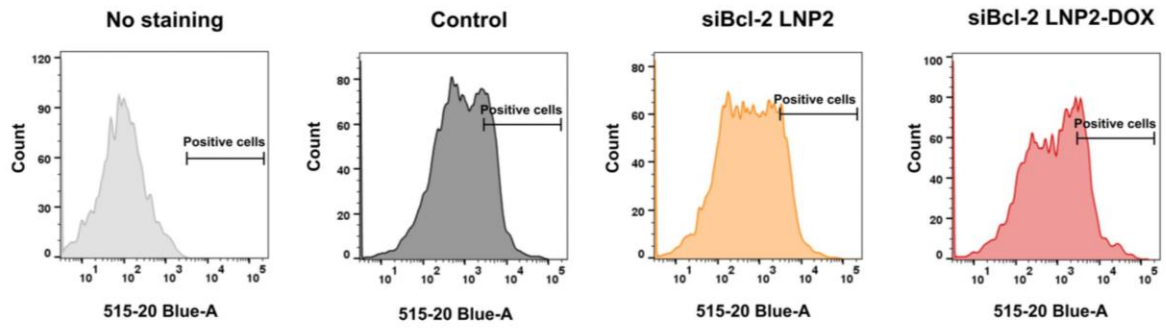


Figure S1. Representative charts of FITC-DEVD-FMK-stained cells analyzed by flow cytometry. Cells were treated with 50 nM Bcl-2 LNP2 and Bcl-2 LNP2-DOX for 6 h and then stained with 1 μ M FITC for flow cytometry analysis.

5. **K. Butowska**, A. Woziwodzka, A. Borowik, J. Piosik, *Polymeric nanocarriers: a transformation in doxorubicin therapies*. *Materials*, **2021**, 14, 2135. [P5]

Review

Polymeric Nanocarriers: A Transformation in Doxorubicin Therapies

Kamila Butowska¹, Anna Woziwodzka¹, Agnieszka Borowik^{1,2} and Jacek Piosik^{1,*} 

¹ Laboratory of Biophysics, Intercollegiate Faculty of Biotechnology, University of Gdansk and Medical University of Gdansk, Abrahamia 58, 80-307 Gdańsk, Poland; kamila.butowska@phdstud.ug.edu.pl (K.B.); anna.woziwodzka@ug.edu.pl (A.W.); agnieszka.borowik@phdstud.ug.edu.pl (A.B.)

² Aging and Metabolism Research Program, Oklahoma Medical Research Foundation (OMRF), Oklahoma City, OK 73104, USA

* Correspondence: jacek.piosik@biotech.ug.edu.pl; Tel.: +48-58-523-6311

Abstract: Doxorubicin, a member of the anthracycline family, is a common anticancer agent often used as a first line treatment for the wide spectrum of cancers. Doxorubicin-based chemotherapy, although effective, is associated with serious side effects, such as irreversible cardiotoxicity or nephrotoxicity. Those often life-threatening adverse risks, responsible for the elongation of the patients' recuperation period and increasing medical expenses, have prompted the need for creating novel and safer drug delivery systems. Among many proposed concepts, polymeric nanocarriers are shown to be a promising approach, allowing for controlled and selective drug delivery, simultaneously enhancing its activity towards cancerous cells and reducing toxic effects on healthy tissues. This article is a chronological examination of the history of the work progress on polymeric nanostructures, designed as efficient doxorubicin nanocarriers, with the emphasis on the main achievements of 2010–2020. Numerous publications have been reviewed to provide an essential summation of the nanopolymer types and their essential properties, mechanisms towards efficient drug delivery, as well as active targeting stimuli-responsive strategies that are currently utilized in the doxorubicin transportation field.

Keywords: doxorubicin; drug delivery; polymers; targeted therapy; anticancer treatment; controlled release



Citation: Butowska, K.; Woziwodzka, A.; Borowik, A.; Piosik, J. Polymeric Nanocarriers: A Transformation in Doxorubicin Therapies. *Materials* **2021**, *14*, 2135. <https://doi.org/10.3390/ma14092135>

Academic Editor: Eun-Kyung Lim

Received: 1 March 2021

Accepted: 20 April 2021

Published: 22 April 2021

Publisher's Note: MDPI stays neutral with regard to jurisdictional claims in published maps and institutional affiliations.



Copyright: © 2021 by the authors. Licensee MDPI, Basel, Switzerland. This article is an open access article distributed under the terms and conditions of the Creative Commons Attribution (CC BY) license (<https://creativecommons.org/licenses/by/4.0/>).

1. Introduction

1.1. Doxorubicin and Other Anthracyclines

Anthracyclines, including doxorubicin (DOX), daunorubicin, and epirubicin, are among the most active antitumor compounds with the widest spectrum of activity in human cancers such as carcinomas, sarcomas, and hematological malignancies. They are widely used (alone or in combination with other cytotoxic agents) in clinical practice for the treatment of lung, breast, ovarian, and urinary bladder cancers, as well as multiple myeloma, soft tissue sarcoma, osteosarcoma, leukemias, and Hodgkin's lymphoma. DOX was initially obtained from *Streptomyces peucetius* actinobacteria isolated from a soil sample, identified, and developed in the 1960s [1,2]. Although DOX was granted marketing authorization nearly five decades ago, it is present on the current World Health Organization Model List of Essential Medicines, listing the most efficient, safe, and cost-effective medicines needed in the healthcare system [3].

Apart from its high efficacy in monotherapy (especially in treatment of metastatic breast cancer), several combination therapies including DOX were also developed. The combination of DOX with cyclophosphamide, vincristine, and prednisone is used for treatment of diffuse large cell non-Hodgkin's lymphomas [4]. The combination of DOX with bleomycin, vincristine, and dacarbazine is beneficial and well tolerated in patients with Hodgkin's lymphoma [4]. Several combination regimens consisting of DOX are used

for treatment of breast cancer (DOX with cyclophosphamide and/or taxotere, DOX with cyclophosphamide and fluorouracil).

Structurally, DOX is a glycoside of anthracyclinone. It contains an anthraquinone chromophore placed within a planar aromatic system of four cycles, bound by a glycosidic bond to daunosamine (Figure 1). Anthraquinone groups can participate in redox reactions, contributing to the generation of reactive chemical species, which might be associated with anthracycline cardiotoxicity [5].

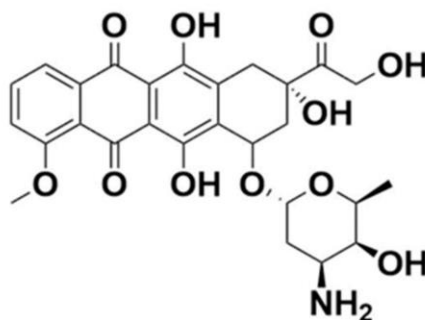


Figure 1. Chemical structure of doxorubicin.

1.2. Doxorubicin Mechanism of Action

To date, several distinct mechanisms of DOX action are discussed (Figure 2). The first and primary one includes the interaction of DOX with mammalian topoisomerase II, stabilization of enzyme–DNA complex, and resulting inhibition of single- and double-strand DNA breaks re-ligation during the DNA replication process [6]. This leads to irreversible DNA damage and cell death. Importantly, this mode of DOX action is specific for proliferating (e.g., cancer) cells which, mitotically–active, are predominantly affected by topoisomerase II–induced DNA breaks [7]. Such a mechanism of action was confirmed in *in vitro* studies on cell lines with mutated or downregulated topoisomerase II, in which resistance to DOX was reported [8–10]. Intercalation of DOX into DNA double–helix is well–evidenced and widely accepted, and 5′TCA was reported as a consensus sequence for the highest DOX affinity [11]. Nevertheless, the actual role of DOX intercalation to DNA in topoisomerase II–mediated DNA damage remains unknown. Topoisomerase II–related DNA breaks are reported at DOX concentrations which fall below the DOX–DNA association constant, along with the fact that selected anthracycline analogs do not intercalate into DNA but still exert cytotoxic activity, might suggest that DOX intercalation to DNA is not essential for its interference with topoisomerase II [12,13].

Intercalation of DOX into DNA, although possibly not involved in targeting topoisomerase II, has an impact on several vital intracellular processes. It can affect the activity of enzymes involved in DNA replication and transcription, such as helicases, DNA, or RNA polymerases [14,15]. Topological DNA changes following DOX intercalation were also reported to be associated with increased nucleosome turnover around promoters, which affected levels of gene expression [16]. DOX-related removal of nucleosomes at open chromatin regions, which alters epigenetic regulation of transcription and contributes to reduced DNA repair of DOX–induced double–strand breaks, was recently reported [17].

Apart from its well–established topoisomerase II–mediated cytotoxicity, DOX, while undergoing intracellular oxidation and reduction cycles, leads to the generation of reactive oxygen species. This exposes nuclear and mitochondrial DNA to oxidative stress and can exert additional cytotoxic effects [18,19]. Indeed, oxidized DNA bases are detected in the blood and urine of patients treated with DOX [20,21]. Additionally, DOX was shown to form covalent adducts with DNA, which can induce apoptosis, further contributing to the overall cytotoxic activity of the drug [22,23]. All in all, at DOX concentrations

reflecting peak plasma concentration during treatment, targeting topoisomerase II seems to be the primary mechanism of antitumor action, whereas, at higher drug concentrations, the toxicity of free radicals and DNA cross-linking may become relevant [24].

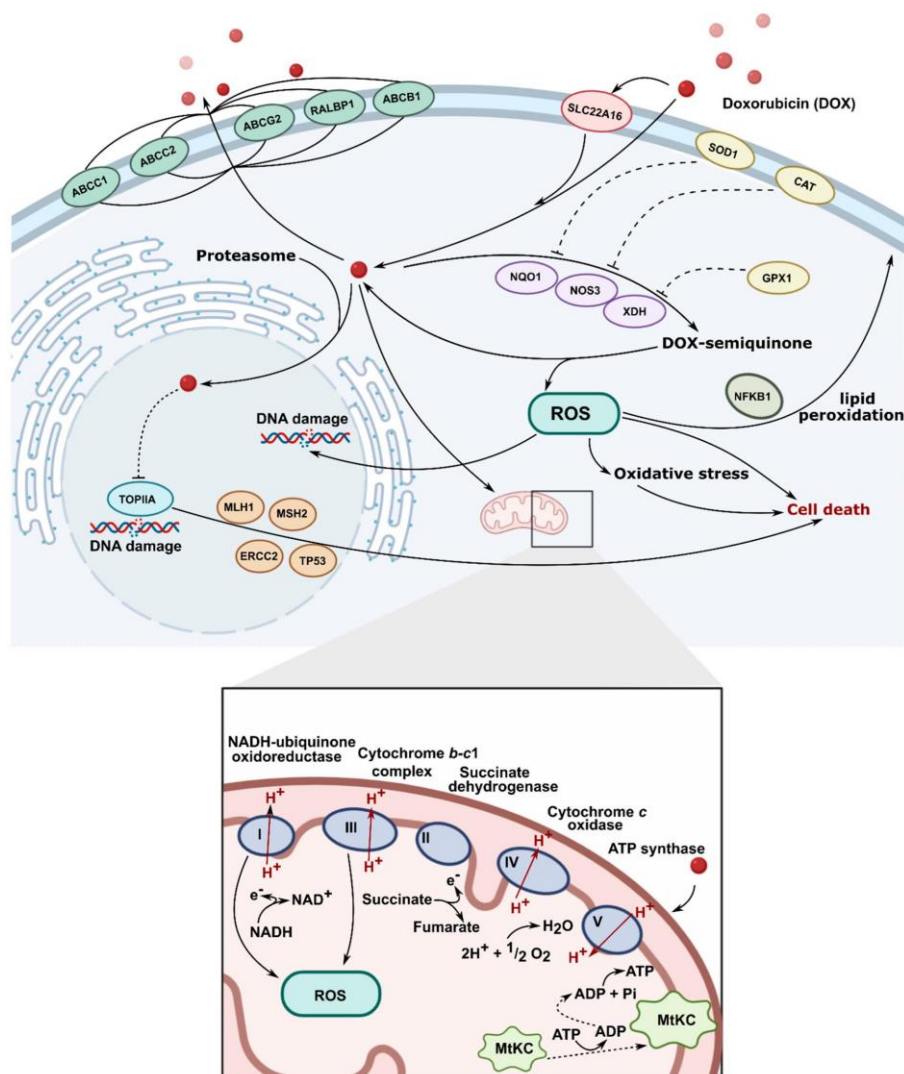


Figure 2. Molecular mechanism of action of doxorubicin (TOPIIA-topoisomerase II, ROS-reactive oxygen species).

1.3. Limitations of DOX Therapy

Two important limitations associated with antitumor therapy with DOX are recognized: development of drug resistance and treatment toxicity, associated with the occurrence of serious adverse effects. The former include enhanced drug efflux (specific for anthracyclines and through multidrug resistance transporters), altered topoisomerase II

activity, and enhanced antioxidant defense [25]. Cardiac toxicity, both acute and chronic, represents the major complication associated with DOX treatment and constitutes the main reason for dose-limited drug administration [26]. Acute cardiotoxic effects such as arrhythmias, hypotension, and electrocardiographic alterations are transient and disappear at treatment cessation. Chronic cardiotoxicity is dose-dependent; more than a quarter of patients receiving DOX with a cumulative dose of 550 mg/m² would develop congestive heart failure [27]. The mechanism responsible for DOX heart toxicity is not fully understood, but oxidative stress disrupting major mitochondrial functions is considered the most presumable.

DOX induces myelosuppression, mainly in the form of leukopenia (principally granulocytopenia), neutropenia, or thrombocytopenia, with up to 80% of patients treated with conventional doses of DOX being affected [4,28]. The severity of myelotoxicity is dose-dependent; therefore, it represents the major dose-limiting side effect of anthracycline therapy.

Besides the heart and bone marrow, toxic effects of DOX are also observed in the liver, kidney, and brain [26]. Other side effects of DOX include nausea and vomiting, stomatitis, mucositis, alopecia, and neurologic disturbances (dizziness, hallucinations) [4,29]. Severe vesicant reactions might also occur upon extravasation of DOX which can lead to severe local tissue necrosis and reduced mobility in the adjacent joints.

Cancer survivors in childhood have more than a two-fold increased risk of acute leukemia and solid tumors at the age of 40, and the history of DOX treatment has a well-established association with the development of secondary cancer [30].

For decades, significant effort has been made to develop new anthracycline derivatives that would markedly reduce DOX toxic effects and at least maintain its antitumor activity [31,32]. Although a few of them (e.g., epirubicin, idarubicin, valrubicin) were granted marketing authorization, no evident or clinically relevant benefit in terms of enhanced effectiveness and/or improved safety profile has been achieved so far. More recently, heteroarene-fused anthracenediones, a combination of anthraquinone and polyphenolic structures, and bis-intercalating agents, have been described as novel promising approaches [33–35].

The rapid development of novel drug delivery systems (DDSs), which are aimed at directing the drug specifically to neoplastic cells, provides promising tools to minimize DOX systemic toxicity. Such an approach, while maintaining DOX satisfactory profile of antitumor activity, would allow the delivery of higher doses of the drug directly to the cancer cells. Here, we review recent advances on new platforms of targeted DOX delivery.

2. Evolution of Drug Delivery Systems

2.1. From Macro- to Nanoscale

The history of DDSs stretches back to 1960 when Folkman discovered a constant rate drug delivery implant for prolonged therapy used a silicone rubber tube (Silastic[®]) loaded with the drug [36,37]. The seminal work of Folkman et al. was an inspiration for scientists who focused on new concepts of zero-order-controlled drug delivery in the macroscale using various types of polymers in a wide field of medicine. In the following years, Ocusert[®] containing an anti-glaucoma drug, Progestesert[®] releasing progesterone in the uterine cavity, or Implanon[®] as sub-dermal devices were developed [38]. In 1976, Folkman and Langer reported a pioneering work showing that proteins and other macromolecules (large molecular weight drugs) could undergo sustained release from non-inflammatory polymers [39]. On the turn of the 1980s and 1990s, other strategies of zero-order DDSs with controlled diffusions such as skin patches and osmotic capsules were investigated. Since the first demonstration of low and large molecular weight drug delivery matrices, DDSs have evolved from zero-order macroscale systems to biodegradable microscopic polymers, using poly(glycolic acid) (PGA), poly(lactic-co-glycolic acid) (PLGA), or copolymers of PGA-PLGA [40]. Then, various approaches were adopted to deliver drugs by rationally designed polymers enter the nano-sized era and showed significant therapeutic potential [41,42].

Indeed, polymeric systems such as polymer–drug conjugates, block copolymers, and polymer–protein conjugates, also lipid and inorganic nanoparticles or multicomponent systems, were widely utilized in combination with therapies [43–46]. During the last decade, there has been significant progress in the development of high-performance DDSs. They became increasingly complex, and it became possible to control their chemical and physical properties. Since many aspects of these topics were thoroughly described in previous reviews, we focused on the latest trends in the doxorubicin delivery systems combined with increasingly innovative systems [47,48].

2.2. Bringing New Life to Carriers

All above mentioned polymeric subclasses used specific polymers with exceptional properties to develop sophisticated and biodegradable DDSs in nanosize ranging from 1 to 100 nm [49,50]. Polymeric-based nanoparticles (PNPs), based on natural and synthetic polymers, have various physicochemical properties, and different architectures and sizes, which allow them to carry drugs to the target [51]. Therefore, the choice of the polymer, drug loading, and shape are crucial for the design of PNPs in a controlled manner to achieve the desired DDSs (Figure 3). Additionally, PNPs show significant solubility and stability, higher targeting specificity, and exhibit controlled drug release by carrier degradation, diffusion through carrier matrix, or dissociation mechanisms e.g., photo-dissociation [52]. From the biological standpoint, polymeric nanocarriers showed a longer half-life in pharmacokinetic studies and have an enhanced permeability and retention effect which allows them to accumulate in cancer tumors rather than in healthy tissues [53]. With this fact in mind, many natural and synthetic polymers, as well as pseudosynthetic ones, attract attention in medicine, as antineoplastic or antimicrobial drug carriers (Figure 4). To note, natural polymers are more biocompatible than synthetic, nevertheless, some natural polymers are highly immunogenic [54]. On the other hand, synthetic polymers are less biodegradable than the natural ones, but this may be altered through structural modifications. Hence, current efforts focused on synthetic polymers to control the monomer class and its ratio, as well as molecular weight and crosslinking of the polymer. Modern polymer chemistry takes advantage of different structures, from a linear block and gradient copolymers to increasingly intricate polymers, including stars, combs, and brushes, to dendronized and (hyper)branched polymers [55–57]. This demanded many polymerization methods to be employed for polymers to be formed in a piece-by-piece fashion. The most effective and widely used methods are controlled radical methods, such as reversible addition fragmentation chain transfer (RAFT), and atom transfer radical polymerization (ATRP), which were reported as more effective than conventional polymerization techniques [58,59]. Considering the wide spectrum of polymers and efficient polymerization methods, numerous potential DDSs appeared to offer many advantages including self-assembly, biocompatibility, and high loading capacity.

After years of research, Doxil[®]—pegylated liposomal DOX delivery systems—was approved by Food and Drug Administration (FDA) in 1995. Additionally, Myocet[®] (non-pegylated liposomal DOX) in 2000 has received Fast Track Designation from FDA for the treatment of HER2 positive breast cancer and has been approved in Europe and Canada. Despite the well-known and approved DOX delivery systems, efforts continued to develop more efficient and safe carriers [60,61].

The first natural polymer–DOX conjugate, called AD-70, which entered clinical trials in 1993, employed polymer derivatives of the oxidized dextran (DX) coupled with DOX (DX–DOX) via Schiff base [62]. AD-70 conjugate was highly selective for DOX delivery in an animal model; unfortunately, in a Phase I clinical study, substantial toxicity was observed leading to thrombocytopenia and hepatotoxicity in the patients.

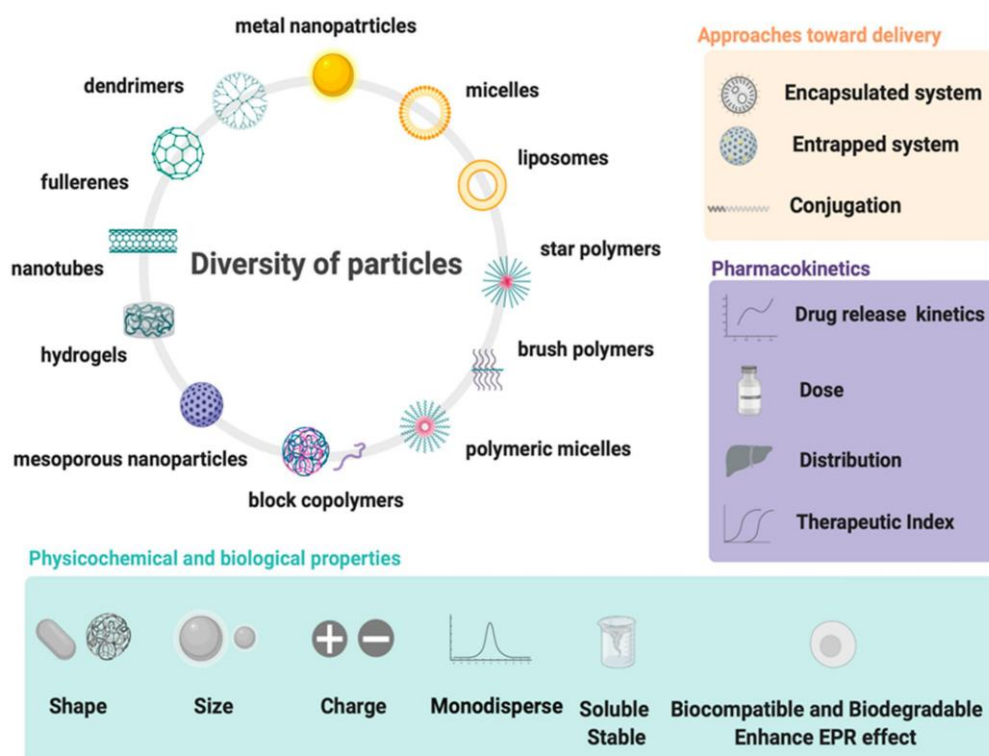
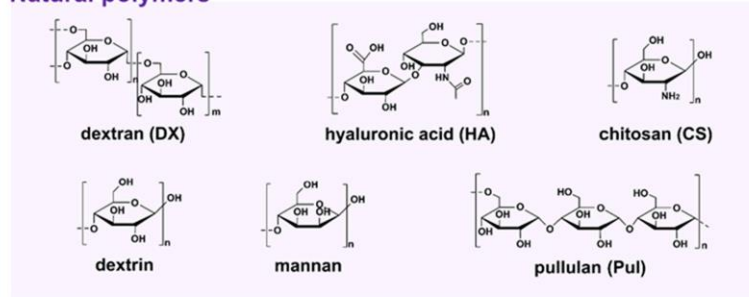


Figure 3. Design and properties requirements for drug delivery systems using wide spectrum of particles.

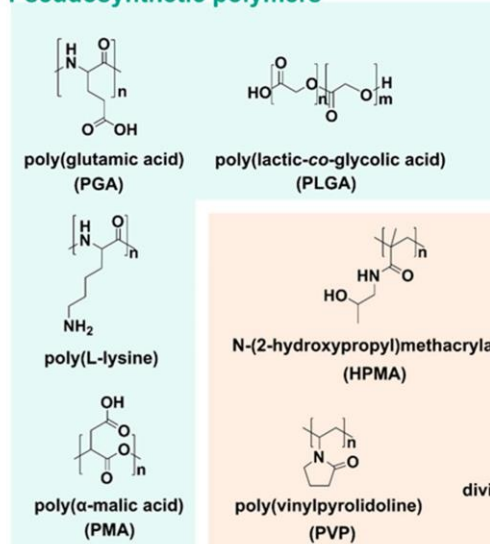
In the following years, Mitra et al. encapsulated DX–DOX conjugate into chitosan (CS) nanoparticles using reverse microemulsion [63]. This resulted in faster regression of tumor volume from $514 \pm 6 \text{ mm}^3$ in the middle of treatment to $170 \pm 7.3 \text{ mm}^3$ at day 90. Throughout 90 days of the study, Balb/C mice treated with DX–DOX encapsulated into CS showed almost 50% survival rate, while mice treated with DX–DOX demonstrated only a 20% survival rate. Furthermore, Janes et al. described a similar conception that included encapsulation of DOX into CS nanoparticles (with encapsulation efficiency ~20%) through the charge repulsion between the polymer and the drug. Encapsulation of the drug in CS was possible via the interaction of a DOX amino group with incorporated DX sulfate [64]. Another strategy for designing DDSs, reported in 2010 by Qi et al., used a simple protocol to develop biocompatible bovine serum albumin (BSA)–DX–CS nanoparticles by heating, with DOX loaded into nanoparticles by diffusion following pH change from 5.4 to 7.4 [65]. Hepatoma H22 tumor-bearing mice treated with 12.0 mg/kg of DOX nanoparticles had prolonged life from 10.3 to 14.8 days, but tumor growth was reduced less effectively compared with free DOX. Similarly, in the study by Du et al., BSA was used to synthesize a water-soluble DOX delivery system with higher tumor selectivity achieved by linking to folic acid (FA), which binds to folate receptors over-expressed on the surface of mammary human cancer cells [66]. With the continuing desire to increase the DOX loading and entrapping capacity into a carrier, Maspoch's group prepared coordination polymer particles generated by connecting Zn^{2+} metal ions through 1,4-bis(imidazol-1-ylmethyl)benzene organic ligands (bix) via coordination polymerization followed by fast precipitation [67]. DOX entrapped into Zn(bix) showed ~80% of drug released in PBS pH = 7.4 at 37 °C within 8 h, suggesting gradual erosion of Zn(bix) in time.

DOX/Zn(bix) diminished human promyelocytic leukemia HL60 cells viability to 25% at higher concentrations $\sim 10 \mu\text{M}$ with IC_{50} of $5.2 \mu\text{M}$. Against the HeLa cell line, Mrówczyński et al. developed polydopamine coated Fe_3O_4 nanoparticles through a coprecipitation method and oxidative polymerization of dopamine loaded with DOX [68]. The maximum of DOX release was achieved after 24 h. The cellular study against HeLa cells showed that after three days of incubation, cell viability dramatically decreased to 6% at a concentration of $100 \mu\text{g}/\text{mL}$.

Natural polymers



Pseudosynthetic polymers



Synthetic polymers

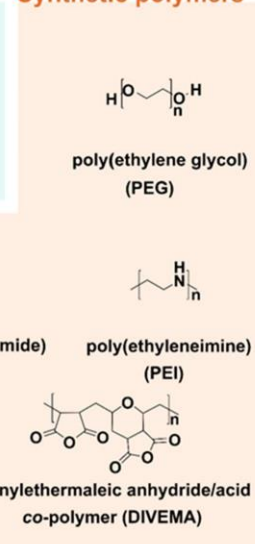


Figure 4. Structures of natural, pseudosynthetic, and synthetic polymers used for drug delivery applications.

Currently, the rise of nanotechnology and polymer science provided many novel DDSs for efficient anticancer therapy by rational design, and allows one to study the behavior of nanoparticles on the cellular level. The theoretical and experimental findings shown in 2020 by Zhang et al. demonstrated the criteria for the preparation of new fluorinated polymers for DDSs, denoted poly(oligo(ethylene glycol) methyl ether acrylate) $_m$ -perfluoropolyether (poly(OEGA)-PFPE; where $m = 5, 10,$ and 20) [69]. Block copolymers containing OEGA and PFPE with different fluorine contents (28.7 weight percentage (wt.%) ($m = 5$, named P5), 17.0 wt.% ($m = 10$, named P10), and 9.8 wt.% ($m = 20$, named P20) were prepared through

RAFT and conjugated with DOX via a hydrazine bond. Molecular dynamics (MD) simulations were consistent with experimental results and showed single-chain folded conformation of DOX-conjugated P20, whereas DOX-conjugated P5 and DOX-conjugated P10 formed micelle-like assemblies. Moreover, MD results, performed with NAMD code, investigating interactions between DOX-conjugated poly(OEGA)_m-PFPE with a cell membrane, highlighted faster diffusion across the membrane of DOX-conjugated P20 than P5 and P10 because of its small hydrophobic core (PFPE). Furthermore, DOX-conjugated P20 showed higher cellular uptake and therapeutic efficacy toward breast cancer cell line MCF-7 than the P5 and P10.

3. Stimuli-Responsive Drug Delivery Systems

3.1. Choose Your Target

Further studies showed that polymers can be combined with inorganic nanoparticles and small molecules to create stimuli-responsive or targeted DDSs (Figure 5) [70–73]. The targeting of DDSs focuses on both active targeting and improving the efficacy by stimuli-responsive approaches. For example, monoclonal antibodies (mAbs) are becoming increasingly popular, i.e., trastuzumab, cetuximab, or bevacizumab, and, apart from their intrinsic anticancer activity, are proposed to be used for selective delivery of antineoplastic drugs to tumors [74–77]. Additionally, to achieve active targeting, a large number of ligands have been employed, including polysaccharides and peptides (i.e., hyaluronic acid and RGD peptide), as well as small molecules like folate or anisamidephenylboronic acid [78,79]. Furthermore, overexpression of enzymes, i.e., proteases, is another approach that can be used to design responsive DDSs [80,81]. In the enzyme-sensitive DDSs, the peptide side chain is designed as a specific substrate of a target enzyme that could directly release the drug from a carrier. Other promising strategies include chemical stimuli-responsive DDSs that can release the drug from a carrier by pH changes and using acid-labile or redox-responsive chemical bonds [82,83]. Among the common physical stimuli, thermo/magnetic-responsiveness and light/ultrasound-triggered stimulus are the most frequently used [84–86]. For all these features, targeting strategies of DDSs present an exciting approach for anticancer treatment.

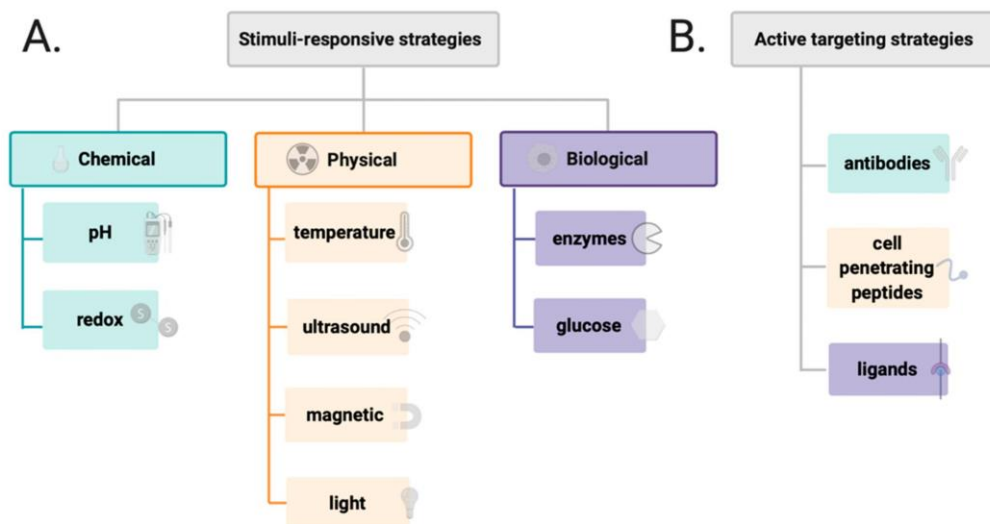


Figure 5. Different types of stimulus applied in the design of drug delivery system (A) and various factors affecting active targeting of drug delivery systems (B).

3.2. Drug Delivery Systems Responsive to Physical and Chemical Stimuli

Cancers are known to acidify their environment by dysregulation of pH dynamics. During neoplastic progression, the extracellular pH of cancer decreases to 6.8 compared with normal cells (7.4), whereas intracellular pH increases to 7.3–7.6 (vs. 7.05–7.2 in normal cells) [87]. Moreover, membrane-bound organelles such as endosomes and liposomes, involved in the endocytic pathway, which is a specific mechanism for some DDSs to enter cells, exhibit remarkably lower pH, approximately 5–6 and 4.5–5, respectively [88,89].

These properties provide a rationale to design a prodrug-based carrier with the time-dependent drug release behavior in the acidic environment of cancer, reported by Zhang et al. [90]. Designed prodrug (DOXDT) consisted of dextran–poly(oligoethylene glycol) methyl ether methacrylate–*co*–methyl glycol methacrylate copolymer prepared by one-step ATRP and conjugated with DOX, forming stable micelles. DOXDT showed pronounced tumor permeability and cytotoxicity. In vivo studies showed that Balb/C mice bearing 4T1 tumors treated with DOXDT (DOX dosage, 5 mg/kg) suppressed the tumor with an 85.5% inhibition rate, and was far more effective than free DOX. Importantly, DOXDT presented a good safety profile toward major organs, including the heart, liver, spleen, lung, and kidney, and minimal systemic toxicity.

Investigations carried out by She et al. showed that dendronized heparin–DOX could be also useful for pH-stimuli delivery of antineoplastic drugs [91]. The dendron conjugated through the hydrazine bond to DOX was attached to azido–heparin via click reaction, resulting in a self-assembled nanocarrier. DOX release from nanocarrier was faster and higher at pH 5.0 (80% of drug release after 56 h) than at the physiological pH of 7.4. In addition, both in vitro and in vivo studies showed high 4T1 breast tumor inhibition and no significant toxicity toward healthy organs.

Due to the cancer acidic environment, PLGA-coated stabilized (Mn, Zn) ferrite nanoparticles loaded with DOX (DOX–PLGA@CS@Mn_{0.9}Zn_{0.1}Fe₂O₄) were designed for pH-triggered DOX release [92]. The pH change from physiological to acidic resulted in a significant increase in the DOX release rate (34.26% for physiological pH vs. 57.18% for acidic pH). DOX–PLGA@CS@Mn_{0.9}Zn_{0.1}Fe₂O₄ was less cytotoxic (from 3 to 125 µg/mL) against HeLa cells compared with free DOX, while at higher concentrations (250 µg/mL) its cytotoxicity was similar to that of DOX.

In an effort to further improve DOX release performance of the DDSs, dual or multi-stimuli responsive DDSs were recently developed [93]. Novel DOX–CuCo₂S₄@PIL nanocarrier, proposed by Fan et al. to be effective in anticancer treatment, responds to both pH- and thermo-stimuli. The primary prepared CuCo₂S₄ nanoparticles were subsequently modified with the poly(tetrabutyl phosphonium styrenesulfonate) (PIL), then the DOX was loaded onto PIL. CuCo₂S₄ utilized the near-infrared (NIR) irradiation to convert light energy into heat to destabilize the PIL and promote drug release. The DOX release of DOX–CuCo₂S₄@PIL at 45 °C and pH 5.0 reached 90.5% compared with 79.5% at 37 °C. At pH 7.4, the release ratio was only 21.8% (37 °C) and 20.5% (45 °C). The in vitro analysis against MCF-7 cells showed the biocompatibility of CuCo₂S₄@PIL carrier even at high concentration. The cytotoxic effects were much higher when the cells were treated with DOX–CuCo₂S₄@PIL in the presence of NIR laser irradiation at 808 nm than without such irradiation. The in vivo effects of DOX–CuCo₂S₄@PIL on the breast tumor-carrying mice were assessed 16 days following the treatment. DOX–CuCo₂S₄@PIL with exposure to NIR laser irradiation at 808 nm resulting in improved tumor inhibition, whereas DOX–CuCo₂S₄@PIL without NIR laser irradiation displayed tumor inhibition the same as free DOX.

Several reports described stimuli-responsive three-dimensional hydrogels as smart DDSs. Xiong et al. prepared the pH- and temperature-responsive nanogels consisting of poly(N-isopropylacrylamide–*co*–acrylic acid) and DOX (DOX–PNA) as promising DDSs against human liver carcinoma cells HepG2 [94]. Under hyperthermia of 43 °C at pH 6.8, the cytotoxicity of DOX–PNA increased by approximately 43% when compared with the equivalent dose of DOX–PNA at 37 °C and pH 7.4.

Omidi et al. developed pH-responsive DOX-loaded hydrogel composed of CS, aminated-graphene, and amino-functionalized cellulose nanowhisker cross-linked by dialdehyde (DOX-CGW) [95]. Field Emission Scanning Electron Microscopes images showed a randomly porous structure with DOX accumulated on the surface of CGW, which remained stable at PBS buffer (pH 7.4) after 6 h, contrarily to distilled water. The significant DOX release rate (63%) from CGW was observed at pH 5.4, whereas approximately 35% of the drug was released at pH 7.4. Ultimately, subcutaneous injection at the back of the rat led to in vivo hydrogel formation 2 min after the injection. This provided a basis for further engineering of CGW as injectable DDSs.

A tremendous amount of work has been done to predict the drug release behaviors of stimuli-responsive hydrogels with artificial intelligence-based techniques such as Artificial Neural Networks (ANNs), Support Vector Machine (SVM), and its adaptation—Support Vector Regression (SVR) [96,97]. Boztepe et al. used these methods to predict the DOX release behavior of interpenetrating polymer network (IPN) hydrogel. IPN hydrogel based on poly(N-isopropyl acrylamide-co-acrylic acid and poly(ethylene glycol) was synthesized by free radical solution polymerization and loaded with DOX (64.81 mg DOX/g polymer) [98]. The DOX release rate was much more rapid at acidic pH and at a temperature above the lower critical solution temperature. The most efficient DOX release from IPN hydrogel was observed at pH 4 and 45 °C (88%), whereas at pH 7 at the same temperature DOX release was two times lower (~40%). Further mathematical ANN studies showed agreement between prediction and observations (i.e., experimental DOX release kinetic data), which proves its usefulness as a tool for the rational design and modeling of DDS-like hydrogels.

Meanwhile, Zhang et al. reported the efficacy of dual-sensitive (pH and redox) nanogels (DSNGs) against triple-negative breast cancer by hydrogel-assisted delivery [99]. Hydrogel composed of oxidized DX was crosslinked by imine bonds with 25% G5-PAMAM dendrimer that degraded under hydrolytic conditions [100]. Furthermore, DSNGs based on oxidized DX were crosslinked with cystamine, introducing a redox-sensitive disulfide bond cleaved in the presence of glutathione-reductant in cancer cells. Additionally, DOX was conjugated by a pH-sensitive imine bond to DX. DSNGs were released from degraded hydrogel, followed by a rapid release of DOX in cancer cells. Cell viability toward MDA MB 231 and 3T3 cell lines treated by DSNGs showed significantly higher toxicity in the presence of glutathione (IC₅₀ values equal to 114 and 2338 nM, respectively), whereas in vivo studies showed tumor volume reduction in the first 24 h post-injection, but slow tumor growth up was accelerated at 72 h, which may limit DSNGs applications.

Recently, Biswas et al. developed PEG functionalized guanosine-quadruplex-based hydrogel (G4PEG) to produce stimuli-responsive DDSs with zero-order DOX release [101]. It is well known that 1,2-cis-diol of guanosine forms dynamic boronate ester bonds with 2-formylphenylboronic acid (FPBA). Moreover, FPBA simultaneously forms dynamic imine bonds with primary amines such as 4-arm PEG-NH₂. Thus, the working mechanism of G4PEG is believed to depend on iminoboronate bonds, which are unstable at lower pH, resulting in sustained DOX release. DOX release rates obtained for acidic and physiological pH were 7.4×10^{-5} and 2.25×10^{-5} mmol/sec, respectively. The cell viability MTT assay using MCF-7 cell line showed weak, concentration-dependent cytotoxic effects of G4PEG with an IC₅₀ value of approximately 2.27 mM. For DOX-loaded G4PEG, the IC₅₀ value was lower (1.3 mM).

3.3. Mitochondrial-Targeting Drug Delivery Systems

Interestingly, despite many unique characteristics of cancer cells, like low extracellular pH and hypoxia, their hyperpolarized mitochondria opened new directions to targeted drug delivery [102]. Many reports demonstrated potential applications of modified polymers to locate drugs inside the mitochondria [103,104].

In 2019, Tan et al. presented micelles for DOX delivering, using glycolipid polymer chitosan-stearic acid (CSOSA), which was modified by lipophilic (4-carboxybutyl)triphenylphospho

bromide (CTPP) cations, to form mitochondria-targeted DDSs (C-P-CSOSA/DOX) [105]. The relatively small C-P-CSOSA/DOX particles, with a size around 100 nm, showed higher cellular uptake in human breast adenocarcinoma cells (MCF-7 cell line) than in human normal liver cells (L02 cell line). Importantly, C-P-CSOSA/DOX demonstrated efficient colocalization into mitochondria in vitro and in vivo, compared with the free DOX. Moreover, in vitro studies showed high cytotoxic effects of C-P-CSOSA/DOX against MCF-7 (IC50 equal 1.45 $\mu\text{g}/\text{mL}$, where for free DOX IC50 was 5 times higher), and increased the generation of reactive oxygen species with simultaneous activation of tumor apoptosis.

More recently, Jiang et al. reported delocalized lipophilic cations conjugated with synthesized anionic, cationic, and charge-neutral polymers [106] to improve mitochondrial targeting. Delocalized lipophilic cations conjugated anionic polymers accumulated in mitochondria when DLC-conjugated with cationic and charge-neutral polymers do not reach the target efficiently. Interestingly, side-chain modifications by hydrophobic hexyl or hydrophilic hydroxyl do not affect the mitochondrial localization, which was observed for 13 cell lines, e.g., adenocarcinoma human epithelial cell line A549, human cervical cancer cells HeLa or human umbilical vein endothelial cells HUVEC. Additionally, cyanine 3-tagged anionic polymers loaded with DOX demonstrated ability to inhibit the mitochondrial metabolic activity more effectively than free DOX after a 24 h treatment of HeLa cells.

3.4. Enzyme-Responsive Drug Delivery Systems

Alternatively, enzyme-sensitive conjugates can serve as a promising vehicle for cancer-targeting DDSs, capable of releasing the drug upon the hydrolysis of the amide bond of a specific peptide by proteases (Figure 6) [107]. Matrix metalloproteinases (MMPs) and cathepsin B (CB) are important representatives of proteases associated with cancer. MMPs are a family of zinc-dependent proteases involved in extracellular matrix degradation and tumor progression [108]. CB is a lysosomal cysteine protease, and its overexpression is correlated with invasion and metastasis of cancer cells [109]. Alternatively, DDSs can be activated by an enzyme to expose targeting ligands for cellular uptake.

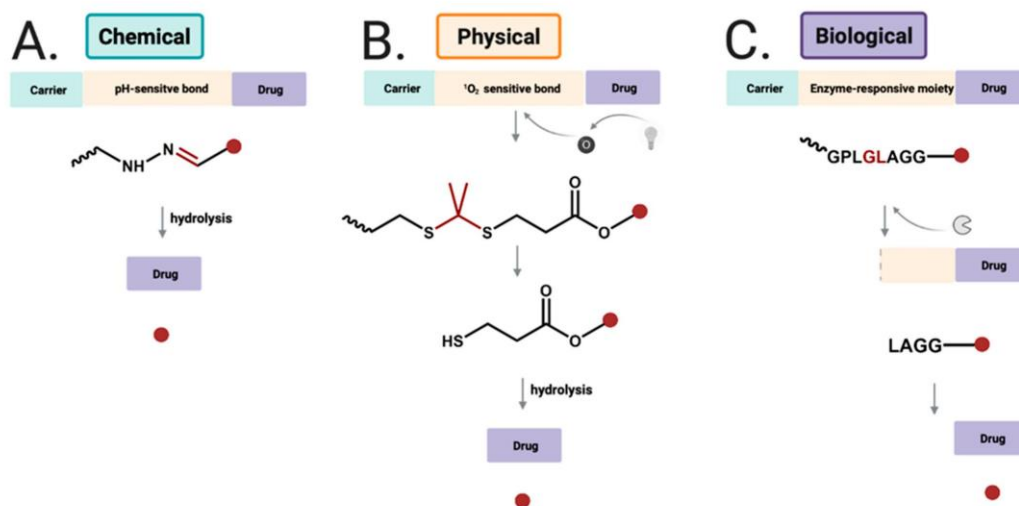


Figure 6. Drug release strategies for (A) chemical-responsive DDSs by hydrolysis of hydrazone bond to release free drug; (B) physical-responsive DDSs using near infrared light to generate singlet oxygen, which undergoes reaction with thioketal group; (C) biological-sensitive DDSs cleaved by enzyme, and further cleaved to release free drug.

Lee et al. synthesized dendrimer-methoxy poly(ethylene glycol)-DOX conjugate (Dendrimer-MPEG-DOX) using four amino acid (GFLG) peptides for CB-dependent targeting [110]. In vitro anti-tumor activity against CT26 colon carcinoma cells showed enhanced cytotoxicity of Dendrimer-MPEG-DOX. Importantly, Dendrimer-MPEG-DOX was more effective than DOX alone in inhibiting tumor growth in the mice CT26 tumor xenograft model. Additionally, it accumulated selectively in the tumor, whereas free DOX was equally distributed within the organism.

In 2020, Luo et al. developed DOX/nifuroxazide (NFX) co-loaded micelles (CLM) with enzyme-sensitive peptide GFLG. Hydroxypropyl methacrylate and oligo(ethylene glycol) methacrylate copolymer with GFLG peptide backbone was conjugated with DOX via acid-labile hydrazine bond [111]. Moreover, NFX was loaded via thin-film hydration and self-assembled into micelles. In vivo and ex vivo studies confirmed that CLM exerted anti-metastatic effect in orthotopic and lung metastatic breast cancer models. Along with the high anti-tumor efficacy of CLM, a reduced DOX cardiotoxicity was reported. On day 21 post-treatment, all mice treated with CLM (3 mg/kg of DOX and 5 mg/mL of NFX) survived with a tumor growth inhibition rate of 57%, whereas in the case of DOX-loaded micelles (3 mg/kg of DOX) inhibition rate was 27%.

Based on previous studies on the cleavage site specificity of MMP-2 and MMP-9, many MMPs-specific peptide sequences were proposed [112]. For example, Kratz et al. demonstrated that GPQRIAGQ peptide incorporated in DOX-human serum albumin conjugate was cleaved efficiently by activated MMP-2/9 [113]. Lee et al., in their study, employed two PEGylated peptide-DOX conjugate micelles using GPLGV and GPLGVRG peptides [114]. In vivo studies showed 72% (micelles using GPLGV) and 63.3% (micelles using GPLGVRG) tumor growth inhibition, compared with untreated control. In another study, two tumor activated prodrug-conjugated polystyrene nanoparticles (TAP-NPs), containing PLGSYL and GPLGIAGQN peptides, demonstrated substantial cytotoxicity toward HT1080, HDE, and HUVEC cells in a time-dependent manner [115]. More prominent effects were observed for HT1080 cells than for healthy and primary cells, and stronger inhibition was reported for TAP-NPs functionalized by GPLGIAGQN than by PLGSYL.

In 2012, Shi et al. synthesized cell-penetrating peptide-DOX conjugate (ACPP) with PLGLAG sensitive sequence that could release DOX in response to MMP-2 and MMP-9 [116]. The conjugate exerted high cytotoxic effects against HT-1080 cells which overexpress MMP-2/9, whereas only low cytotoxic activity was reported against MCF-7 cells characterized by low expression of MMPs. Upon addition of GM6001, an MMP inhibitor, the cellular uptake of ACPP by HT-1080 cells was reduced, demonstrating that the uptake is dependent on MMP activity.

A more investigative approach was used by Zhang et al., who designed DOX loaded on multifunctional envelope-type mesoporous silica nanoparticles (MEMSM) [117]. The surface of DOX-loaded MEMSM was functionalized with β -cyclodextrin (CD) via click chemistry through a disulfide bond. Next, mesoporous silica nanoparticles-CD was modified by the RGD peptide motif, a ligand for cell surface integrins, and subsequently by an MMP substrate PLGVR peptide, covalently coupled with polyanion (PASP) to form a protective layer. In vitro studies demonstrated efficient MEMSM uptake by the squamous carcinoma SCC-7 cells and human colon cancer HT-29 cells via RGD-mediated interactions following removal of PASP layer through cleavage of PLGVR by MMP-2, and DOX release in the presence of glutathione. Viability of both SCC-7 and HT-29 cells incubated with MEMSM (125 μ g/mL) was reduced to 40%, and when MMP inhibitor was added, cell viability exceeded 70%, demonstrating enzyme-enhanced drug uptake and highlighting the role of MMPs in directing the drug to the tumor cells.

A similar approach with the application of another MMP substrate, KDPLGVC peptide, was proposed by Eskandari et al. [118]. The peptide was bound onto the surface of DOX-loaded MSN through amidation reaction, and then grafted with a gold nanoparticle-biotin conjugate (GNP) as end-capping and active targeting agent. Amount of DOX released from MSN-GNP-Bio@DOX increased to 82.5% in the presence of MMP-2 at

pH 5.5, and due to the Au-S bond breaking, release decreased to 10% in the absence of MMP-2 and at pH 7.4. The DDSs demonstrated significant efficacy towards 4T1 biotin receptor-positive cancer cells overexpressing MMP-2 with a high level of cellular uptake and cell viability reduced to 4% after 72 h treatment. In contrast, viability of T47D breast cancer cells, which are characterized by a lack of biotin receptor and low MMPs expression, reached 60% upon the same treatment.

In other studies, DOX was conjugated to humanized IgG1 monoclonal antibody—trastuzumab by MMP-2 sensitive peptide linker (MAHNP-DOX) [119]. Trastuzumab targets human epidermal growth factor receptor 2 (HER2), and inhibits HER2-mediated malignant transformation [120]. In that study, 12-amino acid anti-HER2 peptide mimetic and GPLGLAGDD MMP-2 sensitive peptides were conjugated to DOX as active targeting strategy. MAHNP-DOX treatment decreased the growth rate of HER2 positive breast cancer cell lines BT474 and SKBR3 in a dose-dependent manner (IC₅₀ values 747 and 110 nM for BT474 and SKBR3 cells, respectively). IC₅₀ values were higher (1328.0 and 146.7 nM for BT474 and SKBR3 cells, respectively) when the cells had been pretreated with MMP-2 inhibitor. In vivo experiments on BT474 tumor-bearing mice showed that MAHNP-DOX resulted in 74.7% inhibition of tumor growth 25 days following the treatment. In mice treated with free DOX, inhibition of tumor growth was lower than in mice treated with MAHNP-DOX. Significant body weight loss was observed only in mice receiving free DOX rather than MAHNP-DOX.

Zhang et al. prepared dextran-coated Fe₃O₄ nanoparticles conjugated with DOX and chimeric monoclonal antibody cetuximab (DOX-NPs-Cet) for targeted anticancer therapy [121]. Dextran-coated Fe₃O₄ nanoparticles without DOX and Cet provided desirable stability and good biocompatibility, allowing for their application as drug carriers. DOX-NPs-Cet bound specifically to the epidermal growth factor receptor, which is overexpressed in non-small lung cancer A549 cells, and released DOX directly into the cells via endocytosis. Notably, DOX-NPs-Cet exhibited higher cytotoxicity against A549 cells than DOX-NPs (IC₅₀ values after 48 h 0.22 µg/mL and 0.68 µg/mL, respectively).

In addition, transferrin receptor (TfR) overexpressed in many tumors seems to be a good target for selective drug delivery to enhance cellular uptake via TfR-mediated endocytosis [122]. In 2019, Li et al. designed TfR-targeted binding peptide analog BP9a (CAHLHNRS) coupled with DOX through *N*-succinimidyl-3-maleimidopropionate as a crosslinker [123]. Higher cytotoxic effects were observed toward HepG2 hepatoma cells overexpressing TfR than toward L-O2 normal human liver cells, whereas for free DOX, only poor selectivity for cancer cells was shown.

Moreover, some reports demonstrated that ferritin, an iron storage protein, successfully binds to TfR [124], and has been used to encapsulate chemotherapeutic drugs for targeted delivery. On the other hand, in the absence of iron, ferritin can form the hollow apoferritin, which has the same above-mentioned properties as ferritin.

Chen et al. used DOX-loaded apoferritin (DOX-APO) for delivering into the brain to inhibit the glioma tumor growth [125]. Here, the highly TfR-expressed C6 (glioma cell line) and bEnd.3 (mouse brain microvascular endothelial cells) cell lines were used to determine a significant cellular uptake via TfR receptor and efficient blood-brain barrier penetration by DOX-APO. In vivo studies using C6-bearing mice demonstrated an accumulation of DOX-APO (1 mg/kg DOX) into brain tumor tissues with simultaneous longer mice survival time. Unfortunately, high liver accumulation was observed, which may introduce some limitation in the use of nanoparticle and required further analysis. Recently, H-chain modified apoferritin (TL-HFn) was used to deliver DOX into the cell nucleus after cellular uptake via TfR receptors and lysosome escape [126]. These studies proved that TL-HFn could be used as a safe carrier for small molecules without any cytotoxic effects against HeLa cells. After DOX encapsulation into TL-HFn, the cytotoxicity was observed in a wide range of concentrations (0.016–4.00 mg/mL) and was comparable to the action of free DOX.

Developing a carrier that induces apoptosis specifically in tumors using tumor necrosis factor-related apoptosis-inducing ligand (TRAIL) represents another exciting DDSs

approach [127]. Jiang et al. developed DOX encapsulated liposomes with TRAIL and cell-penetrating peptide R8H3, further coated by hyaluronic acid-cross-linked gel shell (TRAIL/DOX-Gelipo). Hyaluronidase, an extracellular enzyme overexpressed in tumors, degraded hyaluronic acid-cross-linked gel shell, exposed R8H3 to facilitate the cellular uptake via endocytosis, and released TRAIL [128]. After the endosomal escape, DOX accumulated into the cell nucleus to trigger apoptosis. TRAIL/DOX-Gelipo treated by hyaluronidase showed cytotoxicity toward MDA MB 231 cells significantly higher than DOX-Gelipo without TRAIL, with IC_{50} value 83 ng/mL (vs. 569 ng/mL). Additionally, TRAIL/DOX-Gelipo triggered high DOX accumulation in tumor and efficient tumor growth suppression.

4. Conclusions

In this review, we discussed DOX delivery systems and their evolution in the last few years. Since Doxil[®] and Myocet[®], many different DDS concepts appeared to overcome biological barriers and reduce drug side effects. All summarized technologies share common ideas of efficient pharmaceutical cargo transportation through the whole body, followed by DOX maximized accumulation in cancer tissue, improved through controlled release into cancer cells by a wide spectrum of stimuli. For example, DDSs can be sensitive to chemical and physical stimuli such as pH changes or light, as well as biological ones, e.g., enzymes overexpressed by cancer cells. Therefore, choosing the type of delivery system and its design is critical. For these reasons, new synthetic approaches and polymerization methods to create DDSs in a controlled manner with desired features in a relatively short time are a subject of intensive studies. A tremendous amount of effort is being put into maximized execution of DOX therapeutic effects towards targeted cells. Future benefits, that are being expected to be brought with engineered nanotechnology in DDSs, involve overcoming possible physiological conditions against DOX on its road to the targeted site, simultaneously providing sufficient concentration of the drug to cancerous cells in a specified therapeutic window. Carefully designed nanocarriers would also harness their potential to synergistically support DOX in decreasing tumor developments, accompanied by reduced systemic harmfulness. For all the researchers, it is also crucial to consider drawbacks that potentially can be faced in the future during technology translation from the laboratory bench to the clinical trials and product administration to patients. There is no doubt that the DDSs described in this review demonstrate the potential to form efficient and targeted systems for future innovations in the field of DOX delivery. However, many challenges must be improved to achieve clinical trials and FDA approval. In our opinion, biosafety and biocompatibility are one of the most important parameters of DDSs, and their lack of toxicity may reduce the risk of side effects and enhance therapeutic outcomes. As for polymeric DDSs, the major obstacle is their high complexity and architecture which required advanced polymerization methods to obtain a polymer with high efficiency and without impurities. Despite their hurdle and difficulties with synthesis, some simple polymers, like PEG, are commonly used to increase the solubility and biocompatibility of DDSs. Moreover, the rational design of DDSs might be improved by stimuli-responsive moieties conjugated to previously synthesized polymers. Hundreds of stimuli-responsive DDSs have been reported up to now, and showed many advantages, like improvement of pharmacokinetics and accumulation of DOX in the tumor site. Besides, they also may decrease off-target effects and metastasis. However, the application of stimuli-responsive DDSs requires better control of drug dose which is released from the carrier in a time-dependent manner. Unfortunately, many of them are not suitable for *in vivo* studies, because of non-biodegradable character or lack of high therapeutic efficacy. On the other hand, targeted DDSs using, e.g., receptors, are capable to overcome biological barriers associated with cellular uptake by receptor/ligand-mediated endocytosis. Great efforts have been made based on binding ligands and open new opportunities for cellular targeting and DDSs selectivity. This approach is related to surface binding by DDSs and further mechanism of drug release into the cytosol after the endosomal escape. Targeted DDSs have shown

promise as potential therapeutic agents, but a detailed understating of their mechanism of action is needed to avoid nonspecific interactions and achieve delivery to different cancer cells. Given this, DDSs still have a long way to go in terms of optimization and innovation in design and development. We believe that thoroughly reviewed information and critical evaluation of the work progress on DDS in recent years would inspire the creation of new strategies for the DOX ideal carrier development.

Author Contributions: Conceptualization, K.B. and J.P.; writing—original draft preparation, K.B., A.W. and A.B.; writing—review and editing, K.B., A.W., A.B. and J.P.; supervision, J.P.; project administration, K.B. All authors have read and agreed to the published version of the manuscript.

Funding: This research received no external funding.

Institutional Review Board Statement: Not applicable.

Informed Consent Statement: Not applicable.

Data Availability Statement: Data sharing is not applicable to this article.

Conflicts of Interest: The authors declare no conflict of interest.

References

1. Arcamone, F.; Cassinelli, G.; Fantini, G.; Grein, A.; Orezzi, P.; Pol, C.; Spalla, C. Adriamycin, 14-hydroxydaunomycin, a new antitumor antibiotic from *S. Peucetius* var. *caesius*. *Biotechnol. Bioeng.* **1969**, *11*, 1101–1110. [[CrossRef](#)]
2. Ravina, E. Drugs from microbiological sources. In *The Evolution of Drug Discovery: From Traditional Medicines to Modern Drugs*, 1st ed.; Wiley-VCH: Weinheim, Germany, 2011; p. 296.
3. World Health Organization. *World Health Organization Model List of Essential Medicines: 21st List 2019*; World Health Organization: Geneva, Switzerland, 2019.
4. Abraham, R.; Basser, R.L.; Green, M.D. A Risk-Benefit Assessment of Anthracycline Antibiotics in Antineoplastic Therapy. *Drug Saf.* **1996**, *15*, 406–429. [[CrossRef](#)]
5. Zhu, H.; Sarkar, S.; Scott, L.; Danelisen, I.; Trush, M.A.; Jia, Z.; Li, Y.R. Doxorubicin redox biology: Redox cycling, topoisomerase inhibition, and oxidative stress. *React. Oxyg. Species (Apex)* **2016**, *1*, 189–198. [[CrossRef](#)]
6. Zunino, F.; Capranico, G. DNA topoisomerase II as the primary target of anti-tumor anthracyclines. *Anti-Cancer Drug Des.* **1990**, *5*, 307–317.
7. Marinello, J.; Delcuratolo, M.; Capranico, G. Anthracyclines as topoisomerase II poisons: From early studies to new perspectives. *Int. J. Mol. Sci.* **2018**, *19*, 3480. [[CrossRef](#)] [[PubMed](#)]
8. Nielsen, D.; Maare, C.; Skovsgaard, T. Cellular resistance to anthracyclines. *Gen. Pharmacol. Vasc. Syst.* **1996**, *27*, 251–255. [[CrossRef](#)]
9. Versantvoort, C.H.M.; Withoff, S.; Broxterman, H.J.; Kuiper, C.M.; Scheper, R.J.; Mulder, N.H.; De Vries, E.G.E. Resistance-associated factors in human small-cell lung-carcinoma GLC4 sub-lines with increasing adriamycin resistance. *Int. J. Cancer* **1995**, *61*, 375–380. [[CrossRef](#)] [[PubMed](#)]
10. Withoff, S.; Keith, W.N.; Knol, A.J.; Coutts, J.C.; Hoare, S.F.; Mulder, N.H.; De Vries, E.G.E. Selection of a subpopulation with fewer DNA topoisomerase II alpha gene copies in a doxorubicin-resistant cell line panel. *Br. J. Cancer* **1996**, *74*, 502–507. [[CrossRef](#)]
11. Trist, H.; Phillips, D.R. In vitro transcription analysis of the role of flanking sequence on the DNA sequence specificity of Adriamycin. *Nucleic Acids Res.* **1989**, *17*, 3673–3688. [[CrossRef](#)] [[PubMed](#)]
12. Levin, M.; Silber, R.; Israel, M.; Goldfeder, A.; Khetarpal, V.K.; Potmesil, M. Protein-associated DNA breaks and DNA-protein cross-links caused by DNA nonbinding derivatives of Adriamycin in L1210 cells. *Cancer Res.* **1981**, *41*, 1006–1010.
13. Potmesil, M.; Kirschenbaum, S.; Israel, M.; Levin, M.; Khetarpal, V.K.; Silber, R. Relationship of adriamycin concentrations to the DNA lesions induced in hypoxic and euoxic L1210 cells. *Cancer Res.* **1983**, *43*, 3528–3533. [[PubMed](#)]
14. Bachur, N.R.; Yu, F.; Johnson, R.; Hickey, R.; Wu, Y.; Malkas, L. Helicase inhibition by anthracycline anticancer agents. *Mol. Pharmacol.* **1992**, *41*, 993–998.
15. Zunino, F.; Gambetta, R.; Di Marco, A. The inhibition in vitro of DNA polymerase and RNA polymerases by daunomycin and adriamycin. *Biochem. Pharmacol.* **1975**, *24*, 309–311. [[CrossRef](#)]
16. Yang, F.; Kemp, C.J.; Henikoff, S. Doxorubicin enhances nucleosome turnover around promoters. *Curr. Biol.* **2013**, *23*, 782–787. [[CrossRef](#)] [[PubMed](#)]
17. Pang, B.; Qiao, X.; Janssen, L.; Velds, A.; Groothuis, T.; Kerkhoven, R.; Nieuwland, M.; Ovaa, H.; Rottenberg, S.; van Tellingen, O.; et al. Drug-induced histone eviction from open chromatin contributes to the chemotherapeutic effects of doxorubicin. *Nat. Commun.* **2013**, *4*, 1–13. [[CrossRef](#)]
18. Gajewski, E.; Gaur, S.; Akman, S.A.; Matsumoto, L.; van Balgooy, J.N.; Doroshow, J.H. Oxidative DNA base damage in MCF-10A breast epithelial cells at clinically achievable concentrations of doxorubicin. *Biochem. Pharmacol.* **2007**, *73*, 1947–1956. [[CrossRef](#)] [[PubMed](#)]

19. Sinha, B.K.; Mimnaugh, E.G.; Rajagopalan, S.; Myers, C.E. Adriamycin activation and oxygen free radical formation in human breast tumor cells: Protective role of glutathione peroxidase in adriamycin resistance. *Cancer Res.* **1989**, *49*, 3844–3848. [[PubMed](#)]
20. Doroshow, J.H.; Synold, T.W.; Somlo, G.; Akman, S.A.; Gajewski, E. Oxidative DNA base modifications in peripheral blood mononuclear cells of patients treated with high-dose infusional doxorubicin. *Blood* **2001**, *97*, 2839–2845. [[CrossRef](#)]
21. Faure, H.; Mousseau, M.; Cadet, J.; Guimier, C.; Tripiet, M.; Hida, H.; Favier, A. Urine 8-Oxo-7, 8-Dihydro-2'-Deoxyguanosine vs. 5-(Hydroxymethyl) Uracil as DNA Oxidation Marker in Adriamycin-Treated Patients. *Free Radic. Res.* **1998**, *28*, 377–382. [[CrossRef](#)]
22. Coldwell, K.E.; Cutts, S.M.; Ognibene, T.J.; Henderson, P.T.; Phillips, D.R. Detection of Adriamycin–DNA adducts by accelerator mass spectrometry at clinically relevant Adriamycin concentrations. *Nucleic Acids Res.* **2008**, *36*, e100. [[CrossRef](#)]
23. Swift, L.P.; Rephaeli, A.; Nudelman, A.; Phillips, D.R.; Cutts, S.M. Doxorubicin–DNA adducts induce a non-topoisomerase II-mediated form of cell death. *Cancer Res.* **2006**, *66*, 4863–4871. [[CrossRef](#)] [[PubMed](#)]
24. Gewirtz, D. A critical evaluation of the mechanisms of action proposed for the antitumor effects of the anthracycline antibiotics adriamycin and daunorubicin. *Biochem. Pharmacol.* **1999**, *57*, 727–741. [[CrossRef](#)]
25. Cox, J.; Weinman, S. Mechanisms of doxorubicin resistance in hepatocellular carcinoma. *Hepatic Oncol.* **2016**, *3*, 57–59. [[CrossRef](#)]
26. Carvalho, C.; Santos, R.X.; Cardoso, S.; Correia, S.; Oliveira, P.J.; Santos, M.S.; Moreira, P.I. Doxorubicin: The good, the bad and the ugly effect. *Curr. Med. Chem.* **2009**, *16*, 3267–3285. [[CrossRef](#)] [[PubMed](#)]
27. Swain, S.M.; Whaley, F.S.; Ewer, M.S. Congestive heart failure in patients treated with doxorubicin: A retrospective analysis of three trials. *Cancer* **2003**, *97*, 2869–2879. [[CrossRef](#)] [[PubMed](#)]
28. Julka, P.K.; Chacko, R.T.; Nag, S.; Parshad, R.; Nair, A.; Oh, D.S.; Hu, Z.; Koppiker, C.B.; Nair, S.; Dawar, R.; et al. A phase II study of sequential neoadjuvant gemcitabine plus doxorubicin followed by gemcitabine plus cisplatin in patients with operable breast cancer: Prediction of response using molecular profiling. *Br. J. Cancer* **2008**, *98*, 1327–1335. [[CrossRef](#)]
29. Liu, J.; Tu, D.; Dancey, J.; Reyno, L.; Pritchard, K.I.; Pater, J.; Seymour, L.K. Quality of life analyses in a clinical trial of DPPE (tesmilifene) plus doxorubicin versus doxorubicin in patients with advanced or metastatic breast cancer: NCIC CTG Trial MA. *Breast Cancer Res. Treat.* **2006**, *100*, 263–271. [[CrossRef](#)]
30. Turcotte, L.M.; Neglia, J.P.; Reulen, R.C.; Ronckers, C.M.; Van Leeuwen, F.E.; Morton, L.M.; Hodgson, D.C.; Yasiu, Y.; Oeffinger, K.C.; Henderson, T.O. Risk, risk factors, and surveillance of subsequent malignant neoplasms in survivors of childhood cancer: A review. *J. Clin. Oncol.* **2018**, *36*, 2145–2152. [[CrossRef](#)] [[PubMed](#)]
31. Binasci, M.; Bigioni, M.; Cipollone, A.; Rossi, C.; Goso, C.; Maggi, C.A.; Capranico, G.; Animati, F. Anthracyclines: Selected new developments. *Curr. Med. Chem. Anti Cancer Agents* **2001**, *1*, 113–130. [[CrossRef](#)]
32. Weiss, R.B. The anthracyclines: Will we ever find a better doxorubicin? *Semin. Oncol.* **1992**, *19*, 670–686.
33. Shchekotikhin, A.E.; Dezhnekova, L.G.; Tsvetkov, V.B.; Luzikov, Y.N.; Volodina, Y.L.; Tatarskiy, V.V., Jr.; Kalina, A.A.; Treshalina, M.I.; Treshalina, H.M.; Romanenko, V.I.; et al. Discovery of antitumor anthra [2, 3-b] furan-3-carboxamides: Optimization of synthesis and evaluation of antitumor properties. *Eur. J. Med. Chem.* **2016**, *112*, 114–129. [[CrossRef](#)]
34. Zaleski, P.A.; Maini, R.; Leiris, S.J.; Elban, M.A.; Hecht, S.M. Synthesis and biological activities of topopyrones. *J. Nat. Prod.* **2012**, *75*, 577–585. [[CrossRef](#)]
35. Zhang, R.; Wu, X.; Yalowich, J.C.; Hasinoff, B.B. Design, synthesis, and biological evaluation of a novel series of bisintercalating DNA-binding piperazine-linked bisanthrapyrazole compounds as anticancer agents. *Bioorg. Med. Chem.* **2011**, *19*, 7023–7032. [[CrossRef](#)] [[PubMed](#)]
36. Folkman, J.; Long, D.M.; Rosenbaum, R. Silicone rubber: A new diffusion property useful for general anesthesia. *Science* **1966**, *154*, 148–149. [[CrossRef](#)] [[PubMed](#)]
37. Folkman, J.; Long, D.M. The use of silicone rubber as a carrier for prolonged drug therapy. *J. Surg. Res.* **1964**, *4*, 139–142. [[CrossRef](#)]
38. Hoffman, A.S. The origins and evolution of “controlled” drug delivery systems. *J. Control. Release* **2008**, *132*, 153–163. [[CrossRef](#)]
39. Langer, R.; Folkman, J. Polymers for the sustained release of proteins and other macromolecules. *Nature* **1976**, *263*, 797–800. [[CrossRef](#)]
40. Moses, M.A.; Brem, H.; Langer, R. Advancing the field of drug delivery: Taking aim at cancer. *Cancer Cell* **2003**, *4*, 337–341. [[CrossRef](#)]
41. Hossen, S.; Hossain, M.K.; Basher, M.K.; Mia, M.N.H.; Rahman, M.T.; Uddin, M.J. Smart nanocarrier-based drug delivery systems for cancer therapy and toxicity studies: A review. *J. Adv. Res.* **2019**, *15*, 1–18. [[CrossRef](#)] [[PubMed](#)]
42. Janssen, M.; Mihov, G.; Welting, T.; Thies, J.; Emans, P. Drugs and polymers for delivery systems in OA joints: Clinical needs and opportunities. *Polymers* **2014**, *6*, 799–819. [[CrossRef](#)]
43. Guo, X.; Wang, L.; Wei, X.; Zhou, S. Polymer-based drug delivery systems for cancer treatment. *J. Polym. Sci. Part A Polym. Chem.* **2016**, *54*, 3525–3550. [[CrossRef](#)]
44. Letchford, K.; Burt, H. A review of the formation and classification of amphiphilic block copolymer nanoparticulate structures: Micelles, nanospheres, nanocapsules and polymersomes. *Eur. J. Pharm. Biopharm.* **2007**, *65*, 259–269. [[CrossRef](#)]
45. Unezaki, S.; Maruyama, K.; Hosoda, J.I.; Nagae, I.; Koyanagi, Y.; Nakata, M.; Ishida, O.; Iwatsuru, M.; Tsuchiya, S. Direct measurement of the extravasation of polyethyleneglycol-coated liposomes into solid tumor tissue by in vivo fluorescence microscopy. *Int. J. Pharm.* **1996**, *144*, 11–17. [[CrossRef](#)]

46. Yavuz, M.S.; Cheng, Y.; Chen, J.; Cogley, C.M.; Zhang, Q.; Rycenga, M.; Xie, J.; Kim, C.; Song, K.H.; Schwartz, A.G.; et al. Gold nanocages covered by smart polymers for controlled release with near-infrared light. *Nat. Mater.* **2009**, *8*, 935–939. [[CrossRef](#)] [[PubMed](#)]
47. Maso, K.; Grigoletto, A.; Vicent, M.J.; Pasut, G. Molecular platforms for targeted drug delivery. *Int. Rev. Cell Mol. Biol.* **2019**, *346*, 1–50.
48. Zhao, N.; Woodle, M.C.; Mixson, A.J. Advances in delivery systems for doxorubicin. *J. Nanomed. Nanotechnol.* **2018**, *9*, 519. [[CrossRef](#)] [[PubMed](#)]
49. Donaruma, L.G. Synthetic biologically active polymers. *Prog. Polym. Sci.* **1975**, *4*, 1–25. [[CrossRef](#)]
50. Duncan, R. The dawning era of polymer therapeutics. *Nat. Rev. Drug Discov.* **2003**, *2*, 347–360. [[CrossRef](#)] [[PubMed](#)]
51. Avramović, N.; Mandić, B.; Savić-Radojević, A.; Simić, T. Polymeric nanocarriers of drug delivery systems in cancer therapy. *Pharmaceutics* **2020**, *12*, 298. [[CrossRef](#)]
52. Liu, J.; Xiao, Y.; Allen, C. Polymer–drug compatibility: A guide to the development of delivery systems for the anticancer agent, ellipticine. *J. Pharm. Sci.* **2004**, *93*, 132–143. [[CrossRef](#)]
53. Maeda, H. Toward a full understanding of the EPR effect in primary and metastatic tumors as well as issues related to its heterogeneity. *Adv. Drug Deliv. Rev.* **2015**, *91*, 3–6. [[CrossRef](#)] [[PubMed](#)]
54. Grund, S.; Bauer, M.; Fischer, D. Polymers in drug delivery—state of the art and future trends. *Adv. Eng. Mater.* **2011**, *13*, B61–B87. [[CrossRef](#)]
55. Liu, J.; Duong, H.; Whittaker, M.R.; Davis, T.P.; Boyer, C. Synthesis of functional core, star polymers via RAFT polymerization for drug delivery applications. *Macromol. Rapid Commun.* **2012**, *33*, 760–766. [[CrossRef](#)] [[PubMed](#)]
56. Střiba, S.E.; Kautz, H.; Frey, H. Hyperbranched molecular nanocapsules: Comparison of the hyperbranched architecture with the perfect linear analogue. *J. Am. Chem. Soc.* **2002**, *124*, 9698–9699. [[CrossRef](#)] [[PubMed](#)]
57. Yu, Y.; Chen, C.K.; Law, W.C.; Mok, J.; Zou, J.; Prasad, P.N.; Cheng, C. Well-defined degradable brush polymer–drug conjugates for sustained delivery of paclitaxel. *Mol. Pharm.* **2013**, *10*, 867–874. [[CrossRef](#)] [[PubMed](#)]
58. Matyjaszewski, K.; Tsarevsky, N.V. Nanostructured functional materials prepared by atom transfer radical polymerization. *Nat. Chem.* **2009**, *1*, 276–288. [[CrossRef](#)]
59. Moad, G. The emergence of RAFT polymerization. *Aust. J. Chem.* **2006**, *59*, 661–662. [[CrossRef](#)]
60. Barenholz, Y.C. Doxil[®]—the first FDA-approved nano-drug: Lessons learned. *J. Control. Release* **2012**, *160*, 117–134. [[CrossRef](#)]
61. Leonard, R.C.F.; Williams, S.; Tulpule, A.; Levine, A.M.; Oliveros, S. Improving the therapeutic index of anthracycline chemotherapy: Focus on liposomal doxorubicin (Myocet[™]). *Breast* **2009**, *18*, 218–224. [[CrossRef](#)]
62. Danhauser-Riedl, S.; Hausmann, E.; Schick, H.D.; Bender, R.; Dietzfelbinger, H.; Rastetter, J.; Hanauske, A.R. Phase I clinical and pharmacokinetic trial of dextran conjugated doxorubicin (AD-70, DOX-OXD). *Investig. New Drugs* **1993**, *11*, 187–195. [[CrossRef](#)]
63. Mitra, S.; Gaur, U.; Ghosh, P.C.; Maitra, A.N. Tumour targeted delivery of encapsulated dextran–doxorubicin conjugate using chitosan nanoparticles as carrier. *J. Control. Release* **2001**, *74*, 317–323. [[CrossRef](#)]
64. Janes, K.A.; Fresneau, M.P.; Marazuela, A.; Fabra, A.; Alonso, M.J. Chitosan nanoparticles as delivery systems for doxorubicin. *J. Control. Release* **2001**, *73*, 255–267. [[CrossRef](#)]
65. Qi, J.; Yao, P.; He, F.; Yu, C.; Huang, C. Nanoparticles with dextran/chitosan shell and BSA/chitosan core—doxorubicin loading and delivery. *Int. J. Pharm.* **2010**, *393*, 177–185. [[CrossRef](#)]
66. Du, C.; Deng, D.; Shan, L.; Wan, S.; Cao, J.; Tian, J.; Achilefu, S.; Gu, Y. A pH-sensitive doxorubicin prodrug based on folate-conjugated BSA for tumor-targeted drug delivery. *Biomaterials* **2013**, *34*, 3087–3097. [[CrossRef](#)] [[PubMed](#)]
67. Imaz, I.; Rubio-Martinez, M.; García-Fernández, L.; García, F.; Ruiz-Molina, D.; Hernando, J.; Puentes, V.; Maspoch, D. Coordination polymer particles as potential drug delivery systems. *Chem. Commun.* **2010**, *46*, 4737–4739. [[CrossRef](#)] [[PubMed](#)]
68. Mrówczyński, R.; Jurga-Stopa, J.; Markiewicz, R.; Coy, E.L.; Jurga, S.; Woźniak, A. Assessment of polydopamine coated magnetic nanoparticles in doxorubicin delivery. *RSC Adv.* **2016**, *6*, 5936–5943. [[CrossRef](#)]
69. Zhang, C.; Liu, T.; Wang, W.; Bell, C.A.; Han, Y.; Fu, C.; Peng, H.; Tan, X.; Král, P.; Gaus, K.; et al. Tuning of the aggregation behavior of fluorinated polymeric nanoparticles for improved therapeutic efficacy. *ASC Nano* **2020**, *14*, 7425–7434. [[CrossRef](#)]
70. Ahmed, T.A.; Aljaeid, B.M. Preparation, characterization, and potential application of chitosan, chitosan derivatives, and chitosan metal nanoparticles in pharmaceutical drug delivery. *Drug Des. Dev. Ther.* **2016**, *10*, 483. [[CrossRef](#)]
71. Kayal, S.; Ramanujan, R.V. Doxorubicin loaded PVA coated iron oxide nanoparticles for targeted drug delivery. *Mater. Sci. Eng. C* **2010**, *30*, 484–490. [[CrossRef](#)]
72. Li, Y.L.; Zhu, L.; Liu, Z.; Cheng, R.; Meng, F.; Cui, J.H.; Ji, S.J.; Zhong, Z. Reversibly stabilized multifunctional dextran nanoparticles efficiently deliver doxorubicin into the nuclei of cancer cells. *Angew. Chem.* **2009**, *121*, 10098–10102. [[CrossRef](#)]
73. Peng, M.; Li, H.; Luo, Z.; Kong, J.; Wan, Y.; Zheng, L.; Zhang, Q.; Niu, H.; Vermorken, A.; Van de Ven, W.; et al. Dextran-coated superparamagnetic nanoparticles as potential cancer drug carriers in vivo. *Nanoscale* **2015**, *7*, 11155–11162. [[CrossRef](#)] [[PubMed](#)]
74. Attarwala, H. Role of antibodies in cancer targeting. *J. Nat. Sci. Biol. Med.* **2010**, *1*, 53. [[CrossRef](#)]
75. Blakey, D.C. Drug targeting with monoclonal antibodies: A review. *Acta Oncol.* **1992**, *31*, 91–97. [[CrossRef](#)]
76. Kontermann, R. Dual targeting strategies with bispecific antibodies. *MAbs* **2012**, *4*, 182–197. [[CrossRef](#)]
77. Nelson, A.L.; Dhimolea, E.; Reichert, J.M. Development trends for human monoclonal antibody therapeutics. *Nat. Rev. Drug Discov.* **2010**, *9*, 767–774. [[CrossRef](#)]

78. Yoo, J.; Park, C.; Yi, G.; Lee, D.; Koo, H. Active targeting strategies using biological ligands for nanoparticle drug delivery systems. *Cancers* **2019**, *11*, 640. [CrossRef] [PubMed]
79. Zhao, Z.; Ukidve, A.; Kim, J.; Mitragotri, S. Targeting strategies for tissue-specific drug delivery. *Cell* **2020**, *181*, 151–167. [CrossRef]
80. Li, M.; Zhao, G.; Su, W.K.; Shuai, Q. Enzyme-Responsive Nanoparticles for Anti-tumor Drug Delivery. *Front. Chem.* **2020**, *8*, 647. [CrossRef]
81. Qin, X.; Li, Y. Strategies To Design and Synthesize Polymer-Based Stimuli-Responsive Drug-Delivery Nanosystems. *ChemBioChem* **2020**, *21*, 1236–1253. [CrossRef]
82. Mura, S.; Nicolas, J.; Couvreur, P. Stimuli-responsive nanocarriers for drug delivery. *Nat. Mater.* **2013**, *12*, 991–1003. [CrossRef] [PubMed]
83. Yin, Q.; Shen, J.; Zhang, Z.; Yu, H.; Li, Y. Reversal of multidrug resistance by stimuli-responsive drug delivery systems for therapy of tumor. *Adv. Drug Deliv. Rev.* **2013**, *65*, 1699–1715. [CrossRef] [PubMed]
84. Alvarez-Lorenzo, C.; Bromberg, L.; Concheiro, A. Light-sensitive intelligent drug delivery systems. *Photochem. Photobiol.* **2009**, *85*, 848–860. [CrossRef] [PubMed]
85. Linsley, C.S.; Wu, B.M. Recent advances in light-responsive on-demand drug-delivery systems. *Ther. Deliv.* **2017**, *8*, 89–107. [CrossRef]
86. Municoy, S.; Álvarez Echazú, M.I.; Antezana, P.E.; Galdopórpura, J.M.; Olivetti, C.; Mebert, A.M.; Foglia, M.L.; Tuttolomondo, M.V.; Alvarez, G.S.; Hardy, J.G.; et al. Stimuli-Responsive Materials for Tissue Engineering and Drug Delivery. *Int. J. Mol. Sci.* **2020**, *21*, 4724. [CrossRef]
87. White, K.A.; Grillo-Hill, B.K.; Barber, D.L. Cancer cell behaviors mediated by dysregulated pH dynamics at a glance. *J. Cell Sci.* **2017**, *130*, 663–669. [CrossRef]
88. Prasad, P.V.; Purkayastha, K.; Sharma, U.; Barik, M. Ph-sensitive Nanomedicine for Treating Gynaecological Cancers. *J. Woman's Reprod. Health* **2020**, *2*, 35. [CrossRef]
89. Varkouhi, A.K.; Scholte, M.; Storm, G.; Haisma, H.J. Endosomal escape pathways for delivery of biologicals. *J. Control. Release* **2011**, *151*, 220–228. [CrossRef]
90. Zhang, X.; Zhang, T.; Ma, X.; Wang, Y.; Lu, Y.; Jia, D.; Huang, X.; Chen, J.; Xu, Z.; Wen, F. The design and synthesis of dextran-doxorubicin prodrug-based pH-sensitive drug delivery system for improving chemotherapy efficacy. *Asian J. Pharm. Sci.* **2020**, *15*, 605–616. [CrossRef] [PubMed]
91. She, W.; Li, N.; Luo, K.; Guo, C.; Wang, G.; Geng, Y.; Gu, Z. Dendronized heparin–doxorubicin conjugate based nanoparticle as pH-responsive drug delivery system for cancer therapy. *Biomaterials* **2013**, *34*, 2252–2264. [CrossRef]
92. Montha, W.; Maneeprakorn, W.; Buatong, N.; Tang, I.M.; Pon-On, W. Synthesis of doxorubicin-PLGA loaded chitosan stabilized (Mn, Zn) Fe₂O₄ nanoparticles: Biological activity and pH-responsive drug release. *Mater. Sci. Eng. C* **2016**, *59*, 235–240. [CrossRef]
93. Fan, S.Y.; Hao, Y.N.; Zhang, W.X.; Kapasi, A.; Shu, Y.; Wang, J.H.; Chen, W. Poly(ionic liquid)-gated CuCo₂S₄ for pH-/thermo-triggered drug release and photoacoustic imaging. *ACS Appl. Mater. Interfaces* **2020**, *12*, 9000–9007. [CrossRef]
94. Xiong, W.; Wang, W.; Wang, Y.; Zhao, Y.; Chen, H.; Xu, H.; Yang, X. Dual temperature/pH-sensitive drug delivery of poly (N-isopropylacrylamide-co-acrylic acid) nanogels conjugated with doxorubicin for potential application in tumor hyperthermia therapy. *Colloids Surf. B Biointerfaces* **2011**, *84*, 447–453. [CrossRef]
95. Omid, S.; Pirhayati, M.; Kakanejadifard, A. Co-delivery of doxorubicin and curcumin by a pH-sensitive, injectable, and in situ hydrogel composed of chitosan, graphene, and cellulose nanowhisker. *Carbohydr. Polym.* **2020**, *231*, 115745. [CrossRef] [PubMed]
96. Balabin, R.M.; Lomakina, E.I. Support vector machine regression (LS-SVM)—an alternative to artificial neural networks (ANNs) for the analysis of quantum chemistry data? *Phys. Chem. Chem. Phys.* **2011**, *13*, 11710–11718. [CrossRef]
97. Koç, M.L.; Özdemir, Ü.; İmren, D. Prediction of the pH and the temperature-dependent swelling behavior of Ca²⁺-alginate hydrogels by artificial neural networks. *Chem. Eng. Sci.* **2008**, *63*, 2913–2919. [CrossRef]
98. Boztepe, C.; Künkül, A.; Yüceer, M. Application of artificial intelligence in modeling of the doxorubicin release behavior of pH and temperature responsive poly (NIPAAm-co-AAc)-PEG IPN hydrogel. *J. Drug Deliv. Sci. Technol.* **2020**, *57*, 101603. [CrossRef]
99. Zhang, Y.; Dosta, P.; Conde, J.; Oliva, N.; Wang, M.; Artzi, N. Prolonged Local In Vivo Delivery of Stimuli-Responsive Nanogels That Rapidly Release Doxorubicin in Triple-Negative Breast Cancer Cells. *Adv. Healthc. Mater.* **2020**, *9*, 1901101. [CrossRef]
100. Sideratou, Z.; Tsiourvas, D.; Paleos, C.M. Quaternized poly (propylene imine) dendrimers as novel pH-sensitive controlled-release systems. *Langmuir* **2000**, *16*, 1766–1769. [CrossRef]
101. Biswas, A.; Ghosh, T.; Gavel, P.K.; Das, A.K. PEG Functionalized Stimuli Responsive Self-Healable Injectable Dynamic Iminoboronate G-quadruplex Hydrogel for the Delivery of Doxorubicin. *ACS Appl. Biomater.* **2020**, *3*, 1052–1060. [CrossRef]
102. Indran, I.R.; Tufo, G.; Pervaiz, S.; Brenner, C. Recent advances in apoptosis, mitochondria and drug resistance in cancer cells. *Biochim. Biophys. Acta (BBA)-Bioenerg.* **2011**, *1807*, 735–745. [CrossRef] [PubMed]
103. Biswas, S.; Dodwadkar, N.S.; Deshpande, P.P.; Torchilin, V.P. Liposomes loaded with paclitaxel and modified with novel triphenylphosphonium-PEG-PE conjugate possess low toxicity, target mitochondria and demonstrate enhanced antitumor effects in vitro and in vivo. *J. Control. Release* **2012**, *159*, 393–402. [CrossRef]
104. Biswas, S.; Dodwadkar, N.S.; Sawant, R.R.; Koshkaryev, A.; Torchilin, V.P. Surface modification of liposomes with rhodamine-123-conjugated polymer results in enhanced mitochondrial targeting. *J. Drug Target.* **2011**, *19*, 552–561. [CrossRef] [PubMed]

105. Tan, Y.; Yang, X.; Dai, S.; Lian, K.; Wen, L.; Zhu, Y.; Meng, T.; Liu, X.; Yuan, H.; Hu, F. In vivo programming of tumor mitochondria-specific doxorubicin delivery by a cationic glycolipid polymer for enhanced antitumor activity. *Polym. Chem.* **2019**, *10*, 512–525. [[CrossRef](#)]
106. Jiang, Z.; Liu, H.; He, H.; Yadava, N.; Chambers, J.J.; Thayumanavan, S. Anionic polymers promote mitochondrial targeting of delocalized lipophilic cations. *Bioconjugate Chem.* **2020**, *31*, 1344–1353. [[CrossRef](#)]
107. Hu, Q.; Katti, P.S.; Gu, Z. Enzyme-responsive nanomaterials for controlled drug delivery. *Nanoscale* **2014**, *6*, 12273–12286. [[CrossRef](#)]
108. Cathcart, J.; Pulkoski-Gross, A.; Cao, J. Targeting matrix metalloproteinases in cancer: Bringing new life to old ideas. *Genes Dis.* **2015**, *2*, 26–34. [[CrossRef](#)] [[PubMed](#)]
109. Gondi, C.S.; Rao, J.S. Cathepsin B as a cancer target. *Expert Opin. Ther. Targets* **2013**, *17*, 281–291. [[CrossRef](#)]
110. Lee, S.J.; Jeong, Y.I.; Park, H.K.; Kang, D.H.; Oh, J.S.; Lee, S.G.; Lee, H.C. Enzyme-responsive doxorubicin release from dendrimer nanoparticles for anticancer drug delivery. *Int. J. Nanomed.* **2015**, *10*, 5489.
111. Luo, L.; Xu, F.; Peng, H.; Luo, Y.; Tian, X.; Battaglia, G.; Zhang, H.; Gong, Q.; Gu, Z.; Luo, K. Stimuli-responsive polymeric prodrug-based nanomedicine delivering nifuroxazide and doxorubicin against primary breast cancer and pulmonary metastasis. *J. Control. Release* **2020**, *318*, 124–135. [[CrossRef](#)] [[PubMed](#)]
112. Xia, T.; Akers, K.; Eisen, A.Z.; Seltzer, J.L. Comparison of cleavage site specificity of gelatinases A and B using collagenous peptides. *Biochim. Biophys. Acta* **1996**, *1293*, 259–266. [[CrossRef](#)]
113. Kratz, F.; Dreves, J.; Bing, G.; Stockmar, C.; Scheuermann, K.; Lazar, P.; Unger, C. Development and in vitro efficacy of novel MMP2 and MMP9 specific doxorubicin albumin conjugates. *Bioorganic Med. Chem. Lett.* **2001**, *11*, 2001–2006. [[CrossRef](#)]
114. Lee, G.Y.; Park, K.; Kim, S.Y.; Byun, Y. MMPs-specific PEGylated peptide-DOX conjugate micelles that can contain free doxorubicin. *Eur. J. Pharm. Biopharm.* **2007**, *67*, 646–654. [[CrossRef](#)]
115. Guarnieri, D.; Biondi, M.; Yu, H.; Belli, V.; Falanga, A.P.; Cantisani, M.; Galdiero, S.; Netti, P.A. Tumor-activated prodrug (TAP)-conjugated nanoparticles with cleavable domains for safe doxorubicin delivery. *Biotechnol. Bioeng.* **2015**, *112*, 601–611. [[CrossRef](#)]
116. Shi, N.Q.; Gao, W.; Xiang, B.; Qi, X.R. Enhancing cellular uptake of activable cell-penetrating peptide-doxorubicin conjugate by enzymatic cleavage. *Int. J. Nanomed.* **2012**, *7*, 1613.
117. Zhang, J.; Yuan, Z.F.; Wang, Y.; Chen, W.H.; Luo, G.F.; Cheng, S.X.; Zhuo, R.X.; Zhang, X.Z. Multifunctional envelope-type mesoporous silica nanoparticles for tumor-triggered targeting drug delivery. *J. Am. Chem. Soc.* **2013**, *135*, 5068–5073. [[CrossRef](#)] [[PubMed](#)]
118. Eskandari, P.; Bigdeli, B.; Porgham Daryasari, M.; Baharifar, H.; Bazri, B.; Shourian, M.; Amani, A.; Sadighi, A.; Goliaei, B.; Khoobi, M.; et al. Gold-capped mesoporous silica nanoparticles as an excellent enzyme-responsive nanocarrier for controlled doxorubicin delivery. *J. Drug Target.* **2019**, *27*, 1084–1093. [[CrossRef](#)]
119. You, Y.; Xu, Z.; Chen, Y. Doxorubicin conjugated with a trastuzumab epitope and an MMP-2 sensitive peptide linker for the treatment of HER2-positive breast cancer. *Drug Deliv.* **2018**, *25*, 448–460. [[CrossRef](#)] [[PubMed](#)]
120. Menard, S.; Pupa, S.M.; Campiglio, M.; Tagliabue, E. Biologic and therapeutic role of HER2 in cancer. *Oncogene* **2003**, *22*, 6570–6578. [[CrossRef](#)]
121. Zhang, Q.; Liu, Q.; Du, M.; Vermorken, A.; Cui, Y.; Zhang, L.; Guo, L.; Ma, L.; Chen, M. Cetuximab and Doxorubicin loaded dextran-coated Fe₃O₄ magnetic nanoparticles as novel targeted nanocarriers for non-small cell lung cancer. *J. Magn. Magn. Mater.* **2019**, *481*, 122–128. [[CrossRef](#)]
122. Li, H.; Qian, Z.M. Transferrin/transferrin receptor-mediated drug delivery. *Med. Res. Rev.* **2002**, *22*, 225–250. [[CrossRef](#)]
123. Li, S.; Zhao, H.; Fan, Y.; Zhao, G.; Wang, R.; Wen, F.; Wang, J.; Wang, X.; Wang, Y.; Gao, Y. Design, synthesis, and in vitro antitumor activity of a transferrin receptor-targeted peptide-doxorubicin conjugate. *Chem. Biol. Drug Des.* **2020**, *95*, 58–65. [[CrossRef](#)]
124. Liang, M.; Fan, K.; Zhou, M.; Duan, D.; Zheng, J.; Yang, D.; Feng, J.; Yan, X. H-ferritin-nanocaged doxorubicin nanoparticles specifically target and kill tumors with a single-dose injection. *Proc. Natl. Acad. Sci. USA* **2014**, *111*, 14900–14905. [[CrossRef](#)] [[PubMed](#)]
125. Chen, Z.; Zhai, M.; Xie, X.; Zhang, Y.; Ma, S.; Li, Z.; Yu, F.; Zhao, B.; Zhang, M.; Yang, Y.; et al. Apoferritin nanocage for brain targeted doxorubicin delivery. *Mol. Pharm.* **2017**, *14*, 3087–3097. [[CrossRef](#)] [[PubMed](#)]
126. Pan, X.; Su, N.; Li, J.; Huang, H.; Wu, Z.; Sha, K.; Chen, J.; Wu, Z.; Qi, X. Tetralysine modified H-chain apoferritin mediated nucleus delivery of chemotherapy drugs synchronized with passive diffusion. *J. Drug Deliv. Sci. Technol.* **2021**, *61*, 102132. [[CrossRef](#)]
127. Johnstone, R.W.; Frew, A.J.; Smyth, M.J. The TRAIL apoptotic pathway in cancer onset, progression and therapy. *Nat. Rev. Cancer* **2008**, *8*, 782–798. [[CrossRef](#)] [[PubMed](#)]
128. Jiang, T.; Mo, R.; Bellotti, A.; Zhou, J.; Gu, Z. Gel-liposome-mediated co-delivery of anticancer membrane-associated proteins and small-molecule drugs for enhanced therapeutic efficacy. *Adv. Funct. Mater.* **2014**, *24*, 2295–2304. [[CrossRef](#)]

VIII. Oświadczenia współautorów publikacji

Gdańsk, dnia 19.10.2021 r.

Kamila Butowska

Międzyuczelniany Wydział Biotechnologii
Uniwersytetu Gdańskiego i Gdańskiego
Uniwersytetu Medycznego
ul. Abrahama 58
80-307 Gdańsk

OŚWIADCZENIE WSPÓŁAUTORA

Ja niżej podpisana, Kamila Butowska oświadczam, że mój wkład w publikacje wchodzące w skład rozprawy doktorskiej był następujący:

Tytuł: Cytotoxicity of doxorubicin conjugated with C₆₀ fullerene. Structural and in vitro studies.

Autorzy: K. Butowska, W. Kozak, M. Zdrowowicz, S. Makurat, M. Rychłowski, A. Hać, A. Herman-Antosiewicz, J. Piosik, J. Rak

Opublikowanej w: *Structural Chemistry*, 2019, 30, 6, 2327-2338 (DOI: 10.1007/s11224-019-01428-4).

mój udział polegał na: zaprojektowaniu koncepcji i planu badań, wykonaniu syntezy tytułowego koniugatu, przeprowadzeniu pomiarów spektrofotometrycznych i spektrofluorometrycznych oraz przy użyciu DLS, wykonaniu testu cytotoksycznego SRB, analizie otrzymanych wyników, przygotowaniu grafik oraz części manuskryptu dotyczących wykonanych eksperymentów, korekcie manuskryptu.

Tytuł: The product of matrix metalloproteinase cleavage of doxorubicin for anticancer drug delivery: calorimetric, spectroscopic, and molecular dynamics studies on peptide-doxorubicin binding to DNA.

Autorzy: K. Butowska, K. Żamojć, M. Kogut, W. Kozak, D. Wyrzykowski, W. Wiczek, J. Czub, J. Rak, J. Piosik

Opublikowanej w: *International Journal of Molecular Sciences*, 2020, 21, 18, 6923 (DOI: 10.3390/ijms2118623).

mój udział polegał na: zaprojektowaniu koncepcji i planu badań, wykonaniu syntezy tytułowego koniugatu, przeprowadzeniu trawienia enzymatycznego i analizie HPLC, analizie otrzymanych wyników, przygotowaniu grafik oraz przygotowaniu ostatecznej wersji manuskryptu (autor korespondencyjny).

Tytuł: MMPs-sensitive release of doxorubicin as a strategy for cancer targeted therapy.

Autorzy: K. Butowska, W. Kozak, M. Kogut, Z. Pietralik-Molińska, A. Moliński, K.

Kitowska, M. Kozak, J. Czub, R. Sądej, J. Rak, J. Piosik

Przesłanej do: Materials, 2021

Mój udział polegał na: zaprojektowaniu koncepcji i planu badań, wykonaniu syntezy tytułowego koniugatu, wykonaniu pomiarów AFM, przeprowadzeniu testu cytotoksycznego MTT, analizie otrzymanych wyników, przygotowaniu grafik oraz przygotowaniu ostatecznej wersji manuskryptu (drugi autor korespondencyjny).

Tytuł: Doxorubicin-conjugated siRNA lipid nanoparticles for combination cancer therapy.

Autorzy: K. Butowska, X. Han, N. Gong, R. El-Mayta, R. M. Haley, W. Zhong, W. Guo, M. J. Mitchell

Przesłanej do: Acta Pharmacologica Sinica B, 2021

Mój udział polegał na: zaprojektowaniu koncepcji badań, otrzymaniu badanych układów, przeprowadzeniu pomiarów DLS, zeta potencjału i spektrofotometrycznych, wykonaniu testów i analiz in vitro, określeniu profilu uwalniania DOX, uczestniczeniu i przeprowadzeniu części badań in vivo, analizie otrzymanych wyników, przygotowaniu grafik oraz przygotowaniu treści manuskryptu.

Tytuł: Polymeric nanocarriers: a transformation in doxorubicin therapies.

Autor: K. Butowska, A. Woźniowska, A. Borowik, J. Piosik

Opublikowanej w: Materials, 2021, 14, 2135. (DOI:10.3390/ma14092135)

Mój udział polegał na: opracowaniu koncepcji pracy przeglądowej, zebraniu literatury podmiotu, napisaniu głównej części manuskryptu, przygotowaniu figur, przygotowaniu ostatecznej wersji manuskryptu.

A handwritten signature in black ink, appearing to be 'Butecki' followed by a stylized flourish.

Gdańsk, dnia 21.10.2021 r.

dr hab. Jacek Piosik, prof. UG

Pracowania Biofizyki

Międzyuczelniany Wydział Biotechnologii

Uniwersytetu Gdańskiego i Gdańskiego

Uniwersytetu Medycznego

OŚWIADCZENIE

Oświadczam, że mój wkład w poniższe publikacje

Tytuł: Cytotoxicity of doxorubicin conjugated with C₆₀ fullerene. Structural and in vitro studies.

Autorzy: K. Butowska, W. Kozak, M. Zdrowowicz, S. Makurat, M. Rychłowski, A. Hać, A. Herman-Antosiewicz, J. Piosik, J. Rak

Opublikowanej w: Structural Chemistry, 2019, 30, 6, 2327-2338 (DOI: 10.1007/s11224-019-01428-4).

Tytuł: The product of matrix metalloproteinase cleavage of doxorubicin for anticancer drug delivery: calorimetric, spectroscopic, and molecular dynamics studies on peptide-doxorubicin binding to DNA.

Autorzy: K. Butowska, K. Żamojć, M. Kogut, W. Kozak, D. Wyrzykowski, W. Wiczek, J. Czub, J. Rak, J. Piosik

Opublikowanej w: International Journal of Molecular Sciences, 2020, 21, 18, 6923 (DOI: 10.3390/ijms2118623).

Tytuł: Polymeric nanocarriers: a transformation in doxorubicin therapies.

Autorzy: K. Butowska, A. Woźniowska, A. Borowik, J. Piosik

Opublikowanej w: Materials, 2021, 14, 9, 22135 (DOI: 10.3390/ma14092135).

Tytuł: MMP-sensitive release of doxorubicin as a strategy for cancer targeted therapy.

Autorzy: K. Butowska, W. Kozak, M. Kogut, Z. Pietralik-Molińska, A. Moliński, K. Kitowska,
M. Kozak, J. Czub, R. Sądej, J. Rak, J. Piosik

Przesłanej do: Materials

mój udział polegał na : opieką merytoryczną, interpretowaniu wyników) eksperymentów oraz edycji treści manuskrypu.

Podkreślam, iż mgr Kamila Agnieszka Butowska pełniła wiodącą rolę w powstanie powyższych manuskryptów.

(podpis)





Gdańsk, 20 października 2021 r.

prof. dr hab. Janusz Rak
Wydział Chemii
Uniwersytet Gdański

OŚWIADCZENIE

Oświadczam, że mój wkład do niżej wymienionych publikacji, składających się na pracę doktorską mgr Kamili Agnieszki Butowskiej, polegał na uczestniczeniu w: planowaniu projektów, interpretowaniu wyników eksperymentów oraz przygotowaniu poszczególnych manuskryptów.

1. K. Butowska, W. Kozak, M. Zdrowowicz, S. Makurat, M. Rychłowski, A. Hać, A. Herman-Antosiewicz, J. Piosik, J. Rak, Cytotoxicity of doxorubicin conjugated with C60 fullerene. Structural and in vitro studies. *Structural Chemistry*, 2019, 30, 2327–2338.
2. K. Butowska, K. Żamojć, M. Kogut, W. Kozak, D. Wyrzykowski, W. Wicz, J. Czub, J. Piosik, J. Rak, The product of matrix metalloproteinase cleavage of doxorubicin conjugate for anticancer drug delivery: calorimetric, spectroscopic, and molecular dynamic studies on peptide-doxorubicin binding to DNA. *International Journal of Molecular Sciences*, 2020, 21, 6923.
3. K. Butowska, W. Kozak, M. Kogut, Z. Pietralik-Molińska, A. Moliński, K. Kitowska, M. Kozak, J. Czub, R. Sądej, J. Rak, J. Piosik, MMPs-sensitive release of doxorubicin as a strategy for cancer targeted therapy. *Przesłana do Materials*. 2021.

Gdańsk, dnia 05.08.2021 r.

Prof. dr hab. Anna Herman-Antosiewicz
Katedra Biologii i Genetyki Medycznej
Wydział Biologii
Uniwersytet Gdański
Wita Stwosza 59
80-309 Gdańsk

OŚWIADCZENIE WSPÓŁAUTORA

Oświadczam, że w pracy pt. **Cytotoxicity of doxorubicin conjugated with C₆₀ fullerene. Structural and in vitro studies** (autorzy: K. Butowska, W. Kozak, M. Zdrowowicz, S. Makurat, M. Rychłowski, A. Hać, A. Herman-Antosiewicz, J. Piosik, J. Rak), opublikowanej w *Structural Chemistry*, 2019, 30, 6, 2327-2338 (DOI: 10.1007/s11224-019-01428-4) mój wkład w jej powstanie polegał na sprawowaniu nadzoru merytorycznego nad częścią biologiczną badań (testy żywotności) oraz współudziale w przygotowaniu manuskryptu.

Anna Herman-Antosiewicz

Gdańsk, dnia 03.08.2021 r.

dr Aleksandra Hać
Wydział Biologii
Uniwersytet Gdański
Wita Stwosza 59
80-309 Gdańsk

OŚWIADCZENIE WSPÓLAUTORA

Oświadczam, że w pracy:

Tytuł: **Cytotoxicity of doxorubicin conjugated with C₆₀ fullerene. Structural and in vitro studies.**

Autorzy: K. Butowska, W. Kozak, M. Zdrowowicz, S. Makurat, M. Rychłowski, A. Hać, A. Herman-Antosiewicz, J. Piosik, J. Rak

Opublikowanej w: Structural Chemistry, 2019, 30, 6, 2327-2338 (DOI: 10.1007/s11224-019-01428-4).

mój udział polegał na: prowadzeniu hodowli komórkowych, współudziale w projektowaniu i wykonaniu testów żywotności oraz przygotowaniu preparatów do mikroskopii konfokalnej, współudziale w opracowaniu wyników oraz redagowaniu manuskryptu.

Aleksandra Hać

Gdańsk, dnia 25.09.2021 r.

dr inż. Witold Kozak

Wydział Chemii
Uniwersytet Gdański
ul. Wita Stwosza 80/308
80-308 Gdańsk

OŚWIADCZENIE WSPÓLAUTORA

Oświadczam, że w pracy:

Tytuł: **Cytotoxicity of doxorubicin conjugated with C₆₀ fullerene. Structural and in vitro studies.**

Autorzy: K. Butowska, W. Kozak, M. Zdrowowicz, S. Makurat, M. Rychłowski, A. Hać, A. Herman-Antosiewicz, J. Piosik, J. Rak

Opublikowanej w: *Structural Chemistry*, 2019, 30, 6, 2327-2338 (DOI: 10.1007/s11224-019-01428-4).

mój udział polegał na syntezie tytułowego koniugatu oraz na pomocy przy redagowaniu manuskryptu.

Witold Kozak
(podpis)

Gdańsk, dnia 30.07.2021 r.

dr Samanta Romanowska (Makurat)

Wydział Chemii
Uniwersytet Gdański
Wita Stwosza 63
80-308 Gdańsk

OŚWIADCZENIE WSPÓLAUTORA

Oświadczam, że w pracy:

Tytuł: **Cytotoxicity of doxorubicin conjugated with C₆₀ fullerene. Structural and in vitro studies.**

Autorzy: K. Butowska, W. Kozak, M. Zdrowowicz, S. Makurat, M. Rychłowski, A. Hać, A. Herman-Antosiewicz, J. Piosik, J. Rak

Opublikowanej w: *Structural Chemistry*, 2019, 30, 6, 2327-2338 (DOI: 10.1007/s11224-019-01428-4).

mój udział polegał na:

- wykonaniu i opracowaniu wyników obliczeń kwantowochemicznych (TD-DFT).

*Samanta Romanowska
(Makurat)*

Gdańsk, dnia 09.08.2021 r.

dr Michał Rychłowski

Międzyuczelniany Wydział Biotechnologii

Uniwersytetu Gdańskiego i Gdańskiego Uniwersytetu Medycznego

Abrahama 58

80-307 Gdańsk

OŚWIADCZENIE WSPÓLAUTORA

Oświadczam, że w pracy:

Tytuł:

Cytotoxicity of doxorubicin conjugated with C₆₀ fullerene. Structural and in vitro studies.

Autorzy:

K. Butowska, W. Kozak, M. Zdrowowicz, S. Makurat, M. Rychłowski, A. Hać,

A. Herman-Antosiewicz, J. Piosik, J. Rak

Opublikowanej w:

Structural Chemistry, 2019, 30, 6, 2327-2338 (DOI: 10.1007/s11224-019-01428-4).

mój udział polegał na pomocy w zaprojektowaniu doświadczeń z użyciem mikroskopu konfokalnego i wykonaniu zdjęć, oraz współudziale w przygotowaniu manuskryptu.



Gdańsk, dnia 11.08.2021 r.

dr Magdalena Zdrowowicz-Żamojć

Wydział Chemii

Uniwersytet Gdański

Wita Stwosza 63

80-308 Gdańsk

OŚWIADCZENIE WSPÓLAUTORA

Oświadczam, że w pracy:

Tytuł: **Cytotoxicity of doxorubicin conjugated with C₆₀ fullerene. Structural and in vitro studies.**

Autorzy: K. Butowska, W. Kozak, M. Zdrowowicz, S. Makurat, M. Rychłowski, A. Hać, A. Herman-Antosiewicz, J. Piosik, J. Rak

Opublikowanej w: Structural Chemistry, 2019, 30, 6, 2327-2338 (DOI: 10.1007/s11224-019-01428-4).

mój udział polegał na: *przeprowadzeniu testu cytotoksyczności dla badanych związków przy użyciu testu WST-1, opracowaniu i analizie statystycznej uzyskanych wyników.*

Zdrowowicz-Żamojć

Gdańsk, dnia 24.09.2021 r.

dr hab. inż. Jacek Czub, prof. PG

Wydział Chemiczny
Politechnika Gdańska
ul. Narutowicza 11/12
80-233 Gdańsk

OŚWIADCZENIE WSPÓŁAUTORA

Oświadczam, że w pracy:

Tytuł: **The product of matrix metalloproteinase cleavage of doxorubicin for anticancer drug delivery: calorimetric, spectroscopic, and molecular dynamics studies on peptide-doxorubicin binding to DNA.**

Autorzy: K. Butowska, K. Żamojć, M. Kogut, W. Kozak, D. Wyrzykowski, W. Wiczak, J. Czub, J. Rak, J. Piosik

Opublikowanej w: International Journal of Molecular Sciences, 2020, 21, 18, 6923 (DOI: 10.3390/ijms2118623).

mój wkład polegał na: *współdziałanie w zaprojektowaniu symulacji molekularnych, analizie ich wyników oraz napisaniu części tekstu dotyczącego tychże symulacji.*



(podpis)

Warszawa, dnia 24.09.2021 r.

dr Mateusz Kogut

Instytut Fizyki

Polska Akademia Nauk

Aleja Lotników 32/46

02-668 Warszawa

OŚWIADCZENIE WSPÓŁAUTORA

Oświadczam, że w pracy:

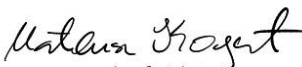
Tytuł: **The product of matrix metalloproteinase cleavage of doxorubicin for anticancer drug delivery: calorimetric, spectroscopic, and molecular dynamics studies on peptide-doxorubicin binding to DNA.**

Autorzy: K. Butowska, K. Żamojć, M. Kogut, W. Kozak, D. Wyrzykowski, W. Wiczak, J. Czuba, J. Rak, J. Piosik

Opublikowanej w: International Journal of Molecular Sciences, 2020, 21, 18, 6923 (DOI: 10.3390/ijms2118623).

mój udział polegał na

współdziałanie w zaprojektowaniu symulacji molekularnych, wykonaniu symulacji, analizie ich wyników oraz napisaniu części tekstu dotyczącego tychże symulacji.


(podpis)

Gdańsk, dnia 25.09.2021 r.

dr inż. Witold Kozak
Wydział Chemii
Uniwersytet Gdański
ul. Wita Stwosza 80/308
80-308 Gdańsk

OŚWIADCZENIE WSPÓLAUTORA

Oświadczam, że w pracy:

Tytuł: The product of matrix metalloproteinase cleavage of doxorubicin for anticancer drug delivery: calorimetric, spectroscopic, and molecular dynamics studies on peptide-doxorubicin binding to DNA.

Autorzy: K. Butowska, K. Żamojć, M. Kogut, W. Kozak, D. Wyrzykowski, W. Wicz, J. Czub, J. Rak, J. Piosik

Opublikowanej w: *International Journal of Molecular Sciences*, 2020, 21, 18, 6923 (DOI: 10.3390/ijms2118623).

mój udział polegał na syntezie tytułowego koniugatu oraz na pomocy przy redagowaniu manuskryptu.

Witold Kozak
(podpis)

Gdańsk, dnia 03.09.2021 r.

Prof. Dr hab. Wiesław Wiczek

Wydział Chemii

Uniwersytet Gdański

Wita Stwosza 63

80-308 Gdańsk

OŚWIADCZENIE WSPÓŁAUTORA

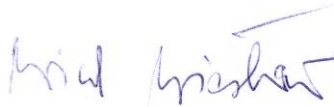
Oświadczam, że w pracy:

Tytuł: The product of matrix metalloproteinase cleavage of doxorubicin for anticancer drug delivery: calorimetric, spectroscopic, and molecular dynamics studies on peptide-doxorubicin binding to DNA.

Autorzy: K. Butowska, K. Żamojć, M. Kogut, W. Kozak, D. Wyrzykowski, W. Wiczek, J. Czub, J. Rak, J. Piosik

Opublikowanej w: International Journal of Molecular Sciences, 2020, 21, 18, 6923 (DOI: 10.3390/ijms2118623).

mój udział polegał na współudziale i sprawowaniu nadzoru merytorycznego w pomiarach spektrofluorymetrycznych.



Gdańsk, dnia 03.08.2021 r.

dr hab. Dariusz Wyrzykowski

Wydział Chemii

Uniwersytet Gdański

Wita Stwosza 63

80-308 Gdańsk

OŚWIADCZENIE WSPÓLAUTORA

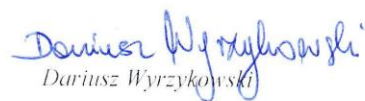
Oświadczam, że w pracy:

Tytuł: **The product of matrix metalloproteinase cleavage of doxorubicin for anticancer drug delivery: calorimetric, spectroscopic, and molecular dynamics studies on peptide-doxorubicin binding to DNA.**

Autorzy: K. Butowska, K. Żamojć, M. Kogut, W. Kozak, D. Wyrzykowski, W. Wiczek, J. Czub, J. Rak, J. Piosik

opublikowanej w: International Journal of Molecular Sciences, 2020, 21, 18, 6923 (DOI: 10.3390/ijms2118623).

mój udział polegał wyłącznie na obsłudze technicznej izotermicznego kalorymetru miareczkowego (wykonaniu pomiarów kalorymetrycznych) oraz przekazaniu uzyskanych wyników Pani Magister Kamili Butowskiej. Powyższej pracy nie wykorzystałem i nie zamierzam wykorzystać w postępowaniu o nadanie jakiegokolwiek stopnia naukowego lub zawodowego.


Dariusz Wyrzykowski

Dr inż. Krzysztof Żamojć

Gdańsk, dnia 03.08.2021 r.

Wydział Chemii
Uniwersytet Gdański
Wita Stwosza 63
80-308 Gdańsk

OŚWIADCZENIE WSPÓLAUTORA

Oświadczam, że w pracy:

Tytuł: **The product of matrix metalloproteinase cleavage of doxorubicin for anticancer drug delivery: calorimetric, spectroscopic, and molecular dynamics studies on peptide-doxorubicin binding to DNA.**

Autorzy: K. Butowska, K. Żamojć, M. Kogut, W. Kozak, D. Wyrzykowski, W. Wiczak, J. Czub, J. Rak, J. Piosik

opublikowanej w:

International Journal of Molecular Sciences, 2020, 21, 18, 6923 (DOI: 10.3390/ijms2118623).

mój udział polegał na przeprowadzeniu wszystkich pomiarów spektrofluorymetrycznych (w stanie podstawowym) oraz opracowaniu i opisanu uzyskanych z nich wyników.


dr inż. Krzysztof Żamojć
Uniwersytet Gdański
Wydział Chemii

Gdańsk, dnia 21.10.2021 r.

dr hab. Jacek Piosik, prof. UG

Pracownia Biofizyki

Międzyuczelniany Wydział Biotechnologii

Uniwersytetu Gdańskiego i Gdańskiego

Uniwersytetu Medycznego

OŚWIADCZENIE AUTORA KORESPONDECYJNEGO

Oświadczam, że mój wkład autorów w poniższą publikację

Tytuł: **MMP-sensitive release of doxorubicin as a strategy for cancer targeted therapy.**

Autorzy: K. Butowska (K.B.), W. Kozak (W.K.), M. Kogut (M.K.), Z. Pietralik-Molińska (Z.P-M.), A. Moliński (A.M.), K. Kitowska (K.K.), M. Kozak (M.K.), J. Czub (J.C.), R. Sądej (R.S.), J. Rak (J. R.), J. Piosik (J. R.)

Przesłanej do: Materials

był następujący:

Koncepcja: K.B., J.R., J.P.; Analiza: K.B., W.K., M.K., Z.P-M., A.M., K.K., M.K, R.S., J.R., J.C., J.P.; Przeprowadzenie eksperymentów: K.B., W.K., M.K., Z.P-M., A.M., K.K.; Finansowanie: J.R., J.P.; Pisanie oryginalnego tekstu manuskryptu: K.B., W.K., M.K., Z.P-M., A.M.; Edycja manuskryptu: K.K, M.K, R.S., J.R., J.C., J.P.; Opieka merytoryczna, J.R., J.P.; administrowanie projektem:, K.B.

Wszyscy autorzy przeczytali i zaakceptowali ostateczną wersję manuskryptu.

(podpis)



Michael J. Mitchell, Ph.D.
Skirkanich Assistant Professor of Innovation
School of Engineering and Applied Science
Department of Bioengineering
Abramson Cancer Center
Institute for Translational Medicine and Therapeutics

University of Pennsylvania
240 Skirkanich Hall, 210 S. 33rd Street
Philadelphia, PA 19104
Phone: 215-898-0882
Email: mjmitch@seas.upenn.edu

Philadelphia, 10/12/2021

CORRESPONDING AUTHOR STATEMENT

Here I declare that authors contribution into the publication:

Title: **Doxorubicin-conjugated siRNA lipid nanoparticles for combination cancer therapy**

Autors: K. Butowska, X. Han, N. Gong, R. El-Mayta, R. M. Haley, W. Zhong, W. Guo, M. J. Mitchell

Submitted on September 29th, 2021, to Acta Pharmaceutica Sinica B

was as follows:

K. Butowska and X. Han contributed equally to this work. K. Butowska, X. Han, and M. J. Mitchell conceived the project and designed the experiments. The experiments were performed by K. Butowska, X. Han, N. Gong, and W. Zhang and interpreted by all authors. K. Butowska, X. Han, and M. J. M. wrote the manuscript. K. Butowska designed and prepared the figures.

All authors edited the manuscript and figures and approved the final version for submission.



M. J. Mitchell

Gdańsk, dnia 19.10.2021 r.

PhD Xuexiang Han

Department of Bioengineering
University of Pennsylvania
240 Skirkanich Hall, 210 S. 33rd St
Philadelphia, PA 19104

AUTHOR STATEMENT

Here I declare that I contributed equal work below with Kamila Butowska

Title: **Doxorubicin-conjugated siRNA lipid nanoparticles for combination cancer therapy.**

Authors: K. Butowska, X. Han, N. Gong, R. El-Mayta, R. M. Haley, W. Zhong, W. Guo,
M. J. Mitchell

Submitted to: Acta Pharmacologica Sinica B, 2021

and my contribution into the publication was as follows:

I participated in project design. I was mentoring Kamila Butowska and help with experiments.

I consent to the use of the manuscript for Kamila's Butowska PhD thesis and further processing.

Xuexiang Han
Oct. 19, 2021

Oklahoma City, dnia 21.09.2021 r.

dr Agnieszka Borowik
Oklahoma Medical Research Foundation
Oklahoma City, OK 73104
Stany Zjednoczone

OŚWIADCZENIE WSPÓLAUTORA

Oświadczam, że w pracy:

Tytuł: **Polymeric nanocarriers: a transformation in doxorubicin therapies.**

Autorzy: K. Butowska, A. Wozniowiczka, A. Borowik, J. Piosik

Opublikowanej w: *Materials*, 2021, 14, 9, 22135 (DOI: 10.3390/ma14092135).

mój udział polegał na:

- pomocy w selekcji literatury źródłowej,
- opracowaniu tekstu manuskryptu – abstrakt,
- wprowadzeniu poprawek i redakcji tekstu.



Agnieszka Borowik

Gdańsk, dnia 7.09.2021 r.

dr Anna Woziwodzka

Międzyuczelniany Wydział Biotechnologii

Uniwersytetu Gdańskiego i Gdańskiego Uniwersytetu Medycznego

ul. Antoniego Abrahama 58

80-307 Gdańsk

e-mail: anna.woziwodzka@ug.edu.pl

OŚWIADCZENIE WSPÓLAUTORA

Oświadczam, że w pracy

Polymeric nanocarriers: a transformation in doxorubicin therapies,

autorstwa: K. Butowska, A. Woziwodzka, A. Borowik, J. Piosik, która została opublikowana

w czasopiśmie *Materials* (2021; 14: 2135, doi: 10.3390/ma14092135),

mój udział polegał na:

- udziale w opracowaniu koncepcji pracy,
- poszukiwaniu i wyselekcjonowaniu literatury źródłowej,
- krytycznej analizie zebranej literatury,
- opracowaniu tekstu manuskryptu – rozdział 'Introduction',
- wprowadzeniu istotnych merytorycznie poprawek do całości tekstu manuskryptu.


Anna Woziwodzka

183

IX. Spis dorobku naukowego

1. Pozostałe publikacje nie wchodzące w skład rozprawy doktorskiej

- [P6] D. O. Zavodovskiy, N. V. Bulgakova, I. Sokołowska, Y. Pryluskyy, U. Ritter, O. O. Gonchar, A. I. Kostyukov, O. V. Vlasenko, **K. Butowska**, J. Piosik, A.V. Maznychenko, *Water-soluble pristine C₆₀ fullerenes increase in force of isometric muscle contraction in inflammatory pain model in rats*. Scientific Reports, **2021**, przesłana
Współczynnik wpływu: 4.379
- [P7] H. Zhang, X. Han, M. G. Alameh, M. S. Padilla, L. Xue, **K. Butowska**, D. Weissman, M. J. Mitchell, *Rational design of anti-inflammatory lipid nanoparticles for mRNA delivery*. Journal of Biomedical Materials Research -Part A, **2021**, w recenzji
Współczynnik wpływu: 4.396
- [P8] X. Han, H. Zhang, **K. Butowska**, K. L. Swingle, M.-G. Alameh, D. Weissman, M. J. Mitchell, *An ionizable lipid toolbox for RNA delivery*. Nature Communications, **2021**, w recenzji
Współczynnik wpływu: 14.919
- [P9] O. O. Gonchar, A.V. Maznychenko, O.M. Klyuchko, I.M. Mankovska, **K. Butowska**, A. Borowik, J. Piosik, I. Sokołowska, *C₆₀ fullerene reduces 3-nitropropionic acid-induced oxidative stress disorders and mitochondrial dysfunction in rats by modulation of P53, Bcl-2 and Nrf2 targeted proteins*. International Journal of Molecular Sciences, **2020**, 21, 6923.
Współczynnik wpływu: 5.923
- [P10] A.V. Maznychenko, N.V. Bulgakova, I. V. Sokołowska, **K. Butowska**, A. Borowik, O.P. Mankivska, J. Piosik, T. Tomiak, O.O. Gonchar, V.O. Maisky, A.I. Kostyukov, *Fatigue-induced Fos immunoreactivity within the lumbar cord and amygdala decreases after C₆₀ fullerene pretreatment*, Scientific Reports, **2020**, 10, 1–12.
Współczynnik wpływu: 4.379
- [P11] H. Myszka, D. Grzywacz, M. Zdrowowicz, P. Spisz, **K. Butowska**, J. Rak, J. Piosik, M. Jaśkiewicz, W. Kamysz, B. Liberek, *Design, synthesis and biological evaluation of betulin-3-yl 2-amino-2-deoxy-B-D-glycopyranosides*. Bioorganic Chemistry, **2019**, 30, 2327–2338.
Współczynnik wpływu: 5.275
- [P12] A. Borowik, **K. Butowska**, K. Konkel, R. Banasiuk, N. Derewonko, D. Wyrzykowski, M. Davydenko, V. Cherepanov, V. Styopkin, Y. Pryluskyy, P. Pohl, A. Królicka, J. Piosik, *The impact of surface functionalization on the biophysical properties of silver nanoparticles*. Nanomaterials, **2019**, 9, 973.
Współczynnik wpływu: 4.034
- [P13] J. Ameixa, E. Arthur-Baidoo, R. Meisser, S. Makurat, W. Kozak, **K. Butowska**, F. Ferreira da Silva, J. Rak, S. Denifl, *Low-energy electron-induced decomposition of 5-trifluoromethanesulfonyl-uracil: a potential radiosensitizer*. The Journal of Chemical Physics, 2018, 149, 164–307.
Współczynnik wpływu: 3.488

Sumaryczny współczynnik wpływu: 46.339

Sumaryczny współczynnik wpływu publikacji [P1] – [P13]: 72.438

2. Rozdziały w monografiach

- [R1] M. Zdrowowicz, L. Chomicz-Mańka, **K. Butowska**, P. Spisz, K. Falkiewicz, A. Czaja, J. Rak, *DNA damage radiosensitizers geared towards hydrated electrons* w *Practical Aspects of Computational Chemistry V*. Ed. J. Leszczyński oraz M. Shukla, Springer, **2022**, ISBN 978-3-030-83243-8.

3. Granty i stypendia badawcze

- [G1] Narodowe Centrum Nauki, Maestro (**2015 – 2016**): *Od modelu molekularnego in silico do odpowiedzi komórkowej in vitro. Modyfikowane nukleozydy jak radio- bądź/i fotosensybilizatory uszkodzeń DNA*.
Rola: Wykonawca
- [G2] Europejski Fundusz Społeczny, Konkurs Amber (**2014 – 2015**): Radiosensybilizatory o wysokim powinowactwie to elektronu-mimetyki tlenu. Badania fizykochemiczne i komórkowe.
Rola: Kierownik

4. Staże naukowe

- Uniwersytet Pensylwanii, Filadelfia, Stany Zjednoczone (**2020 – 2021**)
- Uniwersytet Ludwika Maksymiliana, Monachium, Niemcy (**2014**)

5. Konferencje

Referaty ustne:

- [K2] **K. Butowska**, M. Zdrowowicz, J. Rak, *Badania fizykochemiczne nad właściwościami metronidazolu - potencjalnego radiosensybilizatora uszkodzeń DNA*, IV Poznańskie Sympozjum Młodych Naukowców, Poznań, Polska, **2017**.
- [K3] **K. Butowska**, M. Zdrowowicz, M. Sosnowska, P. Spisz, I. Serdiuk, J. Rak, *Ocena cytotoksyczności pochodnych uracylu jako potencjalnych sensybilizatorów DNA*, XLV Ogólnopolska Szkoła Chemii "Chemia na fali", Rozewie, Polska, **2016**.
- [K4] **K. Butowska**, M. Zdrowowicz, P. Wityk, K. Stoknicki, K. Bobrowski, J. Rak, *Dwie twarze metronidazolu. Protektor czy radiosensybilizator DNA?* XLIII Ogólnopolska Szkoła Chemii "Chemia wydobyta wiedzą", Pokrzywna, Polska, **2015**.
- [K5] **K. Butowska**, *Nitroimidazole jako sensybilizatory stosowane w walce z nowotworami*, XLI Ogólnopolska Szkoła Chemii "W sieci chemii", Karpacz, Polska, **2014**.

Postery:

- [PS2] J. Ameixa, E. Arthur-Baidoo, R. Meibner, S. Makurat, W. Kozak, **K. Butowska**, F. Ferreira da Silva, J. Rak, S. Denifl, *Electron attachment of OTfU: a potential radiosensitizer*, MD-GAS WG1 & WG2 Meeting, on-line, **2021**.
- [PS3] I. Mruk, **K. Butowska**, J. Piosik, *Influence of platinum nanoparticles on the biological activity of doxorubicin*, e-Zjazd Zimowy SSPTChem, on-line, **2020**.
- [PS4] P. Beldzińska, **K. Butowska**, D. Wyrzykowski, J. Piosik, *Interactions of platinum nanoparticles with cisplatin and their influence on the biological activity of the analyzed substance*, e-Zjazd Zimowy SSPTChem, **2020**.

- [PS5] I. Mruk, **K. Butowska**, D. Wyrzykowski, *Modulation of doxorubicin biological activity by platinum nanoparticles*, I Studenckie Sympozjum Chemiczne, on-line, **2020**.
- [PS5] P. Beldzińska, **K. Butowska**, D. Wyrzykowski, J. Piosik, *Interactions of platinum nanoparticles with cisplatin and carboplatin, and their influence on the biological activity of the analyzed substances*, on-line, **2020**.
- [PS6] **K. Butowska**, A. Borowik, K. Konkel, D. Wyrzykowski, J. Piosik, *Functionalized silver nanoparticles interactions with model mutagen ICR-191*, Intercollegiate Biotechnology Symposium "Symbioza", Warszawa, Polska, **2019**.
- [PS7] K. Konkel, **K. Butowska**, D. Wyrzykowski, J. Piosik, *Functionalized silver nanoparticles and their interactions with anthracycline antibiotic - doxorubicin*, Intercollegiate Biotechnology Symposium "Symbioza", Warszawa, Polska, **2019**.
- [PS8] K. Bańkowska, **K. Butowska**, J. Piosik, *Modulation of daunomycin activity by silver nanoparticle*, Intercollegiate Biotechnology Symposium "Symbioza", Warszawa, Polska, **2019**.
- [PS9] K. Konkel, **K. Butowska**, A. Borowik, D. Wyrzykowski, J. Piosik, *Charakterystyka biofizyczna nanocząstek srebra i ich oddziaływania z mutagenem akrydynowym ICR-191*, XXV Konferencja Naukowa Wydziału Farmaceutycznego z OML, Gdańsk, Polska, **2018**.
- [PS10] **K. Butowska**, M. Zdrowowicz, J. Rak, *Metronidazole - a potential radiosensitizer*, 9th PULS Conference on Pulse Investigations in Chemistry, Physics and Biology and 4th PKCM Conference on Reaction Kinetics in Condensed Matter, Łódź, Polska, **2018**.
- [PS11] A. Woziwodzka, A. Borowik, **K. Butowska**, J. Piosik, *Assessing caffeine impact on cell membrane integrity*, 5th European Joint Theoretical/Experimental Meeting on Membranes, Kraków, Polska, **2017**.
- [PS12] **K. Butowska**, *How do oxygen-mimetic radiosensitizers work? Theoretical and experimental studies*, Bioinnovation International Summit, Gdańsk, Polska, **2017**.
- [PS13] **K. Butowska**, M. Zdrowowicz, P. Wityk, J. Rak, *Na drodze do rozwiązania zagadki radiosensybilizującego działania metronidazolu*, XLIV Ogólnopolska Szkoła Chemii "Poznaj naszą chemię", Poznań, Polska, **2016**.
- [PS14] **K. Butowska**, M. Zdrowowicz, P. Wityk, M. Żyndul, K. Stoknicki, K. Bobrowski, J. Rak, *Influence of metronidazole on DNA damage induced by ionizing radiation. Is metronidazole a radiosensitizer or radioprotector?* 55 Zjazd Polskiego Towarzystwa Chemicznego, Gdańsk, Polska, **2015**.
- [PS15] **K. Butowska**, P. Wityk, L. Chomicz, J. Rak, *Oxygen-mimetic radiosensitizers for use in radiotherapy*, International Science Conference-Chemistry, Environmental and Nanotechnology, Gdańsk, Polska, **2015**.
- [PS16] **K. Butowska**, P. Wityk, L. Chomicz, J. Rak, *Jak działają radiosensybilizatory? Badania metoda teorii funkcjonału gęstości (DFT)*, Ogólnopolskie Mikrosympozjum Chemików "Chemia-zaczyna się dziś", Białystok, Polska, **2015**.
- [PS17] P. Wityk, L. Chomicz, M. Wieczor, J. Czub, **K. Butowska**, J. Rak, *A DFT study of radiosensitizers*, CECAM Tutorial: Hybrid Quantum Mechanics/Molecular Mechanics (QM/MM), Approaches to Biochemistry and Beyond, Lozanna, Szwajcaria, **2015**.

- [PS18] P. Wityk, **K. Butowska**, L. Chomicz, J. Rak, *How do oxygen-mimetic radiosensitizers work? A DFT study*, 22nd Young Research Fellows Meeting Chemistry and Biology: a permanent dialogue, Paryż, Francja, 2015.
- [PS19] **K. Butowska**, *Radiosensibilizatory o wysokim powinowactwie do elektronu*, XVII Zjazd Zimowy Sekcji Studenckiej Polskiego Towarzystwa Chemicznego, Wrocław, Polska, **2014**.
- [PS20] **K. Butowska**, *Green Fluorescence Protein - niezwykle białko o szerokim spectrum zastosowań*, XL Ogólnopolska Szkoła Chemii "Chemia zrodzona z natury", Augustów, Poland, **2014**.

Sumaryczna ilość konferencji: 25

6. Nagrody i wyróżnienia

- Narodowa Agencja Wymiany Akademickiej, Program im. Iwanowskiej (**2020 – 2021**): *Multifunctional lipid nanoparticles for overcoming biological barriers to drug delivery*.
- Zwiększone stypendium z dotacji projakościowej dla najlepszych doktorantów MWB UG-GUMed (**2017 – 2021**)